Data-driven semiconducting nanomaterials design for energy applications

by

Yeseul Choi

A dissertation submitted to the Graduate Faculty of
Auburn University
in partial fulfillment of the
requirements for the Degree of
Doctor of Philosophy

Auburn, Alabama

Aug 06, 2022

Keywords: DFT, Thermochemistry, Si-based nanomaterials, SiN nanocluster,
Pyrolytic synthesis, Reaction mechanism, Reactivity, Rate constant

Approved by

Dr. Andrew J. Adamczyk, Chair, Department of Chemical Engineering,
Dr. Mario Eden, Department Chair, Joe T. and Billie Carole McMillan Professor, Department
of Chemical Engineering
Dr. Xinyu Zhang, Associate Professor, Department of Chemical Engineering, Auburn
University
Dr. Michael Hamilton, Director of Alabama Micro/Nano Science and Technology Center,
Department of Electrical and Computer Engineering, Auburn University
Dr. Thomas J. Preston, Soldrevet Chemistry

Abstract

Silicon nitrides and hydrogenated silicon nitrides attract widespread scientific interest across multiple application fields due to their superior combination of optical, mechanical, thermal and optoelectronic properties. The wide range of possible applications of silicon nitrides are structural, cutting tools, passivation layers in solar cells, permeation barriers and encapsulation layers in light-emitting device (LED). The wide bandgap (~5.2 eV) of thin films allows for its optoelectronic application, while the silicon nitrides could act as a host matrix for silicon nano-inclusions (Si-ni) for solar cell devices and lithium ion battery anodes.

In order to produce silicon-based nanoparticles[1, 3-6], there have been various methods such as pyrolysis[7], chemical vapor deposition[8-12], atomic layer deposition[13] and sputtering. Among those methods, a basal protocol to create silicon-alloyed nanoparticles and understand the synthetic mechanism is pyrolysis. Recent comprehensive reviews of silicon nitrides in both monolithic and thin films mostly focus on the current film deposition techniques, silicon nitrides' physical, electronic, optoelectronic properties, and their applications.

Synthesizing nanomaterial thorough pyrolysis is of specific interest regarding simplicity, flexibility, and scalability. Because any mixtures of precursor gases can be built into multi-functional nanoparticles that can be directly used for specific applications instead of focusing on modification of nanostructures after they have been formed.

Co-pyrolysis of SiH_4 and NH_3 is one protocol to create polycrystalline or amorphous silicon nitrides nanoparticles in the gas phase or controlled growth of silicon wafers at a gas-solid interface to form semiconductor-grade materials through chemical vapor deposition (CVD) methods. Polymerization of silicon-alloyed in the gas phase causes deposits on a growing semiconductor surface forming point defects. A detailed understanding of the microkinetics for the gas-phase formation of silicon-based nanoparticles will allow for the improvement of applications in which silicon nanoparticles are desired or side products. Unfortunately, the fundamental explanation of the synthesis is still vague. In order to understand the fundamental of a reaction system, the first step is considered to understand the properties of materials, which can be used as reactants, intermediate structures, and products. The second step is understanding what kind of reaction

occurs in the system. The third step is to be able to present an integrated reaction mechanism in the basic condition. In the final step, we are asked to predict all the possible reactions in a specific reaction condition.

While a limited number of computational studies of silicon nitride nanoparticle formation have been carried out to address these concerns at the elementary step level, augmentation of these models to address multifunctionality, more accurate treatment of kinetics, and the complex, polycyclic nature of silicon nitrides is warranted. Using quantum chemical calculations, statistical thermodynamics, conventional and variational transition state theory, accurate rate coefficients were calculated for over 130 reactions involving 1,2-hydrogen shift, H_2 addition-elimination, substituted silylene addition-elimination, and cyclization-ring opening. Silane and Ammonia co-pyrolysis has been employed for synthesizing, yet rate coefficients of cannot be measured directly for all possible reactions of silicon nitrides of relevant sizes and substituents. Thus, silicon nitrides containing up to 6 silicon atoms, a variety of acyclic and cyclic substituents about the reactive center, and polycyclic nature were explored. The Evans-Polanyi correlation was revised for multifunctional kinetics, and representative pre-exponential factors were calculated. Additionally, thermochemical properties for 113 silicon-alloyed clusters containing up to 6 heavy atoms (Si and Ge, Si and N) were calculated to analyze the polycyclic and multifunctional nature of complex species.

This research serves the understanding of silicon nitrides nanoparticle formation at the molecular level and provides the practical value of the kinetic correlations governing silicon nitrides nanoparticle formation to engineers designing new nanomaterials and reactor systems for semiconductors or tailored nanoparticles.

Acknowledgments

Table of Contents

List of Tables

List of Figures

List of Abbreviations

AAD	Average absolute deviation.
ALD	Atomic layer deposition
BAC	Bond additivity correction
BD	Bonding
CASSCF	The complete active space self-consistent field
CBS	Complete basis set
CC	Coupled cluster theory
CMOS	Complementary metal-oxide semiconductor
CR	Core
CVD	Chemical vapor deposition
DFT	Density functional theory
EDS	Electron dispersion spectroscopy
E_{el}	Electronic energies
FMO	Frontier molecular orbital
HN	Hexagonal planar (SiN)
HOMO	Highest occupied molecular orbital
HW-CVD	Hot wired chemical vapor deposition
ICT	Intramolecular charge transfers
IoT	Internet of things
KS-DFT	Kohn-Sham density functional theory
LED	Light-emitting diodes/light-emitting device
LP	Lone pair
LUMO	Lowest unoccupied molecular orbital
MO	Molecular orbital
MOSFETs	Metal oxide semiconductor field effect transistors
MP	Møller–Plesset perturbation theory
MP2	Møller–Plesset second order perturbation
MRCI	Multi-reference configuration interaction
NBO	Natural bond orbital

NLS	Natural Lewis structure
NMOS	N-channel metal-oxide semiconductors
PECVD	Plasma enhanced chemical vapor deposition
PES	Potential energy surface
PN	Pentagonal planar (SiN)
Pri	Prismane geometries (SiGe)
PriN	Prismane structres (SiN)
PVD	Physical vapor deposition
QST3	Synchronous Transit-guided Quasi-Newton method
RAM	Random access memory
RY	Ryberg
SCF	Self-consistent field
SCF	Self-consistent field
SEM	Scanning Electron Microscopy
SHS	Self-propagating high temperature synthesis
Si:C S/D	Silicon–carbon source/drain stressors
SiGe HBT	Silicon-germanium heterojunction bipolar transistors
SN	Square planar (SiN)
ST	Substituted trigonal planar (SiGe)
STN	Substituted trigonal planar (SiN)
STS	Strain-transfer structure
TP	Trigonal planar (SiGe)
TBP	Trigonal bipyramidal (SiGe)
TBPyN	Trigonal bipyramidal geometries (SiN)
TEM	Transmission electron microscopy
TN	Trigonal planar (SiN)
TP	Trigonal pyramidal (SiGe)
TPyN	Trigonal pyramid (SiN)
TST	Transition state theory
UFP	Ultra fine powders
ZPE	Zero-point vibrational energy

Chapter 1

Introduction

1.1 Overview

We live in a society where life is inconvenient without electronic devices such as smartphones and tablet computers; most of our daily routine is going by these electronic devices. Modern convenience has been made possible by the remarkable development of semiconductors due to the improvement of the degree of integration known as Moore's Law in the manufacture of various electronic devices for the past 50 years. The most contributed components of these electronic devices are integrated circuits chips and batteries, the intensive development of both enables in not only smaller, lighter, and higher performance of devices, but also lower consumption,
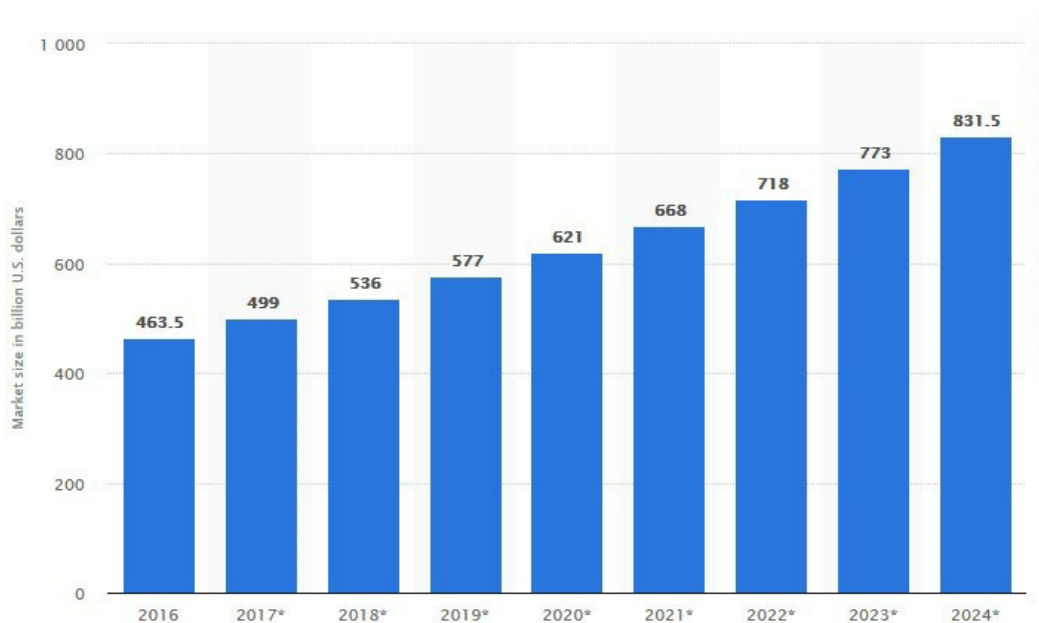
Figure 1.1 Semiconductor market size worldwide from 2016 to 2024 in billion U.S. dollar. [2]

long life, and durability of devices. The **Figure 1.1** shows a steady increase in the global semiconductor industry sales every year from 2016 to 2024. In 2024, it is expected to reach $ 831.5 billion worldwide. With the advent of autonomous vehicles and the Internet of Things that led to the development of semiconductors, demand for semiconductor chips will continue to increase. Moreover, to handle lots of information efficiently for Artificial Intelligence and big data analysis, demand for semiconductor chips will increase explosively in the future. Semiconductors are classified by functions. There are memory semiconductors, system semiconductors and special semiconductors such as discrete devices or optical devices. As examples of different functions of semiconductor, there are random access memory (RAM), transistors, light-emitting diode (LED), and solar cells respectively. The semiconductor of interest here is mainly silicon-based semiconductors usually for system and memory devices.

H. W. Brattain, J. Bardeen, and W. Shockely in Bell Laboratories made the first semiconductor with germanium in 1947, but silicon has replaced for main semiconducting material with thermal stability at high temperature. After the metal oxide semiconductor field effect transistor (MOSFETs) were developed using silicon and silicon oxides in the 1960s, the size of transistors has been reduced by the results that the number of transistor per chip area has been successfully integrated by about two times every two years (Moore's Law). At present, it has been minimized to the size of less than 10 nm scale[14, 15], but the technique of lowering the driving voltage has not been developed relatively compared to the integration techniques.

A new semiconducting material by doping other elements in group 3A-5A to silicon enables us to reduce the size of semiconductor and devise a novel design. As an example of a few nanoscale sizes of SiGe material, author Pi and coworkers synthesized 3nm diameter size of SiGe crystals **Figure 1.2**. The fundamental reason why information and communication devices and

services consume enormous amounts of energy and power is that MOSFETs consume considerable power.
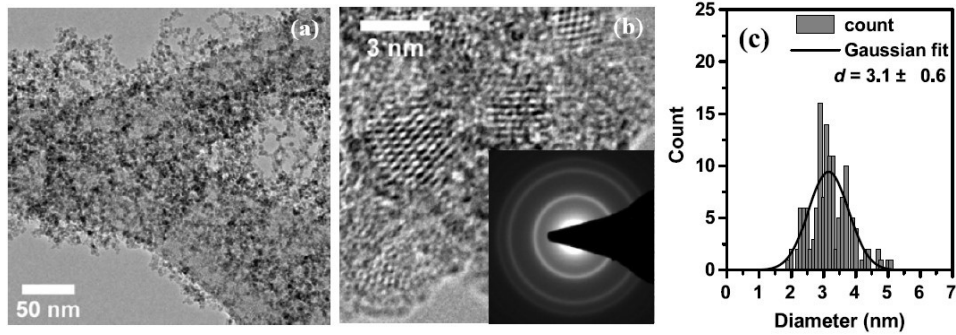
Figure 1.2 $Si_{0.45}Ge_{0.55}$ alloy nanocrystals on a lacy-carbon grid examined by (a) low- resolution and (b) high-resolution TEM. A selected area electron diffraction pattern is shown as the inset of (b). The (c) size distribution is Gaussian with a mean size of 3.1 nm and a standard deviation of 0.6 nm. [13] (Copyright permission obtained from the IOP Publishing, 2009)

Replacing silicon-germanium heterojunction bipolar transistor (SiGe HBT) with complementary metal-oxide semiconductor (CMOS) enabled to achieve higher performance. K-Wang et al.[16] demonstrated n-channel metal-oxide semiconductor (NMOS) transistor with SiGe hetero structure embedded beneath the channel and silicon-carbon source/drain (Si:C S/D) stressors. The additional strain effect by SiGe structure from the S/D stressors to Si channel enabled improvement of 40% in drive current compared to unstrained control devices. **Figure 1.3 (a)** is the cross-sectional transmission electron microscopy (TEM) image of a completed strained transistor with Si:C S/D stressors and embedded SiGe region as an strain-transfer structure (STS). **Figure 1.3 (b)** is the electron dispersion spectroscopy (EDS) measurement results which shows no Ge out-diffusion to gate dielectric interface due to optimized strained-Si channel thickness.

For the Silicon-nitride materials, it has been widely used for the electronic devices such as

oxidation masks, passivation layers, gate insulating layers, dielectric layers and antireflection coatings with a wide band-gap (5.3 eV). Silicon nitride is mostly used for inactive materials,[17-19] however, several groups have reported potential of silicon nitride for anode material of lithium ion battery.[20, 21] Ulvestada et al.[1] suggested silicon nitride conversion reaction with lithium ion and demonstrated electrochemical performance of a-SiN$_x$ thin films with compositions ranging from pure Si to $SiN_{0.89}$. The optical and scanning electron microscopy (SEM) images of $SiN_{0.89}$ thin films by Ulvestada were represented in **Figure 1.4.**

(a) (b)
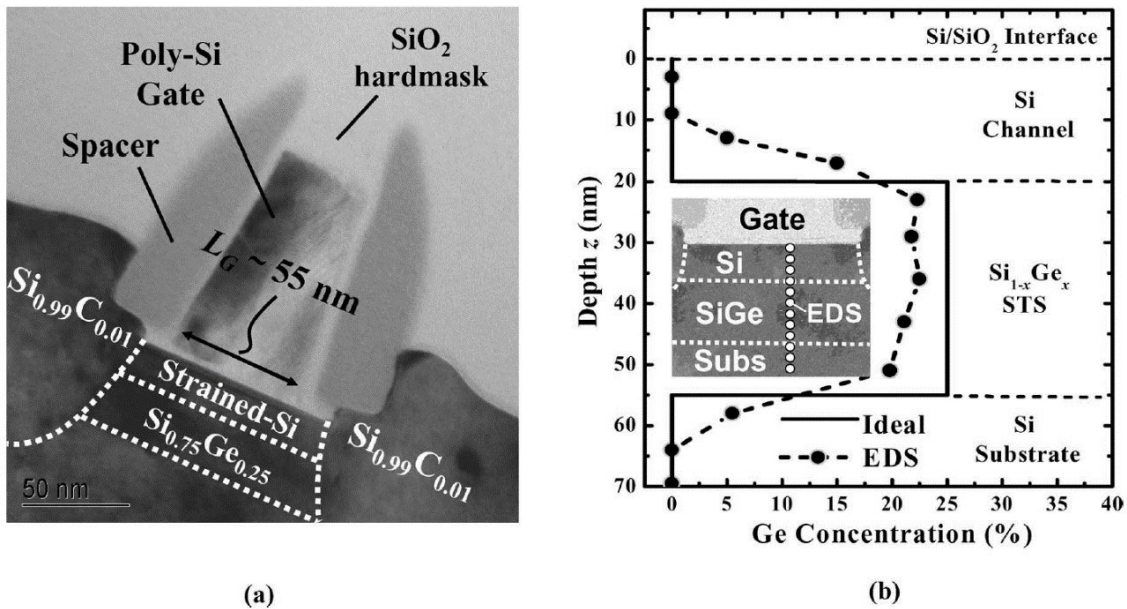
Figure 1.3: (a) Transmission electron microscopy (TEM) image of a strained n-MOSFET with silicon-germanium strain-transfer structure (SiGe STS) and silicon–carbon source/drain (Si:C S/D) stressors. No misfit dislocations were observed at the vertical het heterojunction between the Si:C S/D and the embedded SiGe STS, indicating a pseudomorphic epitaxy growth. (b) Ge concentration profile as a function of depth obtained using electron dispersion spectroscopy (EDS) measurements. A well-controlled thermal budget and an optimum choice of strained-Si channel thickness prevent Ge out-diffusion to the Si/SiO$_2$ interface, which is important for the achievement of good gate dielectric quality and high electron mobility. [16] (Copyright permission obtained from IEEE Publishing, 2008)
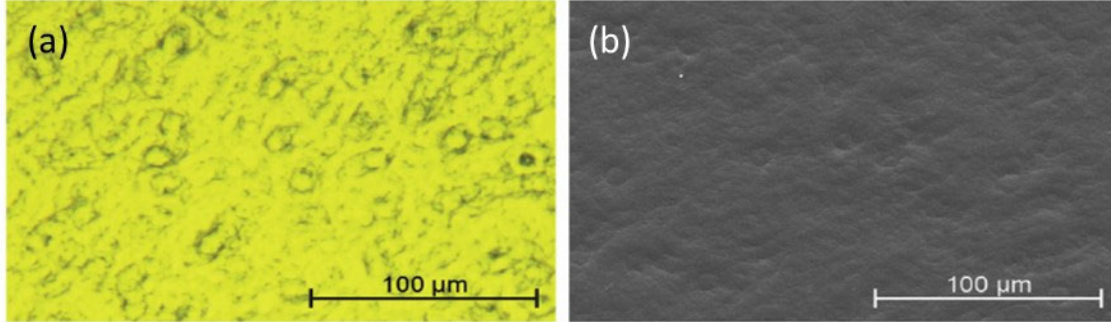
Figure 1.4. Plane view optical (a) and SEM (b) micrographs of the 156 nm $SiN_{0.89}$ film. The structure of the surface is related to the structure of the rolled copper substrate. *Copyright © 2018,* Asbjørn Ulvestad et al. [1]

In order to produce more efficient semiconductors, there have been conducted numerous research, but understanding fundamental mechanism of semiconducting material formation is still deficient. The chemical vapor deposition (CVD) method has been widely used for the synthesis of semiconducting materials by the pyrolysis[22] or non-thermal plasma from precursor gases. Understanding nucleation reaction, which occurs during pyrolysis, is important to produce semiconducting materials with desirable properties. Undesired defects can arise in semiconductor processing because these nanoclusters deposit on the growing substrate as illustrated in **Figure 1.5.**

The first step of understanding nucleation mechanism begins figuring the thermodynamic and electrical properties of nanoclusters. Using calculated thermodynamic properties of materials, we can postulate a kinetic mechanism or kinetic pathway and estimate the reaction rate of the reactant in the system.
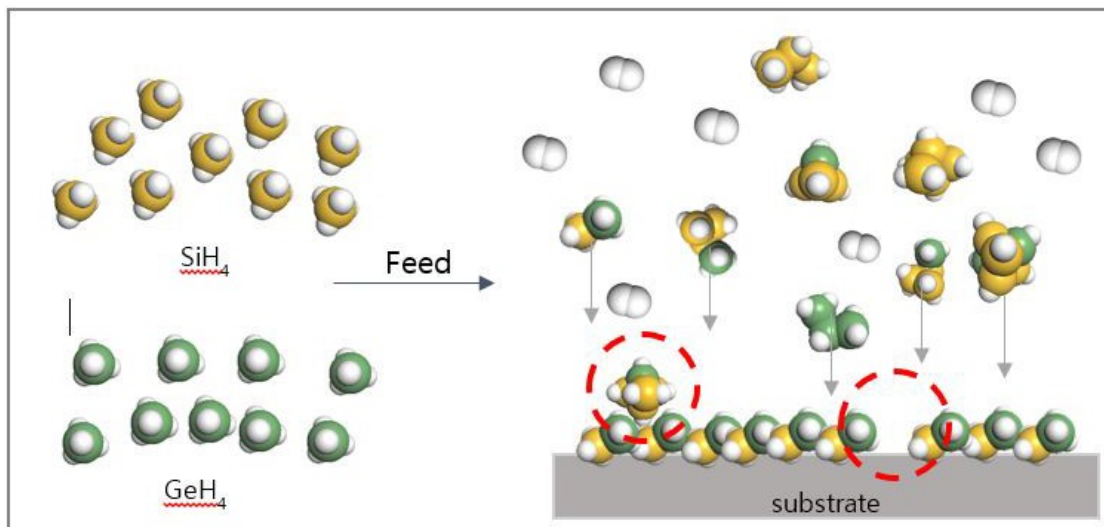
Figure 1.5 Graphic illustration of defect arise during CVD process

From that information, we would expect to design more sophisticated semiconductor and simplify the semiconductor manufacturing process. For this purpose, we have strong motivation to predict the thermodynamic and electrical properties of Ge or N-doped silicon clusters.

1.2 Synthesis of Silicon Nitride Nanoparticles

Since the synthesis of silicon nitride by heating elemental Si in an atmosphere of N generated by the decomposition of potassium cyanide was reported by Balmen in the middle of the last century, silicon nitride has played a leading role among all known refractory compounds, especially during the previous two decades.[23] Due to its remarkable properties such as low density, thermal stability, unique electrical properties, and readily available starting materials, the interest

in silicon nitrides has been sustained.[23] The wide range of possible applications of silicon nitrides in structural, cutting tools,[23] and passivation layers in solar cells, permeation barriers and encapsulation layer in light-emitting device (LED) [3] have attracted attention from specialists in the different research area.

Si₃N₄ nanoparticles can be prepared by many of the standard synthesis technology methods listed in **Table 1**. The main methods of preparing Si₃N₄ powders have relied on mechanosynthesis, now widely used in preparing powders of many refractory compounds and intermetallics.[24-26] The use of ammonia when milling silicon has been shown to be significantly more effective than nitrogen[27], but the produced Si₃N₄ contains impurities and may require further purification or other processing depending on the usage purpose of the material.

Table 1. Main methods of synthesis of silicon nitride powders and their variants.[23]

Method	Main reactions	Main variants of the method
Direct synthesis of components	$3Si + 2N_2 \rightarrow Si_3N_4$ $3Si + 4NH_3 \rightarrow Si_3N_4 + 6H_2$	Self-propagating high temperature synthesis (SHS). Plasma-chemical synthesis. Mechanosynthesis*[28]
Carbothermic reduction	$3SiO_2 + 6C + 2N_2 \rightarrow Si_3N_4 + 6CO$	(T = 1400-1550 °C, P_N = 0.1-6 MPa
Gas-phase synthesis	$3SiCl_4 + 16NH_3 \rightarrow Si_3N_4 + 13NH_4Cl$ $3SiH_4 + 4NH_3 \rightarrow Si_3N_4 + 12H_2$	Plasma-chemical synthesis. Laser synthesis.
	$SiH_4 \rightarrow SiH_2 + H_2 \rightarrow Si + 2H_2$	Thermally induced (pyrolytic synthesis)[29]
	$SiH_4 + xNH_3 \rightarrow SiN_x + (2+1.5x)\,H_2$; (0<x<4/3)	
	$Si + xNH_3 \rightarrow SiN_x + 1.5xH_2$	
Dissosication (pyrolysis)	$3Si(NH)_2 \rightarrow Si_3N_4 + 2NH_3$ $(\frac{1}{n})[SiR_2 - \mathrm{NR}]_n \rightarrow Si_3N_4 + RH + H_2$	Laser induced
Milling	Intensive milling of silicon in ammonia (150h) then treated by vacuum at 800"C for 8h	Contain impurities (O 14.2%, Re 1.3, Ti 2.0%)

Direct synthesis using the self-propagating high-temperature synthesis (SHS) of the compound [30-33] has the advantage of relatively low oxygen contents (0.4-0.6%) compared to other methods, but this is because of the use of pure starting materials such as semiconductor-grade silicon and thoroughly purified nitrogen.[34] However, commercial-grade powders prepared by the SHS method have a much higher content of impurities, for example, their oxygen content is up to 2%. The SHS methods has been heavily used for Si_3N_4 consolidation or synthesis from another silicon alloy such as ferrosilicon.[35-37] Synthesizing silicon nitrides by the self-propagating combustion of silane and ammonia mixtures without oxygen additions has not been reported.[23] Only the synthesis of silicon oxynitride powders has been reported.

The carbothermic reduction of silicon oxide in a nitrogen atmosphere does not offer high purity and requires additional milling and purification. Even though Ekelund et al. have shown the pressure influence on contents of the materials that at nitrogen pressures between 2 and 6 MPa, the evaporation of the silicon monoxide and the formation of nonequilibrium phases can be largely suppressed, thus bringing the carbon and oxygen content of the reaction products under control. [38] and Li et al. synthesized the high-purity α-Si_3N_4 nanopowder without any β-Si_3N_4 impurities using HNO_3 and $CO(NH_2)_2$ as reaction raw materials, $C_6H_{12}O_6 \cdot H_2O$ as carbon source and SiO_2 as silicon source, the carbothermic reduction method still has a limitation that an additional process such as the nitridation method is required for higher purity Si_3N_4 nanopowders.[39]

For ultrafine silicon nitride nanopowders with a particle size of less than 100 nm, the gas-phase synthesis is essential. [38] The gas-phase synthesis stimulates homogeneous nucleation, and thus allows silicon nitride to be prepared in the form of ultra fine powders(UFP) under appropriate conditions, which varies depending on pretreatment methods with plasma, laser, or thermal –

assisted. The reactions between ammonia and the vaporous of silane, silicon tetrachloride or their derivatives, have been widely investigated.[40-45] The starting material $SiCl_4$ has a cost-competitiveness, but silane precursor gives a better-quality product, but also it also require precautions in handling.

From the aforementioned methods, the various forms of commercially produced silicon nitride: fibers, monocrystals, and SiAlON ceramics. [23] The production and properties these type of silicon nitrides have been discussed, but there is no study regarding the synthesis mechanisms of silicon nitrides.[40,46]

1.3 Background

1.3.1 Rate Coefficient Specification

In order to synthesize a novel material or to optimize reaction conditions for specific desired materials, it is important to understand the entire reaction system. For understanding the reaction system, it is required to estimate the rates of all reactions occurring, for that the rate coefficient data is indispensable. The best option for selecting rate coefficients is always experimental data. However, since most reactions in silicon chemistry are very fast, it is difficult to monitor and capture the intermediates in order to quantify individual rate coefficients. In addition, there are few analytic tools to detect or identify the experimentally obtained data, it is challenging to analyze the intermediate structures and even the product molecules. Thus, experimentally measured rate coefficients for reactions comprising silicon nitride nanoparticle formation are scarce. To fill these gaps in the experimental values, the rate coefficients can be predicted with the help of quantum chemistry. The overall schematic used to specify and estimate rate coefficients is shown in **Figure 1.6**. The rate coefficients should be specified considering kinetic correlations. These correlations use thermodynamic properties, thus it is important to obtain accurate thermodynamic properties governing species and reactions in silicon nitride chemistry.

If the experimental thermodynamic properties are not available, we can compute rate coefficients of reacting species. To obtain reliable thermodynamic properties of a given molecule, quantum chemical calculations using commercial software packages was applied. The first step of the quantum calculation is performing geometry optimization to find the minimum energy state of interesting molecules or a first-order saddle point of transition state. Geometry optimization is

achieved by solving the Schrödinger equation shown in **equation (1.1)**,

$$\widehat{H}\Psi = E\Psi \quad \textit{eq (1.1)}$$

where $\widehat{H}$ is the Hamiltonian operator, Ψ is the wavefunction, and E is the electronic energy. The geometry of the molecule is continuously modified until its electronic energy and nuclear repulsion reaches to minimum.
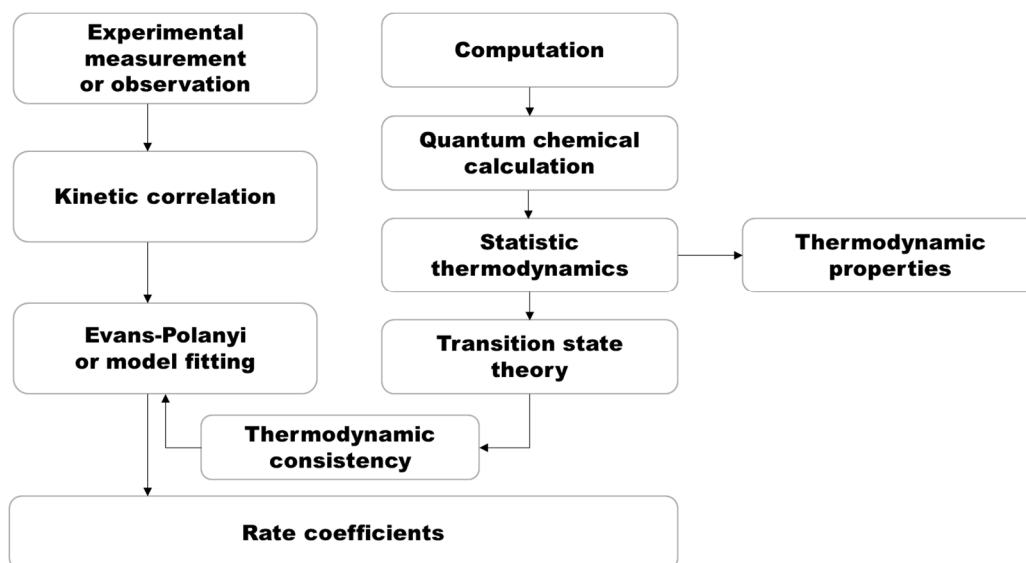
Figure 1.6. Schematic of specification of rate coefficients.

Once the optimal geometry and associated electronic energy in the ground state are identified, the Hessian is evaluated. If all the eigenvalues of the Hessian are positive, the energy of the geometry is a minimum. For a transition state structure, it should be located at a saddle point on the potential energy surface (PES) where one negative eigenvalue of the Hessian is. Once the Hessian elements are specified through geometry optimization, the vibrational frequencies of the molecule can be calculated easily within the rigid-rotor and harmonic oscillator approximation.

Vibrational frequencies are essential for calculating thermodynamic properties such as enthalpy, entropy, and heat capacity via statistical thermodynamics.

From a view of statistical mechanics, macroscopic behavior (thermodynamic observables) of the molecules can be calculated from molecular properties. Statistical thermodynamics assumes that the quantized energy levels associated with a particular system are known. From these quantized energy-level data, a temperature-dependent quantity called the *partition function* can be calculated.

Partition function describes the statistical properties of a system. For instance, in molecules, the energy levels are by electronic and nuclear motion, which can be further subdivided into translation, rotation, and vibration. The molecular partition function can be written as a product in **Equation (1.2),**

$$q(\beta) = q_{trans}(\beta) \cdot q_{rot}(\beta) \cdot q_{vib}(\beta) \cdot q_{elec}(\beta) \qquad \textit{eq (1.2)}$$

where *β = 1/RT, R* is the ideal gas constant, and *T* is temperature.

The electronic partition function is typically based solely on the electronic energy of the ground state. Translational and rotational contributions are only dependent on temperature, mass, and the moment of inertia of the molecule and can be calculated using the simple models of a particle in a box and the rigid rotor, respectively. Using the partition function, all of the thermodynamic properties of the molecules in system can be calculated.

Finally, the thermodynamic properties calculated from the partition function could be employed for the rate coefficient equation derived and based on Transition state theory. The thermodynamic properties are also required to specify the equilibrium constant to preserve microscopic reversibility.

1.3.2 Rate Coefficient

Rate constant (k) quantifies the rate and the direction of a chemical reaction in chemical kinetics. For a simple bimolecular reaction between reactants A and B to form products C and D,

$$aA + bB \leftrightarrow cC + dD$$
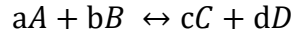
One common form of the reaction rate is,

$$rate = k(T)[A]^m[B]^n \qquad \textbf{\textit{eq (1.3)}}$$

k(t) is the reaction rate constant that depends on temperature, and [A] and [B] are the molar concentrations of reactants A and B in moles per second, assuming the reaction is taking place in the gas-phase. The exponents m and n are called partial orders of reaction and these are not usually equal to the stoichiometric coefficients a and b. Instead, they depend on the reaction mechanism and can be obtained experimentally. For an elementary step, there is a relationship between stoichiometry and rate law, as determined by the law of mass action. Almost all elementary steps are either unimolecular or bimolecular. For this elementary bimolecular reaction, the rate constant usually depends only on temperature and can be calculated from the Arrhenius equation **(equation 1.4)**,

$$k(T) = A \cdot exp(\frac{-E_a}{RT}) \qquad \textbf{\textit{eq (1.4)}}$$

where k is the rate constant at a temperature T, A is the Arrhenius factor or pre-exponential factor, E_a is the activation energy, and R is the molar gas constant. The values for A and E_a are provided by experimental data.

The Arrhenius equation can give the quantitative basis of the relationship between the

activation barrier and the reaction rate. The rate constant is a function of thermodynamic temperature, which is shown in **equation (1.5)**. Then, the reaction rate is given by

$$\text{rate} = A \cdot exp(\tfrac{-E_a}{RT})[A]^m[B]^n \qquad\qquad eq\ (1.5)$$

At temperature T, the molecules (reactants) have energies according to a Boltzmann distribution, and it can be expected that the proportion of collisions with energy greater than activation energy (E_a) to vary with $exp(\tfrac{-E_a}{RT})$. The constant A is the proportionality of collisions, or frequency factor, which expresses the frequency at which reactant molecules are colliding and the likelihood that a collision leads to a successful reaction.

We can also determine the rate constant using Eyring equation from transition state theory (TST), which is a more sophisticated model with statistical thermodynamic consideration than the Arrhenius equation.

$$k(T) = \frac{\kappa k_B T}{h} \cdot exp(\frac{-\Delta G^{\neq}}{RT}) \qquad\qquad eq\ (1.6)$$

Equation (1.6) is the general form of the Eyring equation, where κ is the transmission coefficient, k_B is Boltzmann's constant, h is Planck's constant and $\Delta G^{\neq}$ is the Gibbs energy of activation. Eyring equation from transition state theory requires κ, the transmission coefficient, This κ is often considered to be equal to one meaning that the species passing through the transition state always proceed directly to product and it never reverts to reactants.

Based on one of thermodynamic characteristic, $\Delta G^{\neq} = \Delta H^{\neq} - T \cdot \Delta S^{\neq}$; the temperature dependence Gibbs energy is calculated by these parameters, the enthalpy of activation $\Delta H^{\neq}$ and the entropy of activation $\Delta S^{\neq}$, the Eyring equation can be rewritten as **equation (1.7)**,

$$k(T) = \frac{\kappa k_B T}{h} \cdot exp(\frac{\Delta S^{\neq}}{R}) exp(\frac{-\Delta H^{\neq}}{RT}) \qquad \textit{eq (1.7)}$$

Here, the Gibbs free energy of activation takes into consideration both the activation energy ($\Delta H^{\neq}$) and the possibility of successful collision and the $\frac{k_B T}{h}$ term means the frequency of molecular collision.

The difference between the two models, the Arrhenius and the Eyring, is that Arrhenius equation was empirically obtained by experiments and observation, while the Eyring equation was developed from the statistical thermodynamic consideration of the relationship between reaction rate and energy. This means that Arrhenius model is used for a whole reaction whether it is single or multi-step, however, Eyring model can be involved in individual reaction steps. Thus, two models are not directly comparable unless the reaction is a single step elementary reaction.

Other equations can be employed for rate coefficient calculation. Collision theory considers that reactants are hard spheres with a particular cross-section and offers the **equation (1.8)** for modeling the temperature dependence of the rate constants.

$$k(T) = PZ \cdot exp(\frac{-\Delta E}{RT}) \qquad \textit{eq (1.8)}$$

where P is the probability factor and Z is the collision frequency, and ΔE is activation energy. Because the collision frequency Z is proportional to $T^{1/2}$, this equation shows different temperature dependence of the rate constant.

Another method is Divided Saddle Theory developed relatively-recently. Divided Saddle Theory which has common motifs in general with Bennett-Chandler formalism in particular with the effective positive flux variant [47], provides a practical method taking into account re-crossing

of transition states to reactants. The basic concept of the Divided Saddle Theory is based on the division of the saddle regions of the free energy profile of the rare event into two adjacent segments called Saddle Domains.[47] However this method is not widely used yet, and further studies are underway to assess the efficiency of the method. [47]

1.3.3 Transition State Theory

Transition state theory (TST) provides us Eyring equation which can predict a more accurate rate coefficient. In principle, TST can be used to calculate the rate constant for only elementary reaction or the reaction that follows elementary rate law. It is difficult to find the transition state not only in the laboratory, but also even with the powerful quantum chemical tools due to the high computational cost. TST can solve the difficulties by assuming a special type of chemical equilibrium between reactants and the transitions state species, which is quasi-equilibrium assumption. The basic idea of transition state theory is that rates of reaction can be studied by examining activated complexes near the saddle point, transition state, of a potential energy surface. But the details of how these complexes are formed are not significant.

The Arrhenius equation (**equation 1.4**) has been widely accepted, but the physical interpretation of A and E_a remained vague by the early 20th century. Many chemical kinetic scientists attempted to offer theories that relate A and E_a directly to molecular dynamics in order to explain how chemical reactions occur. This was solved by introducing the concept of standard

Gibbs energy of activation. The progress of a chemical reaction could be described as a point on a potential energy surface with coordinates in atomic momentum and distances.

If we consider the reaction below, where complete equilibrium is achieved between all the species in the system.

$$A + B \rightleftharpoons [A \cdot B_f]^{\neq} \rightarrow P$$

TST assumes that the activated complexes (species in the transition state or saddle point) are in quasi-equilibrium with the reactants even when the reactants and products are not in equilibrium with each other. It is also assumed that the flux of activated complexes in the two directions are independent of each other and only the flux of activated complexes, which is designated $[A \cdot B_f]^{\neq}$ in the **Figure 1.7**, is considered. That is, the reactants are in equilibrium only with $[A \cdot B_f]^{\neq}$.
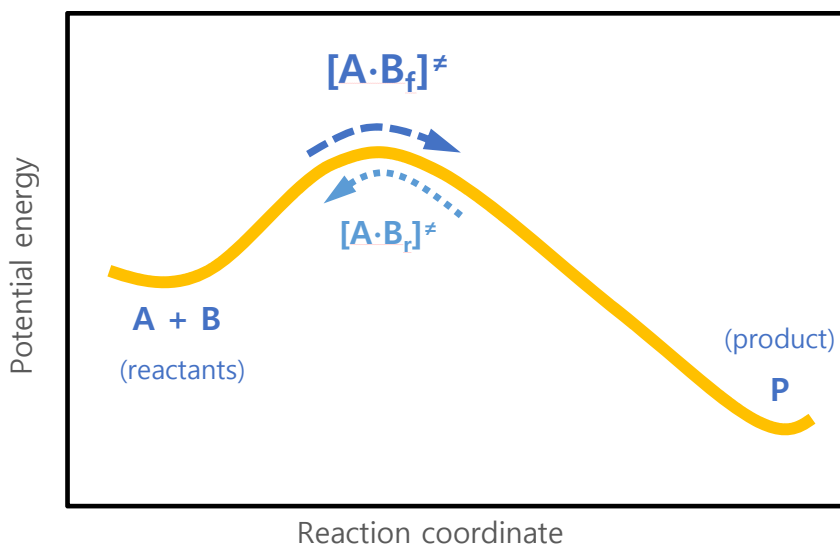
Figure1.7 Potential energy diagram

The activated complexes do not follow a Boltzmann distribution of energies, but using the equilibrium constant $\mathbf{K}^{\neq}$ for the quasi-equilibrium between reactants and the activated complexes, the equation can be written as

$$K^{\neq} = \frac{[A \cdot B]^{\neq}}{[A][B]} \qquad \textit{eq (1.9)}$$

And the reaction rate of production of P is,

$$\frac{d[P]}{dt} = k^{\neq}[A \cdot B]^{\neq} = k^{\neq}K^{\neq}[A][B] = k[A][B] \qquad \textit{eq (1.10)}$$

Where the rate constant $\boldsymbol{k}$ is given by

$$k = k^{\neq}K^{\neq} \qquad \textit{eq (1.11)}$$

Here, $k^{\ddagger}$ is directly proportional to the frequency of the vibrational mode responsible for converting the activated complex to the product. The frequency of this vibrational mode is $\boldsymbol{v}$. Every vibration does not necessarily lead to the formation of product. To account this effect, a proportionality constant $\boldsymbol{\kappa}$, referred to as the transmission coefficient, is introduced. So $\boldsymbol{k}^{\neq}$ can be rewritten as

$$k^{\neq} = \kappa v \qquad \textit{eq (1.12)}$$

For the equilibrium constant $\boldsymbol{K}^{\neq}$, statistical mechanics leads to a temperature dependent expression given as

$$K^{\neq} = \frac{k_B T}{h v} \cdot exp(\frac{-\Delta G^{\neq}}{RT}) \qquad \textit{eq (1.13)}$$

Combining the expressions for $\boldsymbol{k}^{\neq}$ and $\boldsymbol{K}^{\neq}$, **equation (1.11)-(1.13)**, a new rate constant expression can be written as **equation (1.6)**. Based on one of thermodynamic characteristic, $\Delta G^{\neq} = \Delta H^{\neq} - T \cdot \Delta S^{\neq}$, the equation can be written as **equation (1.7)** as well.

TST has been successful in calculating the standard enthalpy of activation, the standard entropy of activation, and the standard Gibbs energy of activation for carbon hydrides and silicon hydrides chemistry. Instead of conducting a TST calculation for every reaction, structure-reactivity correlations can be established from the identified transition states for a number of reactions in a homologous series. The exploit range of TST that has been successfully employed for silicon hydride and carbon hydride chemistry can be extended to silicon nitride chemistry.

Chapter 2

Thermodynamic and Electronic Properties of Hydrogenated Silicon Alloy Nanoclusters

2.1 Silicon Germanium Nanocluster

2.1.1 Introduction

Studies of semiconducting silicon-germanium (SiGe) materials are of technological interest because of their practical application in the microelectronics industry.[48] Moreover, SiGe clusters have attracted great interest for their use in optoelectronic, sensor, and photovoltaic applications.[49-54] Understanding semiconducting nanomaterials formation from the pyrolysis of mixtures of silane (SiH_4) and germane (GeH_4) at even the mildest conditions is still incomplete.[55-57] Homogenous gas-phase nanomaterials formation is a complex phenomenon in which hundreds, or possibly thousands of species, undergo simultaneous reaction. During the chemical vapor deposition of SiGe semiconducting nanomaterials, surface reactions play an important role. However, undesired defects can arise in semiconductor processing because these SiGe clusters deposit on the growing substrate. Since these clusters are important for the fine processing of semiconductors and the synthesis of novel materials, computational modeling can play a very important role in narrowing the gap between controlled experimental studies and practical operating conditions. Similarly, intentional synthesis of SiGe semiconducting nanomaterials[58, 59] in the gas phase can benefit from

an improved mechanistic understanding of formation to tailor efforts in materials design, particularly for self-assembling molecular systems and nanocomposites. Due to tunable semiconductor properties, Si, Ge, and SiGe clusters have also attracted great interest for the development of new materials in nanoscale applications as fundamental building blocks.[36] Both Si and Ge clusters have widely been studied because the structure and bonding of bulk Ge materials are very similar to that of bulk Si materials. Pristine Si and Ge clusters without hydrogen content are chemically reactive and thus not suitable as a building block for self-assembled materials.[60] However, this reactivity can be reduced with surface passivation by hydrogen or other suitable functional groups, such as alkyl functionalities. Si clusters have been studied extensively for their promising structural, thermochemical, and electronic properties.[61-67] For Ge clusters, there have been reported cage types of pure Ge structures with metal-doping.[68-70] Most Ge cluster studies have been conducted to investigate the geometric strain effect of clusters upon increased Ge content for medium to large cluster sizes.[71] However, to the best of our knowledge, analogous studies have not been reported for small- to medium-sized hydrogenated SiGe clusters.

Furthermore, nanocrystals of Ge have received significant interest in recent years.[52] Self-organized quantum dots of Ge were grown on Si substrates.[72] It was observed in Si/Ge superlattices[26, 27] and in Ge quantum, dots grown on Si[72] that interdiffusion between Si and Ge may occur to form alloys under certain growth conditions. Detailed knowledge of the thermodynamics and the nature of Ge–Si bonding is still needed to understand the spontaneous processes leading to the formation of self-organized structures. Compared to the vast data available on solid-state materials, theoretical solid-state studies on materials possessing Si Ge bonds and comprehension of the SiGe chemistry, especially for small clusters, are very rare.[73-76] The limited results which are available on such model clusters are confined to thermodynamic investigations

of the clusters of small sizes less than four atoms,[77, 78] measurement of optical properties of SiGe materials,[79] and a few advanced ab initio calculations on SiGe dimers.[80, 81] Structural characteristics were also determined theoretically for several selected larger clusters by applying semi-empirical methods which include tight-binding molecular dynamics approaches,[82, 83] density functional theory (DFT),[84] and Møller–Plesset second order perturbation (MP2) theories.[85] So far, no theoretical thermodynamic data, which could indirectly validate the calculated structures through comparison against the existing experiments, are available. Thus, detailed theoretical studies connecting the structures, bonding, and thermodynamic properties of Si, Ge, and SiGe clusters are critically needed.

Recently, automated network generation techniques[86] have allowed the kinetics of inorganic cluster and nanoparticle formation, such as Si clusters and nanoparticles, to be described at the mechanistic level.[87, 88] Rate coefficients must be estimated for every elementary step comprising the mechanistic model, and kinetic correlations are used to make this tractable. One common method for predicting activation barriers (E_a) is the Evans-Polanyi correlation; however, these structure-activity correlations require detailed thermochemical information for each reacting species. Recently, the existing group additivity database[89] for the prediction of thermochemical properties of hydrogenated silicon clusters was revised and augmented with new atom-centered groups, ring corrections, and bond-centered groups to accurately capture more complex species. Conversely, there are limited studies available that predict the thermochemical properties of SiGe and Ge clusters, which is the next step for expanding our thermochemistry database for semiconducting nanoparticle formation. For this purpose, we conducted a computational study of hydrogenated Si, Ge, and SiGe alloy clusters ($Si_xGe_yH_z$, $1<X+Y\leq6$) to predict structures, thermochemistry, and electronic properties. This paper presents the thermochemical properties of

46 cyclic and polycyclic Si, Ge, and SiGe clusters and 7 acyclic Si, Ge, and SiGe species, i.e., standard enthalpies of formation, standard entropy values, and constant pressure heat capacities, and specifically examines both multifunctional and monofunctional molecules containing between one and six Si and/or Ge atoms. The hydrogenated clusters in this study involved different degrees of hydrogenation, i.e., the ratio of hydrogen to Si and Ge atoms varied widely depending on the size of the cluster and/or degree of multifunctionality. Species containing different numbers of fused rings comprised of three to four Si or Ge atoms were considered. The composite method of G3//B3LYP was used to calculate the electronic energy, and then statistical thermodynamics was applied to all the hydrogenated Si, Ge, and SiGe clusters to incorporate temperature effects. Enthalpies of formation at 1 atm and 298 K were calculated using atomization energies and corrected with a novel bond additivity correction model. Standard entropies and constant pressure heat capacities were calculated using a temperature-dependent scaling factor for the vibrational frequencies to account for anharmonicity. Our studies have established trends in thermodynamic properties (standard enthalpy of formation (ΔH^o_f), standard entropy (S^o), and constant pressure heat capacity (C_p)), as a function of cluster composition and structure. Furthermore, we compared HOMO-LUMO energy gaps and HOMO and LUMO electron distributions in order to gain insight into the electronic stability of the hydrogenated Si, Ge, and SiGe clusters. Quantum chemical parameters such as electronic chemical potential μ, global hardness η, and the softness σ were also calculated to provide valuable information about chemical stability. These quantum chemical parameters were generalized using a machine learning approach to assess charge transfer during molecular interaction of hydrogenated Si, Ge, and SiGe clusters in the gas phase.

2.1.2 Computational Methodology

Quantum chemical calculations were performed with the Gaussian 16 software.[90] All electronic energies for the hydrogenated Si, Ge, and SiGe clusters and acyclic species were calculated using the G3//B3LYP composite method,[91, 92] which uses B3LYP/6-31G(d) geometries and higher level corrections based on single point energies. To assess different levels of theory, we employed the Gaussian 16 software to perform quantum chemical calculations using the CBS QB3, G3//B3LYP and G4//B3LYP composite methods. The primary difference between the Gn and CBS methods is how the correlation energy is estimated. The Gn methods assume basis set additivity and add an empirical correction to recover part of the remaining correlation energy. The complete basis set (CBS) procedures, on the other hand, attempt to perform an explicit extrapolation of the calculated values.[93] All electronic energies for the hydrogenated Si, Ge, and SiGe acyclic species in this study were calculated using these three levels of theory.

The optimized structures for all 46 hydrogenated Si, Ge, and SiGe clusters investigated in this study are depicted in **Figure 2.1.1**. The hydrogenated clusters of this study can exist in the singlet state and triplet state.[55, 94-96] As shown in **Table 2.1.1**, using the G3//B3LYP method, triplet-singlet splitting values of linear and cluster species were investigated. These calculated triplet-singlet splitting values suggest that the singlet potential energy surface is significantly lower in energy than the triplet potential energy surface. Thus, for all results reported in this study, the electronic wave functions for the hydrogenated Si, Ge, and SiGe clusters were optimized in the singlet state. Geometries and harmonic vibrational frequencies are confirmed local minima on the singlet potential energy surface, i.e., all of the vibrational frequencies are real. It is well-established that hydrogenated Si, Ge, and SiGe nanostructures pass through metastable configurations (or transient chemical species) before reaching a global minimum from molecular dynamics

simulations,[97] but detailed knowledge of the structure and thermochemistry of a wide range of hydrogenated clusters is still needed. The harmonic vibrational frequencies and zero-point vibrational energy (ZPE) were linearly scaled by a temperature-dependent scaling factor of 0.98, respectively, to account for anharmonicity in the normal vibrational modes as a function of temperature as suggested by Scott and Radom and Alecu and co-workers.[98, 99] Using conventional statistical thermodynamics, molecular partition functions based on the harmonic oscillator and rigid rotor approximations were used to calculate thermodynamic properties as a function of temperature.

A closer investigation of the 46 cluster structures in this study reveals no dangling Si-Si, Ge-Ge, and Si-Ge bonds capable of internal rotation for the clusters with the exception of the substituted trigonal planar geometry. Aside from the temperature-dependent scaling factor, anharmonic movements in torsional vibrational modes for the linear chemical species (Si_2H_6, Ge_2H_6, $SiGeH_6$, Si_3H_8, and Ge_3H_8) and the substituted trigonal planar cluster geometries were not treated. Similarly, anharmonicsmall ring movements (e.g.the pseudorotation of cyclopentasilanes and the ring puckering of cyclotetrasilanes incorporated into the multifunctional polycyclic structures) were not treated aside from the temperature- dependent scaling factor.[100, 101] The protocol in our study was implemented because (1) there are reduced anharmonic small ring movements for the more rigid structures in this study, which was verified by the animation of key vibrational modes, (2) the calculation of a revised partition function to account for anharmonic torsional modes and small ring movements was beyond the scope of this study.
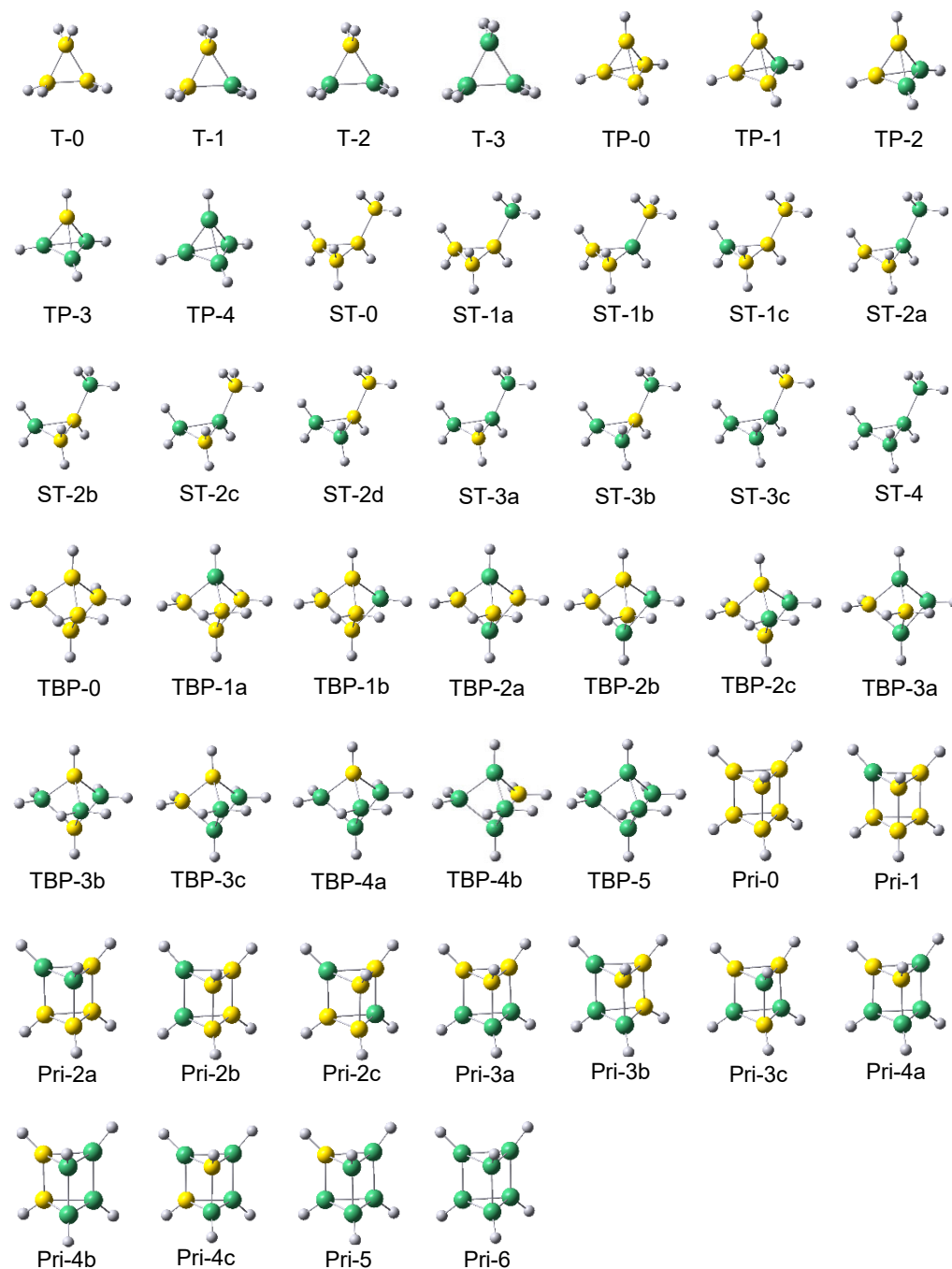
Figure 2.1.1: Optimized $Si_xGe_yH_z$ (x+y=6) cluster geometries using the G3//B3LYP level of theory. The clusters are denoted by T for trigonal planar, TP for trigonal pyramidal, ST for substituted trigonal planar, TBP for trigonal bipyramidal, and Pri for prismane geometries. The indices are incremented by integer values to correspond with the replacement of a Si (yellow) atom by a Ge (green) atom from 0 to N, where 0 is the pure Si cluster and N is the pure Ge cluster. The lower case letter symbol denotes isomers.

Table 2.1.1 Calculated singlet-triplet splitting values of selected Si, Ge, and SiGe species using the G3//B3LYP level of theory, where the splitting value is defined as the difference in total energy of the species between the singlet ground state (S0) and the first excited triplet state (T1). The nomenclature to identify molecular geometries is the same as in Figure 2.1, and representative energy level diagrams can be found in Figure 3.1.7. ZPE denotes zero-point vibrational energy.

G3//B3LYP Electronic energies with ZPE correction				
Spin Multiplicity				
		Singlet	triplet	Singlet-triplet splitting
Species	Index	(Hartrees)	(Hartrees)	(eV)
Si_1H_4	L-1	-291.7112	-291.5693^a	3.9
Ge_1H_4	L-5	-2078.819	-2078.6874^b	3.6
Si_3H_6	T-0	-871.5746	-871.5151	1.6
Ge_3H_6	T-3	-6232.9354	-6232.8851	1.4
Si_5H_8	TBP-0	-1451.5196	-1451.4273	2.4
Si_4GeH_8	TBP-1a	-3238.6407	-3238.5581	2.2
$Si_3Ge_2H_8$	TBP-2b	-5025.7602	-5025.6793	2.2
$Si_4Ge_2H_6$	Pri-2b	-5313.8816	-5313.8201	1.7
$Si_3Ge_3H_6$	Pri-3c	-7101.0080	-7100.9437	1.7
^{a} This molecule exists in a form of dissociation of $\cdot SiH_3$ and $\cdot H$				
^{b} This molecule exists in a form of dissociation of $\cdot GeH_3$ and $\cdot H$				

Enthalpy, H, and entropy, S, are calculated using standard formulas.[102] Calculation of thermochemical properties was performed automatically using the CalcTherm script, which interfaces with electronic structure codes to provide thermochemical properties (S, C_p H) of individual species at elevated temperatures.[103] The external symmetry numbers for the hydrogenated Si-Ge clusters examined in this study impact the molecular partition function for rotation and reduce the rotational entropy by an amount equivalent to R ln σ_{rot},[102] where σ_{rot} is the external symmetry number of the molecule and R is the ideal gas constant.

The enthalpy of formation of a given molecule $Si_xGe_yH_z$ can be calculated from its atomization energies using **equation 2.1.1**[55]

$$\Delta H^{\circ}_{f,298}(Si_xGe_yH_z) = [x\Delta H^{\circ}_{f,298}(si) + y\Delta H^{\circ}_{f,298}(Ge) + z\Delta H^{\circ}_{f,298}(H)] - \Delta H^{\circ}_{f,298}(Si_xGe_yH_z) \qquad \textit{eq (2.1.1)}$$

where the formation enthalpies of atomic silicon, germanium and hydrogen are the experimental values obtained from the JANAF tables ($\Delta H^{\circ}_{f,298}(Si) = 450$ kJ mol^{-1}, $\Delta H^{\circ}_{f,298}(Ge) = 372$ kJ mol^{-1}, $\Delta H^{\circ}_{f,298}(H) = 217.999$ kJ mol^{-1}) and $\Delta H^{\circ}_{f,298}(Si_xGe_yH_z)$. The atomization energy defined as the enthalpy change upon decomposition of a molecule into its component atoms can be evaluated using **equation 2.1.2,**

$$\Delta H^{\circ}_{a,298}(Si_xGe_yH_z) = [xH_{a,298}(Si) + yH_{a,298}(Ge) + zH_{a,298}(H)] - H_{298}(Si_xGe_yH_z) \qquad \textit{eq (2.1.2)}$$

where $H_{298}(Si)$, $H_{298}(Ge)$ and $H_{298}(H)$ are the enthalpies of atomic silicon, germanium and hydrogen at 298 K, respectively, and $H_{298}(Si_xGe_yH_z)$ is the enthalpy of $Si_xGe_yH_z$ at the same temperature. These enthalpies can be calculated as the sum of the electronic energies (E_{el}), zero point energies (ZPE), and thermal corrections (E_{vib}^{298}, E_{trans}^{298}, and E_{rot}^{298}) at 298 K, as follows from canonical molecular partition functions assuming an ideal gas at 1 atm using **equation 2.1.3,**

$$H^{298} = E_{el} + ZPE + E^{298}_{ib} + E^{298}_{rans} + E^{298}_{ot} + \Delta PV \qquad \textit{eq (2.1.3)}$$

All of the quantities on the right-hand side of **equation 2.1.3** are obtained from quantum chemical calculations, and the standard enthalpy of formation of $Si_xGe_yH_z$ is then calculated. The isodesmic bond additivity correction (BAC) proposed by Petersson et al.[104] and applied to silicon hydride chemistry by Wong et al. was extended in our calculations of standard enthalpy of

formation for SiGe and Ge species. This approach uses a set of reference molecules that have experimental data available which then are compared to G3//B3LYP enthalpies of formation from homodesmotic reactions to calculate a set of correction parameters. The inclusion of these correction parameters was shown to lead to values that very closely approximate standard enthalpies of formation based on available experimental data and data calculated using the method of homodesmotic reactions.[105] The novel BAC parameters used in this study to calculate enthalpies of formation for Si, Ge, and SiGe species are regressed and presented in the Results and Discussion section and follow **equation 2.1.4**

$$\Delta H^\circ_{f,298}(BAC) = \Delta H^\circ_{f,298}(\text{calculated}) + \sum_i N_i BAC_i \qquad \textit{eq (2.1.4)}$$

BAC_i is the BAC parameter of a certain bond type i, and the standard enthalpy of formation estimated from BACs, $\Delta H^\circ_f,298$ (BAC), can be defined as the standard enthalpy of formation calculated on the basis of atomization energies, $\Delta H^\circ_f,298$ (calculated), corrected by the summation of the BAC_i parameters multiplied by the number of bonds of that type (N_i).

In order to test the accuracy of our calculations, calculations were carried out on small acyclic Si, Ge, and SiGe hydrides using the CBS-QB3, G3//B3LYP, and G4//B3LYP methods and summarized in **Table 2.1.2.** The calculated results from the G3//B3LYP and G4//B3LYP composite methods were found to be in reasonable agreement with available experimental data for standard enthalpy of formation at 298 K. The performance summary for prediction of thermochemical properties for small acyclic Si, Ge, and SiGe hydride chemistries indicated that the G3//B3LYP and G4//B3LYP composite methods outperform the CBS-QB3 method on estimating standard enthalpy of formation when compared to available experimental data. Calculation of the standard enthalpy of formation at 298 K has been underestimated with CBS-

QB3, G3//B3LYP and G4//B3LYP composite methods. In the case of estimating standard entropy values of the acyclic species, all predicted standard entropies were estimated between 0.5 and 3.8 $Jmol^{-1}K^{-1}$ in average absolute deviation when compared to available experimental data. For constant pressure heat capacity, however, the calculations for all three methods were very accurate with a highest average absolute deviation of 1.1 J mol^{-1} K^{-1} when compared to available experimental data.

Analogously, a previous study on silicon hydrides from our group compared W-1 and G3//B3LYP standard enthalpies of formation at 298 K to available experimental data. The G3//B3LYP composite method agrees with available experimental data within an average absolute deviation of 1.0 kcal.mol^{-1} while the W-1 method captures available experimental data within an average absolute deviation of 2.0 kcal.mol^{-1}. The W-1 method was developed to be an affordable and accurate method for the determination of thermochemistry; however, the improved predictions by the G3//B3LYP method can be attributed to the use of a higher level correction based upon a regression of correction parameters from an experimental data set of 299 energies containing enthalpies of formation, ionization potentials, electron affinities, and proton affinities. Additionally, the G3//B3LYP method was a reasonable choice because the cluster property data set from this study is intended to be used in conjunction with an existing G3//B3LYP database developed by our group for the estimation of silicon hydride thermochemical properties. The G4//B3LYP method did exhibit superior accuracy for the small acyclic species examined with available experimental data; however, we experienced significant self-consistent field (SCF) energy convergence issues for structures larger than four Si and/or Ge atoms in the latest revision of the Gaussian software and this method was not pursued.

Table 2.1.2: Comparison of calculated standard enthalpy of formation, standard entropy, and constant pressure heat capacity at 298 K to available experimental data for small acyclic hydrogenated silicon and germanium species using the CBS QB3, G3//B3LYP, and G4//B3LYP composite methods. Deviation is defined as experiment minus theory. AAD denotes average absolute deviation.

Molecules	net charge	spin multiplicity	$\Delta H^{\circ}_{f,298K}$ (kJ mol^{-1})						
level of theory			Exp[a]	CBS-QB3	Deviation	G3B3	Deviation	G4	Deviation
Si_1H_4	0	1	34.3	22.57	11.7	31.22	3.1	31.52	2.8
Si_2H_6	0	1	80.3	65.39	14.9	75.69	4.6	75.03	5.3
Si_3H_8	0	1	120.9	100.38	20.5	112.46	8.4	111.49	9.4
AAD					15.7		5.4		5.8
$SiGeH_6$	0	1	116.3	71.70	44.6	107.26	9.1	108.62	7.7
Ge_1H_4	0	1	90.8	47.48	43.3	80.71	10.1	81.46	9.3
Ge_2H_6	0	1	162.3	79.07	83.2	139.71	22.6	142.23	20.1
Ge_3H_8	0	1	226.8	108.68	118.1	192.40	34.4	196.51	30.3
AAD					81.6		22.4		19.9

			S^{298K} (J mol^{-1} K^{-1})						
			Exp[a]	CBS-QB3	Deviation	G3B3	Deviation	G4	Deviation
Si_1H_4	0	1	204.6	204.38	0.2	204.56	0.0	204.48	0.1
Si_2H_6	0	1	272.7	273.82	-1.1	273.57	-0.9	274.10	-1.4
Si_3H_8	0	1	N.A.	346.58	-	347.08	-	347.38	-
AAD					0.7		0.5		0.8
$SiGeH_6$	0	1	N.A.	292.66	-	294.27	-	292.91	-
Ge_1H_4	0	1	217.1	217.31	-0.2	217.48	-0.4	217.41	-0.3
Ge_2H_6	0	1	297.0	300.47	-3.5	304.20	-7.2	300.88	-3.9
Ge_3H_8	0	1	N.A.	388.09	-	419.08	-	389.24	-
AAD					1.9		3.8		2.1

			C_P (J mol^{-1} K^{-1})						
			Exp[a]	CBS-QB3	Deviation	G3B3	Deviation	G4	Deviation
Si_1H_4	0	1	42.8	42.52	0.3	42.71	0.1	42.70	0.1
Si_2H_6	0	1	80.0	79.73	0.3	79.49	0.5	79.85	0.2
Si_3H_8	0	1	N.A.	117.55	-	117.13	-	117.71	-
AAD					0.3		0.3		0.2
$SiGeH_6$	0	1	N.A.	82.37	-	82.95	-	82.65	-
Ge_1H_4	0	1	45.0	44.78	0.2	44.88	0.1	45.06	-0.1
Ge_2H_6	0	1	84.9	85.16	-0.3	86.15	-1.2	85.60	-0.7
Ge_3H_8	0	1	N.A.	126.17	-	128.35	-	126.92	-
AAD					0.3		1.1		0.4

Any chemical system (e.g., an atom, molecule, ion, or radical) is characterized by its electronic chemical potential, μ, and by its absolute hardness, η. Thus, the calculated quantum chemical parameters such as the highest occupied molecular orbital energy E_{HOMO}, the lowest unoccupied molecular orbital energy E_{LUMO}, energy gap ΔE, electronic chemical potential μ,

global hardness η, and the softness σ were calculated in our study. The concept behind the derivation of these parameters is related to each other through frontier molecular orbital theory,[106-111] and this concept can be approximated as **equation 2.1.5** and **2.1.6.**

$$-\mu = \frac{I+A}{2} = \chi \qquad\qquad eq\ (2.1.5)$$

$$\eta = \frac{I-A}{2} \qquad\qquad eq\ (2.1.6)$$

Here I is the ionization potential and A is the electron affinity. The inverse values of the global hardness are designated as the softness $\sigma = 1/\eta$. According to Koopmans' theorem, the frontier orbital energies are given by $-E_{HOMO} = I$, and $-E_{LUMO} = A$. It is well-known and controversial that application of Koopmans' theorem to Kohn–Sham (KS) Density Functional Theory (KS-DFT) requires a tuning procedure to be able to "impose" Koopmans' theorem on DFT approximations, thereby improving many of its related predictions in actual applications.[65, 66] Here hybrid functionals systematically calculate HOMO energies that underestimate the first ionization potential values by several electron volts. Nevertheless, these tabulated quantum chemical parameters can be used in two possible ways: as a rank ordering of similar acids (electrophiles) or bases (nucleophiles) to predict relative properties or as a source of values to use in relevant equations such as **equation 2.1.7**. If two systems or molecules, A and B are brought together, electrons will flow from that of lower to that of higher, until the chemical potentials become equal. As a first approximation, the (fractional) number of electrons transferred, ΔN, will be given by **equation 2.1.7**. The difference in electronegativity drives the electron transfer, and the sum of the hardness parameters acts as a resistance. This reactivity index was then generalized beyond the species in this study using a machine learning approach based on multiple linear regression and detailed sensitivity analysis.

$$\Delta N = \frac{\chi_B - \chi_A}{2(\eta_B + \eta_A)} \qquad\qquad eq\ (2.1.7)$$

2.1.3 Results and Discussion

Structures and Vibrational Frequencies

The structures for the 46 hydrogenated Si, Ge, and SiGe clusters and 7 acyclic Si, Ge, and SiGe species that were investigated in the present study were optimized using the B3LYP/6-31G(d) level of theory. The optimized structures for all of the clusters showed complex polycyclic or cyclic nature and a varying level of surface passivation with hydrogen atoms, as illustrated in **Figure 2.1.1**. High-energy sterically strained structural isomers were calculated in this study to capture the diverse range of strain energies possible in hydrogenated Si, Ge, and SiGe clusters. Acyclic (or linear) Si, Ge, and SiGe structures were calculated for species comprised of one to three Si or Ge atoms. For the cluster structures, hydrogenated trigonal planar, trigonal pyramidal, substituted trigonal planar, trigonal bipyramidal, and prismane geometries comprised of varying numbers of three- and four-membered rings were calculated. All electronic wavefunctions for the structures were optimized in a singlet state. We also calculated all structures in this study in the triplet states (see **Table 2.1.1** for selected structures). It was observed that the clusters and acyclic species changed geometry significantly upon excitation to the triplet state. In the case of trigonal planar structures going to the triplet state from the singlet state, the structures optimized to a linear geometry which has a higher standard enthalpy of formation than its analogue in the singlet state. For the three dimensional structures such as trigonal pyramidal, trigonal bipyramidal, and

prismane, the structures transformed to less stereoscopic shapes which appeared similar to cyclohexane in geometry. This strong change in geometry indicated that the structures in this study are very stable in singlet ground state, and thus require significant structural rearrangement to find a stable minima on the triplet potential energy surface. Electronic excitation to a higher spin state may be a viable means to create more reactive intermediates due to the conformational changes in geometry on the path to the triplet state from the singlet state.

Comparison of our predicted values to experiment for geometry parameters are presented here for the acyclic species. For silane, the B3LYP/6-31G(d) predicted Si-H bond distance is 1.486 Å and the experimental value is 1.480 Å.[112] For germane, the predicted Ge-H bond distance is 1.542 Å and the experimental value is 1.525 Å.[113] For disilane, the predicted Si-Si and Si-H bond lengths were 2.350 Å and 1.489 Å, respectively, and experimental values were 2.331 Å and 1.492 Å, respectively. The HSiSi and HSiH bond angles were predicted as 110.6 and 108.3 degrees, respectively, and experimental values were 110.3 and 108.6 degrees, respectively. For digermane, the predicted Ge-Ge and Ge-H bond lengths were 2.448 Å and 1.546 Å, respectively, and experimental values were 2.403 Å and 1.541 Å, respectively. The HGeGe and HGeH bond angles were predicted as 110.7 and 108.2 degrees, respectively, and experimental values were 112.3 and 106.4 degrees, respectively. For H_3SiGeH_3, the predicted Si-Ge, Si-H, and Ge-H bond lengths were 2.398 Å, 1.488 Å, and 1.546 Å, respectively, and the experimental values were 2.358 Å, 1.494 Å, and 1.538 Å, respectively. The HSiH and HGeH bond angles were predicted as 108.5 and 107.9 degrees, respectively, and experimental values were 108.8 and 108.3 degrees, respectively.[114] All of our predicted values for geometry parameters are very well matched to the experimental data for the acyclic Si, Ge, and SiGe species in this study.

Using the nomenclature introduced in **Figure 2.1.1**, an analysis of the geometry parameters

for the cluster species are presented herein. For trigonal planar Si_3H_6 (T-0), the equilateral triangle structure is suggested with a Si-Si bond length of 2.345 Å and a Si-H bond length of 1.486 Å. Substituting Ge atoms systematically for Si atoms in the T-0 geometry, all the mixed SiGe and a pure Ge trigonal planar geometries were created. Addition of a Ge atom to the T-0 geometry increases the length of all the bonds mildly, thereby increasing the size of the full cluster where the fully substituted Ge cluster is the largest in geometric dimensions. For the T-1 geometry, the Ge-Si bond length is 2.405 Å, Si-Si bond length is 2.348 Å, Ge-H bond length is 1.541 Å, and Si Ge-Si apex angle is 58.6 degrees. As observed with the trigonal planar structural series, all other structural geometries (i.e., substituted trigonal planar, trigonal pyramidal, trigonal bipyramidal, and prismane) showed a similar trend of expanding bond lengths when exchanging a Si atom with a Ge atom. Although not presented in **Figure 2.2**, it is noteworthy to discuss the S-0 geometry, or nearly planar cyclic rhombus structure of four Si atoms, which has a Si-Si bond length of 2.371 Å and a Si-H bond length of 1.492 Å. With the angles of the Si-Si-Si bonds at 87.7 and 92.3 degrees and all Si atoms possessing an sp^3 hybridized center, this cyclic structure shows a slightly puckered character and the four-membered ring is not completely planar. Interestingly, the square planar Si_4H_8 is the only structure in the geometry series which showed a stable minimum on the singlet potential energy surface with all real vibrational frequencies. Structures comprised of one four-membered ring and any level of Ge content were unstable, i.e., all structures were found to be higher-order saddle points on the potential energy hypersurface with imaginary vibrational frequencies. A conformational search revealed that a substituted trigonal planar structure in which a hydrogen in the trigonal plane structure is substituted with a silyl or germyl group was a more stable minimum on the singlet potential energy surface with all real vibrational frequencies. We found that the substituted trigonal planar (ST-0) geometries are more stable than the square planar

(S-0) geometries, where a smaller three-membered ring in the ST-0 geometry is preferred over a larger four-membered ring in the S-0 geometry. All ST-0 geometries with varying levels of Si and Ge content have real vibrational frequencies. In the case of Si_4H_8 (ST-0), the average of Si-Si and Si-H bond lengths are 2.346 Å and 1.486 Å, respectively, and the angle between the trigonal plane and the Si atom of the silyl group is 120.6 degrees. These bond distances and angles in the ST-0 structural series are slightly increased as the Si atoms are replaced with Ge atoms.

Compared to the Si atom, the Ge atom has a full 3d shell of 10 electrons and significantly more electrons than the Si atom; however, the respective bond lengths upon Ge substitution are only increased by +3.7% going from the Si-H to Ge-H substitution, respectively, and +2.4% going from Si-Si to Si-Ge substitution, respectively. Another reason for the observed higher stability for the ST-0 geometry than the S-0 geometry can be seen by the fact that the ST-0 geometry has fewer overall spatial constraints than the S-0 geometry. In other words, the ST-0 geometry still has a torsional degree of freedom in vibrational modes for the substituted silyl or germyl group which is lost upon a four-membered ring formation. This explanation could also attribute why the ST-0 geometry is more stable than the TP- 0 geometry, which also lacks any torsional degrees of freedom in vibrational modes. The trigonal pyramidal geometry (TP-0) has on average a shorter Si-Si bond length at 2.327 Å and Si-H bond length at 1.479 Å compared to Si clusters in the other geometry series. In the TP-1 structure, the Si-Si bond length on average is 2.332 Å and the Si Ge bond length is 2.399 Å. The fact that the TP-0 geometry has more contracted Si-Si bond distances than the ST-0 geometry supports the stable nature of ST-0 geometry due to an overall lack of polycyclic nature.

Several structures in this study were initially hypothesized to have both pentacoordinated and hexacoordinated Si and Ge centers; however, only stable clusters comprised of hexacoordinated

Si and Ge centers were isolated. This type of bonding behavior indicates that both Si and Ge centers would exhibit sp^3d or sp^3d^2 hybridization, respectively. In its least strained hypervalent form, sp^3d hybridized Si and Ge centers will form covalent bonds with five neighboring atoms in a trigonal bipyramidal electron pair coordination. These sp^3d hybridized centers were explored for the square bipyramidal (SBP) geometry series. The sp^3d^2 hybridized Si and Ge centers will form covalent bonds with six neighboring atoms in an octahedral electron pair coordination. These sp^3d^2 hybridized Si and Ge centers were explored for trigonal bipyramidal (TBP) geometries. Structures comprised of pentacoordinated Si and Ge were found to be the unstable in the square bipyramidal geometries and these structures favored prismane geometries (Pri) that were instead comprised of sp^3 hybridized Si and Ge atoms. These SBP structures comprised of pentacoordinated Si and Ge centers were unstable, i.e., all structures were found to be higher order saddle points on the potential energy hypersurface comprised of imaginary vibrational frequencies. The unstable SBP structure constructed to have sp3d hybridization is supported with similar work done for Si and Ge complexes where Si complexes were found to be more stable in the hypervalent state with a hexacoordinated complex rather than a pentacoordinated complex. This tendency to form a hexacoordinated Si or Ge centers is further supported by our stable trigonal bipyramidal geometries which exhibit a strained hexacoordinated Si or Ge center in the trigonal center plane of the cluster. For the molecules in our study, results show that a similar preference for hypervalent bonding behavior observed for the Si centers also occurs for the Ge centers. This bonding behavior is likely due to the presence of a complete 3d shell of 10 electrons for the Ge atom which would exhibit more facility to form hybridization involving the d orbital than the Si atom. In this study, all of the Si and Ge atoms are passivated with hydrogen or bonded to other Si or Ge atoms to be in the most stable sp^3 and sp^3d^2 hybridization states. As with the trigonal planar (T-0), substituted

trigonal planar (ST-0), and trigonal pyramidal (TP) geometries, the expansion of bond lengths and bond angles upon substitution of a Ge atom for a Si atom was also observed for trigonal bipyramidal (TBP) and prismane (Pri) geometries. There are studies in the literature for so-called "ultrastable silicon nanoclusters", or hydrogenated pure silicon prismanes comprised of up to 18 silicon atoms. Katin et al.[115] compared the electronic, optical properties, and kinetic stability of $Si_{18}H_{12}$ with the pristine silicon prismane and prismanes embedded with additional C, Si, and Ge atoms. Comparison of this theoretical study with our current study, clusters with a higher density of atoms are subject to have larger spatial confinements which resulted in shorter Si-Si, Si-Ge, and Ge-Ge bond lengths. A similar tendency in bond contraction can be observed by changing the Si atom to a Ge atom in the structures, as opposed to embedding an additional atom in the center of the polycyclic structure.

At the level of theory considered in our study, modeling results have all real vibrational frequencies and represent stable minima on the potential energy surface. Experimental spectroscopic data for the vibrational frequencies of hydrogenated Si, Ge, and SiGe clusters are limited. The unscaled harmonic vibrational frequencies for linear silicon hydrides (SiH_4 and Si_2H_6) and germanium hydrides (GeH_4 and Ge_2H_6) calculated using two different level of theories (G3//B3LYP and G4//B3LYP) were compared against available spectroscopic ex perimental data in **Table 2.1.3**. The unscaled harmonic frequencies for SiH_4, Si_2H_6, GeH_4, and Ge_2H_6 were determined to have mean percentage deviations from experimental val ues of -1.7, -1.8, +0.7, and +5.8 %, respectively, at the G3//B3LYP level of theory. The G4//B3LYP method predicts slightly more accurate vibrational frequencies with the mean percentage deviations of -1.3, -0.9, -0.9, and +2.2 % for SiH_4, Si_2H_6, GeH_4, and Ge_2H_6, respectively.

Table 2.1.3: Comparison of experimental vibrational modes for SiH$_4$, Si$_2$H$_6$, GeH$_4$, and Ge$_2$H$_6$ to unscaled harmonic vibrational modes using the G3//B3LYP and G4//B3LYP composite methods. All vibrational frequency values are reported in cm^{-1}. ([a,c] ref[116], [b] ref[117])

(a) Vibrational Modes of SiH$_4$

mode symmetry	experimental frequency[a]	G3//B3LYP			G4//B3LYP		
		calc. freq.	deviation (exp-calc)	% deviation	calc. freq.	deviation (exp-calc)	% deviation
A$_1$	2187	2252	-65	-3.0	2238	-51	-2.3
E	975	975	0	0.0	975	0.2	0.0
T$_2$	2191	2265	-74	-3.4	2248	-56.6	-2.6
T$_2$	914	917	-3	-0.3	918	-4.3	-0.5
av			-35.5	-1.7		-27.9	-1.3

(b) Vibrational Modes of Si$_2$H$_6$

mode symmetry	experimental frequency[b]	G3//B3LYP			G4//B3LYP		
		calc. freq.	deviation (exp-calc)	% deviation	calc. freq.	deviation (exp-calc)	% deviation
A$_{1g}$	2152	2239	-86.9	-4.0	2217	-65.0	-3.0
A$_{1g}$	909	930	-21.3	-2.3	926	-17.2	-1.9
A$_{1g}$	434	433	0.8	0.2	422	11.7	2.7
A$_{1u}$	131	127	3.6	2.7	127	4.4	3.4
A$_{2u}$	2154	2229	-75.1	-3.5	2210	-55.9	-2.6
A$_{2u}$	844	855	-11.5	-1.4	853	-9.0	-1.1
E$_g$	2155	2239	-83.9	-3.9	2219	-64.0	-3.0
E$_g$	929	943	-13.8	-1.5	944	-14.6	-1.6
E$_g$	625	638	-12.7	-2.0	632	-7.3	-1.2
E$_u$	2179	2252	-72.6	-3.3	2228	-49.0	-2.2
E$_u$	940	957	-17.2	-1.8	957	-17.2	-1.8
E$_u$	379	380	-0.6	-0.2	373	6.4	1.7
av			-25.8	-1.8		-16.8	-0.9

(c) Vibrational Modes of GeH$_4$

mode symmetry	experimental frequency[c]	G3//B3LYP			G4//B3LYP		
		calc. freq.	deviation (exp-calc)	% deviation	calc. freq.	deviation (exp-calc)	% deviation
A$_1$	2106	2051	54.7	2.6	2153	-46.7	-2.2
E	931	936	-4.9	-0.5	924	6.9	0.7
T$_2$	2114	2082	32.5	1.5	2160	-45.9	-2.2
T$_2$	819	824	-5.0	-0.6	819	0.0	0.0
av			19.3	0.7		-21.4	-0.9

(d) Vibrational Modes of Ge$_2$H$_6$

mode symmetry	experimental frequency[d]	G3//B3LYP			G4//B3LYP		
		calc. freq.	deviation (exp-calc)	% deviation	calc. freq.	deviation (exp-calc)	% deviation
A$_{1g}$	2068	2025	42.8	2.1	2124	-55.9	-2.7

A_{1g}	832	835	-2.6	-0.3	838	-5.6	-0.7
A_{1g}	268	238	29.9	11.2	254	14.2	5.3
A_{1u}	146	80	66.0	45.2	105	40.8	28.0
A_{2u}	2077	2031	45.8	2.2	2130	-52.9	-2.5
A_{2u}	756	752	4.4	0.6	753	2.8	0.4
E_u	2091	2067	24.4	1.2	2142	-51.4	-2.5
E_u	879	887	-7.9	-0.9	887	-7.7	-0.9
E_u	370	349	20.7	5.6	354	15.7	4.2
E_g	2081	2058	22.9	1.1	2134	-52.7	-2.5
E_g	880	891	-10.7	-1.2	892	-11.8	-1.3
E_g	567	548	19.4	3.4	557	10.2	1.8
av			21.3	5.8		-12.9	2.2

[a,c] ref[116], [b] ref[117]

Thermochemical Properties

The thermodynamic properties of 7 acyclic Si, Ge, and SiGe hydrides with experimental data available were estimated using the three different quantum chemical methods mentioned in the Computational Methodology section. The deviations between the calculated and experimental values for standard enthalpy of formation, standard entropy, and constant pressure heat capacity are listed in **Table 2.1.2** for these acyclic species. Among the methods used, the G3//B3LYP method was the most accurate for the standard enthalpy of formation calculation for silicon hydrides with an average absolute deviation of 5.4 kJ mol^{-1} from experimental measurements while the G4//B3LYP method was more accurate for the prediction standard enthalpy of formation values for germanium hydrides with an average absolute deviation of 19.9 kJ mol^{-1} from experimental measurements. The G3//B3LYP method had similar predictive accuracy as the G4//B3LYP method for the standard enthalpy of formation for germanium hydrides with an average absolute deviation of 22.4 kJ mol^{-1}. The largest deviations between experimental and calculated predictions for standard enthalpy of formation values observed for germanium hydrides can be attributed to factors not included in the composite methods discussed. This conclusion is supported by reasonably accurate predictions of geometry parameters and vibrational frequencies for the germanium hydrides discussed in the Structures and Vibrational Frequencies section. The quantum chemical factors that lead to large deviations in standard enthalpy of formation prediction include correlation of core and core-valence electrons and relativistic effects such as spin-orbit coupling which becomes progressively more important as heavier elements like Ge are considered. It should be noted that the G3//B3LYP method does include an experimental spin-orbit energy correction term used for atoms and calculated spin-orbit energy correction term for selected diatomic species. For the G3//B3LYP method, the use of a higher level correction factor based

upon a regression of correction parameters from an experimental data set containing standard enthalpies of formation, ionization potentials, electron affinities, and proton affinities differs for Si and Ge hydride species. Namely, there are more Si based species than Ge-based species in this test set for regression of higher level correction factors, i.e., the test set included species with one or two Si atoms and only one Ge atom.

To the best of our knowledge, there is no extensive investigation of thermochemical property estimation or even of vibrational frequency calculations for optimized hydrogenated Si, Ge, and SiGe clusters outside of the works cited in this paper. A total of 46 molecules up to a moderate cluster size, where (Si + Ge) $\leq$ 6, were investigated in this study. The thermochemical properties of all 46 species studied here are reported in the Table 2.4. The most stable ground electronic state for all molecules in this study was found to be the singlet state. As mentioned in the previous section Structures and Vibrational Frequencies, a significant conformational change or spontaneous bond dissociation was observed during optimization of the electronic wavefunction to the triplet state. In all geometries, the addition of Ge atoms to a species increases the standard enthalpy of formation, standard entropy, and constant pressure heat capacity values. The trend based on elemental composition for standard enthalpy of formation predictions by the G3//B3LYP and G4//B3LYP methods was successfully captured for the acyclic hydrides of this study. Due to the semiconducting or non-local nature of electron correlation in the larger clusters with cyclic or polycyclic, rigorous composite methods are required to accurately predict trends in thermochemical properties such as standard enthalpy of formation as function of Si and Ge composition.

Petersson et al.[104] proposed the concept of an isodesmic bond additivity correction (BAC) scheme based on the spirit of isodesmic reactions. With this approach, our study compared small

acyclic molecules with experimental data available in order to calculate the bond additivity corrections necessary for implementation of **equation. 2.1.4.** The novel BAC parameters for Si, Ge, and SiGe species regressed in our study to calculate standard enthalpies of formation are presented in **Table 2.1.5.**

Table 2.1.4: Comparison of calculated thermodynamic properties of hydrogenated Si, Ge, and SiGe clusters using the G3//B3LYP method with and without the bond-additivity corrections (BAC) as denoted in Eq. 2.4. The nomenclature to identify molecular geometries is the same as in **Figure 2.1.1**.

Level of Theory										G3//B3LYP			G3//B3LYP (BAC)		
			Net charge	Spin multi-plicity	Symmetry group	chirality	s_{ext}	$\Delta H°_{f,298K}$ KJ/mol	C_p J/mol.K	S J/mol.K	$\Delta H°_{f,298K}$ KJ/mol	C_p J/mol.K	S J/mol.K		
Atoms			Species												
Si	Ge	H													
Trigonal Planar															
3	0	6	T-0	0	1	D_{3h}		6	261.1	105.4	319.5	268.9	105.3	304.5	
2	1	6	T-1	0	1	C_{2v}		2	278.8	110.3	339.1	286.4	110.2	333.3	
1	2	6	T-2	0	1	C_{2v}		2	296.1	114.7	358.8	313.2	114.6	352.8	
0	3	6	T-3	0	1	D_{3h}		6	313.8	118.7	378.2	349.9	118.6	363.1	
Trigonal Pyramidal															
4	0	4	TP-0	0	1	T_d		12	644.0	122.1	352.9	654.1	121.9	331.9	
3	1	4	TP-1	0	1	C_{3v}		3	655.2	122.7	359.6	661.4	122.6	350.2	
2	2	4	TP-2	0	1	C_{2v}		2	665.7	123.4	367.7	677.5	123.3	361.9	
1	3	4	TP-3	0	1	C_{3v}		3	675.1	124.3	376.1	702.4	124.2	366.9	
0	4	4	TP-4	0	1	T_d		12	683.5	125.4	384.6	735.7	125.4	363.8	
Substituted trigonal planar															
4	0	8	ST-0	0	1	C_S		1	282.7	142.0	381.5	293.3	141.9	381.3	
3	1	8	ST-1a	0	1	C_S		1	316.1	145.8	402.6	330.3	145.7	402.4	
3	1	8	ST-1b	0	1	C_S		1	285.4	146.2	394.5	292.0	146.1	394.3	
3	1	8	ST-1c	0	1	C_1	o	2	300.8	147.0	402.5	311.1	146.9	402.4	
2	2	8	ST-2a	0	1	C_S		1	320.0	149.6	417.7	339.8	149.5	417.5	
2	2	8	ST-2b	0	1	C_1	o	2	334.2	150.8	425.3	348.2	150.7	425.1	
2	2	8	ST-2c	0	1	C_1	o	2	303.1	150.7	413.0	319.1	150.5	412.8	
2	2	8	ST-2d	0	1	C_S		1	318.5	151.6	424.0	338.3	151.5	423.8	
1	3	8	ST-3a	0	1	C_1	o	2	337.5	154.0	437.4	366.8	153.9	437.2	
1	3	8	ST-3b	0	1	C_S		1	351.9	155.3	451.4	375.3	155.2	451.2	
1	3	8	ST-3c	0	1	C_S		1	321.0	154.9	431.8	356.1	154.8	431.6	
0	4	8	ST-4	0	1	C_S		1	355.2	158.2	464.2	403.6	158.1	464.0	

Trigonal Bipyramidal

5	0	8	TBP-0	0	1	D_{3h}		6	282.4	157.6	373.9	295.7	157.4	358.8
4	1	8	TBP-1a	0	1	C_{3v}		3	290.0	160.3	385.7	299.4	160.1	376.3
4	1	8	TBP-1b	0	1	C_{2v}		2	302.9	162.9	392.0	316.0	162.8	386.2
3	2	8	TBP-2a	0	1	D_{3h}		6	298.1	162.4	396.3	303.5	162.2	381.1
3	2	8	TBP-2b	0	1	C_S		1	309.6	165.4	403.3	328.4	165.2	403.1
3	2	8	TBP-2c	0	1	C_{2v}		2	323.2	168.4	411.3	336.0	168.3	405.4
2	3	8	TBP-3a	0	1	C_{2v}		2	317.0	166.8	412.5	335.3	166.6	406.5
2	3	8	TBP-3b	0	1	D_{3h}		6	343.4	173.8	432.3	356.0	173.7	417.2
2	3	8	TBP-3c	0	1	C_S		1	329.1	170.4	422.0	357.2	170.3	421.9
1	4	8	TBP-4a	0	1	C_{3v}		3	348.4	175.5	442.4	386.0	175.4	433.1
1	4	8	TBP-4b	0	1	C_{2v}		2	335.7	171.4	430.0	379.3	171.2	424.1
0	5	8	TBP-5	0	1	D_{3h}		6	354.2	176.0	448.8	416.8	175.8	433.9

Prismane

6	0	6	Pri-0	0	1	D_{3h}		6	587.1	171.3	393.8	602.6	171.2	378.7
5	1	6	Pri-1	0	1	C_S		1	589.5	174.0	405.7	601.0	173.8	405.5
4	2	6	Pri-2a	0	1	C_S		1	591.6	176.1	416.7	608.8	176.0	416.5
4	2	6	Pri-2b	0	1	C_{2v}		2	592.7	175.4	415.6	609.9	175.3	409.7
4	2	6	Pri-2c	0	1	C_2	o	4	591.9	176.4	417.8	599.4	176.3	411.8
3	3	6	Pri-3a	0	1	C_{3v}		3	593.5	178.0	427.2	626.0	177.9	417.9
3	3	6	Pri-3b	0	1	C_1	o	2	594.2	177.7	427.2	617.1	177.6	427.0
3	3	6	Pri-3c	0	1	C_S		1	593.9	178.4	428.9	616.8	178.2	428.7
2	4	6	Pri-4a	0	1	C_S		1	595.7	179.7	438.2	633.9	179.6	437.9
2	4	6	Pri-4b	0	1	C_{2v}		2	596.5	178.9	436.9	634.7	178.8	430.9
2	4	6	Pri-4c	0	1	C_2	o	4	595.8	179.7	438.8	624.4	179.6	432.8
1	5	6	Pri-5	0	1	C_S		1	597.3	181.1	448.6	650.9	181.0	448.3
0	6	6	Pri-6	0	1	D_{3h}		6	598.7	182.7	459.0	677.2	182.6	443.9

Table 2.1.5: Summary of regressed parameters for the Bond Additivity Correction (BAC) of different bond types for standard enthalpy of formation at 298 K calculated from atomization energies and the G3//B3LYP level of theory.

	Si-H	Ge-H	Si-Ge	Si-Si	Ge-Ge
BAC values (KJ/mol)	-0.12	1.83	-0.66	1.28	7.06

The regression statistics show that the most statistically significant BAC parameter is for the Ge-H bond followed by the Ge-Ge bond with p-values of 0.007 and 0.011, respectively. The R^2-value

for the full regression was 0.9992 with an F-value of 525.8 and a p value of 0.002. Thus, the full regression model is statistically significant at the 99.5% confidence interval. The BAC parameters are categorized into five different types according to the Si and/or Ge atoms participating in the respective bond. For all 46 hydrogenated Si, Ge, and SiGe clusters, the resulting standard enthalpies of formation using this BAC approach are listed along with the standard enthalpies of formation obtained from atomization energies without the BAC approach in **Table 2.1.5**. **Figure 2.1.2a-f** depict parity plots to display trends of the BAC impact on prediction of standard enthalpies of formation for key geometry series (T, ST, TBP, TP, and Pri).

On average, the standard enthalpy of formation for all clusters in this study increased after implementation of the required BAC parameters. The most pronounced BAC effect on the standard enthalpy of formation prediction was for the clusters comprised of higher Ge atom content than Si atom content, particularly because the G3//B3LYP method systematically underestimates the standard enthalpy of formation of SiGe and Ge hydrides. The absolute difference in standard enthalpies of formation between the Pri-0 and Pri-6 structures before employing the BAC parameters was 10.8 kJ mol^{-1}. After implementation of the BAC parameters, the standard enthalpies of formation of Pri-0 and Pri 6 structures were 602.6 kJ mol^{-1} and 677.2 kJ mol^{-1}, respectively. Upon implementation of the BAC parameters, the absolute difference in standard enthalpies of formation between the Pri-0 and Pri-6 structures become 74.6 kJ mol^{-1}. Thus, species with more X-X bonds (X = Si or Ge) will exhibit a greater impact of the BAC parameters. This trend in correction of standard enthalpy of formation values can be clearly seen by observing the parity plots in **Figure 2.1.2**, particularly **Figure 2.1.2f** for the prismane clusters.
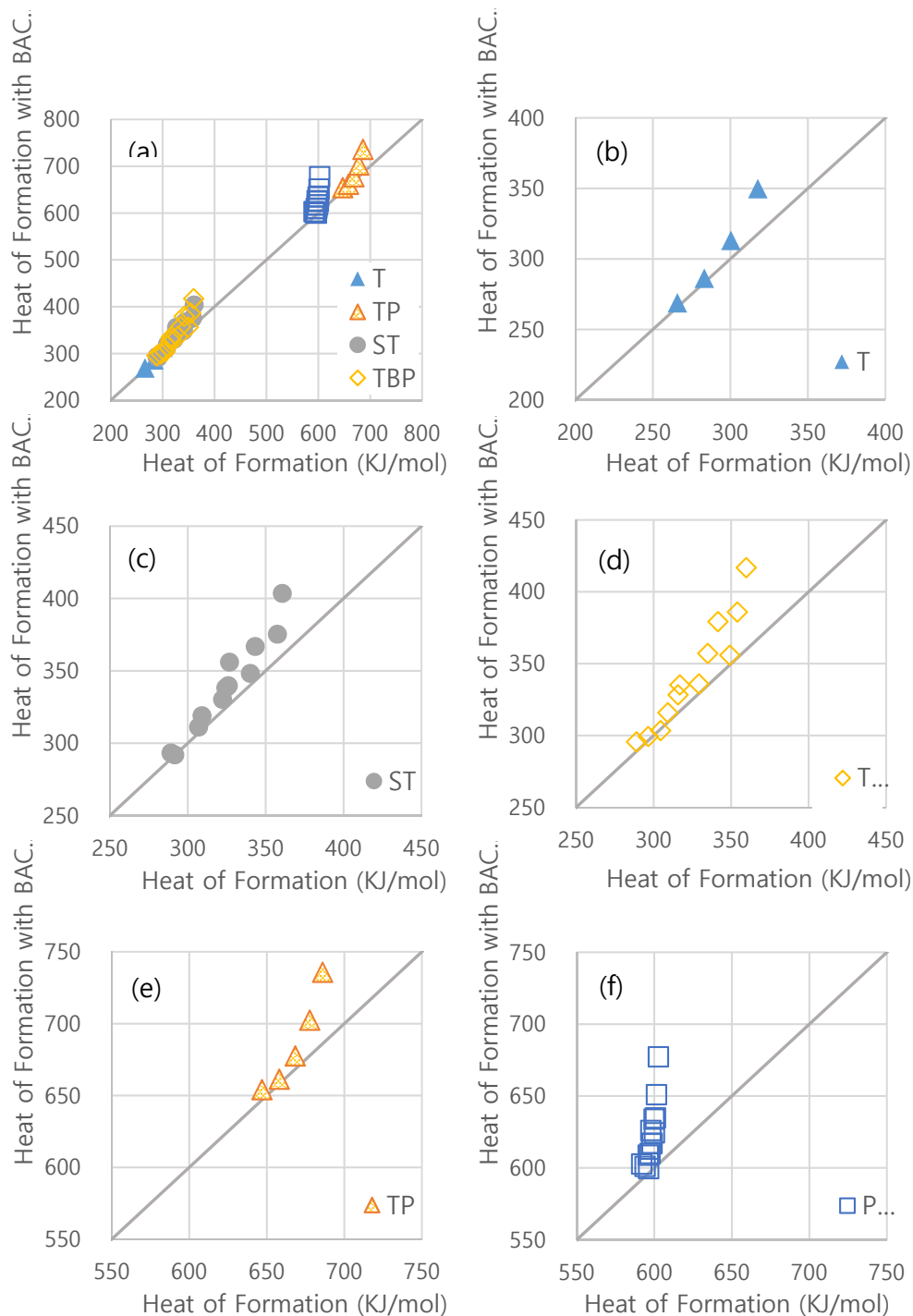
Figure 2.1.2: Parity plots of standard enthalpy of formation for the 46 hydrogenated Si, Ge, and SiGe clusters in this study: (a) all geometries, (b) trigonal planar group, (c) substituted trigonal planar group, (d) trigonal bipyramidal group, (e) trigonal pyramidal group, and (f) prismane group.
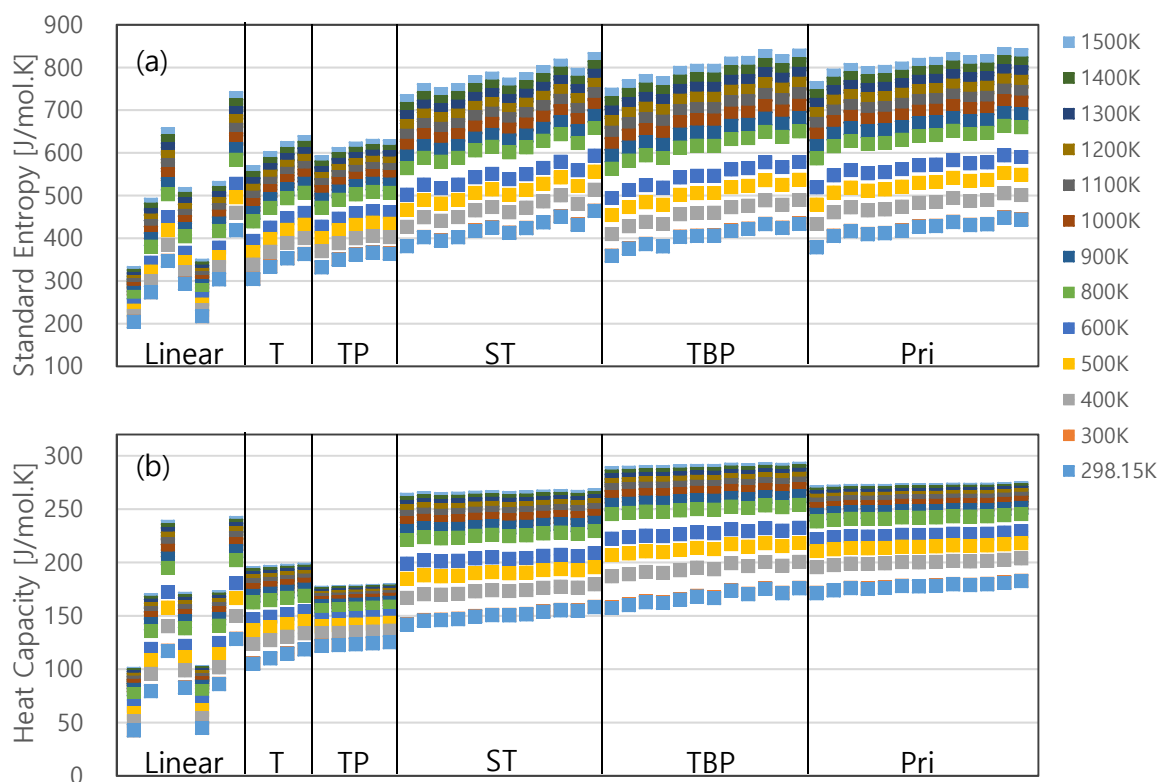
Figure 2.1.3: (a) Standard entropies and (b) constant pressure heat capacities of all hydrogenated Si, Ge, and SiGe clusters in this study over the temperature range of 298.15K to 1500 K using the G3//B3LYP level of theory.

The standard entropies and constant pressure heat capacities for all clusters in this study over the temperature range of 298.15 K to 1500 K are presented graphically in **Figure 2.1.3a-3b** and in **Appendix A1**. The average percent deviations between experimental and calculated values of standard entropy and constant pressure heat capacity for the seven acyclic Si, Ge, and SiGe hydrides were +1.3% and +0.6%, respectively, at the G3//B3LYP level of theory. It is noteworthy to mention that the external symmetry number was identified for all clusters to ensure that accurate standard entropy values were predicted. The effect of external symmetry number on rotational

entropy becomes less pronounced at elevated temperatures because the aforementioned correction factor, R ln σ_{rot}, is not a function of temperature. The clusters with the highest degree of symmetry were the trigonal planar geometries, particularly the pure Si and Ge clusters, TP-0 and TP-4, respectively, which both possess a T_d point group symmetry. The D_{3h} point group symmetry was the next most common point group symmetry with a high degree of symmetry in this study, particularly for the trigonal bipyrimidal (TBP) and prismane (Pri) geometries. Chiral clusters containing at least one Si/Ge atom with four nonidentical substituents were identified in our study. The presence of one chiral center was denoted in **Table 2.1.4** for four substituted trigonal planar and three prismane clusters. The presence of a chiral center in a cluster increases the external symmetry number by a factor of two. **Figure 2.1.3a-3b** display standard entropy and constant pressure heat capacity values, respectively, as a function of temperature and it is interesting to note that standard entropy values are more sensitive to temperature variations than constant pressure heat capacity for the clusters in this study. For both the trigonal planar and trigonal pyramidal geometries, the range of standard entropy and constant pressure heat capacity values from 298 K to 1500 K is lower than the range of standard entropy and constant pressure heat capacity values over the same temperature range for the substituted trigonal planar, trigonal bipyramidal, and prismane geometries. This observation is likely due to the greater number of vibrational degrees of freedom for the larger Si, Ge, and SiGe clusters sizes.

If standard enthalpy of formation values are compared for isomers of a given cluster geometry, relative stabilities can be identified and ranked accordingly. Cluster isomers are present in this study for the substituted trigonal planar (ST), trigonal bipyramidal (TBP), and prismane (Pri) geometries. For instance in **Table 2.1.4** for the trigonal bipyramidal geometry, one can observe that the isomer TBP-2a is more stable than isomers TBP-2b and TBP-2c where standard enthalpies

of formation are 303.5 kJ mol^{-1}, 328.4 kJ mol^{-1}, and 336.0 kJ mol^{-1}, respectively. The isomer TBP 2a differs from TBP-2b and TBP-2c due to the presence of two sp3-hybridized Ge atoms in TBP-2a compared to two sp^{3}d^2-hybridized Ge atoms in TBP-2b and TBP-2c. A similar trend in cluster stabilities is also observed for the other TBP isomers in the TBP-1, TBP-3, and TBP-4 series of cluster geometries, but the differences between the most stable isomer and the least stable isomer in these geometry series are lower with values of 16.6 kJ mol, 21.9 kJ mol, and 6.7 kJ mol, respectively. The difference in stability of isomers is similarly pronounced for the substituted trigonal planar geometry series; however, the greatest difference for the stability of isomers for this study is in the ST-1 series where the ST-1b isomer is most stable. The ST-1b isomer has the molecular formula of Si$_3$Ge$_1$H$_8$ where the Ge is at the center of the cluster and bound to three Si atoms and one H atom. The differences in stability between the most stable isomer and the least stable isomer in the ST-1, ST-2, and ST-3 series are 38.3 kJ mol^{-1}, 20.7 kJ mol^{-1}, and 19.2 kJ mol^{-1}, respectively. The difference in stability of isomers is least pronounced for the prismane clusters with differences ranging 10.5 kJ mol^{-1}, 9.2 kJ mol^{-1}, and 10.3 kJ mol^{-1} for the Pri-2, Pri-3, and Pri-4 series, respectively.

Electronic Properties and Chemical Stability

The highest occupied and lowest unoccupied molecular orbital energies are very informative properties of a molecule or cluster which can be calculated by quantum chemical methods. These molecular orbitals also assign the electron density as a function of position in the molecule or cluster, where electron density for a given molecular orbital i is defined as the square of the

electronic wavefunction, Ψi^2. Knowledge of the highest occupied and lowest unoccupied molecular orbital contours is critical for understanding reactions of clusters as well as optoelectronic properties. The foundation of the frontier orbital theory for the prediction of the most reactive positions in multi electron systems is based on the highest occupied and lowest unoccupied molecular orbitals. Reactive molecules or clusters are characterized by a small highest occupied molecular orbital lowest unoccupied molecular orbital (HOMO-LUMO) energy gap. Both the HOMO and LUMO are the primary molecular orbitals that can be used as predictors of chemical stability and optoelectronic properties.

In our computational study, the HOMO–LUMO energy gap is considered to investigate the role of cluster composition on the chemical stability of hydrogenated Si, Ge, and SiGe clusters. This energy gap is a critical parameter which characterizes the chemical reactivity of the hydrogenated clusters. This chemical reactivity is related to the facility of a molecule to participate in chemical reactions or to create a novel self assembled material through non- bonding molecular interactions. The HOMO–LUMO energy gap can describe the ability for electrons to move from HOMO to LUMO and consequently is considered as an important parameter to analyze the chemical stability of clusters. For instance, if the HOMO–LUMO energy gap were large for a given Si, Ge, or SiGe cluster, this value would correspond to a closed shell electronic configuration and high chemical stability. On the other hand, smaller HOMO–LUMO energy gaps for given Si, Ge, and SiGe clusters reflect that the respective cluster may interact easily with other molecules to form a covalent bond and these types of molecules are on average more chemically reactive.

Calculated HOMO-LUMO energy gaps of hydrogenated Si and Ge clusters and acyclic Si and Ge hydrides at the G3//B3LYP level of theory are presented in **Figure 2.1.4**. The highest HOMO-LUMO energy gaps are for acyclic Si and Ge hydrides comprised of one or two Si/Ge

atoms ranging from 12.4 to 14.6 eV for Si-containing species and 12.0 to 14.2 eV for Ge-containing species. The calculated HOMO LUMO energy gaps for pure Ge species are always lower than for pure Si species, where the largest absolute difference of 0.62 eV is observed for the trigonal bipyramidal geometry. The smallest absolute difference of 0.06 eV between HOMO-LUMO energy gaps for pure Si and Ge species is observed for the trigonal pyramidal geometry. The trigonal pyramidal geometry is the most strained geometry in our study as previously discussed in the Structures and Vibrational Frequencies section. On average, the HOMO-LUMO energy gap decreases with increase in the polycyclic nature of the pure Si or Ge cluster.
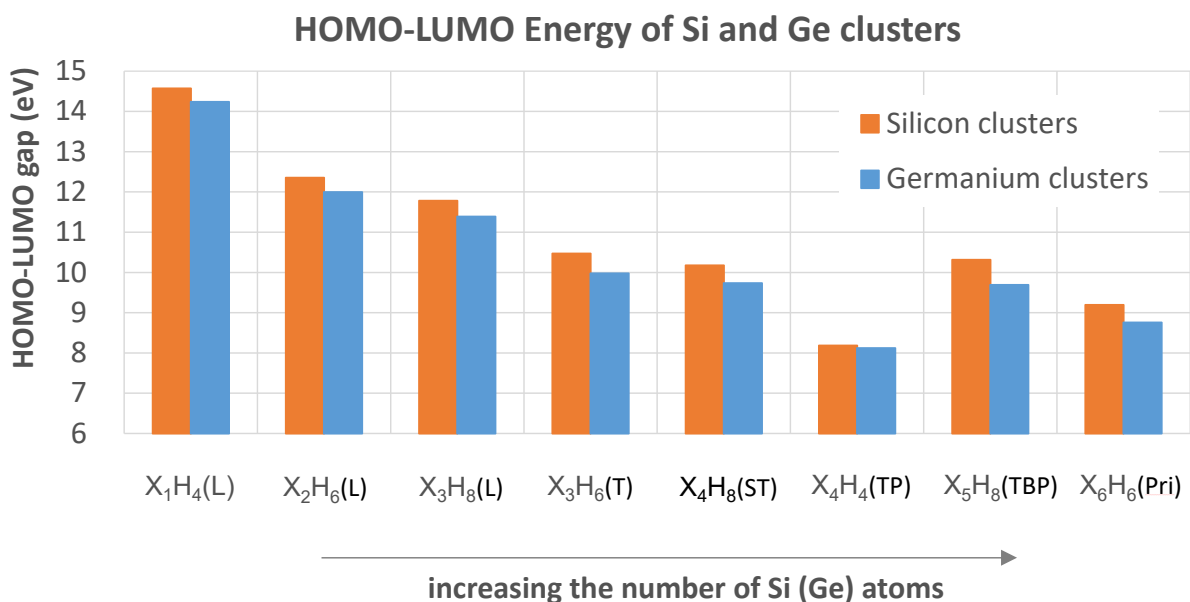
Figure 2.1.4: Comparison of calculated HOMO-LUMO energy gaps for pure silicon and germanium clusters using the G3//B3LYP level of theory. The nomenclature to identify cluster geometries is the same as in **Figure 2.1.1.**
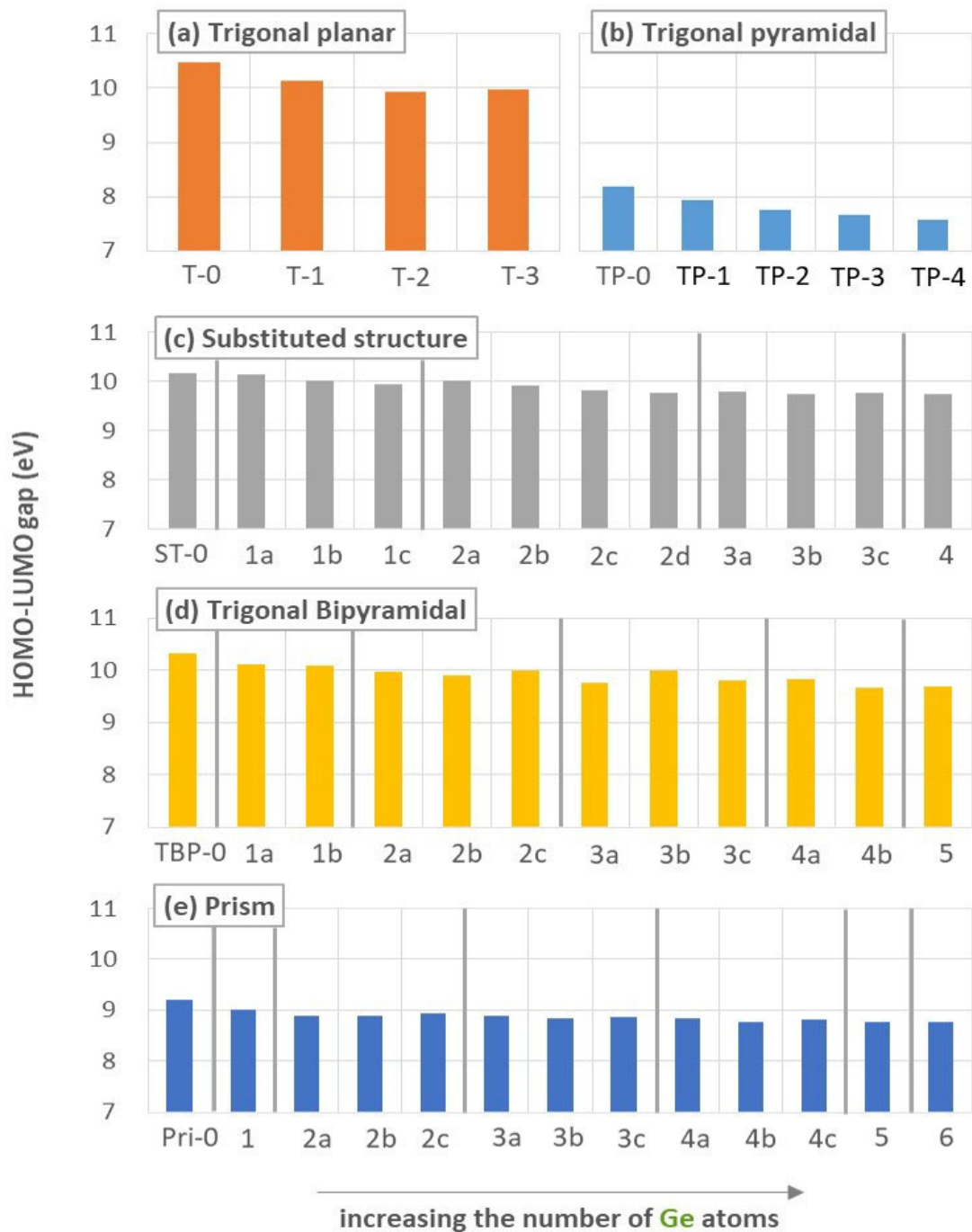
Figure 2.1.5: Comparison of calculated HOMO-LUMO energy gaps for all hydrogenated Si, SiGe, and Ge clusters in this study using the G3//B3LYP level of theory. The nomenclature to identify cluster geometries is the same as in **Figure 2.1.1**.

Figure 2.1.5a-e present calculated HOMO LUMO energy gaps of all clusters in our study, particularly highlighting the effects of alloy cluster composition and isomers. The most precipitous fall in HOMO-LUMO energy gap is for the trigonal bipyramidal geometry followed by the trigonal planar, substituted trigonal planar, prismane, and trigonal pyramidal geometries at 0.49, 0.44, 0.44, and 0.43 eV, respectively. It is interesting to note that the corresponding band gap energy of bulk semiconductor materials is lowered at elevated temperatures as increased atomic vibrations increase interatomic spacing which decreases the potential seen by the electrons in the material, thus reducing the size of the observed band gap energy. It can be expected that a similar phenomenon may be observed for the larger clusters in this study. For instance, bulk pure Si has a band gap energy of 1.17 and 1.11 eV at 0 and 300 K, respectively, and bulk pure Ge has a band gap energy of 0.744 and 0.660 eV at 0 and 300 K, respectively.

Many semiconducting materials or material precursors are characterized as hyperpolarizable and are analyzed by means of vibrational spectroscopy, i.e. Infrared or Raman spectroscopy. In the case of Raman spectroscopy, the corresponding analysis of the electronic wavefunction indicates that the electron absorption corresponds to the transition from the ground state to the first excited state and is conventionally described by the one electron vertical excitation from the HOMO to the LUMO. For most clusters in this study, the HOMO is delocalized over the entire structure. By contrast, the LUMO is still largely delocalized over the entire structure but also extends well beyond the center of mass of the nuclei positions. Consequently, the HOMO-LUMO transition implies an electron density transfer to the limits of the molecular orbitals and this phenomena is consistent with semiconducting material behavior. This extreme delocalization of electron density suggests facile electron density transfer between neighboring clusters in the absence of a formal covalent bond formation, which can be useful for the development of self-

assembling nanomaterials. Examples of this LUMO behavior can be seen in **Appendix A.1.** for the trigonal planar (T), trigonal pyramidal (TP), and prismane (Pri) geometries, where this behavior is most pronounced in structures that contain one or more Ge atoms. **Figure 2.1.6** presents a comparison of calculated contour surfaces of the frontier molecular orbitals (HOMO, LUMO) for the TBP-1 cluster using the B3LYP/6-31G(d), G3//B3LYP, and G4//B3LYP levels of theory. It is important to highlight how the LUMO contour changes significantly between the B3LYP/6-31G(d) and G3//B3LYP levels of theory; however, the HOMO contour is essentially the same between these two level of theory. The HOMO and LUMO contour predictions at the G4//B3LYP level of theory show the strongest inclusion of electron correlation effects as can be observed in **Figure 2.1.6** for the TBP-1 cluster.

Since molecular orbital (MO) theory is by far the most widely used by chemists and chemical engineers, it is important to place the HOMO-LUMO energy gap in a MO framework for reacting chemical systems. That is, according to the notation introduced in the Computational Methodology section, hard molecules have a large HOMO-LUMO energy gap, and soft molecules have a small HOMO-LUMO energy gap. A small HOMO-LUMO energy gap is correlated to small vertical excitation energies to the manifold of excited energy states. Therefore, soft molecules, with a smaller energy gap than hard molecules, will be more polarizable by definition. High polarizability is the most characteristic property attributed to soft Si, Ge, and SiGe clusters. HOMO-LUMO energy gaps should be small for the most favorable bonding or non-bonding interaction between molecules or clusters, i.e., both reactants or molecules should exhibit soft character. As listed in **Table 2.1.6**, the trigonal pyramidal and prismane Si, Ge, and SiGe clusters are the softest species in this study, and thus most reactive due to smaller energy gaps than the remaining clusters and acyclic species. Consequently, these clusters also have a 1:1 Si-to-H or Ge-

to-H atomic ratio, whereas the other species in this study have a lower Si or Ge atomic ratio to H.

On average, less passivation with hydrogen will result in a more reactive cluster or acyclic species.

As defined in the Computational Methodology section, molecular hardness, softness, and chemical

potential calculated from the G3//B3LYP level of theory are presented in **Table 2.1.6.**
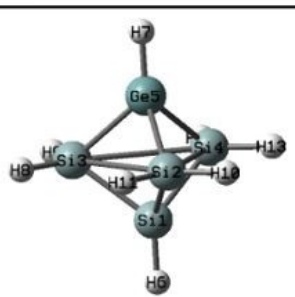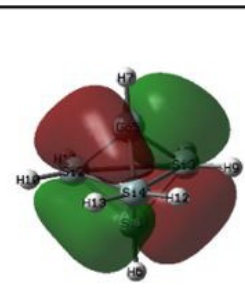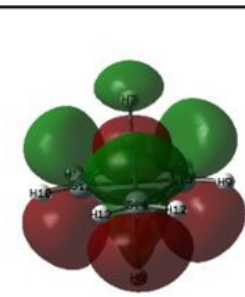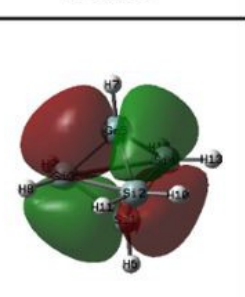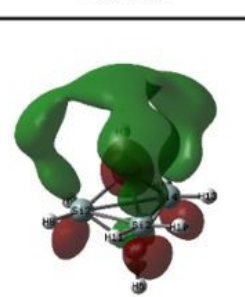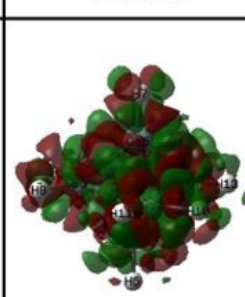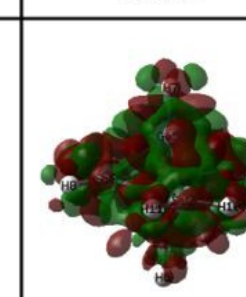
Figure 2.1.6: Comparison of calculated contour surfaces of frontier molecular orbitals (HOMO, LUMO) for the TBP-1 cluster using the B3LYP/6-31G(d), G3//B3LYP, and G4//B3LYP levels of theory. The HOMO and LUMO orbital distributions are presented using an isovalue of 0.02. The nomenclature to identify cluster geometry is the same as in **Figure 2.1.1**.

Table 2.1.6: Calculated quantum chemical molecular descriptors for hardness (η), chemical potential (μ), and softness (σ) at the G3//B3LYP level of theory for all hydrogenated Si, Ge, and SiGe clusters and acyclic species in this study. Hardness in eV, chemical potential in eV, and softness in eV^{-1}

	Index	η	μ	σ		Index	η	μ	σ
1	L-1	7.3	-5.9	0.14	28	ST-4	4.9	-3.6	0.21
2	L-2	6.2	-4.9	0.16	29	TBP-0	5.2	-3.9	0.19
3	L-3	5.9	-4.6	0.17	30	TBP-1a	5.1	-3.9	0.2
4	L-4	6.1	-4.8	0.16	31	TBP-1b	5	-3.8	0.2
5	L-5	7.1	-5.7	0.14	32	TBP-2a	5	-3.9	0.2
6	L-6	6	-4.7	0.17	33	TBP-2b	4.9	-3.8	0.2
7	L-7	5.7	-4.4	0.18	34	TBP-2c	5	-3.8	0.2
8	T-0	5.2	-3.8	0.19	35	TBP-3a	4.9	-3.8	0.21
9	T-1	5.1	-3.7	0.2	36	TBP-3b	5	-3.9	0.2
10	T-2	5	-3.7	0.2	37	TBP-3c	4.9	-3.8	0.2
11	T-3	5	-3.7	0.2	38	TBP-4a	4.9	-3.8	0.2
12	TP-0	4.1	-2.9	0.24	39	TBP-4b	4.8	-3.8	0.21
13	TP-1	4	-2.9	0.25	40	TBP-5	4.8	-3.8	0.21
14	TP-2	3.9	-3	0.26	41	Pri-0	4.6	-3.4	0.22
15	TP-3	3.8	-2.9	0.26	42	Pri-1	4.5	-3.4	0.22
16	TP-4	3.8	-2.9	0.26	43	Pri-2a	4.4	-3.4	0.22
17	ST-0	5.1	-3.8	0.2	44	Pri-2b	4.4	-3.4	0.22
18	ST-1a	5.1	-3.8	0.2	45	Pri-2c	4.5	-3.4	0.22
19	ST-1b	5	-3.7	0.2	46	Pri-3a	4.4	-3.4	0.22
20	ST-1c	5	-3.7	0.2	47	Pri-3b	4.4	-3.4	0.23
21	ST-2a	5	-3.7	0.2	48	Pri-3c	4.4	-3.4	0.23
22	ST-2b	5	-3.7	0.2	49	Pri-4a	4.4	-3.4	0.23
23	ST-2c	4.9	-3.6	0.2	50	Pri-4b	4.4	-3.4	0.23
24	ST-2d	4.9	-3.6	0.2	51	Pri-4c	4.4	-3.4	0.23
25	ST-3a	4.9	-3.6	0.2	52	Pri-5	4.4	-3.4	0.23
26	ST-3b	4.9	-3.6	0.21	53	Pri-6	4.4	-3.4	0.23
27	ST-3c	4.9	-3.6	0.2					

Developing materials with desired optoelectronic properties has always been at the forefront of the semiconducting electronics industry. The optical properties of Si clusters and nanocrystals have been intensively studied due to the possible technological applications of Si in the

semiconductor industry. It has been shown that the large HOMO–LUMO energy gaps of metal encapsulated silicon clusters coupled with their weak reactivity make these structures most suitable for optical absorption and photoluminescence in the visible region. Some of these studies have been driven by the desire to understand the quantum effects of confinement in reduced structural dimensions. To control the triplet/singlet excited states in a designed manner for a desired optoelectronic property, the rational adjustment of the singlet-triplet energy gap ($\Delta E'_{ST}$) between the first singlet (S_1) and triplet (T_1) excited states is the key as depicted in **Figure 2.7a-7b**. Insight into this latter value can be found by the difference between the HOMO-LUMO energy gap and the singlet-triplet splitting energy value (ΔE_{ST}) between the singlet ground state (S_0) and first excited triplet electronic spin state (T_1). Here we complement and extend optoelectronic studies for Si, Ge, and SiGe clusters by calculating the HOMO-LUMO energy gap, which provides insight into the energy gap between the singlet ground state (S_0) and first excited singlet state (S_1), and relating this energy value to the energy splitting between the singlet ground state (S_0) and first excited triplet electronic spin state (T_1), (ΔE_{ST}).

For instance, examination of **Table 2.1.1** for the singlet-triplet energy splitting values (ΔE_{ST}) of SiH_4 and GeH_4 reveals values of 3.9 and 3.6 eV, respectively. Examination of **Figure 2.1.4** for the HOMO-LUMO energy gaps of SiH_4 and GeH_4 reveals values of 14.6 and 14.2 eV, respectively. Similar analysis can be extended to the other species in this study using Table 1 for singlet-triplet splitting energy values (ΔE_{ST}), and **Figures 2.1.4** and **2.1.5** for HOMO-LUMO energy gap values. On average, our theoretical studies suggest that the Ge-doped clusters will exhibit a lower HOMO-LUMO energy gap and singlet-triplet splitting energy value (ΔE_{ST}). Our results suggest that the vertical excitation energy from a singlet spin state to the excited singlet spin state is positively correlated with the HOMO-LUMO energy gap for a molecule optimized in the ground singlet spin

state. Given our preliminary findings on varying levels of passivation, our calculations also suggest that other surface termination schemes may increase cluster chemical stability such that properties of the respective cluster can be used for optoelectronic materials. In **Figure 2.1.7a-7b,** representative energy level diagrams of two optoelectronic processes determined by singlet-triplet splitting ($\Delta E'_{ST}$) between energies of the lowest singlet (E_{S1}) and triplet (E_{T1}) excited states are presented for the sake of clarity.
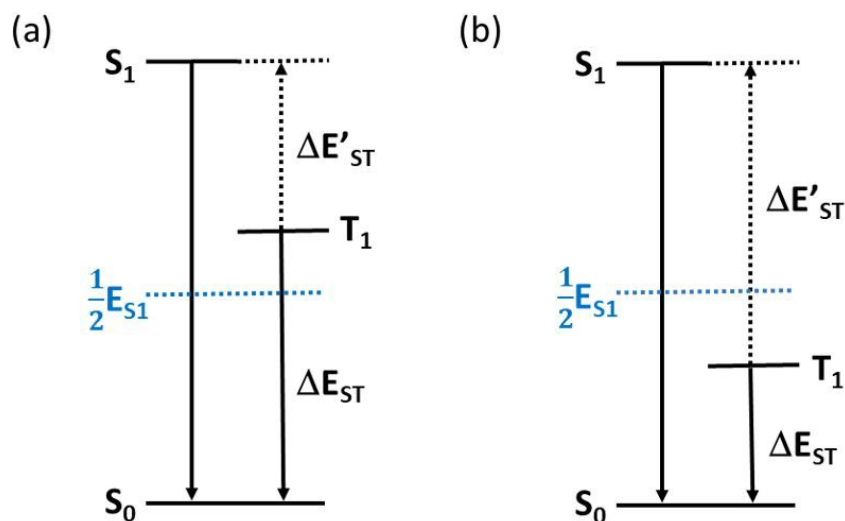
Figure 2.1.7: Representative energy level diagrams of two optoelectronic processes determined by singlet-triplet splitting ($\Delta E'_{ST}$) between energies of the lowest singlet (E_{S1}) and triplet (E_{T1}) excited states. Process (a) has a small $\Delta E'_{ST}$ value, and process (b) has a large $\Delta E'_{ST}$ value. The singlet-triplet splitting values (ΔE_{ST}) between energy of the ground state singlet (E_{S0}) and first excited triplet state (E_{T1}) which are reported in **Table 2.1.1** for selected species are also labelled for the sake of clarity. Downward arrows are associated with emissions, and upward arrows are associated with transitions.

Rational design and optimization of nanoclusters for semiconducting nanomaterial applications traditionally requires the systematic synthesis and examination of various cluster molecules. This conventional "trial-and-error" approach generally requires considerable time and labor costs. Prediction of the cluster properties with a machine learning approach would facilitate the rational design and optimization of nanomaterials, and this approach would allow the discovery of nanostructures with desired properties rapidly and efficiently. Developing this "nanostructure informatics" approach would create a practical method to develop a robust predictive model for nanocluster reactivity. A convenient set of quantum chemical parameters to train our models using a machine learning approach is the fractional electrons transferred during molecular interaction of reactants which was previously introduced in the Computational Methodology section. The fractional electrons transferred during molecular interaction of reactants, ΔN, is correlated to the degree of nucleophilicity and electrophilicity of the reactants, which is highly desirable for tailored nanomaterials design such as self-assembling nanomaterials.

Generalization of Electronic properties using a machine learning approach

Implementation of **equation 2.1.7** to calculate fractional electrons transferred during molecular interaction of reactants, ΔN, using the quantum chemical parameters in **Table 2.1.6** are presented in **Figure 2.1.8**. In **Figure 2.1.8,** we present 2809 data points representing ΔN values for the interaction of all 53 hydrogenated Si, Ge, and SiGe species in this computational study. The graphical representation in **Figure 2.1.8** very conveniently visualizes the key nucleophilic and electrophilic characters of all potential molecular interactions in this study. Dark red and dark blue

regions of this data set represent interactions with the largest ΔN values. The sign of the ΔN value represents the directionality of the electron transfer process. For instance, if one chooses a reactant B from the x-axis and moves vertically along the y-axis of **Figure 2.1.8**, a negative ΔN value signifies that reactant B is a nucleophile when interacting with the corresponding reactant A for the molecular interaction.
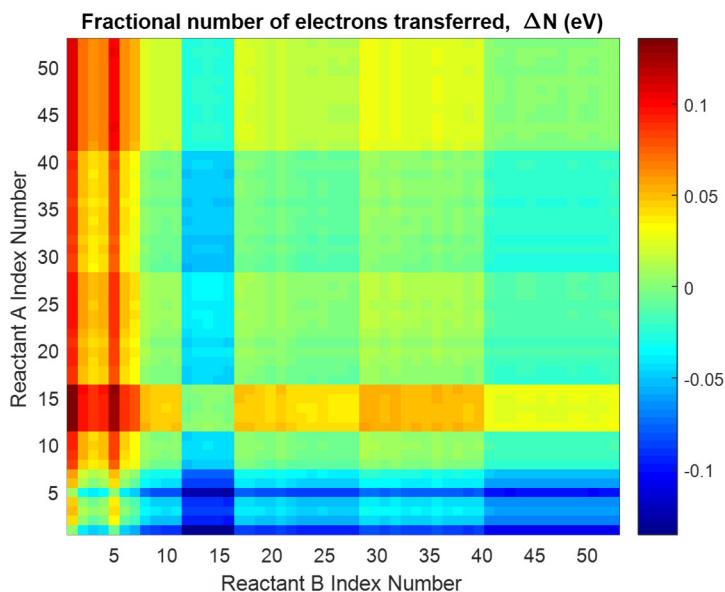
Figure 2.1.8: Contour map of the calculated fractional electrons transferred in eV (ΔN) for molecular interactions of all 53 molecules in this study. ΔN follows **equation 2.1.3** where the frontier molecular orbital energies are calculated using the G3//B3LYP level of theory. The reactant index number follows the numbering scheme of **Table 2.1.6.**

Conversely, reactant A for that same interaction has more electrophilic character during the interaction. The ΔN values in **Figure 2.1.8** are derived directly from quantum chemical calculations at the G3//B3LYP level of theory; however, our study was generalized beyond these calculations by introducing a machine learning approach to create a robust multiple linear

regression equation to predict this ΔN value for molecular interactions not explicitly examined in this study. **Equation. 2.1.8** is proposed for this purpose where ΔN is a function of the molecular weight of reactants A and B, i, the degree of passivation of reactants A and B, i, and the regression coefficients, Ci. The degree of passivation of the reactants is defined as the atom count of total heavy atoms, Si and Ge, divided by the atom count of total hydrogen atoms. The use of the molecular weight and degree of cluster passivation allows for the implementation of nanomaterials design efforts independent of the need to perform computationally expensive quantum chemical calculations during the initial screening efforts of nanomaterials design.

$$\delta N = C_1 * \omega_A + C_2 * \pi_A + C_3 * \omega_B + C_4 * \pi_B \qquad eq\ (2.1.8)$$

Table 2.1.7a contains two models which follow Eq. 8 and were regressed using a machine learning approach to statistical data analysis. **Table 2.1.7b** also contains the regression analysis including the statistical significance and errors of the different models evaluated. Model 1 is comprised of regression coefficients, Ci, for a training set of all 2809 data points for ΔN in this study. The overall model was deemed significant if the F-test satisfied the 99 % confidence level (i.e., the p-value was below $\alpha = 0.01$). In fact, the total regression for Model 1 was statistically significant at the 99.99% confidence interval, and all four regression coefficients, Ci, were also statistically significant at the 99.99% confidence interval despite the total regression for Model 1 having an R^2-value of 0.6660. Although not presented in **Table 2.1.7,** an additional set of four cross terms were added to the full regression **equation 2.1.8** of the forms, $C_{ij}\,\omega_i\,\omega_j$, $C_{ij}\,\pi_i\,\omega_j$, and $C_{ij}\,\pi_i\,\pi_j$ to determine if the R^2-value could be improved. These additional cross terms did not improve the R^2-value for the full regression and were not statistically significant at the 95% confidence interval. **Figure 2.1.9** displays a parity plot for Model 1 of fractional electrons transferred in eV,

ΔN, for the training set of 2809 molecular interactions calculated from the G3//B3LYP level of theory.

Finally, the best predictive model for ΔN values and its four regression coefficients, Ci, were validated using the sensitivity analysis proposed by Mavrovouniotis. This approach removes 10% of the molecular interactions randomly (or 281 ΔN values for our study), and the four regression coefficients are refitted. The new regression coefficients are then used to predict the ΔN values of the removed molecular interactions. The differences between these ΔN values and the values predicted from the original four regression coefficients are then calculated to assess the sensitivity of the regression coefficients. Model 2 presented in **Table 2.1.7** evaluates the sensitivity analysis of the four regression coefficients, Ci, for the prediction of ΔN values. A performance summary for the prediction of ΔN values for the removed molecular interactions using the refitted regression coefficients and the regression coefficients from the full regression containing 2809 molecular interactions is presented in **Table 2.1.7c**. The run using the refitted regression coefficients had an average absolute deviation value of 0.01881 eV for the validation set of 281 molecular interactions compared to the G3//B3LYP values, which is a negligibly higher error than the errors obtained using the regression coefficients from the full regression containing 2809 molecular interactions. Namely, the average absolute deviation value of 0.01879 eV was obtained for the validation set of 281 molecular interactions compared to the G3//B3LYP values when using the regression coefficients from Model 1. Thus, the predictive capability of our multiple linear regression model for molecular interactions, or ΔN values, not included in the training set is very good. This generalization for the prediction of molecular interaction properties is necessary because computational and/or experimental investigation of all potential interactions of Si/Ge/SiGe clusters is not feasible.

Table 2.1.7: (a) Coefficients for the full regression containing 2809 ΔN values (Model 1) and for the regression containing 10% of the ΔN values randomly removed (Model 2), (b) statistical analysis for the least squares regressions and summary of errors, (c) performance summary of the sensitivity analysis using the refitted coefficients (Model 2) and the coefficients from the full regression (Model 1). AAD denotes average absolute deviation.

(a) Regression coefficients

	C_1	C_2	C_3	C_4
Model 1	0.08245	0.000071	-0.08245	-0.000071
Model 2	0.08309	0.000067	-0.08186	-0.000074

(b) Training set

	R^2-value	Regression F-Test		AAD (eV)	std dev
		F-value	P-value		
Model 1	0.6660	1398.46	<0.001	0.0172	0.0144
Model 2	0.6690	1275.56	<0.001	0.0170	0.0143

(c) Validation set

Regression parameters	AAD (eV)	std dev
Model 1	0.01879	0.01491
Model 2	0.01881	0.01491
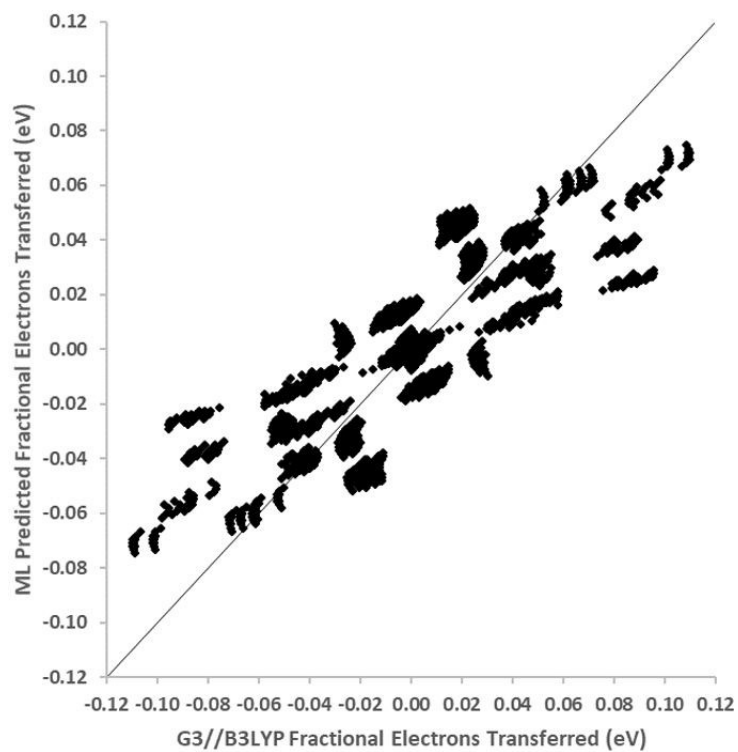
Figure 2.1.9: Parity plot of fractional electrons transferred in eV for the training set of 2809 molecular interactions from the G3//B3LYP level of theory. ML denotes prediction of fractional electrons transferred using the machine learning model regressed in this study.

2.1.4 Conclusion: Si, Ge and SiGe Nanomaterials Properties

In summary, DFT calculations were performed to study the relative stabilities, thermodynamic properties and electronic properties of hydrogenated Si, Ge, and SiGe nanoclusters. For comparison, the properties of pure Si_xH_y and Ge_xH_y clusters are also investigated. The optimized geometries of the *$Si_xGe_yH_z$* clusters were investigated systematically using quantum chemical calculations and conventional statistical thermodynamics. All electronic energies for the clusters were calculated using Gaussian-n methods, which use B3LYP geometries and higher-level corrections based on single point energies. To validate our approach, we compared our computational methodology to other composite methods such as the complete basis set (CBS-QB3) and G4//B3LYP methods, as well as to available experimental data. The geometry parameters of all the molecules increased nominally as Ge atoms were substituted for Si atoms; however, the geometric change was small when compared to the changes observed in the electronic properties. Detailed vibrational frequency analysis has confirmed that all species reported in this study are minima on the potential energy surface and possess all real vibrational frequencies. As Si atoms were exchanged for Ge atoms in a given cluster geometry, the calculated thermochemical properties increased proportionally with the number of Ge atoms in the cluster. The calculated HOMO-LUMO energy gaps are proportionally decreased, as the cluster size increases in total heavy atom count, Si or Ge atoms.

Standard enthalpy of formation at 298 K and standard entropy and constant pressure heat capacity at elevated temperatures, i.e., 298-1500 K, were calculated for the 46 hydrogenated Si, Ge, and SiGe clusters and 7 acyclic Si, Ge, and SiGe species in this study using the G3//B3LYP composite method and statistical thermodynamics with anharmonic vibrational frequency corrections. The hydrogenated Si, Ge, and SiGe clusters contained between one and six Si and/or

Ge atoms and polycyclic nature by way of fused three- to four-membered rings, as well as different degrees of dehydrogenation or multifunctionality. Quantum chemical descriptors based on the G3//B3LYP method, electronic chemical potential, , and absolute hardness and softness, and , respectively, were calculated and generalized using a machine learning approach to predict the reactivity of Si, Ge, and SiGe alloy clusters and acyclic species in the gas phase. A statistically significant predictive model at the 99.9% confidence interval was regressed to allow for nanomaterials design efforts independent of the need to perform computationally expensive quantum chemical calculations during the initial screening efforts of nanomaterials design.

2.2 Silicon-Nitride Ceramic Nanomaterials

2.2.1 Introduction

Silicon nitride is used in a variety of important technological applications. Due to the high strength, high thermal stability, low density, resistance, silicon nitride (Si_3N_4-based ceramics) has attracted great interest for their multi usages for such as cutting tools, anti-friction bearings in turbine[118-120] and electronic application[17, 121]. Specifically, silicon nitride (Si_3N_4) is a wide band-gap (5.3eV) semiconductor material[121], silicon nitride thin film is used as insulating, masking and passivating materials[19] in integrated circuits in the microelectronics industry.[1, 17, 122]

So far, more than six different crystalline polymorphs of Si_3N_4 including α- and β-Si_3N_4 have been reported in the literature[123, 124]. Silicon nitride which can be prepared in several different synthetic routes is an important material for barrier coatings in electronic devices and amorphous Si_3N_4 powder also occurs as an intermediate during the α-Si_3N_4 synthesis. Basically, four different methods of synthesis of silicon nitride from powders were reported; 1) Direct synthesis from elemental silicon with nitrogen, 2) Carbothermic reduction of SiO_2 and carbon under N_2 flow, 3) Diimide process; $SiCl_4$ is reacted with NH_3 at 0~20 ºC to form amorphous, polymeric silicon diimide ($[Si(NH)_2]_n$) which transforms into amorphous silicon nitride upon annealing at higher than 1000 ºC, 4) Dissociation (pyrolysis/CVD) of volatile silicon compounds such as SiH_4, $SiCl_4$ with NH_3.[23, 125] In addition to these classical routes to Si_3N_4, alternatives have been suggested. These include, for example, Self-propagating high-temperature synthesis (SHS-process), plasma- or laser-enhanced techniques.[126-128] The pyrolysis of silicon-containing polymers, especially polysilazanes gives amorphous as well as crystalline silicon nitride, depending on the pyrolysis temperature [129].

In order to prepare silicon nitride materials for the electronic devices as passivation layers,

gate insulating layers, dielectric layers, and antireflection coatings, plasma-enhanced- chemical-vapor-deposition (PECVD)[130, 131] is considered the most efficient method compared to thermal low-pressure chemical-vapor-deposition (LPCVD), which may take place at temperatures approaching 1000 ºC where undesirable side reactions are activated. Although silicon nitride has been researched intensively and the conditions of silicon nitride synthesis have been demonstrated in many studies, a fundamental understanding of the hydrogenated silicon nitride materials synthesis process is still not clear. Here, the homogeneous synthesis of silicon nitride in the gas phase is a multiple step process in which numerous chemical species undergo simultaneous reaction and experimentally measuring the intermediate species is very difficult or impossible under commercial operating conditions. Furthermore, silicon-based materials have attracted many scientists' interests as anode materials of lithium ion battery systems; specifically, applications of amorphous SiN nanoparticles or films in lithium-ion battery systems have been of current research focus.[1] Because SiN compounds behave as both an inactive matrix and a Li-ion conductor, SiN nanoparticles contribute to improving rate performances and cycling stability while maintaining its dense SiN structure after many cycles of battery operation.[132]

Since electronic, optoelectronic, and photovoltaic properties of silicon nitride are controlled or otherwise affected by defects, the manner by which the nature and number of defect sites of silicon nitride changes with the preparation method is critical knowledge still needed for the both academic and industrial communities. Usually, the deposition of silicon nitride is performed at a temperature of 700 ºC or above in the vapor phase from precursors such as SiH_4, $SiCl_4$, or SiH_2Cl_2 with NH_3. Surface reaction mechanisms are critical steps during the chemical vapor deposition of $Si_xN_yH_z$ thin films. Nevertheless, understanding silicon nitride nanomaterials synthesis from the co-pyrolysis of silane (SiH_4) and ammonia (NH_3) is still inadequate. With new potential demand

for anode materials in a lithium-ion battery, a better fundamental understanding of the SiN synthesis process is necessary. Our gas-phase learnings presented herein will enlighten both processes where gas-phase nanomaterials are desired and undesired. Our study contributes to enabling more efficient and target-oriented research on novel materials discovery and design by understanding a comprehensive synthe sis process with the thermodynamic and electronic properties of each reacting species. That is, for CVD processes where surface reactions are desired, gas-phase nanomaterials synthesis is undesired and will cause defects in growing thin films where low-defect conformality is desirable.

Limited experimental and theoretical properties are available on such Si-N binary molecules, molecular ions, and solid silicon nitride products. In the literature, there are synthesis experiments with measurement of concentrations of formed $Si_xN_yH_z$ via vacuum ultraviolet laser single photon-ionization coupled with time-of-flight mass spectrometry and a few advanced ab initio investigation of gas-phase reactions between monosilane and ammonia[7, 133-137]; however, no theoretical thermodynamic properties, which could ultimately confirm the predicted structures through comparison against the available experiments, are available. Therefore, comprehensive computational studies linking the structures, bonding, thermodynamic and electronic properties of silicon and silicon-nitride clusters are very much desired and the purpose of our study herein. The results of our study by means of a data driven approach serve as a database needed for materials discovery and design research using machine learning algorithms[105, 138]; thus, our presented study or data set can be seamlessly applied in multiscale computational methods for improving materials properties that span different length scales.[139]

In summary, we have provided a novel set of electronic structures, thermodynamic data and insights into the reactivity of 60 representative silicon-nitride-based ceramic nanoclusters during

the initial stages of cluster formation under pyrolysis conditions. The properties are predicted using the G3//B3LYP composite method[71, 140] statistical thermodynamics with corrections for vibrational anharmonicity, and a data-driven approach to generalize cluster reactivity. As far as we are aware, this is the most extensive set of silicon-nitride-based ceramic nanocluster thermochemistry data set available which is useful for modeling reaction kinetics and tailoring materials design.

2.2.2 Computational Methodology

Extensive details regarding the computational methodology for calculation of optimized electronic structures and statistical thermodynamics, including corrections for vibrational anharmonicity, have been discussed. The quantum chemical values have been used in our data-driven approach to assess cluster reactivity which is presented here. A brief synopsis is provided in **Tables 2.2.1** and **2.2.2** where triplet-singlet splitting values and a level of theory study are presented. In short, the singlet state was lowest energy electronic wavefunctions used in our investigation, and the G3//B3LYP composite method was most accurate for thermochemistry prediction against available experimental data for Si and N containing hydrides. The G3//B3LYP level of theory was also preferred for self-consistency because our previous studies used the same level of theory [57, 141, 142]. In this study, however, due to a large electronegativity difference between N/Si and N/H atoms, more flexible basis sets were potentially needed and explored. For this purpose, we added different levels of polarization functions and diffusion functions to the B3LYP functional. The B3LYP with a polarized triple-zeta 6-311++G(d,p) basis set predicted most accurately the standard enthalpy of formation only for ammonia, but predictions for silicon hydrides were poor. On the other hand, G3//B3LYP estimated overall reasonably accurate values.

Table 2.2.1: Calculated singlet-triplet splitting values

	G3B3 Electronic Energies with Zero-Point Vibrational Energies		
	Spin Multiplicity		
	Singlet	Triplet[a]	Triplet-Singlet Splitting
Molecules	(Hartree)	(Hartree)	(eV)
A2N1	-347.0658	-346.9058	4.4
A3N1b	-637.6295	-637.4591	4.6
TN1	-636.3952	-636.3402	1.5
STN0	-1162.1246	-1162.0639	1.7
STN1b	-926.9654	-926.9058	1.6
PN2	-982.3779	-982.2198	4.3
HN1	-1508.0901	-1507.9761	3.1
TPyN1	-924.4658	-924.4579	0.2
TBPyN1a	-1216.3215	-1216.2637	1.6
TBPyN2	-981.1041	-981.0553	1.3
PriN1	-1504.4395	-1504.3949	1.2

[a] All molecules in triplet state exist in a form of dissociation.

One of the significant features of density functional theory (DFT) is its suitability for defining chemical reactivity through the conceptual DFT theory molecular descriptors. Conceptual DFT was developed by Parr et al.[143], which depends on the statement that the ground state energy of an N-electron system is specified by the Hohenberg-Kohn theorem. Within the DFT theorem, the electron density can be defined as dependent on the number of electrons N and the external potential v(r), which are themselves derived exclusively by the density, in other words $E[(r)] = E[N;v(r)]$. Upon reaction, the number of electrons in a molecule changes according to a counter reagent, and whether it is electrophilic or nucleophilic, respectively. Therefore, the reactivity of a molecule to chemical reactions is determined by its response to changes in N and v(r). The electronic chemical potential, can be defined as the functional derivative of the energy with respect

to N when v(r) is held constant, which is the contrast of the electronegativity. [144]

$$\mu = \left(\frac{\partial E}{\partial N}\right)_{v(r)} \qquad\qquad eq\ (2.2.4)$$

The quantitative expression for the chemical hardness, η, which can be expressed as the changes of the electronic chemical potential μ of the system with respect to the N at a fixed v(r),[145]

$$\eta = \left(\frac{\partial \mu}{\partial N}\right)_{v(v)} = \left(\frac{\partial^2 E}{\partial N^2}\right)_{v(r)} \qquad\qquad eq\ (2.2.5)$$

The chemical Hardness η can be thought as a resistance of a molecule to exchange electron density within the environment.[106, 107, 109, 145] With the finite difference approximation, **equation 2.2.6 is** obtained.

$$-\mu = \frac{I+A}{2} = \chi \qquad\qquad eq\ (2.2.6)$$

$$\eta = \frac{I-A}{2} \qquad\qquad eq\ (2.2.7)$$

Here I and A represent the ionization potential and the electron affinity of a molecule, respectively. The inverse values of the global hardness are designated as the softness $\sigma = 1/\eta$.

Any chemical system (e.g., an atom, molecule, ion, or radical) is characterized by its μ and η. Using the Koopmans' theorem[110, 111] and Kohn–Sham (KS) Density Functional Theory (KS-DFT), these energies can be approached by $-E_{HOMO} = I$ and $-E_{LUMO} = A$. Thus, the calculated quantum chemical parameters such as the highest occupied molecular orbital energy E_{HOMO}, the lowest unoccupied molecular orbital energy E_{LUMO}, energy gap ΔE, electronic chemical potential μ,

global hardness η, and the softness σ were calculated in our study. Here hybrid functionals systematically calculate HOMO energies that underestimate the first ionization potential values by several electron volts. Nevertheless, these tabulated quantum chemical parameters can be used in two possible ways: as a rank ordering of similar acids (electrophiles) or bases (nucleophiles) to predict relative properties or as a source of values to use in relevant equations such as **equation 2.2.8**. If two systems or molecules, A and B are brought together, electrons will flow from that of lower χ to that of higher χ, until the chemical potentials become equal. As a first approximation, the (fractional) number of electrons transferred, ΔN, will be given by **equation 2.2.8**. The difference in electronegativity drives the electron transfer, and the sum of the hardness parameters acts as a resistance. This reactivity index was predicted as well in this study.

$$\Delta N = \frac{\chi_B - \chi_A}{2(\eta_B + \eta_A)} \qquad\qquad \textit{eq (2.2.8)}$$

In order to better understand the stability of hydrogenated SiN alloy clusters, the natural boding orbital (NBO) analysis were conducted using NBO 6.0 program as implemented in the Gaussian 09 package with the B3LYP/6-31G(d) level. NBO calculation is important for the understanding of delocalization effect from the lone pair electrons (donor, i) to anti-bonding orbitals (acceptor,j). The interaction between the donor and acceptor orbitals can be used to measure the degree of intramolecular delocalization or hyperconjugation. The stabilization energy derived from the interactions was estimated by the second order perturbation interaction energy (E2), describe as **equation 2.2.9**.[146]

$$E(2) = \Delta E_{ij} = q_i \frac{F(i,j)^2}{E_{(j)} - E_{(i)}} \qquad\qquad \textit{eq (2.2.9)}$$

where q_i is the donor orbital occupancy (2 for closed-shell, 1 for open-shell), $E_{(i)}$ and $E_{(j)}$ are diagonal elements (orbital energies), and $F(i, j)$ is the off-diagonal NBO Fock matrix elements.

2.2.3 Results and Discussion

Electronic Structures and Vibrational Frequencies

The electronic structures for the 27 silicon and silicon-nitride clusters and 33 acyclic silicon and silicon-nitride molecules that were considered in the presented study and optimized by means of the B3LYP/6-31G(d) level of theory. The optimized geometries for each of the clusters exhibited complex polycyclic properties with the varying number of nitrogen atoms in each species, as shown in **Figure 2.2.1**. A range of strained structural isomers were examined to include the multitude of strain energies likely in hydrogenated silicon and silicon-nitride clusters. Acyclic silicon and silicon-nitride clusters were examined for species containing 1 to 6 heavy atoms (Si, N). Our study only considered Si-H, Si-Si, N-H, and Si-N bonds, and N-N bonds were not considered. For the cluster geometries in **Figure 2.2.1**, trigonal planar (TN), square planar (SN), substituted trigonal planar (ST), pentagonal planar (PN), hexagonal planar (HN), trigonal pyramidal (TPyN), trigonal bipyramidal (TBPyN), and prismane (PriN) geometries containing of various 3- and 4-membered rings were predicted. All electronic wave functions for the clusters were optimized in a singlet state. Alternative spin states for the electronic wave function are listed in **Table 2.2.1**. Dissociation was observed for most acyclic species and clusters when excited to the triplet state.

Utilizing the nomenclature presented in **Figure 2.2.1**, an investigation of the geometric

parameters for the clusters are presented. Evaluation of our calculated values against experiment or predicted values from the literature for geometry parameters are shown for the acyclic species. For disilane, the calculated Si-Si and Si-H bond lengths were 2.350 Å and 1.489 Å, accordingly, and experimental values were 2.331 Å and 1.492 Å, respectively.[113]
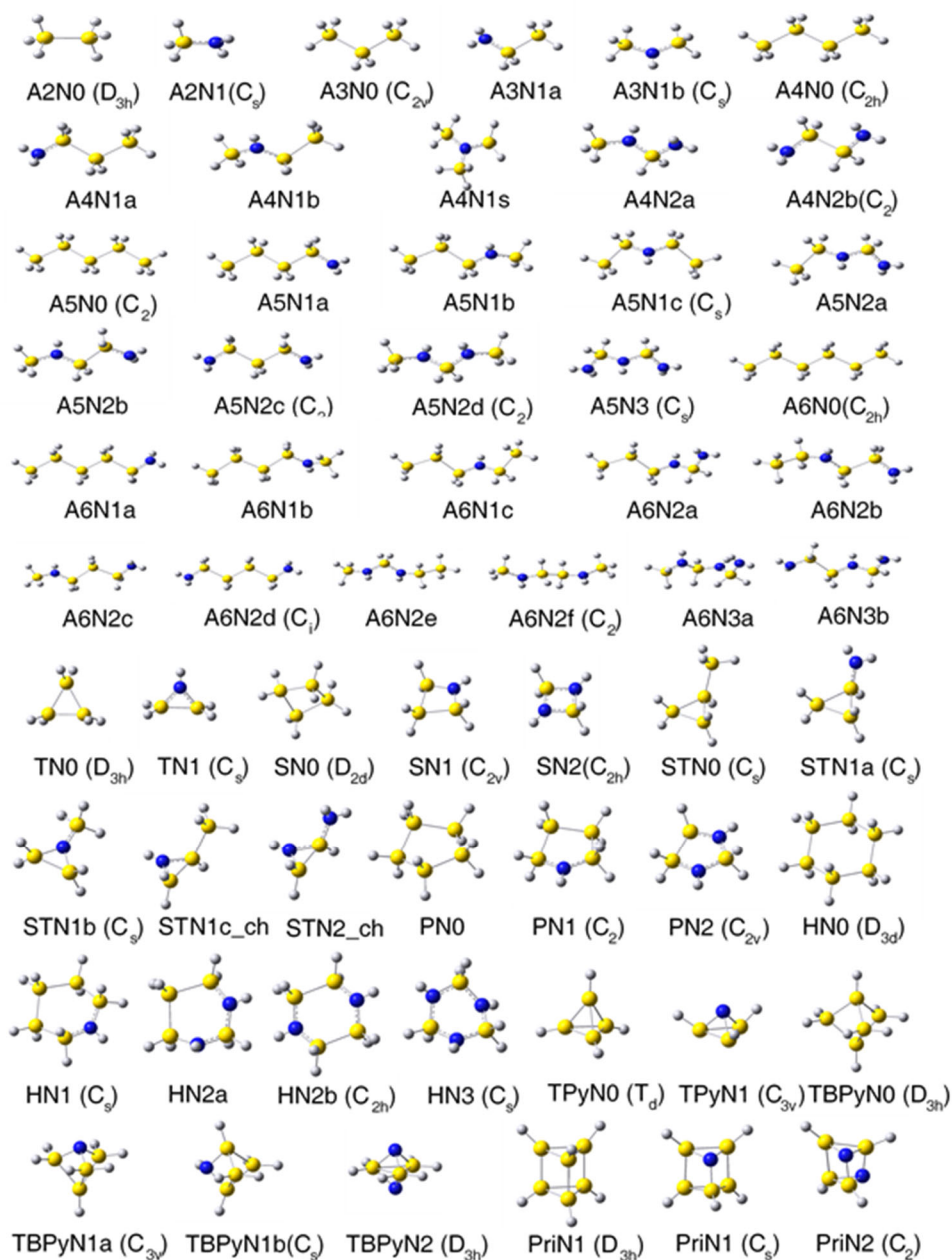
Figure 2.2.1: Optimized $Si_xN_yH_z$ cluster geometries. The naming convention for the cluster geometries is explained in the Computational Methodology. The indices are incremented by integer values to correspond with the replacement of a silicon (yellow) atom by a nitrogen (blue) atom from 0 to 3, where 0 is the pure Si Cluster. The lower case letter symbol denotes isomers.

The H-Si-Si and H-Si-H bond angles were calculated as 110.6 and 108.3 degrees, respectively, and experimental values were 110.3 and 108.6 degrees, accordingly.[113] For silylamine (A2N1), the predicted Si N, Si-H and N-H bond lengths were 1.738 Å, 1.487 Å and 1.104 Å, respectively. These are well matched with literature values[136, 147], which were 1.740 Å, 1.490 Å, and 1.021 Å. The H-Si-N, H-Si-H, H-N-H bond angles were predicted as 107.7, 107.0 and 110.0 degrees, respectively. For trisilane (A3N0), the predicted Si-Si and Si-H bond lengths were the same values as for disilane. The Si-Si-Si, HSi1H and HSi2H bond angles were predicted as 112.9, 108.4 and 107.1 degrees, where 1 and 2 denote middle and terminal silicon atoms in trisilane, respectively. In $H_3Si-H_2Si-NH_2$ species (A3N1a), the predicted Si-N and Si-Si bond lengths were 1.745 Å and 2.350 Å and the N-Si-Si bond angle was 108.9 degrees. For $H_3Si-HN-SiH_3$ species (A3N1b) when the nitrogen is bound to two silicon atoms, the Si-N bond length was predicted slightly smaller than Si-N bond of A2N1 as 1.743 Å and the Si-N-Si bond angle was 129.4 degrees. For the $H_2N-H_2Si-NH_2$ species (A3N2), the predicted Si-N bond length was 1.727 Å which was the shortest length among all Si-N lengths in this study. The predicted N-Si-N bond angle was 108.3 degrees.

For trisilylamine (A4N1s), the predicted Si-N and Si-H bond lengths were 1.753 and 1.487 Å, respectively, and the Si-N-Si bond angle was 120.0 degrees. These predicted values are reasonably agree with literature values by Beagley et al.[148] and Hedberg[149], which are 1.734 1.748 Å for the Si-N bond, 1.485 1.506 Å for the Si-H bond, and 119.4 119.6 degrees for the Si-N-Si bond angle. Calculated values for geometry parameters for all clusters are in practical agreement with literature data for the acyclic $Si_xN_yH_z$ species. As with small acyclic species, it was predicted that there are similar bond lengths and angle values in larger acyclic species (indices A5 through A6 in **Figure 2.2.1**).

For the cluster Si_3H_6 (TN0) of trigonal planar geometry, the equilateral triangle structure is proposed with a Si Si bond length of 2.345 Å and a Si-H bond length of 1.486 Å. Addition of one N atom to the TN0 geometry to make the cyclic H¬2Si-H2Si-NH species (TN1) decreases the bond lengths between heavy atoms as compared to species TN0 and the overall size of the cluster. Here the substituted N atom in the cluster is smaller in atomic diameter than the Si atom, thus the cluster exhibits a smaller overall diameter and more contracted bond lengths in TN1 than TN0. For the TN1 geometry, the Si-Si bond length is 2.253 Å, the Si-N bond length is 1.745 Å, the Si-H bond length is 1.490 Å, N-H bond length is 1.011 Å, and Si N-Si apex angle is 80.4 degrees. The size of the trigonal planar cluster TN1 was contracted compared to the size of TN0 and the apex angle increased.

As detected with the trigonal planar structures, the additional structural geometries (i.e., substituted trigonal planar, trigonal pyramidal, trigonal bipyramidal, and prismane) exhibited a comparable trend of contracted bond lengths with increased nitrogen content. In addition, the nitrogen atom in all planar cluster species in the study exhibited an sp^2 hybridized center which possesses planar trigonal geometry. This is confirmed from the fact that converting the Si-Si-Si angle to the Si-N-Si angle increased the value from 109.5 to 120 degrees. Furthermore, the atoms near N were placed on the same plane with N, or the plane that is close to the N atom. This occurrence is readily noticeable in species trisilylamine (A4N1s) and substituted trigonal planar molecule (STN1b). STN1b is essentially a trisilylamine molecule which has undergone a 1,2-hydrogen elimination reaction.

As we mentioned in our previous study, the cyclic rhombus cluster (SN0) of 4 silicon atoms with a marginally puckered nature, has a Si-Si bond length of 2.371 Å and a Si-H bond length of 1.492 Å with the angles of the Si-Si-Si bonds at 87.7 and 92.3 degrees.[150] For the SN1 species, the

Si-N and Si-Si bond lengths are 1.760 Å and 2.360 Å, respectively. The Si N Si, N-Si-Si, Si-Si-Si bond angles are 109.9, 87.5 and 75.2 degrees, respectively. For the SN2 geometry, the Si-N bond is 1.752 Å and the N-Si-N and Si-N-Si bond angles are 86.8 and 93.1 degrees. Also, the SN2 geometry is no longer a puckered four-member ring as with the SN0 and SN1 species. For the substituted trigonal planar structure (STN2_ch) which is an isomer of the square planar type structure (SN2), the square planar type structure is more stable with lower overall electronic energy. This stability in SN2 is likely due to the formation of four Si-N bonds as opposed to 3 Si-N and 1 Si-Si bonds in STN2_ch; moreover, the NH substituent in SN2 has less steric hindrance than the NH substituent in STN2_ch. We also found a similar trend of cyclic species becoming more planar and contracted as the number of N atoms increases in pentagonal (PN) and hexagonal (HN) planar geometries.

However, the average bond length of Si-N is increased to 1.821 Å in the polycyclic trigonal bipyramid structures (TBPyN) from the smaller Si-N bond lengths of 1.74-1.76 Å observed in the monocyclic and acyclic species. This bonding behavior observed in the TBPyN species is due to the steric hindrance with neighboring atoms; specifically, the strained nitrogen centers are far from the stable planar sp^2 hybridized center which normally possesses a planar trigonal geometry. Similar to the trigonal bipyramidal (TBPyN) structures, the expansion of bond lengths are observed for polycyclic trigonal pyramidal (TPyN) and prismane (PriN) species as the average Si-N bond lengths of 1.843 Å and 1.817 Å are observed, respectively.

Multiple clusters were initially thought to behave as resonance structures. However, NBO analysis confirmed that the nitrogen atom of the silicon-nitride species in the present study has hybridization in various orbitals, sp^λ, which λ range is from 1.67 in acyclic or planar species to 3.62 in prismane geometries, and the Si atom has hybridization in from 1.86 to 5.83, respectively.

It is confirmed that a higher value for occurs more in 3-dimensional geometries, or geometries which are polycyclic in nature. The acyclic and planar structures are relatively more stable than the 3-dimensional (or polycyclic) species, because most of N atoms are sp^2 hybridized centers and the lone pair electrons are in p orbitals, which can lead hyperconjugation phenomena with the neighboring Si atoms. Our NBO analysis is further discuss later in this study under the Section Natural Bonding Orbital (NBO) Analysis.

As far as we know, there are not many studies on hydrogenated silicon nitride nanocluster materials. From the literature review, most of the silicon nitride studied is present in solid-state crystalline forms. Andrievskii[23] and Yashima et al[151] compared the geometric characteristics of different phases of Si_3N_4. Comparing these solid-state studies with our current gas-phase nanomaterials study, we identified two points of overlap worthy of highlighting here: 1) the Si¬-N bond lengths in our most stable acyclic and monocyclic species match those of solid-state materials (i.e., 1.73 to 1.75 Å) and 2) Si-N compounds prefer to be present in planar type structures rather than strained 3-dimensional cluster type geometries or polycyclic in nature with small ring sizes. Additionally the calculated vibrational frequencies for selected species with available experimental data were compared. As shown in **Table 2.2.2**, the G3//B3LYP method was accurate in capturing the vibrational modes of nitrogen-containing hydrides.

Table 2.2.2. Comparison of Experimental Vibrational Modes for NH_3 and SiN_3NH_2 to Unscaled Harmonic Vibrational Modes Using the G3//B3LYP Composite Method

(a) Vibrational Modes of NH_3

type of mode	experimental frequency [a]	G3B3		
		calc. freq.	deviation (exp-calc)	% deviation
NH_3 a-stretch	3443.6	3568	-124.6	-3.6
NH_3 s-stretch	3336.2	3436	-100.3	-3.0
NH_2 scissors	1626.1	1727	-100.7	-6.2
N-H defrom	968.3	1132	-163.5	-16.9
average			-122.3	-7.4

(b) Vibrational Modes of SiH_3NH_2

type of mode	experimental frequency [b]	G3B3		
		calc. freq.	deviation (exp-calc)	% deviation
NH_2 a-stretch	3547	3645	-98.3	-2.8
NH_2 s-stretch	3445	3555	-110.1	-3.2
SiH stretch	2172	2191	-19.0	-0.9
NH_2 scissors	1564	1630	-65.8	-4.2
SiH_3 deform.	996	1012	-16.4	-1.7
SiH_3 deform.	983	993	-10.1	-1.0
SiH_3 deform.	970	942	27.6	2.8
SiN stretch	845	833	11.5	1.4
Deform.	670	709	-39.3	-5.9
average			-35.5	-1.7

a   Ref[152]

b   Ref[153]

Thermochemical Properties

The thermodynamic properties of ammonia (NH_3), disilane (AN20), trisilane (AN30) and SiN with experimental data available were estimated using the B3LYP with the various basis set. The deviations between the calculated and experimental values for standard enthalpy of formation, standard entropy, and constant pressure heat capacity are listed in **Table 2.2.3** for the simple acyclic species. Among the methods used, the G3//B3LYP method was the most accurate for the standard enthalpy of formation calculation for silicon hydrides, with an average absolute deviation of 18.7 kJ mol^{-1} from experimental measurements. The G3//B3LYP method was more accurate for the prediction standard enthalpy of formation values for ammonia with an absolute deviation of 2.9 kJ mol^{-1} from experimental measurements. The largest deviation between experimental and calculated predictions for standard enthalpy of formation for ammonia was observed by B3LYP method can be attributed to factors not included in the composite methods discussed. Due to the correlation of semiconducting or non-local nature of electron of Si atom and lone pair electrons of N atom in the clusters, rigorous composite methods are required to predict trends in thermochemical properties, such as standard enthalpy of formation as function of Si and N composition.

To the best of our knowledge, there is no extensive investigation of thermochemical property estimation or even of vibrational frequency calculations for optimized hydrogenated Si and SiN clusters outside of the works cited in this paper. A total of 59 molecules up to a moderate cluster size, where (Si + N) $\leq$ 6, were investigated in this study. The thermochemical properties of all 59 species studied here are reported in **Table 2.2.3.** The most stable ground electronic state for all molecules in this study was found to be the singlet state. As mentioned in the previous section,

Structures and Vibrational Frequencies, a significant conformational change or spontaneous bond dissociation was observed during optimization of the electronic wavefunction to the triplet state. (**Table 2.2.2**)

In all geometries, the addition of N atoms to a species decreases the standard enthalpy of formation significantly, and also decreases standard entropy and constant pressure heat capacity values. This is the result of the conjugation effect of Si and N atoms. It is observed that a cyclic cluster is more stable than an acyclic molecule with the HN3 and A6N3a even though both have the same number of Si and N atoms. The stability of molecules depends on the position of N atom, so the structure with more Si-N bonds is significantly more stable than other isomers. It is shown to A5N2d and A5N2c in **Table 2.2.4** and **Figure 2.2.2**. This can also be aligned the fact that the bond dissociation energy values of Si-N is much higher than the one of Si-Si, which are 439 kJ mol^{-1} and 327 kJ mol^{-1}, respectively.[154]

Table 2.2.3. Comparison of Calculated Thermodynamic Properties of Hydrogenated Si and SiN Clusters using the G3//B3LYP Method.

Level of Theory									G3//B3LYP		
Atoms				net charge	spin multi-plicity	Symmetry group	chirality	σ_{ext}	$\Delta H°_{f,298K}$	C_p	S
Si	N	H	Molecules						KJ/mol	J/mol.K	J/mol.K
Acyclic species											
2	0	6	A2N0	0	1	D_{3d}		6	75.7	79.5	273.5
1	1	5	A2N1	0	1	C_s		1	-44.6	63.8	262.5
3	0	8	A3N0	0	1	C_{2v}		2	112.5	117.1	346.9
2	1	7	A3N1a	0	1	C_1		1	2.9	102.2	323.4
2	1	7	A3N1b	0	1	C_s		1	-60.2	94.3	328.1
1	2	6	A3N2	0	1	C_2		2	-147.1	87.6	288.1
4	0	10	A4N0	0	1	C_{2h}		2	147.7	154.8	412.3
3	1	9	A4N1a	0	1	C_1		1	39.0	139.9	387.7
3	1	9	A4N1b	0	1	C_1		1	-13.8	133.2	388.6
2	2	8	A4N2a	0	1	C_1		1	-163.1	117.8	356.3
2	2	8	A4N2b	0	1	C_{2h}		2	-70.1	124.6	351.1
5	0	12	A5N0	0	1	C_2		2	182.7	192.5	476.6
4	1	11	A5N1a	0	1	C_1		1	74.1	177.7	453.2
4	1	11	A5N1b	0	1	C_1		1	21.7	170.9	454.2
4	1	11	A5N1c	0	1	C_s		1	32.1	171.9	449.0
3	2	10	A5N2a	0	1	C_1		1	-116.9	156.7	416.8
3	2	10	A5N2b	0	1	C_1		1	-87.2	155.7	421.2
3	2	10	A5N2c	0	1	C_2		2	-33.9	162.5	415.6
3	2	10	A5N2d	0	1	C_2		2	-179.4	148.0	413.6
2	3	9	A5N3	0	1	C_s		1	-263.7	141.5	384.6
6	0	14	A6N0	0	1	C_{2h}		2	217.5	230.3	541.4
5	1	13	A6N1a	0	1	C_1		1	109.0	215.4	518.0
5	1	13	A6N1b	0	1	C_1		1	56.6	208.5	519.7
5	1	13	A6N1c	0	1	C_1		1	67.5	209.6	513.4
4	2	12	A6N2a	0	1	C_1		1	-81.4	194.4	481.8
4	2	12	A6N2b	0	1	C_1		1	-41.1	194.7	487.4
4	2	12	A6N2c	0	1	C_1		1	-51.4	193.5	487.6
4	2	12	A6N2d	0	1	C_1		1	0.6	200.4	488.9
4	2	12	A6N2e	0	1	C_1		1	-133.0	187.0	483.8
4	2	12	A6N2f	0	1	C_2		2	-104.2	186.7	479.9
3	3	11	A6N3a	0	1	C_1		1	-281.2	172.4	453.3
3	3	11	A6N3b	0	1	C_1		1	-190.0	179.1	449.3
3-dimentional clusters											
3	0	6	TN0	0	1	D_{3h}		6	261.1	105.4	304.6
2	1	5	TN1	0	1	C_{2v}		2	121.8	81.3	282.0
4	0	8	SN0	0	1	D_{3d}		4	205.2	137.9	339.4
3	1	7	SN1	0	1	C_s		2	53.7	114.8	350.9
2	2	6	SN2	0	1	C_1		2	-128.9	95.8	290.1
4	0	8	STN0	0	1	C_1		1	282.7	142.0	372.2
3	1	7	STN1a	0	1	C_1		1	190.9	129.3	355.6
3	1	7	STN1b	0	1	C_1		1	89.7	114.8	341.0
3	1	7	STN1c_ch	0	1	C_2	o	2	158.5	120.6	353.0
2	2	6	STN2_ch	0	1	C_{2v}	o	2	18.2	106.6	323.6
5	0	10	PN0	0	1	C_{2h}		1	195.3	174.0	436.7
4	1	9	PN1	0	1	C_s		2	41.6	152.4	386.1
3	2	8	PN2	0	1	T_d		2	-139.2	132.0	352.9

6	0	12	HN0	0	1	C3v	6	211.4	210.3	447.6
5	1	11	HN1	0	1	D3h	1	65.7	190.3	428.3
4	2	10	HN2a	0	1	C3v	1	-109.5	170.0	403.0
4	2	10	HN2b	0	1	Cs	2	-78.3	168.0	408.9
3	3	9	HN3	0	1	D3h	1	-327.0	148.0	369.9
4	0	4	TPyN0	0	1	D2d	12	644.0	122.0	347.1
3	1	3	TPyN1	0	1	C2v	3	540.6	98.5	310.7
5	0	8	TBPyN0	0	1	C2h	6	282.4	157.6	373.9
4	1	7	TBPyN1a	0	1	Cs	3	184.6	133.3	342.8
4	1	7	TBPyN1b	0	1	Cs	1	232.6	139.5	348.0
3	2	6	TBPyN2	0	1	Cs	6	145.6	114.0	318.5
6	0	6	PriN0	0	1	D3h	6	587.1	171.3	378.9
5	1	5	PriN1	0	1	C_s	1	477.7	147.3	365.0
4	2	4	PriN2	0	1	C_2	2	396.4	127.2	335.3

This observation is the result of the hyperconjugation effect of the electrons from Si and N atoms participating in one or more neighboring Si-N bonds in a cyclic cluster or acyclic molecule. For instance, it is observed that a cyclic cluster is more stable than an acyclic molecule where the cyclic HN3 ($H°_{f,298K}$ = -327.0 kJ mol^{-1}) is more stable than acyclic A6N3a ($H°_{f,298K}$ = 269.4 kJ mol^{-1}) even though both have the same number of silicon and nitrogen atoms. However, the stability of molecules depends on the position of N atom, so a structure with more Si-N bonds is significantly more stable than other isomers with fewer Si-N bonds. This is shown clearly with acyclic isomers A5N2d ($H°_{f,298K}$ = 169.4 kJ mol^{-1}) and A5N2c ($H°_{f,298K}$ = 23.7 kJ mol^{-1}) in **Table 2.2.3** and **Figure 2.2.2**, respectively, where A5N2d has four Si-N bonds and A5N2c has two Si-N bonds. Furthermore, relative molecular stability can also be aligned with the fact that the average bond dissociation energy value of Si-N at 439 kJ mol^{-1} is much higher than the average bond dissociation value of Si-Si at 327 kJ mol^{-1}.

Across the temperature span relevant to pyrolysis conditions, the standard entropies and constant pressure heat capacities are shown in **Figures 2.2.3** and **2.2.4** as well as in **Appendix A2**. The average absolute deviations among experimental and calculated properties of standard entropy and constant pressure heat capacity for the NH_3, disilane, and silicon-nitride diatomic molecule

were 0.4 J mol^{-1} K-1 and 0.6 J mol^{-1} K^{-1}, respectively. In prediction of the vibrational contributions to the molecular partition function, it is often approximated that molecules comprised of torsional vibrational modes that deviate from the harmonic oscillator approximation and can behave as hindered or free rotations. Here the hindered rotation of a given dihedral angle capable of torsion within the molecule is an intermediate motion between simple harmonic motion and free rotation. However, treating internal rotations as free rotations is a valid approximation for pyrolysis conditions when the barriers to rotation for Si–Si and Si-N bonds in acyclic hydrogenated silicon nitrides are low.
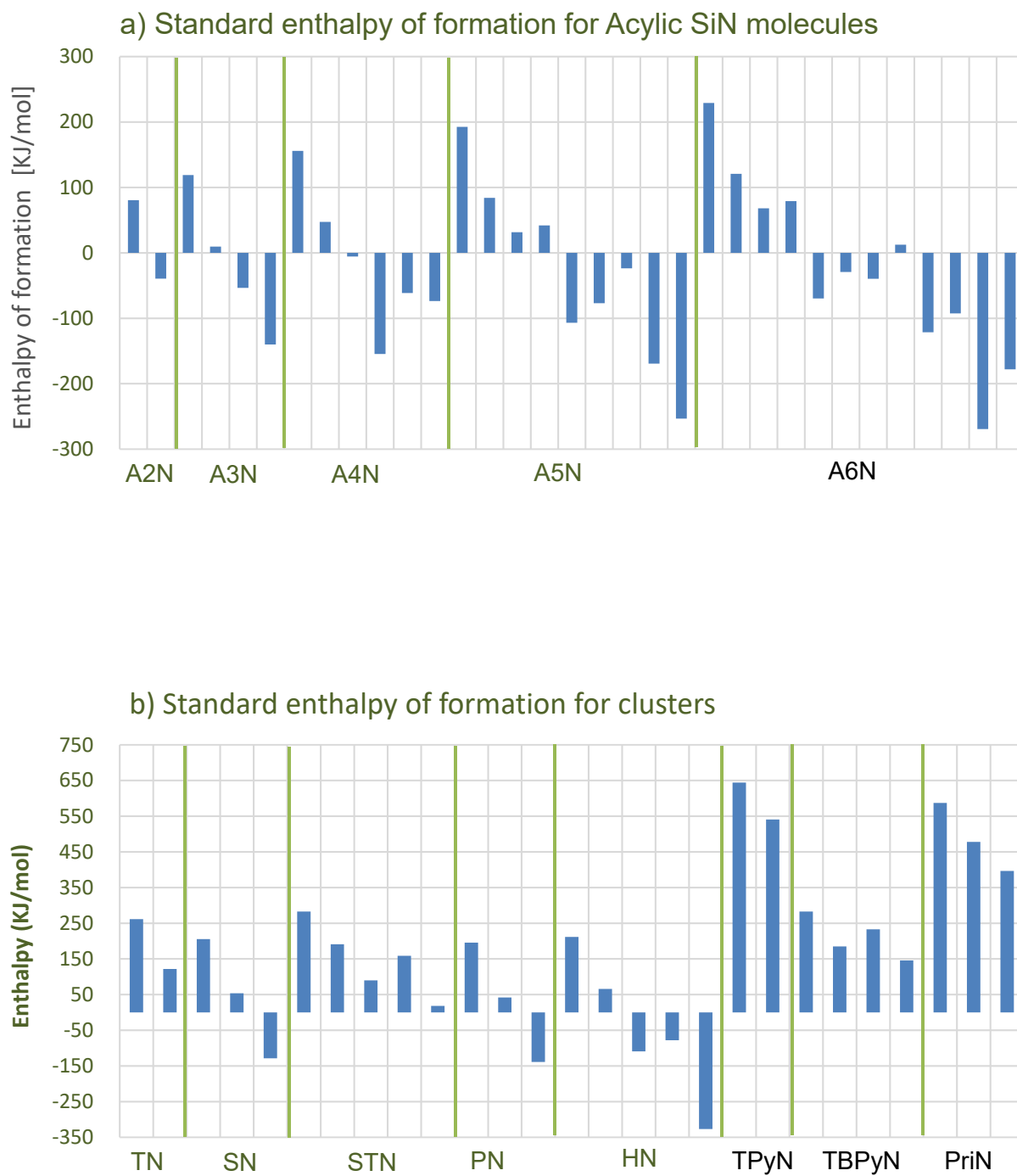
Figure 2.2.2 Calculated standard enthalpy of formation from experimental atomization energies.
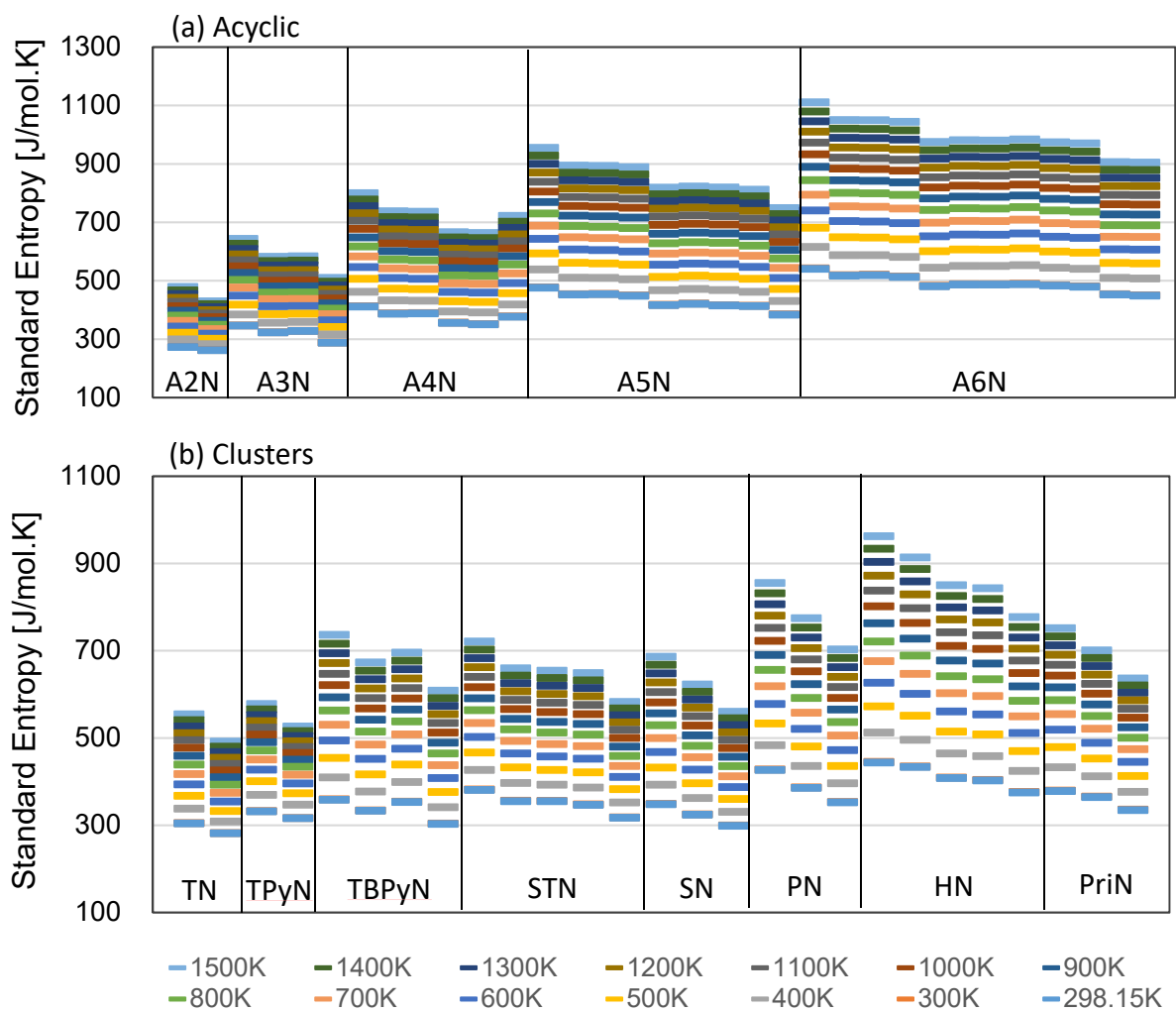
Figure 2.2.3 Calculated standard entropies values.
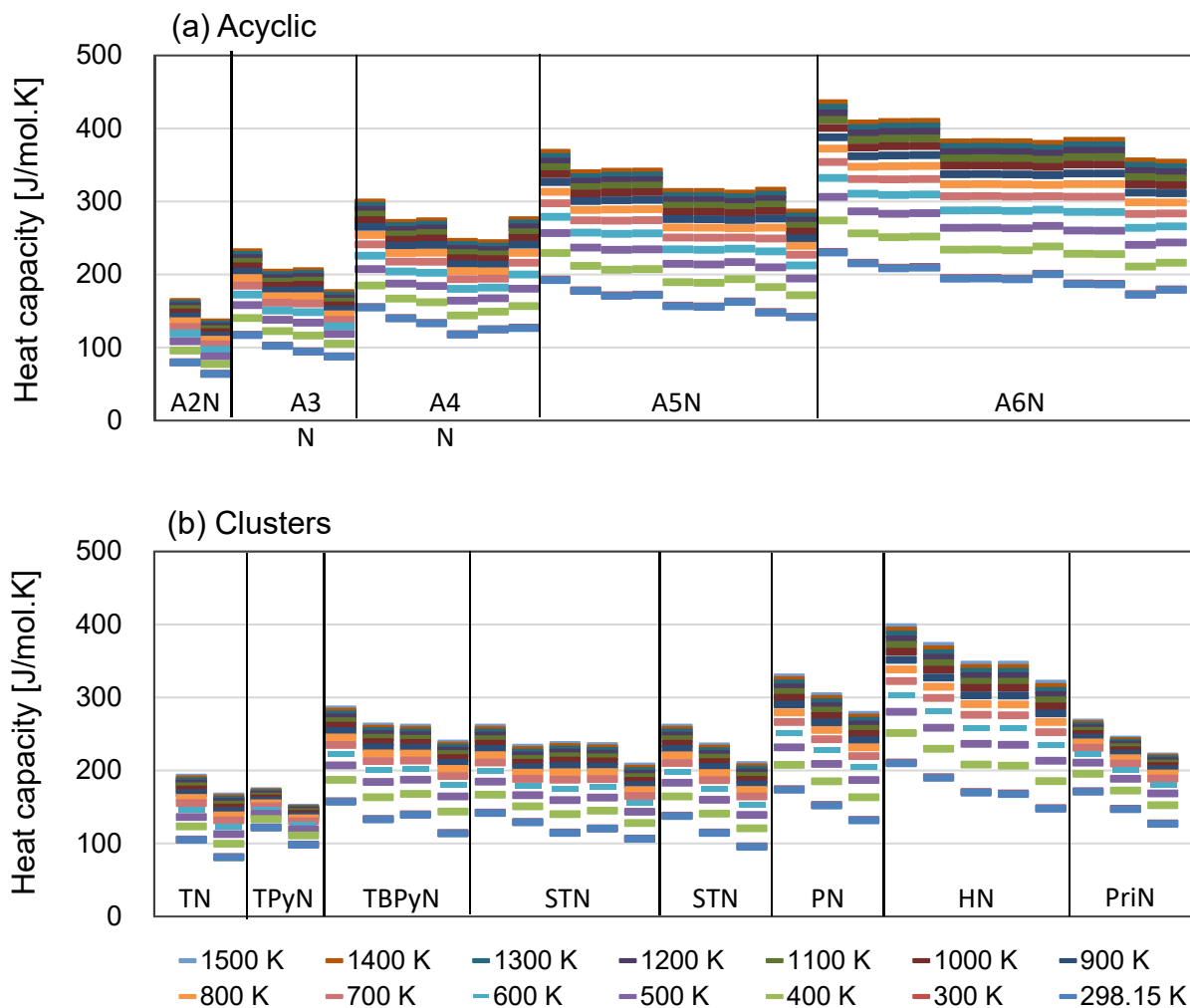
Figure 2.2.4 Calculated constant pressure heatcapacities.

To assess the degree of the effects of internal rotation, potential energy scans at the B3LYP/6-31G(d) level of theory were performed for each of the Si-Si and Si-N bonds in acyclic molecules capable of rotation. It was determined that the barrier energies of internal rotation of most acyclic species within this study were not significant to consider internal rotation effect as the barrier to rotation was on average 4.22 kJ mol^{-1}, so these vibrational modes were instead treated as free rotations. This internal rotation correction made the thermochemistry values to deviate further from the experimental data, which was not a favorable correction to our predictions. This result could be explained by (1) a limitation of the 1-D hindered rotor model, which is not flexible for considering the coupling of internal rotations, and (2) the hyperconjugation effect of the Si-N bonds was not captured at the B3LYP/6-31G(d) level of theory as the hyperconjugation effect would yield larger barriers to rotation thus favoring the harmonic oscillator approximation. Both of these further enhancements to the internal rotation correction were outside the scope of this investigation; however, our studies here do suggest that the torsional modes in the silicon-nitride species are best treated as harmonic oscillators given comparison to reported experimental properties. Comparing the standard enthalpy of formation values for isomers of a cluster geometry series allows for relative stabilities to be identified and ranked. Structural isomers exist in this investigation for acyclic molecules (A3N, A4N, A5N and A6N), the substituted trigonal planar (STN), hexagonal planar (HN), and trigonal bipyramidal (TBPyN) geometries. For example, in **Table 2.2.4**, for the acyclic molecule with 5 heavy atoms (A5N), it is seen that the isomer A5N2d is more stable than isomers A5N2a, A5N2b and A5N2c where standard enthalpies of formation are 169.4 kJ mol^{-1}, -106.9 kJ mol^{-1}, -77.1 kJ mol^{-1} and -23.7 kJ mol^{-1}, respectively. The acyclic isomer A5N2d differs from A5N2a, A5N2b and A5N2c isomers due to the number of Si-N bonds in the molecule. The silicon atom is sp^3-hybridized to form a sigma bond with adjacent N and H

atoms in the aforementioned isomers. Due to the difference of electronegativity, the Si atom has a relatively positive charge and the N and H atoms have relatively negative charges. Accordingly, the bond of Si-N is a polar covalent bond that is stronger than a non-polar covalent bond of Si-Si. An analogous trend in cluster stabilities is also seen for the cyclic STN isomers in the STN1a, STN1b, and STN1c_ch geometry series, but the differences among the most stable isomer and the least stable isomer in these geometries is less prominent than the aforementioned acyclic series with values of 190.9 kJ mol^{-1}, 89.7 kJ mol^{-1}, and 158.5 kJ mol^{-1}, accordingly. The difference in stability of cyclic isomers is equally prominent for the hexagonal planar and trigonal bipyramidal geometry series; nonetheless, the largest difference among isomer stabilities which are comprised of cyclic character is in the STN1 series where the STN1b isomer is most stable. The STN1b cyclic isomer comprised of the molecular formula, Si3N1H7, where the nitrogen atom is at the cluster center and bound to 3 silicon atoms. The difference in cyclic isomer stability is least prominent for the hexagonal planar clusters with differences ranging -109.5 kJ mol^{-1} and -78.3 kJ mol^{-1} for the HN2a and HN2b, accordingly.

Generalization of Electronic Properties and Chemical Stability

Frontier molecular orbitals, which can be predicted by quantum chemistry, such as highest occupied and lowest unoccupied molecular orbitals (HOMO and LUMO), play a significant part in the chemical stability of molecules. Detailed information of the HOMO and LUMO contours is essential for unraveling reactions of clusters and synthesis of silicon-nitride-based ceramic nanomaterials. Here, in the context of covalent bond formation, the HOMO represents the ability to donate an electron (or maximum valence band in larger clusters) and the LUMO represents the

ability to accept an electron (or minimum conduction band in larger clusters). The energy gap between HOMO and LUMO determines optoelectronic properties, chemical hardness-softness of molecules and clusters, as well as chemical reactivity. We employed the $Si_xN_yH_z$ clusters in **Figure 2.2.1** as a training or representative set of cluster geometries, and then calculated DFT molecular descriptors using the predicted electronic structures. In **Table 2.2.4**, DFT molecular descriptors are predicted for chemical potential, hardness, and softness. The interaction energies between each cluster pair were estimated as fractional electrons transferred using the DFT descriptors in **Table 2.2.4** and **equation 2.2.5**. The electron transfer upon interaction of two clusters indicating the probability of reaction is shown as a contour map in **Figure 2.2.6**. It is important to visualize relative reactivity between species because one can begin to determine which reactions are more probable in the gas phase in a reaction space comprised of many species. Selecting a proper reaction modeling candidate from a relative reactivity contour map is a good starting point for investigation of kinetic parameters of the more complex reaction chemistry during actual synthesis. Since finding a transition state for predicting kinetic parameters is one of the most computationally demanding tasks for reaction modeling research, locating or screening probable species or reaction pathways by a data driven approach is essential.

Predicted HOMO-LUMO energy gaps of silicon and silicon-nitride clusters are listed in **Figure 2.2.5**. The calculated HOMO LUMO energy gaps for silicon and silicon-nitride species are in the range from 8.2 to 12.3 eV. The HOMO-LUMO energy gaps of acyclic silicon-nitride hydrides are always higher than for pure silicon and silicon-nitride cluster species. In acyclic hydrides, the HOMO-LUMO gaps decreases as the size of molecules increase, which indicates the reactivity of the acyclic hydrides increase. Also, it is worthy to note that the variation of HOMO-LUMO gaps in each geometries differs with the position of the nitrogen atom in the molecule.

Generally, the HOMO-LUMO gap slightly decreases when the Si atom located at the end of the molecule is replaced with the N atom, which is shown in A2N1, A3N1a, A4N1a and so on. This can be explained by the difference of electronegativity between silicon and nitrogen atoms. The partially negative-charged nitrogen atom makes a polar covalent bond with partially positive-charged neighboring Si atom, this induces polarity in a molecule which contributes to reactivity of the molecule. Thus, if a nitrogen atom is located at the end of a molecule, the molecule behaves like an amine. On the other hand, when a Si atom with two neighboring Si atoms was replaced with a nitrogen atom, the HOMO-LUMO energy gap increased with examples of A3N1b and A4N2a. This stabilization effect is discussed in the NBO analysis section with further details.

Table 2.2.4 Calculated quantum chemical molecular descriptors for hardness (η), chemical potential (μ), and softness (σ)

	Species Index	η (eV)	μ (eV)	σ (eV^{-1})		Species Index	η (eV)	μ (eV)	σ (eV^{-1})
1	A2N0	6.2	-4.9	0.16	31	A6N2f	5.6	-4.4	0.18
2	A2N1	6.1	-4.9	0.16	32	A6N3a	5.8	-4.8	0.17
3	A3N0	5.9	-4.6	0.17	33	A6N3b	5.6	-4.4	0.18
4	A3N1a	5.8	-4.7	0.17	34	TN0	5.2	-3.8	0.19
5	A3N1b	6.0	-4.8	0.17	35	TN1	5.4	-4.1	0.19
6	A3N2	6.0	-4.8	0.17	36	SN0	5.4	-4.1	0.18
7	A4N0	5.7	-4.4	0.18	37	SN1	5.4	-4.2	0.19
8	A4N1a	5.7	-4.5	0.18	38	SN2	5.9	-4.6	0.17
9	A4N1b	5.7	-4.5	0.17	39	STN0	5.1	-3.8	0.20
10	A4N2a	5.9	-4.8	0.17	40	STN1a	4.9	-3.8	0.20
11	A4N2b	5.7	-4.5	0.18	41	STN1b	5.4	-4.1	0.18
12	A4N1s	6.0	-4.8	0.17	42	STN1c_ch	5.2	-4.0	0.19
13	A5N0	5.5	-4.3	0.18	43	STN2_ch	5.1	-3.9	0.20
14	A5N1a	5.5	-4.4	0.18	44	PN0	5.6	-4.4	0.18
15	A5N1b	5.6	-4.4	0.18	45	PN1	5.5	-4.4	0.18
16	A5N1c	5.7	-4.5	0.18	46	PN2	5.9	-4.7	0.17
17	A5N2a	5.6	-4.5	0.18	47	HN0	5.6	-4.4	0.18
18	A5N2b	5.6	-4.4	0.18	48	HN1	5.5	-4.3	0.18
19	A5N2c	5.6	-4.4	0.18	49	HN2a	5.4	-4.2	0.19
20	A5N2d	5.9	-4.8	0.17	50	HN2b	5.5	-4.5	0.18
21	A5N3	5.9	-4.8	0.17	51	HN3	5.9	-4.7	0.17
22	A6N0	5.4	-4.2	0.18	52	TPyN0	4.1	-2.9	0.24
23	A6N1a	5.4	-4.3	0.18	53	TPyN1	4.4	-4.0	0.23
24	A6N1b	5.5	-4.3	0.18	54	TBPyN0	5.2	-3.9	0.19
25	A6N1c	5.6	-4.4	0.18	55	TBPyN1a	5.4	-4.3	0.19
26	A6N2a	5.5	-4.4	0.18	56	TBPyN1b	5.0	-3.7	0.20
27	A6N2b	5.4	-4.3	0.18	57	TBPyN2	5.5	-4.3	0.18
28	A6N2c	5.5	-4.4	0.18	58	PriN0	4.6	-3.4	0.22
29	A6N2d	5.5	-4.3	0.18	59	PriN1	4.6	-3.5	0.22
30	A6N2e	5.6	-4.5	0.18	60	PriN2	4.8	-3.6	0.21
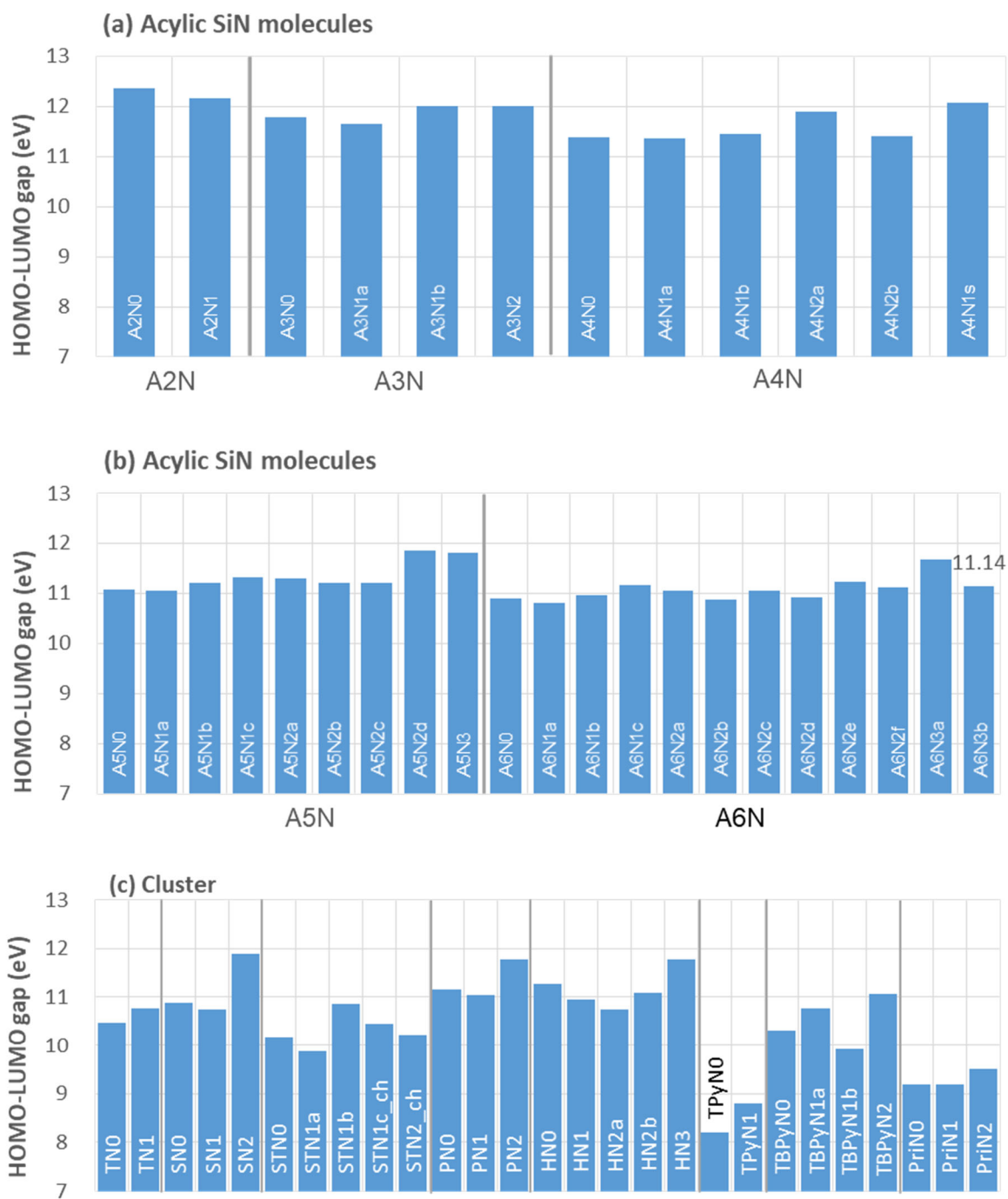
Figure 2.2.5 Calculated HOMO−LUMO energy gaps.
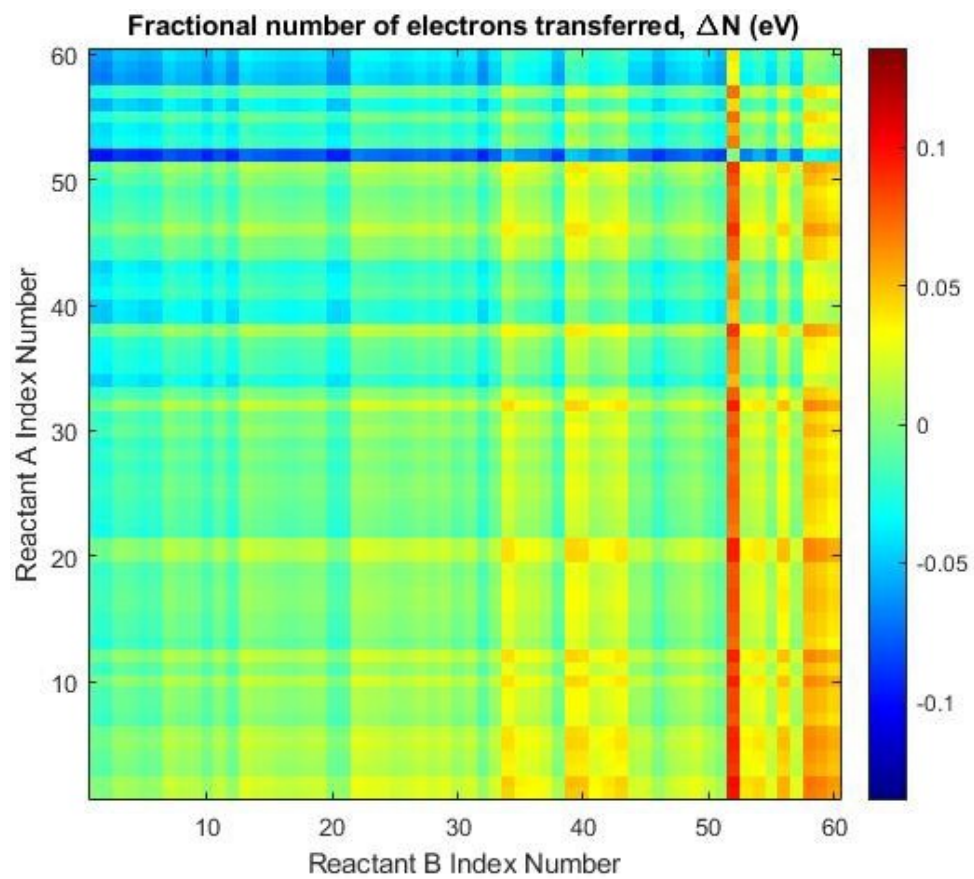
Figure 2.2.6 Contour map of the calculated fractional electrons transferred in eV (ΔN).

The largest absolute difference within a geometry series of 1.15 eV between HOMO- LUMO energy gaps is observed for the square planar geometry, and the smallest absolute difference of 0.18 eV between HOMO-LUMO energy gaps is observed for the two-member acyclic hydrides. The trigonal pyramidal geometry series showed the lowest HOMO-LUMO energy gap and consequently had the most geometric strain. The HOMO-LUMO energy gap is reduced on average with an increase in the polycyclic character of the silicon or silicon-nitride cluster. **Figures 2.2.5a** to **5c** present calculated HOMO LUMO energy gaps of all chemical species investigated, specifically stressing the effects of alloy cluster composition and structural isomers. The most notable decrease in the HOMO-LUMO energy gap is for the square planar geometry series trailed by the trigonal bipyramidal, hexagonal planar, substituted trigonal planar, six-membered acyclic hydrides, five-membered acyclic hydrides, pentagonal planar, trigonal pyramidal, four-membered acyclic hydrides, three membered acyclic hydrides, prismane, trigonal planar and two-membered acyclic hydrides geometry series at 1.15, 1.14, 1.04, 0.87, 0.81, 0.72, 0.60, 0.53, 0.36, 0.32, 0.30 and 0.18 eV, respectively. It is noteworthy to compare the band gap energy of HN_3 and a $Si_3N_3H_3$ molecule. Nabati[51] and coworkers investigated the stability and aromaticity of six-membered heterocyclic species, $Si_nN_{6-n}H_n$ (n=0-6), and $Si_3N_3H_3$ showed relatively low aromaticity and lowest reactivity. This can be explained as the reason why HN3 is the one of the most stable clusters in our study as well.

For acyclic silicon and silicon-nitride hydrides and planar geometries, the HOMO is delocalized across the cluster as shown in **Figure A3** in **Appendix A.3**. On the contrary, the LUMO is predominantly localized over the N atom(s) in the silicon-nitride species. Consequently, the HOMO-LUMO transition suggests an electron density transfer to the edges of the molecular orbitals and this behavior is consistent with stability findings from

Thermochemical Properties section. For the three-dimensional cluster, both the HOMO and LUMO contours are delocalized across the cluster. The widespread delocalization of electron density likely denotes facile electron density transfer among neighboring clusters without necessarily forming a covalent interaction or bond which can be useful for the design of self assembling ceramic nanomaterials which may or may not be sintered thereafter. Instances of this LUMO character can be seen in **Figure A3** for the trigonal pyramidal (TPyN), the trigonal bipyramidal (TBPyN) and prismane (PriN) geometries. On the other hand, the localization of electron density around a specific atom suggests the possibility of designing a particular nanostructure or there is not much place to transfer electron density into LUMO which means reaction would be less probable.

Natural Bonding Orbital (NBO) Analysis

The NBO analysis provides useful information for understanding of intra- and inter-molecular orbitals interactions, re-hybridization, and delocalization of electron density within a molecule. It is used for investigating hyperconjugative interactions (or intramolecular charge transfers, ICT) between Lewis type (bonding or lone pair) filled orbitals and non-lewis type (antibonding * and Rydberg) vacant orbitals in a molecular system. The E(2) value from the NBO analysis is the energy of hyperconjugative interactions (or stabilization energy) and shows the interaction between donor and acceptor groups (bond-anti bond interactions) by 2nd-order perturbation theory. Delocalization of electron density between occupied Lewis type orbitals and formally unoccupied non-Lewis orbitals corresponds to a stabilizing donor acceptor interaction. A

large magnitude of the E(2) value represents a more extensive interaction between electron donors and acceptors, which is usually hyperconjugation of the entire molecular system. This analysis is often referred to as a "delocalization" correction or departure from the idealized Lewis structure description. In order to elucidate the delocalization of electron density, natural bonding orbitals and Wiberg bond index analyses for selected A4N and HN geometry series are depicted in **Figures 2.2.7** and **2.2.8.**

Wiberg Bond index (Total by atom)

A4N0

	1	2	3	4	5	6	7	8	9	10	11	12	13	14
	Si	H	H	Si	H	H	H	Si	H	H	Si	H	H	H
	3.921	0.985	0.985	3.88	0.981	0.982	0.981	3.921	0.985	0.985	3.88	0.982	0.981	0.981

A4N1a

	1	2	3	4	5	6	7	8	9	10	11	12	13
	Si	H	H	Si	H	H	H	Si	H	H	N	H	H
	3.914	0.984	0.986	3.882	0.98	0.981	0.98	3.579	0.969	0.961	2.495	0.834	0.832

A4N2a

	1	2	3	4	5	6	7	8	9	10	11	12
	Si	H	H	Si	H	H	H	N	H	N	H	H
	3.238	0.947	0.948	3.494	0.959	0.964	0.961	2.324	0.815	2.481	0.833	0.831

A4N1s No Wiberg index   Strongly delocalized structure accepted

Figure 2.2.7 Calculated Wiberg bond indices (total by atom) for selected acyclic silicon and silicon-nitride species: (a) A4N0, (b) A4N1a, (c) A4N2a, and (d) A4N1s. The hybridization of the atoms and the weight of each atom in each localized electron pair bond is labelled on the ball and stick molecular structures. Silicon, nitrogen, and hydrogen atoms are denoted as yellow, blue, and white, respectively.

The results of second-order perturbation theory analysis of Fock Matrix in NBO basis for the selected A4N and HN geometry series are presented in Table A.4 in **Appendix A.4.** The A4N0 molecule (tetrasilane) is a fully hydrogenated structure in which four Si atoms are linearly connected to each other, and there are only Si-Si and Si-H bonds present in the molecule. Similar to the C-C bond in the hydrocarbon analogue butane, the Si-Si bond forms a sigma bond of $SP^{2.68}$-$SP^{2.76}$ (Si11-Si8) character as shown in **Figure 2.2.7**. The electron configuration of the silicon atom (Si4 atom in A4N0), as an example, is [core] $3S^{1.11}$ $3P^{2.40}$ $3d^{0.03}$, which is a hybridization state of orbitals with intermediate character. The natural electron configuration (effective valence for each atom) results of A4N0 and other molecules of the A4N and HN geometry series are shown in **Table A4** in **Appendix A.4**. It can be said that electrons are relatively evenly distributed in both Si-Si and Si H bonds due to the relatively small difference of electronegativity between the silicon and hydrogen atoms, 1.9 and 2.2, respectively. A4N1a, where the last silicon atom of A4N0 is replaced by a nitrogen atom, forms a covalent bond N11-Si8 in a hybridized state with N11 ($SP^{1.67}$) and Si8 ($SP^{3.58}$) character. Here, the N11 Si8 bond is a polar covalent bond where the electron distribution is 79.3% for N11 and 20.7% for Si8 atom. In the A4N1a molecule, the intermediate atom-centered Wiberg bond indices of Si8 (3.579) and N11 (2.495), which are less than 4.0 and 3.0 for silicon and nitrogen atoms, respectively, indicate deviation from the idealized Lewis structure description where electrons are delocalized throughout the molecule for stabilization. In addition, the E(2) energy value for the N11 LP (lone pair) electrons contributing to the Si8-H10 sigma antibond * is considerably high at 10.03 kcal mol^{-1}. A hypervalent bonding implies a transfer of the electrons from the central (hypervalent) atom to the nonbonding molecular orbitals which it forms with (usually more electronegative) ligands. Compared to other stabilization energy values of AN40 in **Table A4 (a)**, values of the energy within AN41a are on average higher when a

nitrogen atom is present. Also, the sigma bonds of Si8-H9 and Si8-H10 near the N11 atom contribute to the stability of A4N1a with higher E(2) values than E(2) values for similar interactions in the A4N0 molecule. In the A4N2a and A4N1s molecules, it is shown that as both the number of Si-N bonds and vicinal sigma antibonds increase, the hyperconjugative interactions of the LP of N8 and N10 atoms to each sigma antibond are better distributed. Moreover, even the core electrons (CR) of the Si atom in A4N2a and A4N1s contribute stabilization to nearby sigma antibonding orbitals, * Si-N and * Si-H.

In the molecules of the HN group, the HN0 molecule is cyclohexasilane formed by six silicon atoms as a ring and a fully hydrogenated structure. Since the Si-Si bond length is much longer than the C-C bond, there are no stable cis- and trans-type isomers unlike the hydrocarbon analogue cyclohexane. As shown in Figure 8, the Si-Si bond in HN0 is a sigma bond composed of silicon in the hybridization states of $SP^{2.82}$-$SP^{2.82}$ character. The natural electron configuration for the silicon atom is [core] $3s^{1.15}3p^{2.57}3d^{0.03}4p^{0.01}$, which is a hybridization state of orbitals with intermediate character similar to the configuration of the silicon atom in A4N0 presented earlier. The HN1 molecule, in which a silicon atom is replaced by a nitrogen atom to create the HN0 molecule, has polar covalent bonds for the Si1 N16 and Si5-N16 bonds. The Si1-N16 and Si5-N16 bonds have hybridized states for silicon and nitrogen with $SP^{3.86}$-$SP^{1.70}$ character, respectively.

Figure 2.2.8 Calculated Wiberg bond indices (total by atom) for selected cyclic silicon and silicon-nitride species: (a) HN0, (b) HN1, and (c) HN3. The hybridization of the atoms and the weight of each atom in each localized electron pair bond is labelled on the ball and stick molecular structures. Silicon, nitrogen, and hydrogen atoms are denoted as yellow, blue, and white, respectively.

The HN1 molecule has higher reactivity than the HN0 molecule due to the polarity offered by the N16 atom. In the cyclic HN1 molecule, the intermediate atom-centered Wiberg bond indices of Si8 (3.543) and N11 (2.319), which are less than 4.0 and 3.0 for silicon and nitrogen atoms, respectively, indicate deviation from the idealized Lewis structure description to a greater extent than in the acyclic A4N1a molecule. Furthermore, the E(2) value of hyperconjugative interaction between the LP electrons of N16 to the * Si1-Si2, * Si1-H7, * Si4-Si5 and * Si5-H11 are 3.66, 8.38, 3.57, and 8.38 kcal mol^{-1}, respectively. This stabilizing contribution to * Si-H is higher than to * Si-Si. Also, the CR electrons of the Si1 and Si5 atoms bonded to N16 contribute to * Si5-N16 and * Si1 N16, respectively. In the HN3 molecule, where all silicon atoms are bonded to two nitrogen atoms, stabilization between the CR electrons of silicon atoms and LP electrons of nitrogen atoms to sigma antibonds nearby occurs over the entire molecule. This results in lower

reactivity and higher stability of the HN3 molecule, which is shown in **Figure 2.2.8** and **Table A4(g)** in **Appendix A.4.** It is interesting to note that ICT occurs from the LPs of of nitrogen atoms to not only Si-H antibonding but Si-N antibonding as well. The presence of more nitrogen atoms in a molecule contributes a greater amount of stabilization energy from antibonding interactions. This stabilization of charge transfer is consistent with the result of the HOMO LUMO energy gaps in **Figure 2.2.5**.

2.2.4 Conclusions

Quantum chemical and statistical thermodynamics calculations were conducted to examine the relative stabilities, thermochemistry, and electronic properties of 60 hydrogenated silicon and silicon-nitride nanoclusters. To validate the G3//B3LYP composite method, we assessed our computational methodology against the B3LYP functional and various basis sets, such as 6-31G(d,p), 6-311G(d,p), 6 311++G(d,p), as well as against available literature data for small silicon and silicon-nitride species. The geometry parameters (bond lengths, bond angles, cluster diameter) of all the species decreased on average and the calculated thermochemical properties (H_f, S, and C_p) reduced proportionally as the nitrogen content of the cluster increased. For instance, the length of the Si-Si bond in A2N0 is 2.350 Å, and the length of Si N bond length in A2N1 is shown as 1.738 Å, indicating that the bond length of all species decreased on average with nitrogen substitution. Accordingly, the diameter of clusters decreased as the nitrogen content of the cluster increased. Because of the characteristics of Si atom which forms bonding in a tetrahedral structure and the N atom which has a trigonal planar structure after forming a bond with a Si atom, the bond

angles increased in all species as the nitrogen content increased. As a result, the cluster geometry of the planar type is more probable than the 3-dimensional structure due to introduced geometric strain. Similarly, the calculated HOMO LUMO energy gaps are proportionally increased with increase in nitrogen content in both cyclic planar and clusters. However, when comparing A4N1a, A4N1b, A4N1s, SN1 and TpyN1 species, which have the same amount of Si and N atoms in each molecule, the calculated enthalpy of formation (H_f) increased significantly in the order of A4N1s, A4N1b, A4N1a, SN1, and TPyN1, respectively, while the HOMO-LUMO energy gap decreased in the same order. Molecular descriptors, electronic chemical potential (μ), absolute hardness (η), and absolute softness (σ) were calculated and then generalized by means of a data-driven approach to evaluate relative reactivity. As shown in the HOMO-LUMO energy gap data previously, the species with the highest reactivity was the TPyN group, and most of the other clusters showed low reactivity with increased stability as the N content increased. From this relative reactivity data, we predicted which reactants or reaction pathways would be more probable in the gas phase, providing a very useful basis for further studies to estimate kinetic parameters. In addition, the results from this type of data-driven investigation or approach can be used as an input for machine learning algorithms by serving as a training data set. To assess the stability of the hydrogenated silicon and silicon-nitride nanoclusters, natural bonding orbital (NBO) analysis was performed to measure the degree of hyperconjugation for selected A4N and HN group species. Species with a large number of Si-N bonds showed generally lower reactivity and higher stability than those that did not, and the contribution of Si-N bonding to the lower reactivity and higher stability was well correlated with the degree of hyperconjugation from NBO analysis.

Chapter 3

Stabilizing Silicon Nitride Nanoparticles in Hydrogen Atmosphere I

3.1 Introduction

Due to the increase in demand for IoT (Internet of Things) devices, the development of artificial intelligence technology and the increase in demand for non-face-to-face work environments, the demand for computers and smart devices is rising sharply.[1] Hence, the demand for semiconductor chips, which are essential parts of those devices, is also exploding. Interest in these silicon-based semiconducting materials will continuously increase because silicon has the potential as a quantum computing platform.[2-5] Also, silicon-based materials are a platform that can operate above one Kelvin, which will reduce the costs of building quantum systems and accelerate the realization of commercial-grade quantum computers.[6, 7] Silicon spin qubits are particularly appealing because devices based on silicon could be produced using modern semiconductor manufacturing techniques and knowledge. Among various semiconducting materials, silicon nitride is used as insulating, masking and passivating materials due to its wide band-gap (5.3eV) in integrated circuits in the microelectronics industry. [8, 9]

Silicon nitride which can be prepared in several synthetic routes, in addition to classical methods, alternatives such as plasma-enhanced chemical vapor deposition, catalytic and laser-enhanced techniques have been adapted in the industries. Although silicon nitride has been researched intensively and the conditions of silicon nitride synthesis have been demonstrated in many studies and industrial sites[10, 11], it appears that the fundamental understanding of the hydrogenated silicon nitride synthesis process is still unclear. Since their electronic, optoelectronic, and photovoltaic properties can be controlled or affected by defects, understanding the synthetic process is very important. In the chemical vapor deposition process, surface reactions play a key role. To better understand the surface reaction mechanisms, more detailed knowledge of the kinetics of the fundamental reaction classes is still needed.

The deposition of silicon nitrides occurs at around 700 ºC temperature conditions in the gas phase reactions from the Si-precursors such as SiH_4, SiH_2Cl_2, and $SiCl_4$ with NH_3.[12] As mentioned earlier, studies on gaseous synthesis reactions are still incomplete. Therefore, the kinetics of a vapor phase reaction between silane and ammonia will not only explain the mechanism but also can be extended to a tool for finding optimal experimental conditions to design a novel material.

As silicon-based materials show ranging physical, chemical, and optical characteristics depending on the ratio of Si to H, the characteristic of silicon nitride is also affected by the relative ratio of Si:N:H atoms. Different stoichiometric silicon nitrides can be prepared by the various synthetic processes. Unfortunately, most experimental studies had the purpose of defining the optimal conditions for synthesizing specific materials. It is well known that plasma-enhanced chemical vapor deposition (PECVD) techniques have a strong influence on the chemical composition of amorphous SiN_x films[13-17]. By changing the gas flow ratio and the deposition

parameters, the respective band gap, refractive index and composition of the films can be carefully tuned[18]. From this property of SiN_x films, the bandgap of nano devices can be controlled. Furthermore, depending on the deposition parameters, nanoparticles may be incorporated inside the films, forming defects or a composite film, where the size of the nanoparticles can be tailored. If the nanoparticle size changes, the bandgap of the material changes drastically. Compared to the amount of literature related to the material characteristics of silicon nitrides films and nanoparticles, the fundamental research on reaction mechanisms and kinetics is still scarce. Guler et al conducted photoluminescence experiments to obtain information about luminesce of nanoparticles embedded in silicon nitride thin films. Here various SiN films were prepared using different ratios of SiH_4 versus $SiH_4 + NH_3$ under plasma-enhanced chemical vapor deposition (PECVD).[19] Regarding the photoluminescence characteristics, it was also predicted that it was due to a defect.

Hu et al. reported a detailed mechanistic model for gas-phase reactions between silane and ammonia to small species silicon nitrides theoretically,[20] but the size of the final product species in the mechanism is too small for us to consider the gas-phase reaction for synthesizing SiN nanoparticles. Marshall et al. studied the characteristic of the dative Si-N bond and the kinetics of Si-N bond dissociation reactions between amines and silylenes.[21] Nguyen et al. determined the mechanisms of the reactions of SiO (silicon monoxide) and NH_3 and presented energetic data obtained in coupled-cluster theory with complete basis set.[22] Kovacevic et al. represented a possible reaction map of a gas mixture of SiH_4 and NH_3 in the plasma environment.[23] Hu et al. have shown the detailed reaction pathways between gas-phase silane and ammonia using *ab initio* calculations, but their focus was on only the hydrogen elimination reaction family.[20] Besides the studies of the hydrogen shift reaction within silicon hydrides,[24-26] the rate coefficients for a specific reaction family under co-pyrolysis of silane and ammonia have not been reported to the best of our

knowledge.

This study presents the first application of Transition state theory (TST) approach to silicon nitride gas-phase chemistry and specifically investigates the hydrogen shift reaction for molecules containing up to 6 heavy atoms (Si + N). All elementary steps of reactions are limited to monofunctional compounds, that is, molecules possessing either a π bond or divalent center, but not both. The composite method of G3//B3LYP[43] was used to calculate the electronic energy, and then statistical thermodynamics was applied to all reactants and transition states to incorporate temperature effects. Single event rate coefficients at 1 atm and 298-1500 K were calculated using transition state theory (TST), and then activation energies, E_a, and single event pre-exponential factors, $\tilde{A}$, were regressed. Generalized Evans-Polanyi models were then suggested for the different types of hydrogen shift mechanisms based on selected descriptors.

Suggested Evans-Polanyi models can be adapted using machine learning algorithms to predict reaction rate coefficients for larger species not in this study (or training set). This is called supervised machine learning and is the most common sub-branch of machine learning. The Evans-Polanyi models are a predictive statistical process where the model finds the significant relationship between activation energy and enthalpy of the reaction. To estimate how accurately the models in this study will perform, we conducted k-fold cross-validation and bootstrap regression analysis.

3.2. Computational Methodology

Quantum Chemical Calculations, Transition State Theory, and Statistical Thermodynamics.

In order to understand the SiH_4 and NH_3 reaction networks thoroughly, it is essential to establish the elementary reactions. For this, we hypothesized several elementary reactions for the silicon-nitride system and simultaneously benchmarked against current databases for the silane pyrolysis system in the absence of ammonia. As the first reaction family, we investigated the intramolecular hydrogen shift or migration reaction and predicted the rate coefficients of the reactions. Hydrogen shift reaction for silicon hydrides stabilizes unstable substituted silylenes with a divalent center by forming a silene with a π bond.[27] In addition to the validation of stabilization of a divalent silicon center experimentally[28-34] and theoretically[27, 35-42], our previous studies investigated the 1,2 hydrogen shift reaction which is a two-step process, i.e., the reaction proceeds from a substituted silylene to a hydrogen-bridged intermediate species and then the intermediate is transformed into the double-bound silene.[24] However, the hydrogen shift reaction for a SiH_4 and NH_3 reacting feed has not been studied, and our study explored the microkinetic mechanism of the hydrogen transfer under silane and ammonia co-pyrolysis conditions. **Figure 3.1** is the simplest 1,2-hydrogen shift from aminosilylene from the reaction network of a silane and ammonia co-pyrolysis feed.
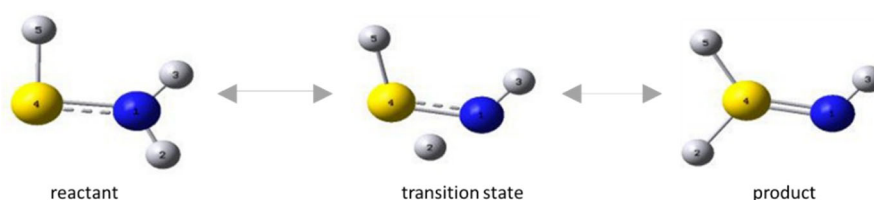
Figure 3.1. Reference reaction (reaction A) for the hydrogen shift from nitrogen to divalent silicon.

Quantum chemical calculations were performed with Gaussian 16 for all the reactions summarized in **Figure 3.2.**[44] All electronic energies for acyclic and cyclic substituted silylenes, substituted silenes (Si=Si) and imines (Si=N), transition states, and hydrogen bridged intermediates were calculated using the G3//B3LYP method[43], which uses B3LYP geometries and higher-level corrections based on single point energies. Geometries and harmonic frequencies of the lowest energy conformers were determined at the B3LYP/6-31G(d) level. Systematic dihedral angle scan calculations were conducted to identify the lowest energy conformer. Multiple conformers exist by rotation of the Si-Si and Si-N bonds. Conformers can be found through the potential energy surface (PES) scan by changing the dihedral angle corresponding to the rotating bond. We conducted PES scans for all Si-Si and Si-N bonds in the species and confirmed that our reacting species lay on the lowest energy surface. For example, the reactant of reaction A has a conformation with the lowest electronic energy where the dihedral angle of H5-Si4-N1-H3 is 0 or 180 degrees and with the highest electronic energy where the angle is 120 degrees. The highest energy difference between conformers of reactant A is 28.04 kcal·mol^{-1}, and we adopted the geometry of the lowest one. The harmonic frequencies and zero point energy were scaled by factors of 0.96 and 0.98, respectively, to account for anharmonicity in the normal vibrational modes as suggested by Scott and Radom.[45] It was reasonable to choose G3//B3LYP level of theory since we have shown an excellent prediction for thermodynamic properties of hydrogenated silicon nitrides.[46]

Using conventional statistical thermodynamics, partition functions based on the harmonic oscillator and rigid rotor approximations were used to calculate thermodynamic and kinetic properties as a function of temperature. The anharmonic effect can be quantified using the one-dimensional hindered rotor approximation. With one-dimensional hindered rotor approximation,

dihedral scans of reacting species were conducted selectively. In reference reaction, the Si-N bond of the reactant (**Figure 3.1**) required 28.04 kcal·mol^{-1} energy for the rotation, which also indicated no rotation impact will be observed during the hydrogen shift reaction. As we stated in our previous study, the energy barrier for the sigma Si-N bond in reactant B2 was barrierless or negligible (0.11 kcal·mol^{-1}) while the one for the Si:-N in the same species overlapped 24.16 kcal·mol^{-1}. The harmonic oscillator model is a reasonable choice with the given rotation barrier height for the Si:-N bond. The barrier of Si-Si bond rotation is too small, so a free rotor model is recommended. But Si-Si bonds can be canceled out because these bonds are not reaction centers for H migration and exist in all phases of reaction. Therefore, we focused only on non-canceling bonds, and no one-dimensional hindered rotation correction was applied for the hydrogen shift reactions in this study. We considered anharmonicity by employing scaling factors.
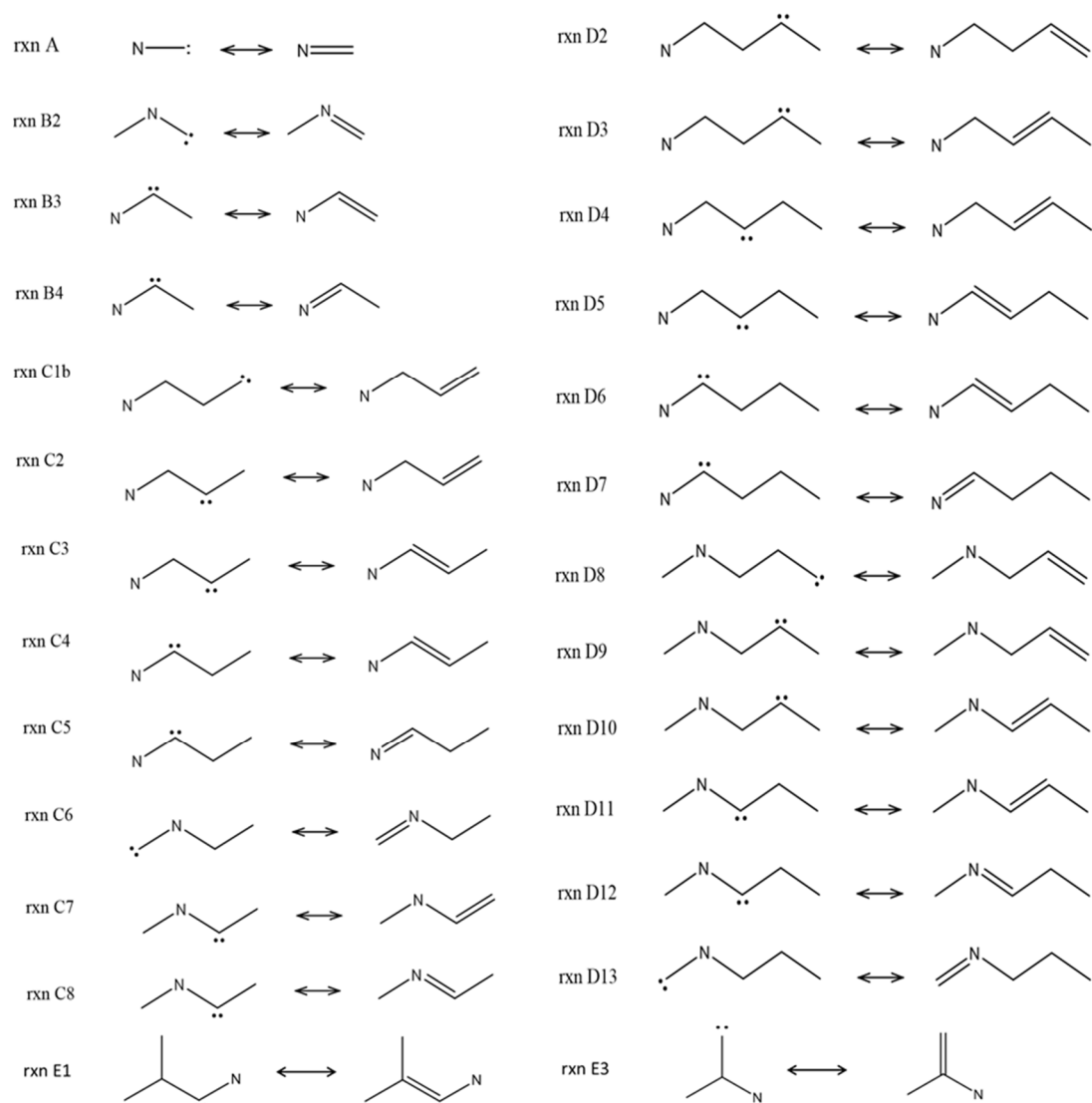
Figure 3.2. Hydrogen shift reactions from acyclic and cyclic substituted silylenes to respective substituted silenes and imines in this study. The reactions are categorized according to the number of Si and N atoms in the reactant. All different reactant isomers product isomers were considered. Unlabeled atoms in each molecules are Si atom, not C atom.
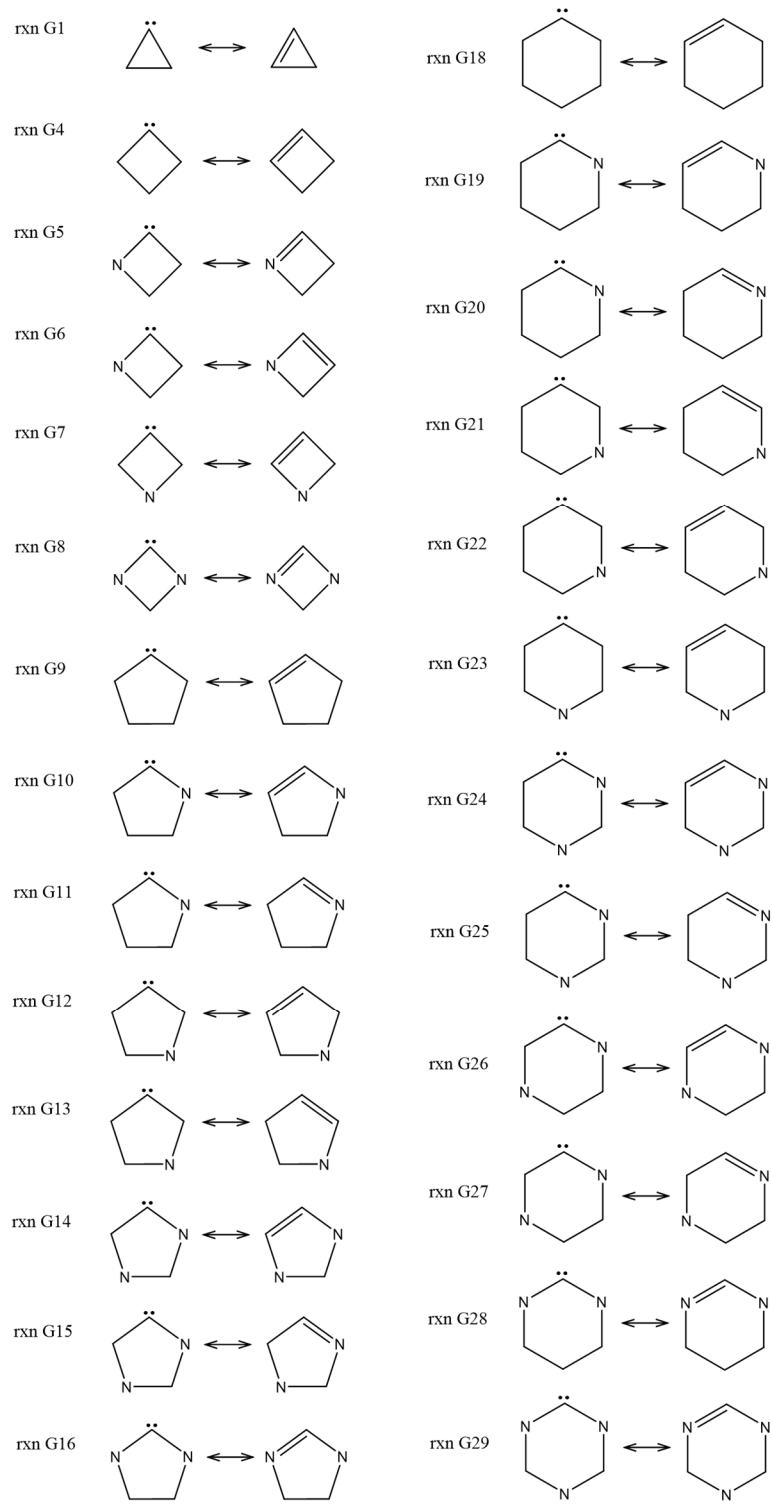
Figure 3.2. Continued.

109

In order to find the transition states, the potential energy surface interpolation method, the Synchronous Transit-guided Quasi-Newton method (QST3), was used. Each transition state was confirmed that it has one imaginary frequency and follows the intrinsic reaction coordinate to the desired reactant and product. Rate coefficients were calculated by conventional TST [102] according to the **equation (3.1)** at 1 atm assuming an ideal gas state,

$$k^{TST}(\text{T}) = n_d \tilde{k} = n_d \Lambda \exp\left(\frac{\Delta S^{\neq}}{R}\right) \exp\left(\frac{-\Delta H^{\neq}}{RT}\right) \qquad \boldsymbol{eq(3.1)}$$

Where Λ, defined in **equation (3.2)**,

$$\Lambda = \kappa(\text{T}) \frac{k_B T (V_m^0)^{-\Delta n}}{h} \qquad \boldsymbol{eq(3.2)}$$

$\tilde{k}$ is the single event rate coefficient: $\kappa(\text{T})$ is the Wigner tunneling correction[155] at temperature T; k_B is Boltzmann's constant; h is Planck's constant; $\Delta H^{\neq}$ is the enthalpy of activation; Δn is the change in the number of moles going from the reactant to the transition state (i.e., zero in both directions for isomerization); and n_d is the reaction path degeneracy, or number of single events. $\Delta H^{\neq}$ and $\Delta S^{\neq}$ are calculated using standard formulae.[102]

The single event parameters of the Arrhenius relationship, $\tilde{A}$ and E_a, were obtained by fitting ln k versus T^{-1} over the temperature range 298-1500 K. This procedure was performed automatically using the CalcK script previously employed by our group for silicon nanoparticle formation kinetics.[55-57, 141, 142] The rate coefficient is important for constructing a mechanistic model. One of method for predicting E_a is the Evans-Polanyi correlation[156] in **equation (3.3)**,

$$E_a = E_0 + \alpha \Delta H_{Rxn} \qquad \boldsymbol{eq(3.3)}$$

where E_0 and α are parameters that are determined from linear regression against predicted values and are constant for a hydrogen shift between Si and N in silicon nitrides. E_0 is the intrinsic barrier of the reaction and ΔH_{Rxn} is the standard enthalpy of reaction. ΔH_{Rxn} is calculated using the the CalcK script. To obtain a generalized model from linear regressions, for the hydrogen shift between Si and N, the intrinsic barrier, E_0, for the both forward and reverse reactions were constrained to be equal to maintain enthalpic consistency. For hydrogen shift between Si and Si due nitrogen atom doping effects, multiple linear regressions were conducted according to **equation (3.4)**,

$$E_a = E_0 + \alpha\Delta H_{Rxn} + \beta N + \gamma d + \delta D_{rel} \qquad \boldsymbol{eq(3.4)}$$

where $E_0, \alpha, \beta, \gamma, and\ \delta$ are parameters that were determined from multiple linear regression against theoretical values and are constant for hydrogen shift between Si and Si in silicon nitride species. E_0 is the intrinsic barrier of the reaction. ΔH_{Rxn} is the standard enthalpy of reaction. N is defined as the number of the nitrogen atoms in the silicon nitride species. d is defined as the direction of hydrogen transferring (where H is transferring towards N atom, $d = 1$, where H is transferring away from N atom, or where there is no N atom in the species, $d = 0$). D_{rel} is defined as the relative distance between the N atom to the nearest divalent Si center. For example, the D_{rel} of reaction C1b is three and reaction C2 is two.

NBO7.0 program under the Gaussian16 software package was used to perform natural population analysis by the natural bond orbital method at B3LYP method with 6-31G(d) basis

set.[53] By comparing the Wiberg Bond index of the corresponding bonds within the reaction, the progress of electron transfer from a reactant to the corresponding product through transition states was captured. WBI was used to calculate the relative position of transition states and an intermediate between a reactant and a product.

K-fold cross-validation was conducted for three regression models, respectively. Since the number of reactions depends on the reaction type, the k value was set differently. The k value for the reaction between Si: and N, the endothermic reaction between Si and Si:, and the exothermic reaction between Si and Si: are 19, 12, and 17, respectively. First, all the dataset was shuffled randomly and was split into k groups. For each reaction type, a group out of k was considered a validation set and the remaining k-1 groups as a training set. Using machine learning principles similar to our previous studies on SiGe species[54], a robust regression model was obtained from each training set, and the model was confirmed with the remaining validation set. For each reaction type, the regression was conducted k times, and the k number of regression models were statistically analyzed.

Also, we accounted for how much random variation there is in the regression coefficient with changes in the dataset. Bootstrapping regression was performed 500 times for each reaction type, then the average coefficient and 90 percentile confidence interval coefficient were suggested.

4.3 Results and Discussion

4.3.1 Competitive pathways for hydrogen migration

A total of 52 hydrogen shift reactions of substituted silylene species comprised of nitrogen were mapped using G3//B3LYP. In this study, two different types of hydrogen shift were investigated; one is hydrogen shifting between N and divalent Si and the other is between Si and divalent Si. The hydrogen shift from N to divalent Si is always an endothermic process, but from Si to divalent Si, hydrogen transferring is categorized as two different processes, and endothermic or exothermic shift depends on the relative distance from N to the reaction center. Mapping of the hydrogen shift potential energy surface for all 52 hydrogen shift reactions showed different reaction phenomena depends on the corresponding reaction enthalpies. The endothermic H transfer (from N to divalent Si and the H transfer from Si to divalent Si where the N atom is adjacent to reaction center) showed a single barrier between reactants and products while the exothermic H shift between Si to the divalent Si, with no next nearest N atom to the reaction center or N is not bound to reaction center, presented two distinct barriers linked by a hydrogen bridged intermediate. It was observed that the exothermic H shift behavior in silicon nitrides matches our previous study investigating the 1,2 H shift reaction in silicon hydrides.[24] As opposed to the 1,2 hydrogen bridging in silicon hydrides which has a two-step pathway, hydrogen shifting from the N to divalent Si in a substituted silyl amine to form an imine is a single pathway. This can be explained by the smaller molecular orbital in nitrogen and the stronger electronegativity of the nitrogen atom than for the silicon atom. In order to compare the different reaction pathways in a systematic manner for this type of process, several heats of formation for the conversion of the reactant into the intermediate and of the intermediate into the product are shown in the **Table 3.1**. Intrinsic reaction coordinate

calculations confirmed the absence of an intermediate for the endothermic reactions; between N and Si: shift (A, C6, and G20) and between Si and Si: shift (B3 and G10).

Table 3.1. Enthalpy of reaction at 298 K and 1 atm for conversion of reactant to the intermediate (step 1) and conversion of the intermediate to product (step 2) for several reactions. The indexing follows **Figure 3.2**. (Blue for the endothermic H transfer from N to Si: yellow for the endothermic H transfer from Si to Si:, and white for the exothermic H transfer from Si to Si:).

Reaction	Type	ΔH_{298} rxn (kcal·mol^{-1})		
		Step 1	Step 2	Overall
A	N to Si: (endo)	x	x	13.53
B3	Si to Si: (endo)	x	x	7.94
C2	Si to Si: (exo)	0.49	-10.06	-
C3	Si to Si: (exo)	-9.80	-2.74	-
C6	N to Si: (endo)	x	x	6.42
D5	Si to Si: (exo)	-9.10	-2.30	-
D9	Si to Si: (exo)	-0.31	-8.22	-
D10	Si to Si: (exo)	-8.61	-2.97	-
G9	Si to Si: (exo)	-1.67	-9.48	-
G10	Si to Si: (endo)	x	x	2.77
G12	Si to Si: (exo)	-2.13	-6.91	-
G13	Si to Si: (exo)	-9.2	-1.47	-
G20	N to Si: (endo)	x	x	1.34

Figure 3.3 shows the transition state geometries and intermediates for several key H shift reactions. The structural changes depend on the type of H shift and can be seen by comparing these geometries. The species that undergoes endothermic processes, which are from N to divalent Si (reaction A and G20) and from Si to divalent Si (B3 and G6) present the single geometry of the

transformation from the reactants to products. However, exothermic H shift from Si to divalent Si (C2 and G13) was represented with two geometric changes from reactant to intermediate through transition state 1 (TS1) and from intermediate to product through transition state 2 (TS2). The structure of the reactive center changes most notably with H shift from N to divalent Si then one form Si to divalent Si. Only endothermic H shift reaction between N and Si has the transition state in which the shape of the reaction center is more symmetric. For example, the ratio of distance of N1-H3 and Si4-H3 is 1 in transition state of reaction C5. However, both endothermic and exothermic H shift in between Si and Si have the geometry of transition state, the ratio of the distance Si-H and Si:-H is about 0.7, and the bond of H-Si: is shorter than the bond of H-Si. The significant transition state in exothermic H shift between Si and Si is always the second transition state along the pathway. The transition state of both endothermic and exothermic H shift reaction is more like product geometry, and this was shown clearly in the Gibbs energy surface diagram (**Figure 3.4**).
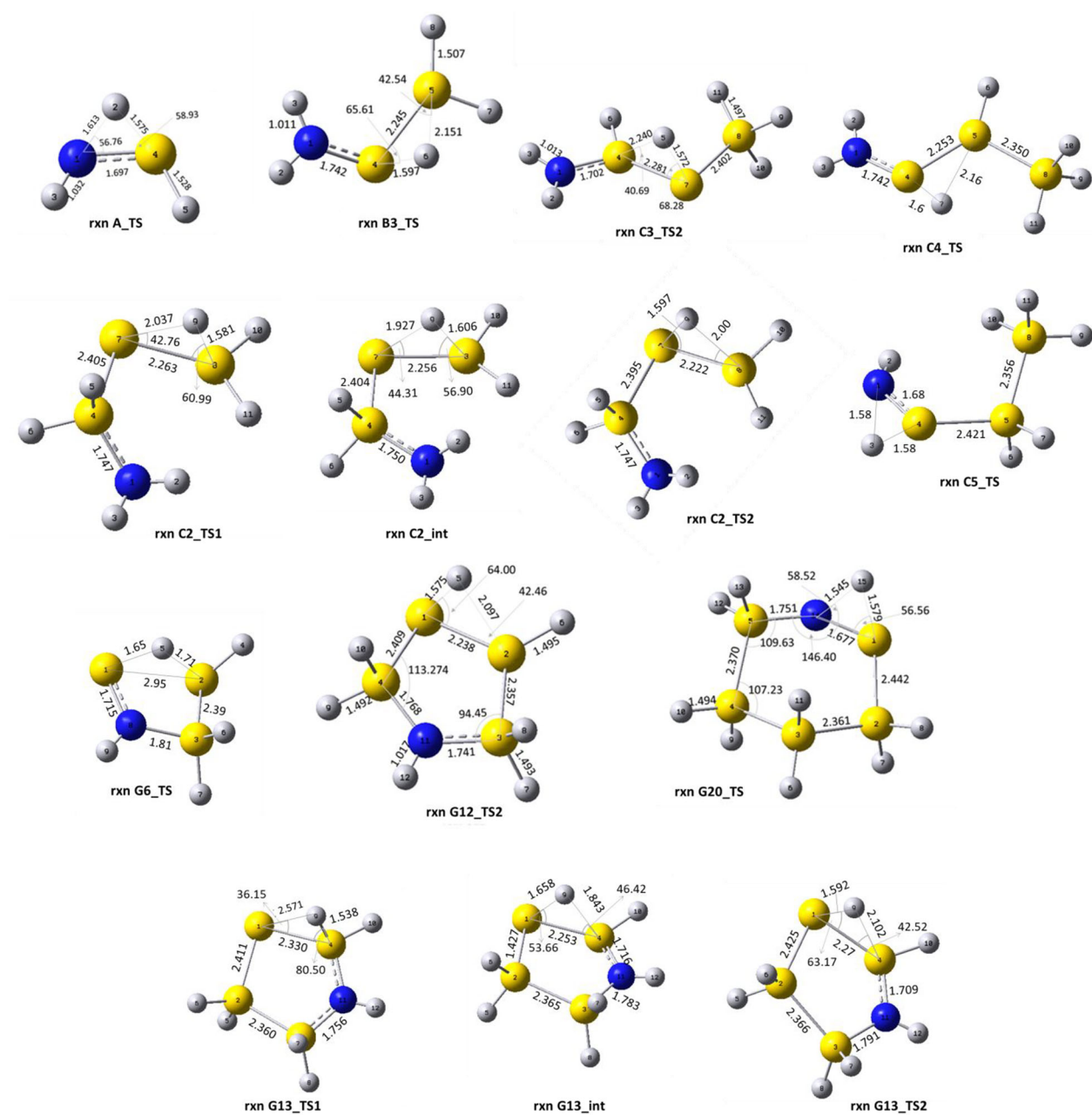
Figure 3.3. B3LYP/6-31G (d) optimized geometries of the lowest-energy conformer of the rate-determining transition state and intermediates for several key reactions.

3.3 Results and Discussion

3.3.1 Thermodynamic Properties of Hydrogen Migration

Different reaction pathways of hydrogen shift reaction in silicon nitrides are depicted in the **Figure 3.4**. Several reactions were selected as key representative reactions for each hydrogen shift type. The dashed-lines are describing the acyclic species behavior, and the solid line are for cyclic species. The shape of the Gibbs free energy diagram was determined according to the type of hydrogen shift reaction rather than simply the structural difference of the species. The hydrogen shift reaction between N and divalent Si, reaction C5 and G11, is a single step reaction which has very high activation energy. Therefore, the species in which the unshared pair Si is bound to N or is located near N prefers to remain as the divalent species rather than form a substituted imine species that is comprised of a Si=N double bond. On the other hand, hydrogen shift reactions between Si and divalent Si in silicon nitrides showed different patterns depending on the relative distance between N and the reaction center. The hydrogen shift reaction of the species where the N atom is located adjacent to the reaction center is also a single step endothermic reaction but has lower activation barrier than the reaction between N and Si:. The hydrogen shift of the silicon nitrides where the reaction center is far away from N atom is a two-step exothermic reaction mechanism, and has much lower activation energies than both aforementioned hydrogen shift reactions. For example, the substituted silylene species where the reaction center is located relatively far away from N within the molecule, reactions C2 and G12, have a mild driving force to transform into silene (Si=Si) species through the hydrogen shift isomerization. Each transition state resembles the structure of the nearest stable species, and the depicted structure of transition states in **Figure 3.3** were well-correlated to the trend of Gibbs free energy surfaces in **Figure**

3.4(a). In the case of reaction C5, the transition state is located in the middle of the reaction coordinate, which is also indicated by the corresponding reaction center configuration in **Figure 3.3**. The distance between atoms N1-H3 and Si4-H3 are the same at 1.58 Å and the angles of H3N1Si4 and H3Si4N1 are is 57.7 degrees and 57.3 degrees, respectively.
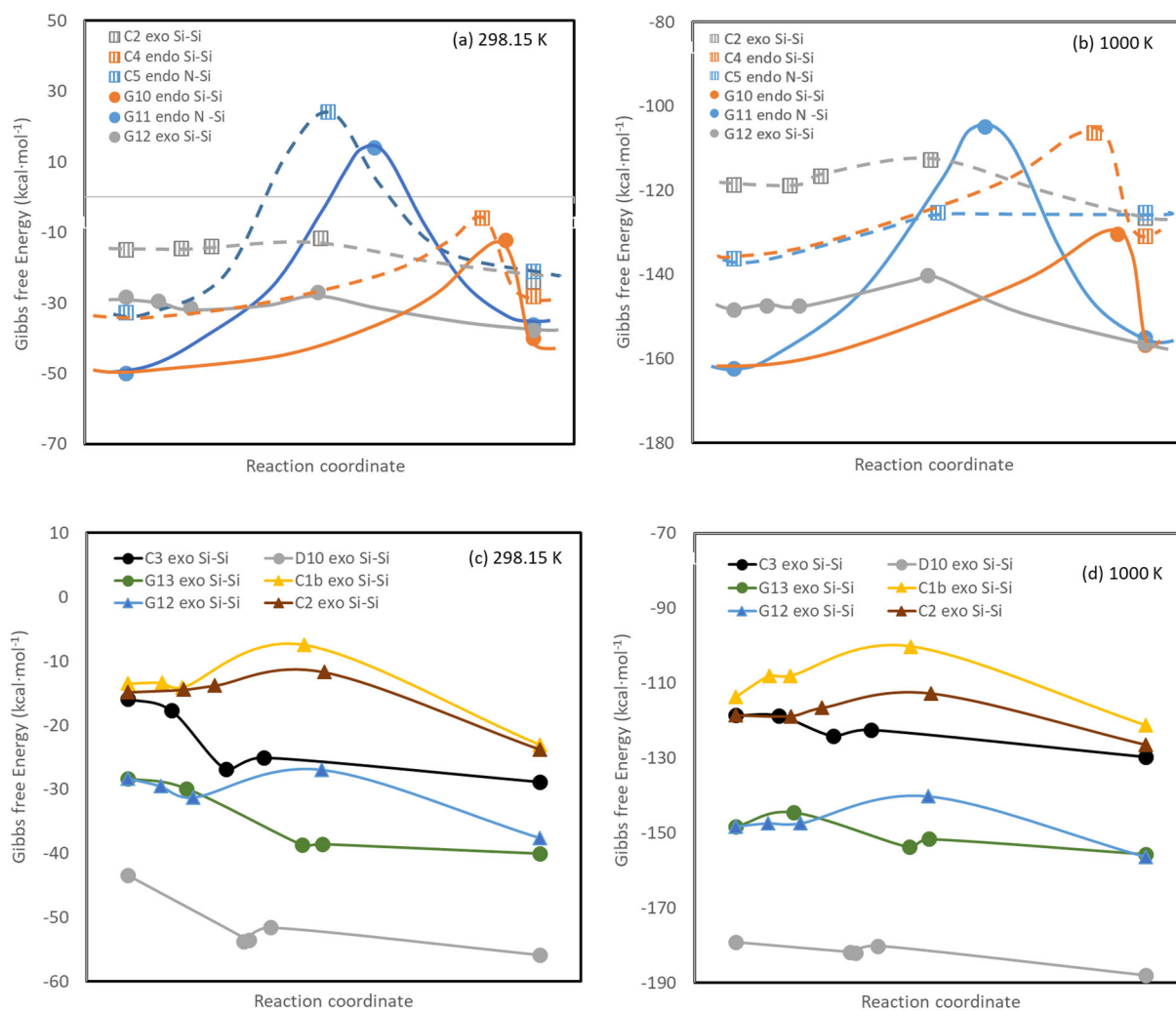
Figure 3.4. The Gibbs free energy surface diagram: Hydrogen shift reactions for acyclic and cyclic species at a) 298.15K and b) 1000 K and selected exothermic hydrogen shift reactions between Si and S at c) 298.15 K and d) 1000 K.

3.3.2 Rate-determining Step for Hydrogen Migration (or shift) Comprised of Hydrogen-bridged an Intermediate

Both endothermic hydrogen shift reactions between N and Si: and Si and Si: possess one barrier, whereas the exothermic hydrogen shift reactions have two different barriers and a stable hydrogen-bridged intermediate, as was observed in silane only pyrolysis conditions without ammonia. Interestingly, for exothermic hydrogen shift between Si and divalent Si, two different trends of mechanism were observed. As shown in the Gibbs free energy surface diagram in **Figure 3.4(b)**, all reactions have two transition states and one intermediate depicted as an energy valley situated between TS1 and TS2. For both exothermic shift cases, the overall value the activation energies are similar. The reactions C1b, C3 and G12 showed similar behavior with the 1,2 hydrogen shift reaction compared to silicon hydrides not containing nitrogen doping, which is that, the activation barrier in the second step is much higher than the first step. However, in the reactions C3, D10, and G13, the first step has much higher activation energy than the second step. The difference in the shape of the Gibbs free energy diagram was caused by the direction of hydrogen transfer, whether the hydrogen moves closer to nitrogen or away further from nitrogen.

It is convenient to consolidate the two-step conversion of unsaturated silyl amine to a product substituted silene and its reverse reaction into one overall transformation. After calculating the rate coefficient for individual steps of exothermic reactions in the **Table 3.1**, the first step to the adduct from the reactant of the reactions C2, D9, G9, and G12 was determined for the barrierless step, and the second step from the adduct to the product substituted silene was the rate-determining step. On the other hand, the first step of the reactions C2, D9, G9, and G12 was rate-determining and the second step was the barrierless step. The overall rate coefficient for the

exothermic H shift reaction between Si to the non-paired Si was calculated as k = $K_1 k_2$, for the reaction where hydrogen is shifting towards nitrogen, where K_1 is the equilibrium constant for the first step, and k_2 is the rate coefficient for the second step. For the reactions where hydrogen is moving away from nitrogen, the overall rate coefficient was calculated as k = $k_1 K_2$, where k_1 is the rate coefficient for the first step, and K_2 is the equilibrium constant for the second step.

3.3.3 Kinetic Parameters of Hydrogen Migration

To understand the H migration (or shifting) behavior under the SiH_4 and NH_3 co-pyrolysis condition, we compared the kinetic parameters of reactions.

Acyclic silicon nitride species

When the divalent reaction center exists as a secondary divalent Si, a hydrogen shift occurs easily from the neighboring secondary Si than from the primary one which clearly indicated activation energy values 4.28 kcal·mol^{-1} for the forward reaction C2 and -0.57 kcal·mol^{-1} for the forward reaction C3. The relative distance between the N atom and the divalent Si can affect to the kinetics due to the strong electronegativity of the N which attracts electron a higher electron density. The H shift toward the secondary divalent Si reaction among acyclic species are all exothermic reactions, forming the double bond or substituted silene (forward reaction) is more probable. When the secondary divalent Si is bound to the N atom, the hydrogen transferring tends not to occur. From the comparison between reaction C3 and C4, the substituted silene product can be formed more easily when the divalent Si reaction center is located further from the N atom.

Similar trends were also observed from the comparison of the rate coefficient of reaction B3 and

B4, C4 and C5, the activation energy for reverse reaction is smaller than the forward reaction.

The barrier of H shift reaction was more affected by the type of H shift reaction than the

structural effect of the substituted silyl group at the reaction center. This was support by the

average activation barriers of 56.61, 27.91 and 4.92 kcal·mol^{-1} for the H shift between N<->Si:,

endothermic H shift between Si <-> Si:, and the exothermic H shift between Si <-> Si:, respectively.

The difference of activation barrier within the same type of H shift reaction was insignificant

compared to the difference between reaction types.

Table 3.2. Single event Arrhenius parameters, zero point energy corrected barriers, and standard enthalpies of reaction for hydrogen shift reaction. (Blue for the endothermic H transfer from N to Si: yellow for the endothermic H transfer from Si to Si:, and white for the exothermic H transfer from Si to Si:).

Reaction	reaction type	Eo kcal·mol^{-1}	log A s^{-1}	A	Ea kcal·mol^{-1}	Eo_r kcal·mol^{-1}	Log A_r s^{-1}	A_r	Ea_r kcal·mol^{-1}	DHRxn kcal·mol^{-1}
A		58.83	13.38	2.40E+13	59.06	47.73	13.26	1.82E+13	47.73	13.53
B2		55.42	13.73	5.37E+13	55.95	50.43	13.04	1.10E+13	50.57	7.2
B4		57.1	13.7	5.01E+13	57.43	47.97	13.43	2.69E+13	48.07	11.63
C5		56.9	13.59	3.89E+13	57.21	47.48	13.32	2.09E+13	47.55	11.95
C6		54.34	13.45	2.82E+13	54.82	50.00	13.15	1.41E+13	50.13	6.42
C8		53.07	14.47	2.95E+14	53.69	50.45	12.83	6.76E+12	50.75	4.83
D7		58.39	12.61	4.07E+12	58.38	48.98	12.11	1.29E+12	48.71	12.12
D12		52.71	14.44	2.75E+14	53.29	50.36	13.98	9.55E+13	50.74	4.39
D13	Endothermic H shift between N and Si:	54.06	13.91	8.13E+13	54.55	50.05	13.07	1.17E+13	50.17	6.08
G5		59.87	13.47	2.95E+13	60.29	47.58	13.58	3.80E+13	47.91	14.22
G8		70.34	13.04	1.10E+13	70.52	41.11	13.16	1.45E+13	41.27	31.14
G11		52.04	13.22	1.66E+13	52.44	47.58	13.44	2.75E+13	47.94	6.2
G15		55.17	13.25	1.78E+13	55.41	47.29	13.44	2.75E+13	47.53	9.54

G16		62.3	13.4	2.51E+13	62.71	46.77	13.47	2.95E+13	47.13	17.25
G20		49.29	13.52	3.31E+13	49.72	49.71	13.77	5.89E+13	50.07	1.34
G25		53.32	13.86	7.24E+13	53.72	51.31	13.69	4.90E+13	51.58	3.95
G27		53.67	13.22	1.66E+13	54.03	51.52	13.47	2.95E+13	51.85	3.88
G28		53.98	13.39	2.45E+13	54.39	48.49	13.48	3.02E+13	48.87	7.07
G29		57.82	12.9	7.94E+12	57.98	49.07	13.41	2.57E+13	49.35	10.1
B3		27.24	13.36	2.29E+13	28.04	20.13	13.36	2.29E+13	20.6	7.94
C4		26.16	13.11	1.29E+13	26.9	22.2	13.32	2.09E+13	22.76	4.31
C7		25.4	13.03	1.07E+13	25.77	19.73	13.06	1.15E+13	20	5.97
D6		26.14	13.12	1.32E+13	26.92	21.89	13.34	2.19E+13	22.45	4.72
D11		37.13	12.78	6.03E+12	37.66	34.26	13.01	1.02E+13	34.79	2.84
G1	Endothermic H shift between Si and Si:	7.15	13.08	1.20E+13	7.67	6.48	13.09	1.23E+13	6.98	0.83
G6		21.96	12.78	6.03E+12	22.23	13.61	12.87	7.41E+12	13.75	8.85
G7		49.56	13.78	6.03E+13	50.23	39.14	13.58	3.80E+13	39.63	11.07
G10		28.25	13.11	1.29E+13	28.88	25.48	13.72	5.25E+13	26.16	2.77
G14		20.51	13.18	1.51E+13	21.18	4.33	13.01	1.02E+13	4.71	17.03
G19		23.06	12.88	7.59E+12	23.55	22.63	13.29	1.95E+13	23.17	0.39
G24		25.9	13.24	1.74E+13	26.47	17.18	13.05	1.12E+13	17.58	9.44
G26		14.75	12.48	3.02E+12	15.23	7.18	12.83	6.76E+12	7.41	8.25
C1b		7.25	12.15	1.41E+12	7.19	15.72	12.5	3.16E+12	15.79	-9.11
C2		4.35	12.4	2.51E+12	4.28	12.8	12.52	3.31E+12	12.73	-8.58
C3	Exothermic H shift between Si and Si:	-0.74	12.45	2.82E+12	-0.57	11.39	12.76	5.75E+12	11.71	-12.54
E1		4.09	12.7	5.01E+12	4.56	2.86	13.1	1.26E+13	3.3	1.14
E3		-0.03	12.29	1.95E+12	0.05	10.03	12.4	2.51E+12	10.15	-10.49
D2		1.6	12.4	2.51E+12	1.78	9.42	12.61	4.07E+12	9.56	-7.74
D3		4.53	12.83	6.76E+12	4.74	15.63	12.9	7.94E+12	15.8	-11.22
D4		4.78	11.91	8.13E+11	4.71	15.04	12.12	1.32E+12	15	-10.51
D5		-0.94	12	1.00E+12	-0.87	10.12	12.73	5.37E+12	10.36	-11.4
D8		1.41	12.39	2.45E+12	1.51	10.88	12.79	6.17E+12	11.17	-10.26
D9		11.17	12.9	7.94E+12	11.27	19.51	12.88	7.59E+12	19.62	-8.53
D10		-0.89	12.22	1.66E+12	-0.79	10.03	12.83	6.76E+12	10.39	-11.57
G4		4.93	12.95	8.91E+12	5.25	16.97	13.12	1.32E+13	17.52	-12.64
G9		4.05	12.77	5.89E+12	4.2	14.61	12.47	2.95E+12	14.92	-11.15
G12		2.42	12.27	1.86E+12	2.47	11.23	12.46	2.88E+12	11.32	-9.04
G13		-0.67	12.51	3.24E+12	-0.46	9.57	13.23	1.70E+13	10.02	-10.68
G18		17.17	12.42	2.63E+12	17.53	25.74	12.6	3.98E+12	26.17	-8.77
G21		0	12.45	2.82E+12	0.11	11.38	12.98	9.55E+12	11.69	-11.82
G22		2.67	12.7	5.01E+12	2.9	13.74	12.83	6.76E+12	14.01	-11.33
G23		6.68	12.94	8.71E+12	6.95	14.33	12.75	5.62E+12	14.51	-7.52

Cyclic silicon nitride species

The H shift reactions in four different sizes of endocyclic substituted silylene with nitrogen doping species were investigated. For three-member ring species, none of substituted silylenes containing nitrogen were able to be optimized due to steric hindrance. The triangular cyclic geometry does not offer enough space for the N atom to bond with other silicon because N prefers to have a tetrahedral geometric electron configuration with the lone electron pair primarily on the N atom. The H shift in 1N endocyclic species tends to occur easily in the larger ring. As we observed in acyclic species, an H bound to Si is more likely to transfer than one bound to N in the cyclic species as well, shown in the activation energy for reaction G10 and G11, 28.88 kcal·mol^{-1} and 52.11 kcal·mol^{-1}, respectively. Since the cyclic species maintain the narrower distance between atoms than acyclics, the relative distance between the reactive center and N atom would not be a significant factor.

The number of N atoms in the cyclic species also affects the underlying reaction kinetics. The H shifting within a molecule with two nearby N atom requires almost ten times the activation energy (E_a 21.18 kcal·mol^{-1} for reaction G14) than a situation where there is only one N atom (E_a 2.47 kcal·mol^{-1} for reaction G12). Interestingly, the reactant G14 does not convert to a double bonded cyclic species and prefers to remain as an species with a diradical center. Similar trends were also observed from the comparison G18, G19 and G24. The larger the number of N atoms in the endocyclic geometry, the more the reverse hydrogen shift reaction is preferred. This indicates that the larger size nanoparticle can be synthesized in the low concentrate H_2 gas of silane and ammonia co-pyrolysis, leaving the unpaired divalent Si radical center to react with other silyl radicals in the pyrolysis system.

3.3.4 NBO (Natural Bond Orbital) Analysis

The extent of bond formation or bond decomposition along a reaction pathway was analyzed by the concept of bond order. This analysis has been used to investigate the molecular mechanism of chemical reactions mainly for gas phase hydrocarbons with different functional groups, however, our group has had success for similar silicon nitride species.[46] To examine the nature of the hydrogen migration (or shift) process, the Wiberg bond indexes have been calculated by using NBO 7.0 analysis as implemented in Gaussian16. Bonds indexes were tabulated for those bonds changed in the reaction pathway (Si-H, N-H, Si-Si, and Si-N), and bond indexes of the selected hydrogen shift reactions were listed in the **Table 3.3**. Corresponding labeled structures were depicted in the **Figure 3.3**. The reaction C2 proceeds the H9 shift from Si8 to Si7 through two transition states and one stable hydrogen bridged intermediate state to produce substituted silene species located at 8.58 kcal·mol^{-1} below the reactant at the G3//B3LYP level of theory. After H9 has shifted, the bond order of Si7-Si8 is 1.901 in the product species which represents a double Si bond (Si=Si).

In the reaction C4, the reaction mechanism involves the simultaneous breaking of the Si5-H7 and forming Si4-H7 bonds though one transition state to produce a substituted imine located at 4.31 kcal·mol^{-1} above the reactant. While the H7 is transferring, the Si4-Si5 bond index is also increasing to 1.491, which has the characteristics of both a single and double bond. Also, the slight decrease in N1-Si4 bond though the reaction indicates that electrons are well-delocalized over the N1-Si4 and Si4-Si5 bonds, which is the conjugation effect between lone pair orbital of nitrogen and the Π orbital of Si4-S5i bond. In addition to H shift from N to divalent Si, H shift from Si, bound with nitrogen, to a divalent Si is also endothermic reaction, and has a single step of reaction unlike other H shifting from Si to divalent Si due to this similar conjugation effect.

In cyclic species, generally lower bond indices were obtained than for acyclic species because of the well-distributed electrons over the ring bonds, whereas the conjugation effect on acyclic species is more located to the N atom and near Si-Si Π bond. Due to the more favorable electron movement by the conjugation effect, H shift occurs more often in cyclic species than acyclic species, this also was supported by the fact that activation barriers are also generally lower in cyclic species.

Table 3.3. Bond order analysis for the hydrogen shift reaction at the B3LYP/6-31G(d) level using NBO analysis. (Wiberg Bond Index)

C2	N1-H3	N1-Si4	Si4-H5	Si4-H6	Si4-Si:7	Si7-H5	Si:7-Si8	Si7-H9	Si8-H9	Si8-H10	Si8-H11	
Bi (R)	0.818	0.75	0.885	0.921	0.985	0.032	1.024	0.034	0.947	0.935	0.935	
Bi(TS1)	0.818	0.757	0.883	0.921	0.968	0.023	1.143	0.242	0.733	0.934	0.912	-
Bi(I)	0.817	0.753	0.883	0.928	0.934	0.02	1.209	0.347	0.589	0.924	0.899	
Bi(TS)	0.817	0.751	0.883	0.921	0.921	0.017	1.416	0.667	0.288	0.919	0.89	
Bi (P)	0.818	0.766	0.885	0.918	0.965	0.016	1.901	0.951	0.009	0.951	0.951	

C3	N1-H3	N1-Si4	Si4-H5	Si4-H6	Si4-Si:7	Si7-H5	Si:7-Si8	Si7-H9	Si8-H9	Si8-H10	Si8-H11
Bi (R)	0.819	0.764	0.872	0.911	0.987	0.036	0.988	0.014	0.94	0.947	0.936
Bi(TS1)	0.816	0.776	0.806	0.908	1.04	0.109	0.983	0.013	0.939	0.946	0.937
Bi(I)	0.805	0.835	0.466	0.895	1.107	0.445	0.969	0.025	0.94	0.934	0.945
Bi(TS)	0.802	0.917	0.167	0.875	1.153	0.768	0.969	0.027	0.932	0.945	0.945
Bi (P)	0.805	0.868	0.018	0.919	1.491	0.938	0.986	0.012	0.94	0.95	0.934

C4	N1-H2	N1-H3	N1-Si4	H3-Si4	Si4-Si5	Si5-H6	Si5-H7	Si4-H7	Si5-Si8	Si8-H9	Si8-H10	Si8-H11
Bi (R)	0.802	0.809	0.962	0.004	0.928	0.94	0.95	0.008	0.983	0.952	0.952	0.953
Bi(TS)	0.815	0.817	0.788	0.002	1.42	0.895	0.305	0.64	0.992	0.946	0.944	0.957
Bi (P)	0.806	0.805	0.868	0.004	1.491	0.938	0.015	0.919	0.986	0.94	0.934	0.95

C5	N1-H2	N1-H3	N1-Si4	H3-Si4	Si4-Si5	Si5-H6	Si5-H7	Si4-H7	Si5-Si8	Si8-H9	Si8-H10	Si8-H11
Bi (R)	0.802	0.809	0.962	0.004	0.928	0.94	0.95	0.008	0.983	0.952	0.952	0.953
Bi(TS)	0.82	0.338	1.309	0.615	0.867	0.95	0.95	0.006	0.976	0.954	0.952	0.954
Bi (P)	0.834	0.018	1.662	0.9	0.908	0.955	0.948	0.007	0.971	0.953	0.955	0.955

G6	Si1-Si2	Si1-H5	Si1-N8	Si2-Si3	Si2-H4	Si2-H5	Si3-H6	Si3-H7	Si3-N8	N8-H9
Bi (R)	0.905	0.007	0.9	0.971	0.952	0.952	0.912	0.912	0.659	0.78
Bi(TS)	0.286	0.456	0.922	0.971	0.922	0.416	0.904	0.921	0.609	0.783
Bi (P)	1.304	0.889	0.906	0.92	0.922	0.035	0.911	0.908	0.627	0.77

G12	Si1-Si2	Si1-Si4	Si1-H5	Si1-H9	Si2-Si3	Si2-H5	Si2-H6	Si3-N11	Si4-H9	Si4-H10	Si4-N11
Bi (R)	0.98	0.981	0.012	0.028	0.942	0.942	0.947	0.705	0.893	0.913	0.696
Bi(TS1)	0.968	0.992	0.018	0.031	0.94	0.949	0.952	0.705	0.891	0.917	0.696
Bi(I)	1.124	0.965	0.296	0.017	0.916	0.669	0.927	0.727	0.898	0.91	0.676
Bi(TS)	1.408	0.898	0.708	0.01	0.915	0.239	0.915	0.728	0.915	0.895	0.673
Bi (P)	1.89	0.967	0.951	0.008	0.967	0.008	0.951	0.704	0.902	0.895	0.704

G13	Si1-Si2	Si1-Si4	Si1-H5	Si1-H9	Si2-Si3	Si2-H5	Si2-H6	Si3-N11	Si4-H9	Si4-H10	Si4-N11
Bi (R)	0.98	0.981	0.012	0.028	0.942	0.942	0.947	0.705	0.893	0.913	0.696
Bi(TS)	0.937	1.191	0.008	0.715	0.945	0.946	0.946	0.634	0.215	0.897	0.849
Bi (P)	0.975	1.426	0.012	0.927	0.956	0.934	0.939	0.646	0.027	0.908	0.841
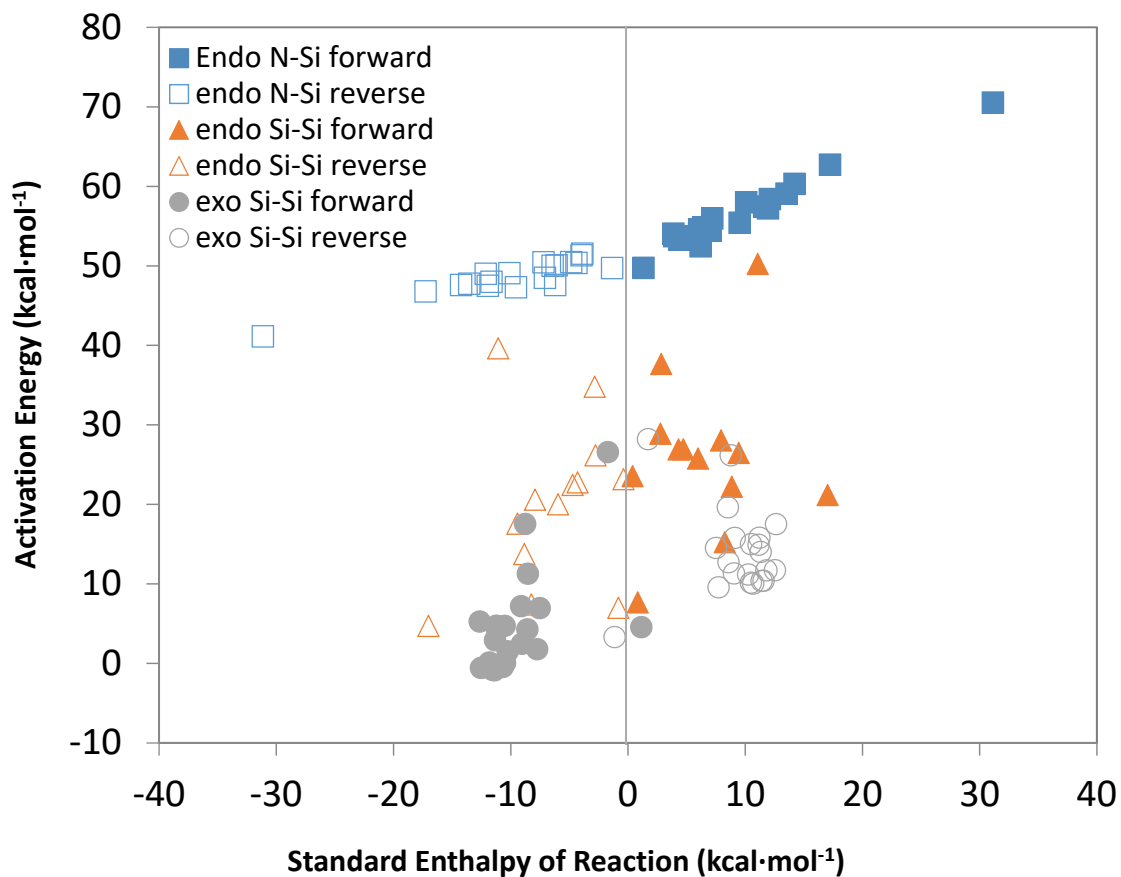
Figure 3.5. Activation Energy distribution according to three different types of hydrogen shift reactions: Blue square represents hydrogen shift between N and Si:, Orange triangle represents endothermic hydrogen shift between Si and Si:, and Gray circle represents exothermic hydrogen shift reaction between Si and Si:. The solid symbol means forward reaction, and the hollow symbol means reverse reaction.

3.3.5 Kinetic Parameter Model Generalization

Regression Analysis for H-shift Reactions

To develop a model for predicting activation energy, the activation energies of all reactions were plotted against the corresponding enthalpy of the reactions (**Figure 3.5**). The range of activation energies is clearly different with the type of hydrogen shift reaction. Only the energy barrier of the endothermic H shift reaction between N and Si:, which has the highest value, showed a strong linear correlation with the enthalpy of the reaction. In **Figure 3.6**, the regression model of the hydrogen shift between N and divalent Si were described. The statistical analysis for the Evans-Polanyi parameters are listed in the **Table 3.4**. All hydrogen shift reactions from N to divalent Si were captured well by one regression equation or fit. The Evans-Polanyi parameters, E_o, and α, were calculated from linear regression with the least-squares method to maintain enthalpic (or thermodynamic) consistency. The generalized model for H shift reaction between N and Si: predicted the activation energy with a 91% R-squared value.
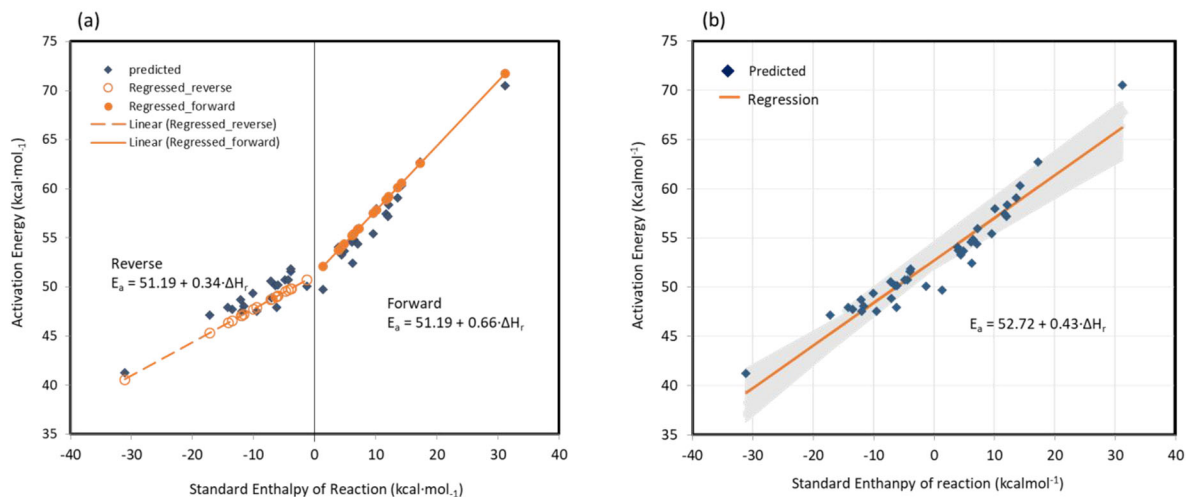
Figure 3.6. Plot of activation energy versus overall standard enthalpy of reaction (at 298.15K) for hydrogen migration (or shift) reactions between N and Si:. The blue diamonds are the predicted activation energy values from DFT calculations, the orange line is the best straight line fit to the overall activation energy with the parameters obtained from **Table 3.4**. (a) Regression model when the sum of two coefficients (slope values) is fixed to be one and the intrinsic barrier, E_0, for forward and reverse reactions was constrained to be equal. (b) Regression model with no constraints and the gray band represents the range of slope coefficients after bootstrapping (or sensitivity) analysis under 90% confidence intervals.

Table 3.4. Statistical analysis for regression parameters of hydrogen shift reactions in this study

		E_0	α	β	γ	δ
H shift reaction between N and Si		52.72	0.43			
	Regression Statistics	R^2	Adjusted R^2	p-value	Observations	
		0.92	0.91	1.23E-17	38	
H shift between Si and Si (endothermic)	parameters	E_0	α	β	γ	δ
		54.73	0.48	-9.8	-19.7	0
	Regression Statistics	R^2	Adjusted R^2	p-value	Observations	
		0.77	0.73	1.39E-06	24	
H shift between Si and Si (exothermic)	parameters	E_0	α	β	γ	δ
		2.99	0.49	0	0	2.04
	Regression Statistics	R^2	Adjusted R^2	p-value	Observations	
		0.76	0.73	1.12E-08	34	

The predictive models for hydrogen shift between Si and divalent Si when nitrogen was present in the molecule (alloying or doping effects) required more descriptors in the regression model for statistical significance. Our study has introduced additional descriptors which incorporate the impact of the nitrogen in the species for hydrogen migration (or shift) favorability; N is the number of the nitrogen atoms in the silicon nitride species, d is the direction of hydrogen transferring (where hydrogen is transferring towards N, $d = 1$, where hydrogen is transferring away from N, d = -1, or where there is no N atom in the species, $d = 0$), D_{rel} is a relative distance from N to the divalent Si. For endothermic hydrogen shift reaction, since the reaction center of all reactions is located right next to the nitrogen atom, the relative distance from N to reaction center is 1 for all reaction, so the D_{rel} was neglected. The exothermic hydrogen shift between Si and divalent Si occurs in the species where the reaction center is farther away from the N element. Here, the parameter for the number of the nitrogen, and the direction of hydrogen transfer can be removed.

The parameters were obtained using multiple linear regression analysis for all reactions (**Table 3.5**). The overall models were deemed significant if the F-test satisfied the 95% confidence level.

Table 3.5. The generalized model for predicting activation energy for hydrogen shift reaction in silicon nitrides and average single event pre-exponential coefficient.

Reaction type	Generalized model	log Â (s^{-1})
H shift reaction between N and Si	$E_a = 52.72 + 0.43*\Delta H_{Rxn}$	13.50
ft between Si and Si (endothermic)	$E_a = 54.73 + 0.48*\Delta H_{Rxn} -9.8N -19.7d$	13.04
t between Si and Si (exothermic)	$E_a = 2.99 + 0.49*\Delta H_{Rxn} + 2.04 D_{rel}$	12.54

k-Fold cross-validation

Due to the large number of atomic configurations and the complexity of the Si-N hydride species, it was not simple to assign the validation sets separately. k-Fold cross-validation is a common procedure to evaluate models on a limited but still complex dataset. The results of a k-fold cross-validation run are often summarized with the mean of the model but we also summarized with minimum, maximum and standard deviation as well in **Table 3.6**. The model with the mean coefficients for each reaction type showed coefficients very close to those coefficients of our regression model except for the endothermic H shift between Si and Si: atoms. This is because the dataset of endothermic H shift between Si and Si: were widely spread out in values compared to H shift between N and Si: and exothermic shift between Si and Si: atoms, as depicted in **Figure 3.5**.

Bootstrapping regression models

The bootstrapping method can be another alternative to analysis the sensitivity and robustness of our generalized models. Bootstrapping is a resampling method to create many simulated samples by replacement. Bootstrapping is a powerful approach for checking the stability of regression coefficients and is an important tool for machine learning purposes. Bootstrapping regression models give insight into the variability of model parameters. Using our regression models for each H shift type in this study, we resampled each reaction type a minimum of 500 times and then calculated the mean at the 90% confidence interval. In **Figure 3.6**, the range of 90th percentile coefficients for the regression model of H shift between N and Si: is depicted as a gray band. The calculated statistics resulting from bootstrapping were tabulated in **Table 3.7**. The mean from the bootstrapping draws a line that is very close to the regression models except for the endothermic H shift between Si and divalent Si. As aforementioned, the activation energy values for endothermic H shift between Si and Si: atoms were widely spread, it was burdensome to find the correlation between characteristic factors. k-Fold cross-validation and bootstrapping results indicate that none of the coefficients match well except for the α value.

Table 3.6. k-Fold cross-validation analysis result.

Reaction type	k value		E_0	α	β	γ	δ	residual
H shift reaction between N and Si	19-fold	min	52.58	0.40	-	-	-	-3.67
		average	52.72	0.43	-	-	-	0.07
		max	52.83	0.45	-	-	-	5.50
		SD	0.06	0.01	-	-	-	1.66
H shift between Si and Si (endothermic)	12-fold	min	-23.95	0.15	-4.71	-6.58	-	-23.95
		average	22.57	0.47	-1.10	0.05	-	-1.58
		max	30.92	0.84	0.67	4.41	-	17.68
		SD	2.92	0.16	1.56	2.96		9.25
H shift between Si and Si (exothermic)	17-fold	min	1.89	0.46	-	-	1.74	-4.24
		average	2.98	0.49	-	-	2.05	-0.02
		max	3.67	0.51	-	-	2.64	9.01
		SD	0.49	0.01	-	-	0.22	2.16

Table 3.7. The statistics result from bootstrapping regression models

	E_0		α	β	γ	δ
H shift reaction between N and Si	5% percentile	52.29	0.38	-	-	-
	mean 95%	52.69	0.43	-	-	-
	percentile	53.08	0.48	-	-	-
t between Si and Si (endothermic)	5% percentile	-12.03	-0.42	-11.72	-11.85	-
	mean 95%	0.13	0.43	-2.27	0.76	-
	percentile	14.57	1.28	5.97	13.12	-
between Si and Si (exothermic)	5% percentile	-2.65	0.40	-	-	0.71
	mean 95%	0.06	0.49	-	-	2.04
	percentile	3.58	0.56	-	-	3.19
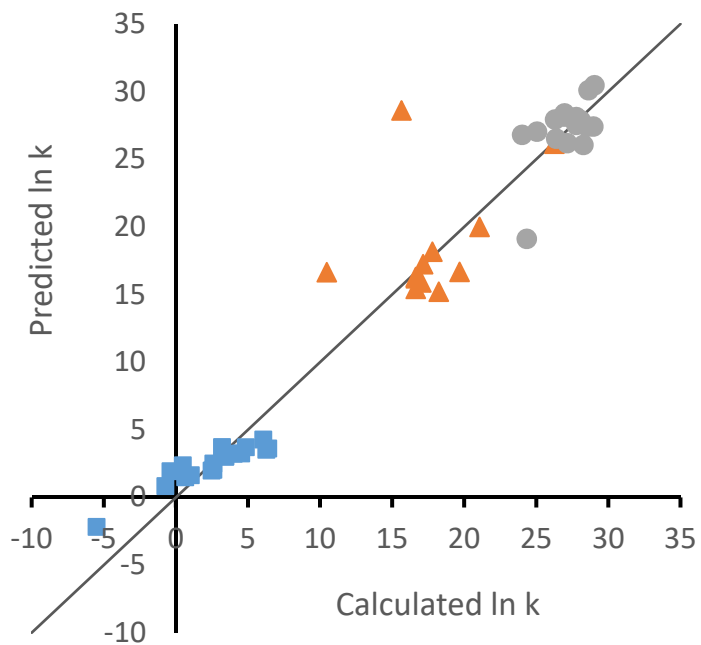
Figure 3.7. Parity plots of the rate coefficients of hydrogen migration (or shift) reaction in silicon nitrides at 1000K and 1 atm (Blue square: H shift between N and Si:, orange triangle: endothermic H shift between Si and Si: and gray circle: exothermic H shift between Si and Si:)

Parity plots depicting how well the suggested model captures the predicted rate coefficient from our CalcK script at 1000K for hydrogen shift reaction are shown in **Figure 3.7**. More than 98% of ln k values from the regression model were well-matched with the values predicted by the CalcK script.

To the best of our knowledge, there has not been a model predicting activation energy for hydrogen shift reactions in SiN hydride species. Our study classified three different H-shift reactions from the results calculated using quantum chemical calculations and statistical thermodynamics, and presented models for predicting activation energy for each reaction. The robustness of the H-shift between N and Si: and exothermic H-shift between Si and Si: models were validated with the bootstrapping method for sensitivity analysis. We found that the regression models comprised of a coefficient in the range listed in **Table 3.6** have good predictability at a 90% confidence interval. The models presented in this study can be used as tools to calculate activation energy using reaction enthalpy and other factors for experimentalists. The models also can be employed to calculate kinetics in reaction mechanism generator programs such as RMG, AMOX, NetGen, REACTION, and EXGAS. These models are essential because, under the pyrolysis conditions, there are numerous species like neutral and radical species including reactive intermediates. It is challenging to consider all reactions in which those species are involved. However, applying these models to the Arrhenius equation makes it more convenient to calculate the kinetics and perform an integrated analysis of a reaction system. In addition, incorporating these models with the machine learning approach is expected to improve its accuracy in predicting reaction mechanisms and generating chemical mechanisms.

3.4 Conclusions

Rate coefficients and Arrhenius parameters for the hydrogen migration (or shift) reaction in silicon nitride species have been calculated for 52 reactions using G3//B3LYP, statistical thermodynamics, and conventional transition state theory. The overall reaction of substituted cyclic and acyclic silylenes to their respective silene and imine species by 1,2-hydrogen shift reaction was analyzed by three different types of H shift reaction using overall reaction thermodynamics: (1) endothermic H shift between N and Si:, (2) endothermic H shift between Si and Si: and (3) exothermic H shift between Si and Si:. For two-step pathways, the rate-determining step was determined to be from the intermediate to the substituted silene, and then kinetic parameters for the overall reaction were calculated. The single event pre-exponential factors, $\tilde{A}$, and activation energies, E_a, for the three different classes of hydrogen shift reactions of silicon nitrides were computed. The hydrogen shift reaction was explored for acyclic and cyclic monofunctional silicon nitrides, and the type of hydrogen shift reaction gives the most significant influence on the kinetic parameters.

The reactant geometry should be considered first to understand which H shift reaction is most competitive among three different types of hydrogen migration. For the reactant, where D_{rel} is 1, it was discovered that the endothermic hydrogen shift between Si-Si was the most competitive pathway between the two types of endothermic hydrogen migration. However, SiN is thermodynamically more favorable to maintain divalent Si: than to form a double bond through hydrogen migration. This indicates that nanoparticles can be grown from the residual divalent Si by reacting with other radical species under silane and ammonia co-pyrolysis. On the other hand, for the reactant with D_{rel} of 2 or higher, exothermic hydrogen transfer between Si and Si: occurs favorably. Since the species with double bonds are more stable thermodynamically, this result indicates that nanoparticle growth will be more difficult under these conditions.

From the detailed micro reaction mechanism investigated in this study and the generalized models for predicting the activation barrier, it is expected that the investigated hydrogen migration or isomerization reaction behavior for the kinetics of polycyclic silicon nitrides or the larger silicon nitrides species can be predicted with reasonable accuracy.

Chapter 4

Stabilizing Silicon Nitride Nanoparticles in Hydrogen Atmosphere II

4.1 Introduction

In order to produce silicon-based nanoparticles[1, 3, 4], there have been various methods such as pyrolysis[7], chemical vapor deposition[8-12], atomic layer deposition[13] and sputtering. Among those methods, a basal protocol to create silicon-alloyed nanoparticles and understand the synthetic mechanism is pyrolysis. Recently, the has been a growing interest in pyrolysis, because the mechanical, optical, and electronic characteristics of silicon nitrides can be tightly controlled and systematically customized as a function of nitrogen concentrations. Synthesizing nanomaterial thorough pyrolysis is of specific interest regarding simplicity, flexibility, and scalability. Because any mixtures of precursor gases can be built into multi-functional nanoparticles that can be directly used for specific applications instead of focusing on modification of nanostructures after they have been formed. For example, in Si-based nanomaterials, especially for the anode of Li-batteries, a variety of morphology designs based on nanoengineering have been suggested such as nanowires[157-159], nanotubes[160], core-shell structures[157, 161], hollow structures[162], and porous structures[163, 164]. However, these include complex synthesis routes that are not easily scalable or inexpensive. On the other hand, the pyrolysis method provides simplicity and facility, a fundamental understanding pyrolysis precisely is essential. Chae at el. demonstrated synthesizing Si-rich silicon nitride nanoparticles via pyrolysis, where Si and N are homogeneously distributed, the SiN nanoparticles successfully alter the intrinsic electrochemical property of the Si anode by improving mechanical stability and ionic conductivity with Si_3N_4[132].

Understanding the mechanism for the pyrolytic formation of SiN nanoparticles will enable improvements in chemical vapor deposition (CVD)[165, 166] techniques which floating nanoparticles are an unfavorable product. H_2 addition is the key reaction class during pyrolysis which directly affects the sticking coefficient of silicon nitrides by passivating the molecular surface with terminal hydrogen atoms. Hence a deeper understanding of H_2 addition and elimination under the pyrolysis conditions is needed to elucidate the details of silicon nitride nanoparticle formation. During the co-pyrolysis of silane and ammonia, H_2 addition and elimination reaction paths can prevent or promote surface reactions of silicon nitrides. H_2 addition and elimination are essential mechanisms for growing SiN nanoparticles and controlling the size of nanoparticles in the gas phase. Small SiN nanoparticles are a desired building block for nanomaterial design in novel electronic and optical (or photoelectronic) applications where size, crystallinity, and surface functionalization play important roles[128, 165, 167].

H_2 addition in silicon nitrides is a reaction in which silicon nitrides containing divalent centers can stabilize a lone electron pair of a silicon atom; however, under pyrolysis conditions, H_2 elimination is a reaction path to generate reactive amino silylenes. Since H_2 elimination from silane or disilane is the first step in synthesizing polycrystalline silicon or amorphous silicon Nanoparticles under silane pyrolysis[168-172], the 1,1-elimination reaction is the most favorable unimolecular decomposition pathway for silicon hydrides[57], we can approximate that H_2 can be eliminated from a silicon nitride by 1,1-elimination mostly. Thus we benchmarked only 1,1-H_2 elimination in silicon nitrides in the present study. H_2 addition and elimination reaction pathways have been studied and confirmed theoretically and experimentally for reactions comprised of substituted silylenes with up to two silicon atoms[7, 172-176], and it also has been extended to ten silicon atoms[57], H_2 addition and elimination reaction pathways have not been studied in SiN yet[136, 177, 178]. Furthermore, the amount of hydrogen incorporation affects the physical, optical, and dielectric properties of silicon nitrides and the nature of the Si-H versus N-H bonding also will play a significant role in tailoring the resulting characteristic of silicon nitrides[3, 167, 179-182], understanding of H_2 additions and elimination reactions in silane-ammonia co-pyrolysis is indispensable.

In the present work, the purpose is "to investigate the kinetic and thermodynamic parameters, pre-

exponential factors, and barrier heights of these reactions, and to make consideration of the nature of the molecular mechanism of the H_2 addition and elimination of silyl amides using density functional theory (DFT)[183] methods and the natural bond orbital analysis (NBO)[184, 185] technique.

4.2 Computational Methodology

Quantum Chemical Calculations, Transition State Theory, and Statistical Thermodynamics.

Hydrogen addition and elimination is another hypothesized elementary reactions for the silicon-nitride pyrolysis system following our previous hydrogen migration reaction. This reaction family was also benchmarked against current databases for the silane pyrolysis system. Under the silane and ammonia co-pyrolysis condition, a hydrogen molecule will be added to a divalent silicon in amino silylenes in the way that each hydrogen atom bonded with the divalent silicon atom. Hydrogen addition reaction for silicon nitride hydrides stabilizes unstable substituted amino silylenes with a divalent center by forming two sigma bonds. Conversely, the reverse reaction, which is the hydrogen elimination reaction, is forming a reactive amino silylene with a divalent Si species by removing the hydrogen molecule. Species with divalent Si can contribute to nanoparticle growth by direct nucleation reaction with other silicon or silicon nitride nanoparticle in the pyrolysis system. Unfortunately, the hydrogen molecular addition and elimination reaction under silane and ammonia co-pyrolysis condition has not been studied.

Quantum chemical calculations were conducted with Gaussian 16[90] for all the reactions depicted in Figure 1. All electronic energies for acyclic and cyclic aminosilylenes, aminosilanes, transition states and H_2 were calculated using the G3//B3LYP method[71, 140], which uses B3LYP geometries and higher-level corrections based on single point energies. Choice of the G3//B3LYP level of theory was already proven by an excellent prediction for thermodynamic properties of hydrogenated

140

silicon nitrides and rate constant for hydrogen migration reactions in our previous works.

Geometries and harmonic frequencies of the lowest energy conformers were determined at the B3LYP/6-31G(d) level. The lowest energy conformers were found through the potential energy surface (PES) scan by changing the dihedral angle corresponding to the rotating bond, i.e Si-N, Si-Si, Si-H, and N-H bonds. All silicon nitrides species and hydrogen molecule of this study were optimized in the singlet state. The calculated triplet-singlet splitting values for reference reaction (reaction 1) suggest that the singlet potential energy surface for hydrogen addition and elimination is significantly lower in energy than the mixed triplet-singlet potential energy surface. The harmonic frequencies and zero-point energy (ZPE) were scaled by factors of 0.96 and 0.98, respectively, to account for anharmonicity in the normal vibrational modes as suggested by Scott and Radom[98]. Using conventional statistical thermodynamics, partition functions based on the harmonic oscillator, one-dimensional hindered rotor, and rigid rotor approximations were used to calculate thermodynamic and kinetic properties as a function of temperature. As we conducted in our previous reports, the harmonic oscillator model is a reasonable choice with the given rotation barrier height for the Si:−N bond in the reactant 3A (24.16 kcal·mol−1)[186]. Generally, a free rotor model is recommended for silicon nitride species, because the barriers of Si−N, Si-Si:, and Si-Si bond rotation are small, such as 4.95 kcal·mol−1, 6.23 kcal·mol−1, and 0.54 kcal·mol−1, respectively. However, these bonds are not reaction centers for H_2 addition and elimination reaction and exist in all steps through the reaction, thus, can be canceled out. Therefore, we employed the harmonic oscillator model for the hydrogen addition and elimination reaction and considered vibrational anharmonicity by employing scaling factors aforementioned.

In order to find the transition states, the potential energy surface interpolation method, the Synchronous Transit-guided Quasi-Newton method (QST3), was used. Each transition state was confirmed that it has one imaginary frequency and follows the intrinsic reaction coordinate to the desired reactants and product. Rate coefficients were calculated by conventional transition state theory

(ref) according to the **equation** (**4. 1**) at 1 atm assuming an ideal gas state,

$$k^{TST}(T) = n_d\tilde{k} = n_d\Lambda\exp\left(\frac{\Delta S^{\neq}}{R}\right)exp\left(\frac{-\Delta H^{\neq}}{RT}\right) \quad eq(4.1)$$

Where Λ, defined in**equation** (**4. 2**),

$$\Lambda = \kappa(T)\frac{k_B T(V_m^0)^{-\Delta n}}{h} \quad eq(4.2)$$

$\tilde{k}$ is the single event rate coefficient: $\kappa(T)$ is the Wigner tunneling correction(ref) at temperature T; k_B is Boltzmann's constant; h is Planck's constant; $\Delta H^{\neq}$is the enthalpy of activation; Δn is the change in the number of moles going from the reactant to the transition state (i.e., zero in both directions for isomerization); and n_d is the reaction path degeneracy, or number of single events. $\Delta H^{\neq}$ and $\Delta S^{\neq}$ are calculated using standard formulae[102].

The single event parameters of the Arrhenius relationship, $\tilde{A}$ and E_a, were obtained by fitting ln k versus T^{-1} over the temperature range 298-1500 K. This procedure was performed automatically using the CalcK script previously employed by our group for silicon nanoparticle formation kinetics[55-57, 141, 142, 150, 186, 187]. The rate coefficient is important for constructing a mechanistic model. One of method for predicting E_a is the Evans-Polanyi correlation(ref) in **equation** (**4. 3**),

$$E_a = E_0 + \alpha\Delta H_{Rxn} \quad eq(4.3)$$

where E_0 and α are parameters that are determined from linear regression against predicted values and are constant for a hydrogen shift between Si and N in silicon nitrides. E_0 is the intrinsic barrier of the reaction and ΔH_{Rxn} is the standard enthalpy of reaction. ΔH_{Rxn} is calculated using the the CalcK script. To obtain a generalized model from linear regressions, for the hydrogen shift between Si and N, the intrinsic barrier, E_0, for the both forward and reverse reactions were constrained to be equal to maintain enthalpic consistency. For hydrogen addition and elimination reaction of silicon nitrides due nitrogen

atom doping effects, multiple linear regressions were conducted according to **equation (4.4)**,

$$E_a = E_0 + \alpha \Delta H_{Rxn} + \beta N + \delta D_{rel} \qquad \boldsymbol{eq(4.4)}$$

where $E_0, \alpha, \beta, and\ \delta$ are parameters that were determined from multiple linear regression against theoretical values and are constant for hydrogen shift between Si and Si in silicon nitride species. E_0 is the intrinsic barrier of the reaction. ΔH_{Rxn} is the standard enthalpy of reaction. N is defined as the number of the nitrogen atoms in the silicon nitride species. D_{rel} is defined as the relative distance between the N atom to the nearest divalent Si center. For example, the D_{rel} of reaction 2 and 4 are two and three, respectively.

NBO7.0 program[184] under the Gaussian16[90] software package was used to perform natural population analysis by the natural bond orbital method at B3LYP method with 6-31G(d) basis set. By comparing the Wiberg Bond index of the corresponding bonds within the reaction, the progress of electron transfer from a reactant to the corresponding product through transition states was captured. An attempt was made to interpret the H_2 addition and removal reaction by expressing the NBO orbital as a reactivity diagram[188], and to compare it with the same reaction mechanism of silicon hydride. The stability of the selected reacting species was also explained by the resonance structure of the NBO results[189, 190].

K-fold cross-validation was conducted for a regression model for predicting the activation barrier of hydrogen addition and elimination reaction of silicon nitrides. The k value for the hydrogen addition and elimination reaction is seven. First, all the dataset was shuffled randomly and was split into 7 groups. A group out of 7 groups was considered a validation set and the remaining 6 groups as a training set. The regression was conducted 7 times, and the 7 regression models were statistically analyzed.

4.3 Results and Discussion

A total of 21 hydrogen addition and elimination reactions of substituted silylene species comprising nitrogen were mapped using G3//B3LYP, as depicted in **Figure 4.1**.[191] Mapping of the hydrogen addition and elimination potential energy surface for selected reactions (reaction 1, 5, 16, 17 and 21) showed all 21 hydrogen addition and elimination reactions showed different reaction paths depends on the geometry of reacting molecular structures. We categorized hydrogen addition and elimination reaction in three groups; (A) Aminosilylene of relative distance between divalent Si and N (D_{rel}) is 2 or longer (purple group), (B) Amionsilylene has two nitrogen bonded to divalent Si (N-Si:-N) (gray group), and (C) Amionsilylene has two nitrogen and D_{rel} is 1 (white group). Hydrogen addition reaction is always an exothermic process. Group (A) which has no adjacent nitrogen atom to the divalent silicon presented two distinct barriers linked by a stable intermediate. Group (B) and (C) showed a single barrier between reactants and product. As we observed in our previous hydrogen migration reaction, the smaller size of molecular orbital of nitrogen provides more spacious room for any reaction. Thus, it is less challenging for hydrogen molecule to access to the reaction center of Group (B) and (C). In order to compare the different reaction mechanisms in a systematic manner for hydrogenation addition and elimination process, intrinsic reaction coordinate (IRC) calculations were conducted. The existence of an intermediate in reactions of Group (A) was observed, whereas Group B and C were a path reaction without any intermediate stage.
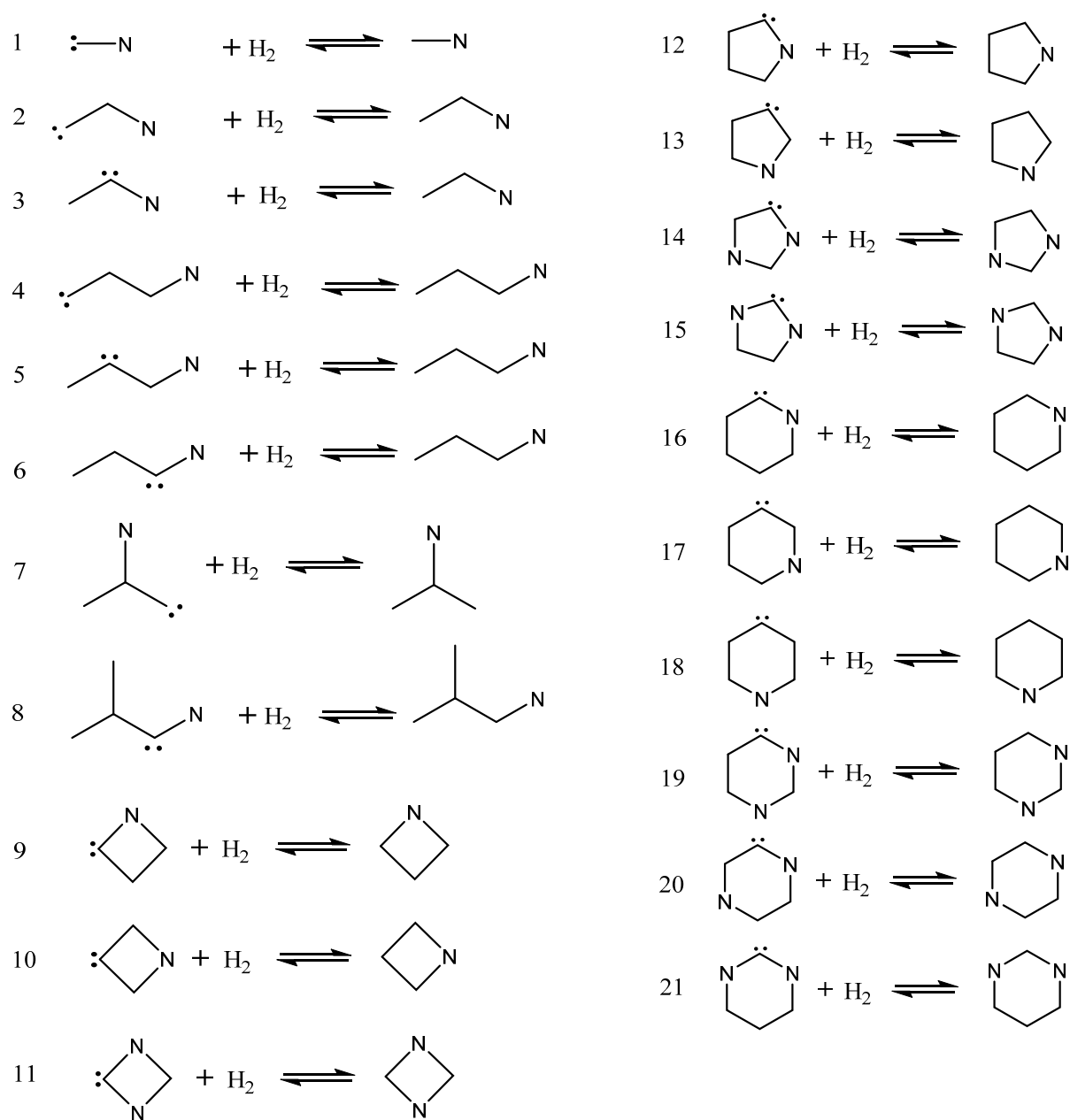
Figure 4.1. Hydrogen molecule addition and elimination reactions of acyclic and cyclic silicon nitrides. Unlabeled atoms in each molecules are Si atom, not C atom.

Figure 4.2 shows the transition state geometries and intermediates for several key hydrogen addition and elimination reactions. Despite of different steps of the reaction, the structural difference in the rate determining transition state was not captured depending on the groups. This indicates that all the hydrogen addition reactions in this study undergo the same mechanism.
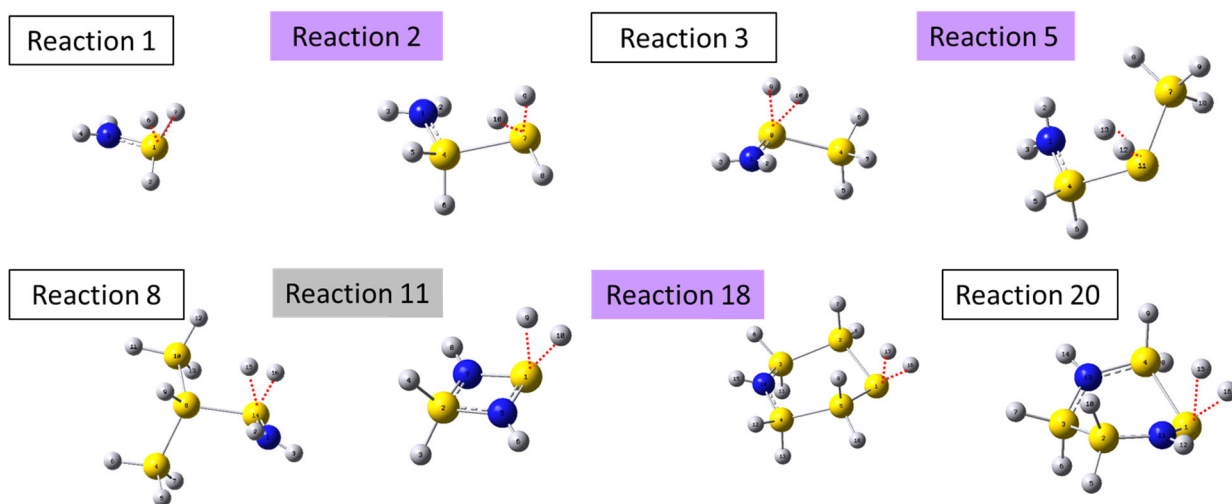
Figure 4.2 B3LYP/6-31G(d) optimized geometries of the lowest-energy conformer of the rate-determining transition state for several key reactions of hydrogen addition and elimination reaction.
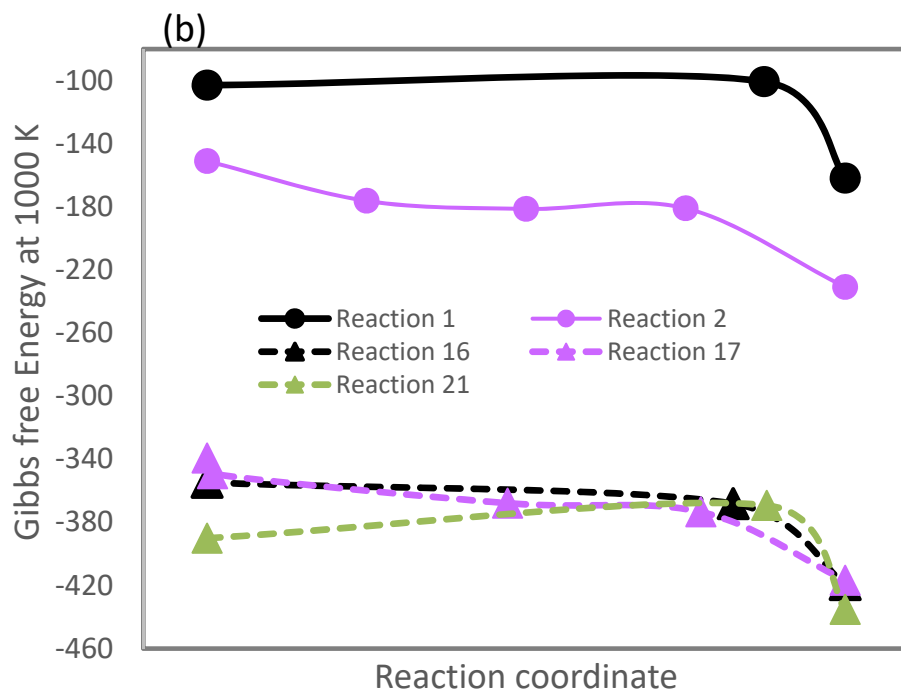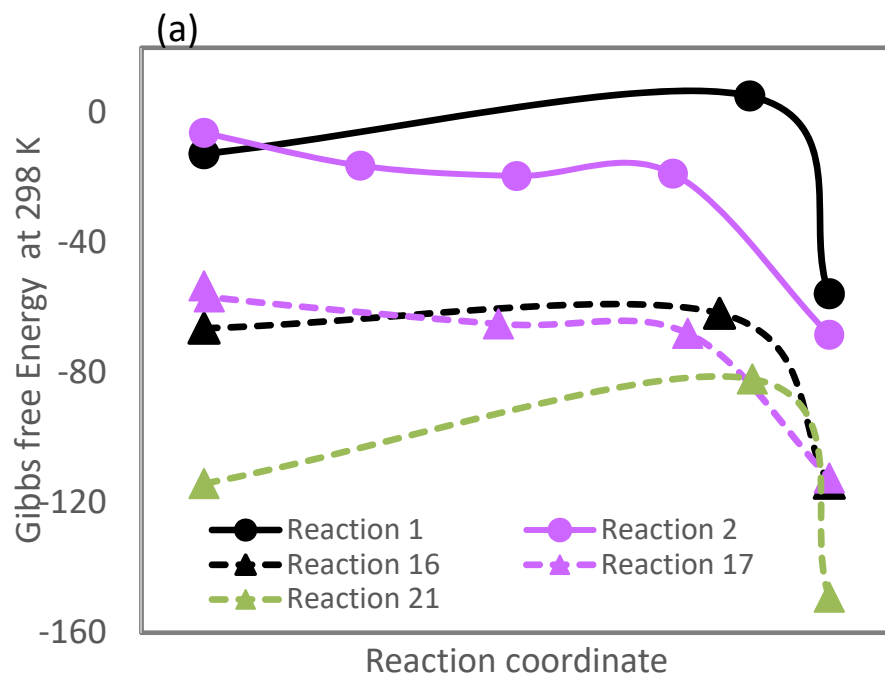
Figure 4.3 Gibbs free energy surface diagram: Hydrogen addition an elimination reactions for acyclic and cyclic species at (a) 298.15 K and (b) 1500 K. Each color represents; purple (group A), gray (group B) and black (group C).

4.3.1 Thermodynamic Properties and Rate-determining Step for Hydrogen Addition Reaction Comprising an Intermediate.

Hydrogen addition and elimination reactions in small silicon nitrides are depicted in **Figure 4.3** Several reactions were selected as key representative reactions for each group. The solid lines are describing the acyclic species behavior, and the dash lines are for cyclic species. The shape of the Gibbs free energy diagram was determined according to the type of hydrogen addition and elimination reaction which caused by the structural difference of the species. The hydrogen addition and elimination reaction of group A (purple), which is two step reaction, has negligible activation energy. It is convenient to consolidate the two-step conversion of unsaturated silyl amine to a product amino silane and its reverse reaction into one overall transformation. After calculating the rate coefficient for individual steps of exothermic reactions, the first step to the intermediate from the reactant of the reactions of group A was determined for the barrierless step, and the second step from the intermediate to the product amino silane was the rate-determining step. Thus, the overall rate coefficient for reactions of group A was calculated as $k = K_1k_2$, where K_1 is the equilibrium constant for the first step and k_2 is the rate coefficient for the second step.

4.3.2 Kinetic Parameters of Hydrogen Addition and Elimination

To understand the Hydrogen addition and elimination behavior under the SiH_4 and NH_3 co-pyrolysis condition, we compared the kinetic parameters of reactions.

According to groups, distinct differences were observed in the Arrhenius plot from the kinetic parameter calculations. In **Figure 4.4**, Group A has a negligible or a negative value of activation energy, as observed in the Gibbs free energy surface diagram **(Figure4.3)**. The activation barrier of Group A is close to zero, whereas Group B and C have steep slopes. For instance, reactions 4 and 5 have much

lower activation barriers for hydrogen addition than reaction 6, which are -1.26, -5.67, and 25.59 kcal.mol^{-1}, respectively. This is due to the hyperconjugation effect aforementioned in our previous study of the thermodynamic and electronic properties of SiN nanoparticles and the hydrogen migration reaction[186, 187]. There is an additional pi bond between divalent Si and N atom, and electrons in this bond are more delocalized by the hyperconjugation. Hence, higher energy is required to make two new sigma bonds between divalent Si and approaching hydrogen molecule in amino silylenes than in silylenes. This is because the pi bond in amino silylenes should be dissociated before new sigma bonds form. Then, a lone pair of electrons of Si interact with hydrogen to make sigma bonds. The same trend was observed in cyclic species from the comparison between reactions 12, 13, 14, and 15. Reaction 13(Group A) has the lowest activation barrier with -4.37 kcal.mol^{-1} followed by reactions 12, 14, and 15 with activation energy 17.86, 19.95, and 47.83 kcal mol^{-1}. This indicates that the position of the N atom has a more significant influence on the rate constant than the number of N atoms within the species. For example, comparing reactions 14 and 15, which have the same number of N atoms, the barrier of reaction 15 is more than twice as high. Interestingly, except for reaction 18, the rate constant of all reactions in the group A decreased slightly with increasing temperature, whereas all reactions in groups B and C increased significantly. The H_2 elimination reaction from the fully saturated SiN hydrides shows the same trend, as the temperature increased, the rate constant also increased, and it was more affected by temperature than the H_2 addition reaction. In comparing acyclic and cyclic species, the cyclic species require less energy than the acyclic species in the H_2 elimination reaction. In contrast, no such trend was observed with the H_2 addition reaction. At room temperature, the equilibrium of all reactions is close to the product. However, the thermodynamic equilibrium shifts towards the reactants as the temperature rises. For Group A reactions, the equilibrium is slightly inclined towards the products even at 1500 K, so the H_2 addition reaction is dominant slightly. In the case of Groups B and C, the equilibrium continues to shift toward the reactants, and the H_2 elimination

reaction becomes dominant from 1200-1300 K. This indicates that a temperature condition higher than at least 1200K is required to make SiN radicals as nano-building blocks for designing nano materials by removing H_2 molecules under pyrolysis conditions. Kinetic parameter values for rate constants are summarized in **Table 4.1**.

The difference in electronegativity between the N atom and the divalent Si can affect the kinetics by contributing to the higher dissociation energy of the N−H bond than one of the Si−H bond. The large gap of electronegativity between H and N atoms also causes a specific dipole−dipole attraction within the molecules, such as hydrogen bonding, making H dissociation difficult.

Table 4.1 Single event Arrhenius parameters, zero pint energy corrected barriers, and standard enthalpies and standard Gibbs energies reactions. (Each color represents purple: Group A, gray : Group B, and white : Group C.)

reaction	E_0 kcal·mol^{-1}	logA	E_a kcal·mol^{-1}	E_{o_r} kcal·mol^{-1}	Log A_r	E_{a_r} kcal·mol^{-1}	ΔH_{Rxn} kcal·mol^{-1}	ΔG kcal·mol^{-1}
1	26.45	12.87	26.16	60.70	18.58	61.07	-35.70	-27.63
2	-2.81	12.29	-3.4	49.41	18.58	49.89	-53.90	-45.19
3	19.87	12.39	19.56	53.76	18.36	54.11	-35.39	-26.93
4	-0.5	11.9	-1.26	50.55	18.32	50.91	-52.77	-43.91
5	-5.2	11.78	-5.67	45.91	18.09	46.42	-52.83	-44.00
6	20.7	12.76	20.59	54.26	18.47	54.71	-34.98	-26.86
7	-1.85	11.82	-2.56	49.76	18.42	50.19	-53.37	-44.24
8	20.44	13.05	20.44	53.85	18.73	54.34	-34.78	-26.69
9	21.02	12.31	20.54	53.42	18.94	53.89	-34.11	-25.22
10	-1.9	12.46	-2.27	43.94	18.73	44.38	-47.42	-39.02
11	51.12	12.55	50.45	73.62	19.03	74.07	-24.28	-15.28
12	18.39	12.13	17.86	53.48	18.40	53.76	-36.67	-28.28
13	-3.73	11.85	-4.37	44.66	18.19	45.00	-50.12	-41.64
14	20.12	12.79	19.95	54.20	19.00	54.78	-35.61	-27.28
15	48.06	13.18	47.83	71.20	18.80	71.57	-24.50	-16.59
16	14.6	11.79	13.99	52.82	18.16	53.03	-39.84	-30.87
17	-3.83	11.85	-4.43	45.13	18.08	45.55	-50.72	-41.99
18	2.19	12.43	1.76	48.50	18.69	48.97	-47.98	-39.18
19	17.09	12.32	16.5	52.91	18.08	53.02	-37.32	-29.19
20	18.45	11.89	17.99	51.40	19.34	52.81	-34.84	-25.82
21	39.22	12.76	38.63	67.75	18.09	67.87	-30.00	-22.48
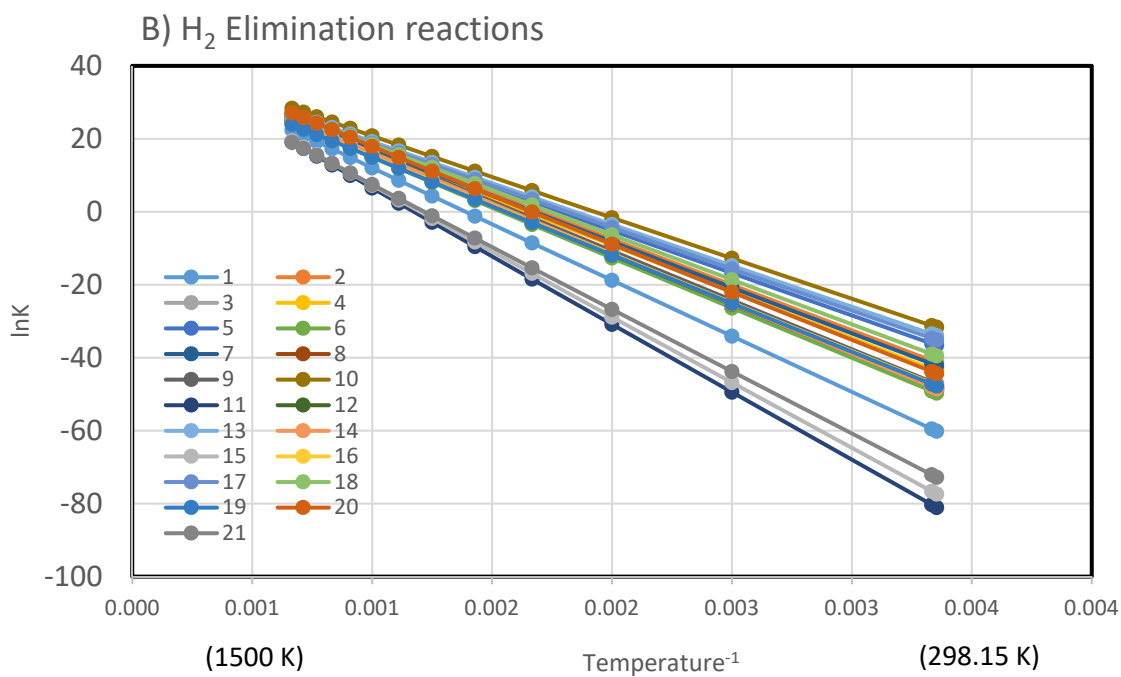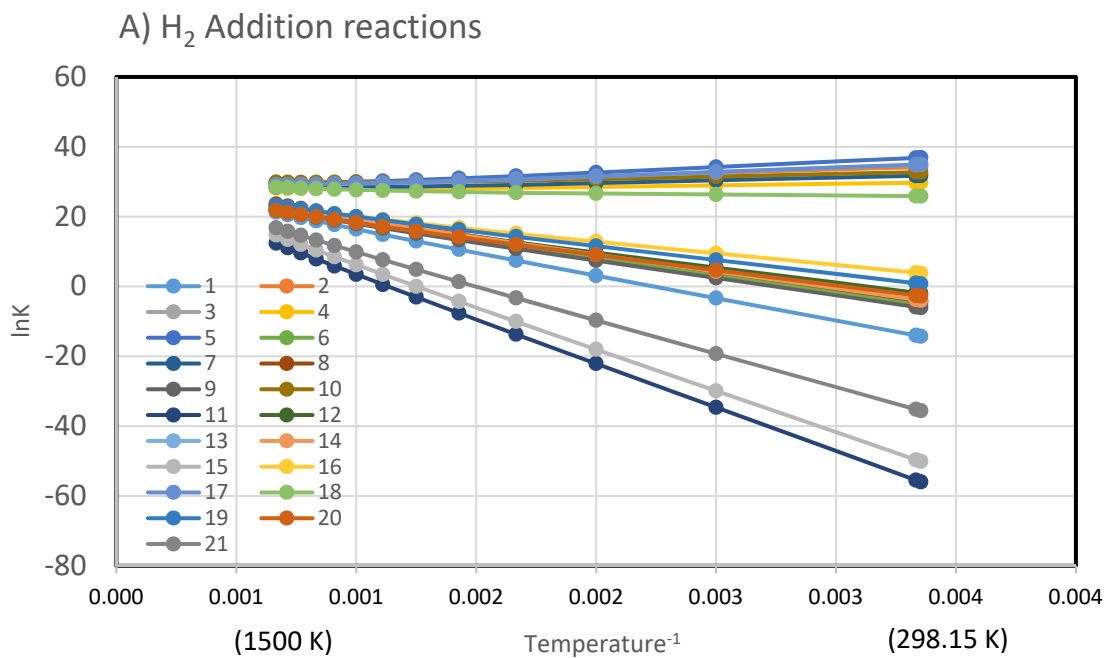
Figure 4.4 The Arrhenius plots of A) hydrogen addition (forward) and B) elimination (reverse) reactions in this study.

152

4.3.3 Natural Bond Orbital Analysis

N can form pi bond by offering its own lone pair electron to an adjacent atom. It was clearly observed from the cyclic species which N offer them to the adjacent divalent Si in **Figure 4.5 and 4.6**. Reactant 12 with one N and :Si has a pi bond formed by the contribution of lone pair on N (**Figure 4.5. B**) and an lone pair on Si (**Figure 4.5. C**). LP in N moves freely within the molecule and contributes to the resonant structure, whereas LP in Si is stationary and the reactant 12 mostly maintains the structure of **Figure 4.5(a)**. In the silicon nitride which one divalent Si and two Ns Si is not only symmetrical, but electrons are further delocalized due to two lone pairs of electron on N. Because of the hyperconjugation effect caused by freely moving electrons within the molecule, reactant 15 has two major resonance structures, which greatly contribute to molecular stability. Even if we assume that the resonance effect is neglected in amino silylenes, the LP of Si is always more stable than both the LP of N and the Si-N pi bond orbital, so nitirided silylenes are more stable than silylenes under pyrolysis conditions. This indicates that amino silylenes (:SiN) may play better as precursors than silylenes to control nanoparticle synthesis, because amino silylene can longer during pyrolysis.
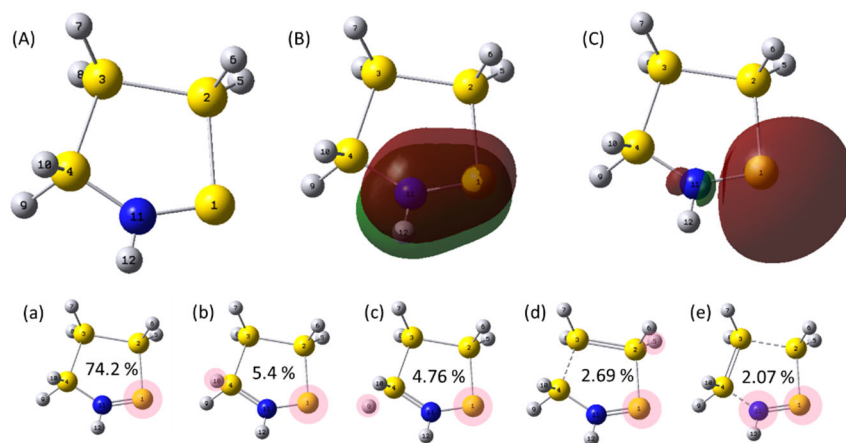
Figure 4.5. Resonance structure of reactant 12. Only structures that offer a major contribution to resonance are represented.
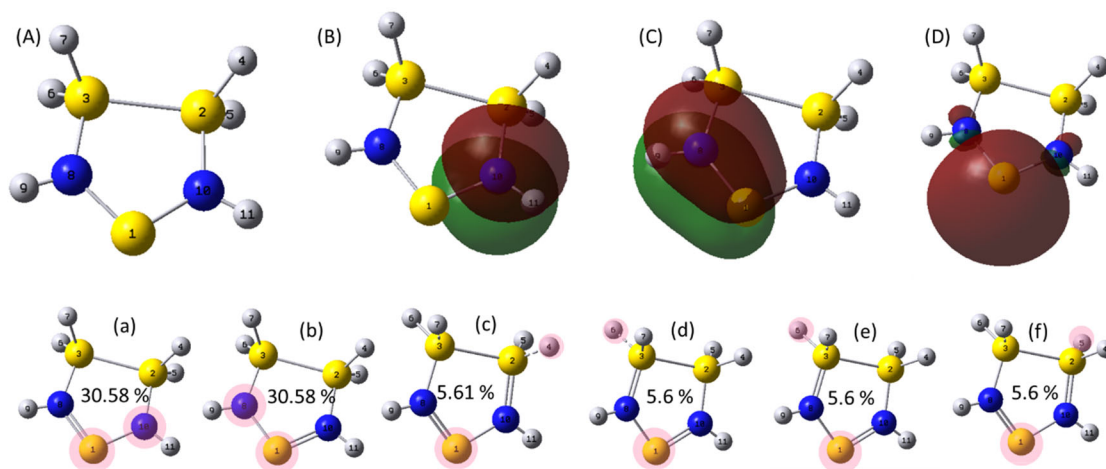
Figure 4.6. Resonance structure of reactant 15. Only structures that offer a major contribution to resonance are represented.

Molecular orbital theory provides information about the chemical bonding of molecules. Interpretation of molecular orbital helps us understand molecules' chemical properties and their behaviors. Especially, the frontier molecular orbitals in a molecule are mainly responsible for its reactivity. Frontier molecular orbital (FMO) theory has been successfully employed in carbon hydride[192] and silicon hydride chemistry[57] to predict rate coefficients using $E_{HOMO} - E_{LUMO}$ energy gaps[193] between the reactants[194, 195]. Furthermore, the reaction mechanism can be understood more clearly using the molecular orbital diagrams. A fundamental principle of molecular orbital theory is, that when atoms bond to form molecules, a certain number of atomic orbitals combine to form the same number of molecular orbitals, and the electrons involved are redistributed among the orbitals. However, the molecular orbital, which consists of a linear combination of atomic orbitals, does not provide an intuitive interpretation. Because molecular orbital diagram is mainly suited only for simple diatomic molecules, and becomes more complex when discussing even simple polyatomic molecules, such as silane. Instead of molecular orbitals, natural bond orbital (NBO)[146, 196-201] can be more useful for an orbital diagram of polyatomic molecules, since NBO is a calculated bonding orbital with

maximum electron density. NBO shows how contributions of *each* type are generally found *mixed* into molecular orbitals(MO), by classifying each MO into contributions of bonding "BD"-type, antibonding "BD*"-type and nonbonding "LP"-type NBOs. Except a few core-type MOs, which are clearly related to a single core "CR"-type NBO, most MOs are represented as complicated with irregular *mixtures* of LP, BD, and BD* type[184]. While MO-mixtures are often found to vary dramatically, NBOs retain highly recognizable forms of orbitals with slight conformational changes. Hence, NBO can explain the reaction mechanism in a more intuitive way than MO does, an NBO diagram for reaction 1 was depicted in **Figure 4.7.**

For the H_2 addition reaction, there are two different orbital interactions to form Si1-H6 and Si-H7 sigma bonds. One is the interaction between the pi bond orbital of :Si-N (HOMO of reactant A), or the lone pair orbital of divalent Si (HOMO-1 or reactant A), and the anti-sigma bond orbital of hydrogen molecule (LUMO of H_2). The other is the interaction between the anti pi bond orbital of :Si-N (LUMO of reactant A) and the sigma bond orbital of hydrogen (HOMO of H_2). The required energy for interacting between LUMO of H:SiNH$_2$ (reactant A) and HOMO of H_2 (reactant 2) is much lower than the one for interacting HOMO of H:SiNH$_2$ and LUMO of H_2, which are 10.81 and 17.74 eV, respectively. The major route for forming two Si-H bonds is the interaction between LUMO of H:SiNH$_2$(reactant A) and HOMO of H_2(reactant B). The two Si-H bonds formed as a result of H_2 addition have the same level of energy as the existing Si-H bonds.

In order for the H_2 elimination reaction to occur, two sigma bonds must be broken at the same time. The corresponding orbitals for Si-H bond in the product are not the HOMO, and the energy difference between HOMO (Lone pair of N) and HOMO-1 (Si-H sigma bond) is 3.27eV. H_2 elimination in silicon nitrides is more difficult to happen than one in silicon hydrides, because it requires more energy than HOMO –HOMO-1 of Si2H6, which has only a 0.54 eV difference.
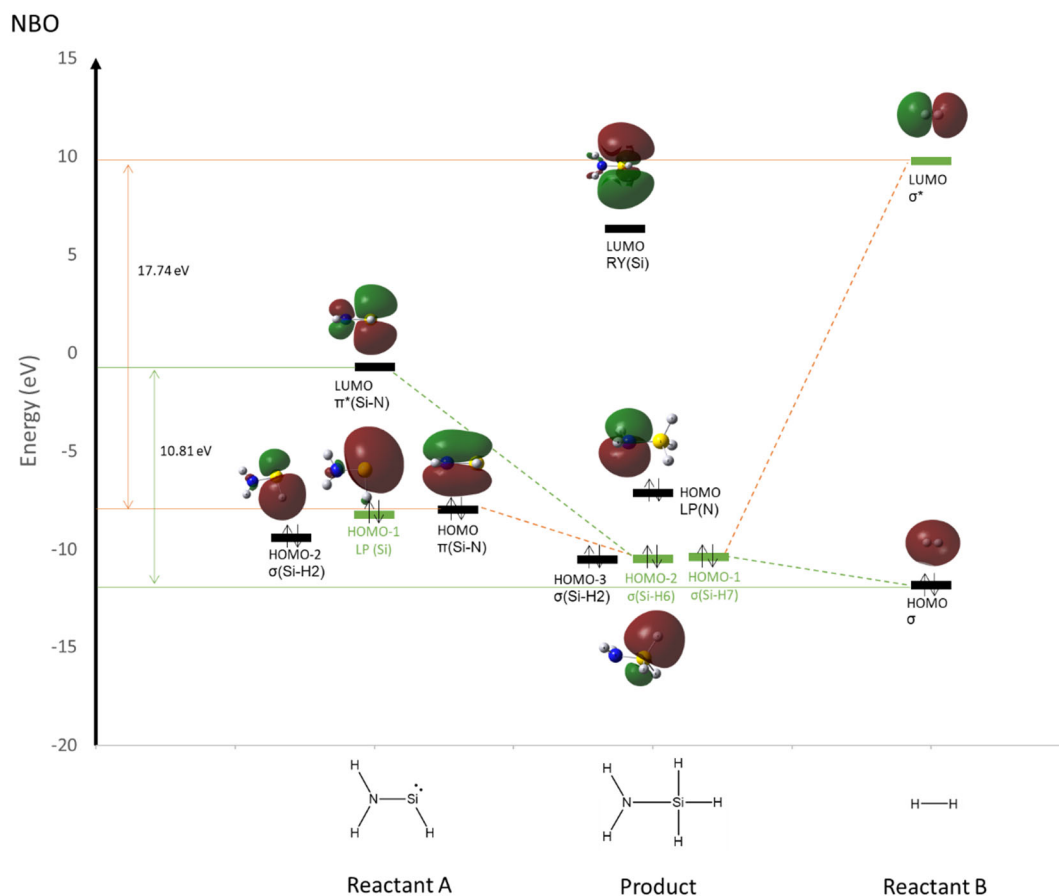
Figure 4.7. NBO interaction diagrams for Hydrogen addition and elimination reaction of Amino silylene.

4.3.4 Kinetic Parameter Model Generalization

Regression Analysis for H₂ addition and Elimination reactions

To develop a model for predicting activation energy, the activation energies of all reactions were plotted against the corresponding enthalpy of the reactions in **Figure 4.8**. The range of activation energies is apparently distinct according to the type of hydrogenation and dehydrogenation reaction. H_2 addition and elimination reactions of amino siylenes are seen to have a strong linear correlation with the enthalpy of the reaction. Hydrogen addition and elimination reaction of silicon nitride were

captured well by one regression equation. The Evans−Polanyi parameters, E_0, and α, were calculated from linear regression with the least-squares method to maintain thermodynamic consistency. The generalized H_2 addition and elimination reaction model predicted the activation energy with a 99% R square value. The parameters were obtained using linear regression analysis for all reactions **(Table 4.2)**.

Table 4.2 Generalized model for predicting activation energy for the hydrogen addition and elimination reaction in silicon nitrides. $\tilde{A}$ has units of $cm^3.mol^{-1}.s^{-1}$ and s^{-1} for addition reaction and elimination reaction, respectively.

E_0	α	β	γ	$\log\tilde{A}\_f$	$\log\tilde{A}\_r$	SSE	R^2
60.96	1.55	11.57	1.95	12.44	18.54	255.35	0.99

Validation of Regression parameter

k-Fold Cross-Validation

The numerous case of the atomic arrangement of silicon nitrides made it difficult to construct a validation set and remain complexity in hydrogen addition and elimination reactions. Hence 7-fold cross-validation is conducted to evaluate our regression model. The results of a 7-fold cross validation analysis are summarized with the mean of the model, minimum, maximum and standard deviation in **Table 4.3**.

To check the variance between the model and the averaged model from 7 -fold cross-validation, we also conducted an ANOVA test. In the result of the ANOVA test, the F test statistics is less than the F critical value, which are 8.92E -05 and the 5.98, respectively. In addition, the p-value of ANOVA test was 0.993, which indicated there is no sufficient evidence to distinguish the two models.

Parity plots depicting how well the suggested model captures the predicted rate coefficient from our CalcK script at 298.15 K for the hydrogenation and dehydrogenation reaction are shown in **Figure 4.9**. More than 98% of the activation energy and ln k values from the regression model matched well with the values predicted by the CalcK script, 98.9% and 98.5%, respectively.
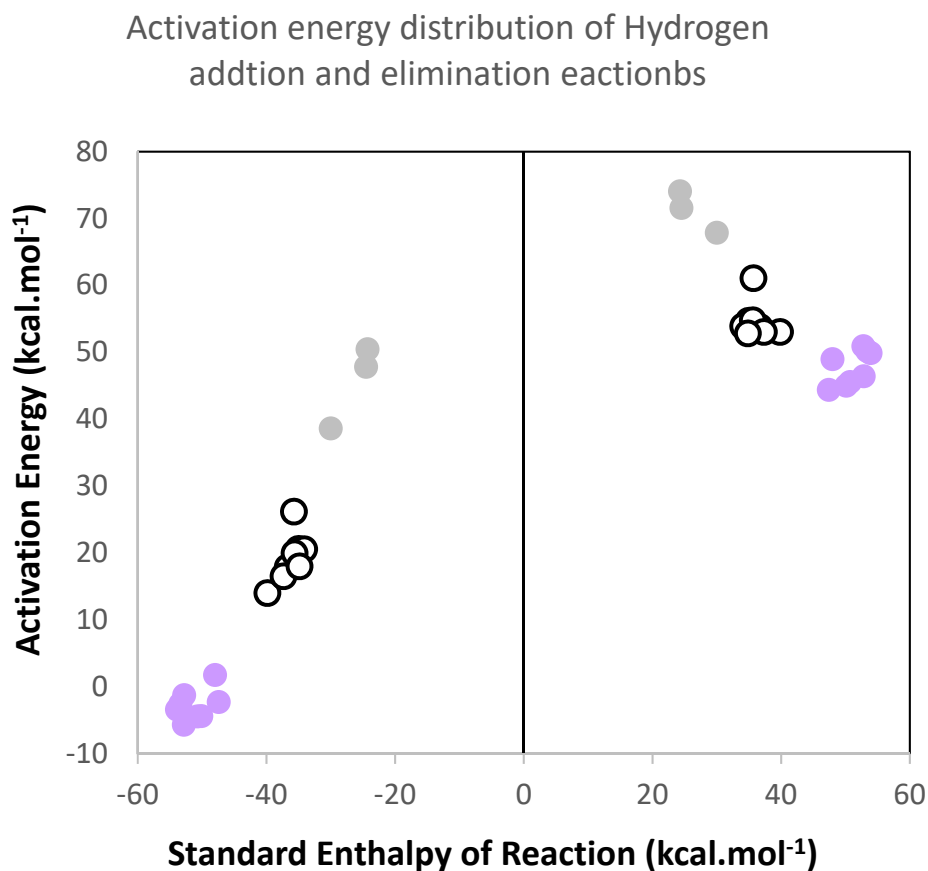
Figure 4.8. Activation energy distribution according to three different types of hydrogen shift reactions: Purple color solid circles represent Group (A), gray color represents Group (B), and white circles represent Group (C).

Table 4.3. 7-Fold cross-validation analysis result

	E_0	α	β	γ	residual
Min	60.42	1.52	10.52	1.09	-4.10
Average	62.19	1.57	11.19	1.85	6.59
Max	64.35	1.62	11.84	2.37	11.25
variance	1.73	0.00	0.25	0.26	22.53
standard deviation	1.31	0.04	0.50	0.51	4.75
standard error	0.50	0.02	0.19	0.19	1.79
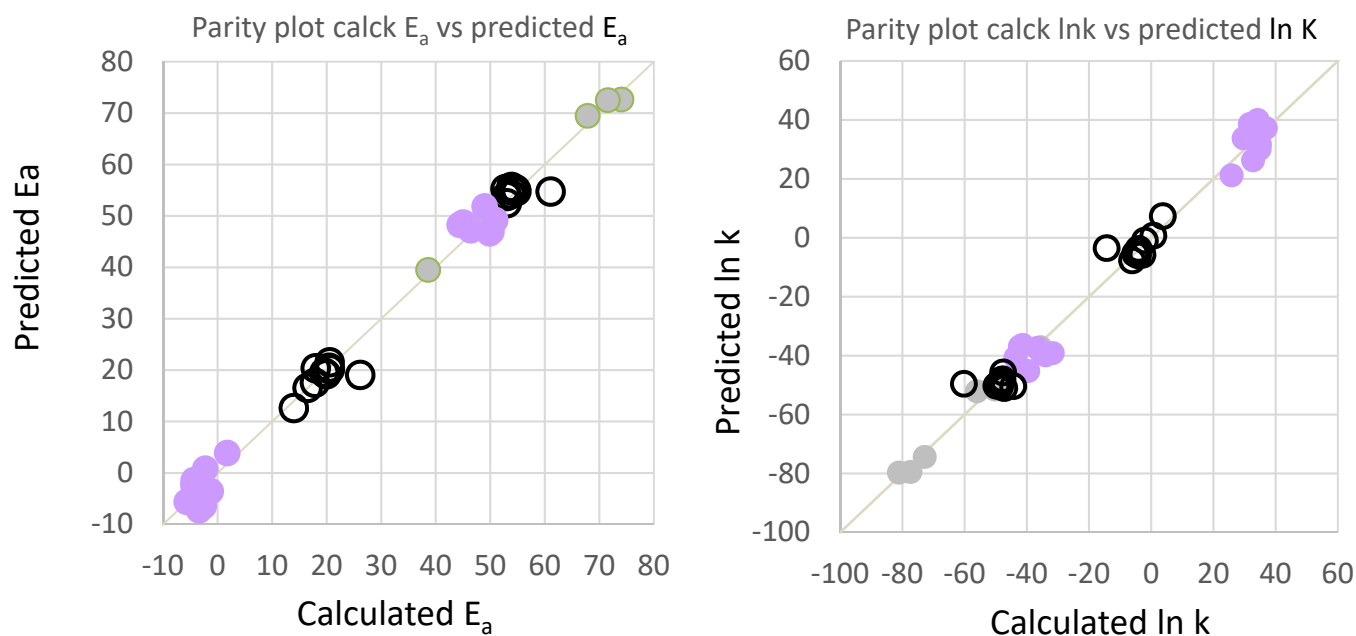
Figure 4.9. Parity plots of activation energy and the rate coefficients of hydrogen addition and elimination reaction in silicon nitrides at 298.15 K and 1 atm Purple color solid circles represent Group (A), gray color represents Group (B), and white circles represent Group (C).

4.4 Conclusions

The Rate coefficients and Arrhenius parameters for the hydrogen addition and elimination reaction in silicon nitride species have been calculated for 21 reactions using G3//B3LYP, statistical thermodynamics, and conventional transition state theory. The overall reaction of substituted cyclic and acyclic amino silylenes to their respective amino silanes by 1,1-hydrogen addition and elimination was analyzed by three different types patterns depending on the geometry of reactants. Only reactions of the group (C) were found to as two-step reactions that pass through a stable intermediate to produce saturated silicon nitrides. Although the reaction pathways are different, all hydrogen addition and removal reactions are similar in the structure of the reaction centers of the rates determining transition state. The single event pre-exponential factors, $\tilde{A}$, and activation energies, E_a, for hydrogen addition and elimination of silicon nitrides were calculated. The hydrogen addition and elimination reaction was explored for acyclic and cyclic monofunctional silicon nitrides, it was found that the reactant geometry give no influence on kinetic parameters. The mechanism of hydrogen addition and elimination reaction was intuitively explained through NBO analysis, and the stability of amino silylene species was explained by the resonance and hyperconjugation effects. A model was provided to predict the activation energies for hydrogen addition and removal reactions of silicon nitride species. To the best of our knowledge, the kinetic parameters of the hydrogenation and removal reactions of silicon nitride at this microkinetic level have not been reported and the model was validated by k-fold cross method.

Chapter 5

Silicon Nitride Nanoparticles Growth

5.1 Introduction

Silicon nitrides and hydrogenated silicon nitrides attract widespread scientific interest across multiple application fields due to their superior combination of optical[127, 131], mechanical[119], thermal and optoelectronic properties. The wide range of possible applications of silicon nitrides are structural, cutting tools,[23] passivation layers in solar cells, permeation barriers and encapsulation layers in light-emitting device (LED)[3] The wide bandgap (~5.2 eV) of thin films allows for its optoelectronic application, while the silicon nitrides could act as a host matrix for silicon nano-inclusions (Si-ni) for solar cell devices and lithium ion battery anodes.[3, 13 1 29]

Due to the tunable refractive index of SiN_x, the Si_3N_4 layers enable better electrical conductivity are synthesized mostly by the chemical vapor deposition (CVD) methods, [136, 202, 203, 204] such as plasma enhanced (PE-CVD)[8, 205-209], hot wire (HW-CVD) [210] while physical vapor deposition (PVD), sputtering, is also widely used. [3, 13] Besides these fabrication methods, atomic layer deposition (ALD)[211] is a rising technology, which can control the deposition at the atomic level and provide extremely thin silicon nitride layers.

Gas-phase synthesis such as various CVDs and ALDs are all 'deposition methods' and are suitable for making film-type silicon nitrides. Recent comprehensive reviews of silicon nitrides in both monolithic and thin films dominate current film deposition techniques and silicon nitrides' physical,

electronic and optoelectronic properties and their applications. However, during the deposition process, gaseous-phase nucleation also occurs. In addition to solid-gas interface reactions, deposition, gaseous nucleation forms amorphous silicon nitride nanoparticles that can create defects and affects the film quality. However, the understanding of gas-phase silicon nitrides is still scant, and there are not many studies.

After the recent discoveries of the potential of silicon nitrides as a host matrix, the study of pyrolytic silicon nitrides synthesis from silane and ammonia and its new applications have been reported. Kilian et. al demonstrated a scalable gas-phase synthesis in a hot-wall reactor to produce amorphous silicon nitride nanoparticles for achieving sufficient capacity for alternative anode of lithium ion batteries.[29] Chae et al. synthesized Si-rich silicon nitrides nanoparticles with extreme phase homogeneity using a gas phase synthesis in their specialized vertical furnace.[132]

During the pyrolysis of silane in the atmosphere of NH_3, three thermodynamically favorable reactions exist. First, the thermal decomposition of SiH_4 and formation of Si. Second, the direct reaction of SiH_4 and NH_3 to form silicon nitrides. And last, the nitridation of silicon which was form by the decomposition reaction.[29] Since the silane pyrolysis initiates with the formation of highly reactive silylene species,[56, 212] the direct reaction between silylene and ammonia can be considered as the major pathway to form silicon nitrides as substituted silylene addition is a key reaction class in silicon hydride pyrolysis, which directly affects nanocluster size distributions.[56, 213]

Beginning with the molecular structure study of silizamine by Gordon[214], Parisel et. al investigated small size of silicon nitrides radicals [215], Hu et al. conducted a theoretical study using ab initio calculations for a series of hydrogen-eliminated species contacting a N-Si covalent or dative bond in gas phase reaction of SiH_4 and NH_3. They provided a detailed reaction mechanisms of the Si-N-H system, and potential energy diagrams for the reactions.[216] Kovacevic et. al provided detailed reaction mechanisms that lead to creation Si-N bonds for silicon nitride growth in the SiH_4-NH_3 plasma

with relative energies for all species in the reactions.[137] However, a detailed exploration of substituted silylene addition to silicon nitrides has not been reported yet, and this information is necessary to describe silicon nitride cluster growth kinetics. Understanding kinetics is the first step in designing a novel material by optimizing the reaction conditions for the desired product. Thus, in this paper, we investigated a total of 40 silylene addition and elimination reactions and 23 cyclization and decyclization reactions of silicon nitrides containing up to 8 heavy atoms (Si and N) using density functional theory (DFT). All elementary steps of reactions are limited to monofunctional compounds. The composite method of G3//B3LYP was used to calculate the electronic energy, then statistical thermodynamics was employed to all reactants transition states, and products to incorporate temperature effects. The kinetic parameters; single event rate coefficients at 1 atm and 298−1500 K were calculated using transition state theory (TST), and then activation energies, E_a, and single event pre-exponential factors, $\tilde{A}$, were regressed. Generalized Evans−Polanyi models were suggested for each type of reactions. Suggested Evans−Polanyi models can be adapted using machine learning algorithms to predict reaction rate coefficients for larger species not in this study (or training set). This is called supervised machine learning and is the most common sub-branch of machine learning. The Evans−Polanyi models are a predictive statistical process where the model finds the significant relationship between activation energy and enthalpy of the reaction. To estimate how accurately the models in this study will perform, we conducted k-fold cross validation and statistical analysis.

5.2 Computational Methods

Quantum Chemical Calculations, Transition State Theory, and Statistical Thermodynamics.

Silylene addition and elimination is another hypothesized elementary reactions for the silicon-nitride pyrolysis system following our previous study, hydrogen migration reaction and hydrogenation addition and elimination reaction.

Quantum chemical calculations were performed with Gaussian 16. All electronic energies for silyl amines, silylenes, ammonia, transition states, and adducts were calculated with the G3//B3LYP method.

We confirmed that the singlet potential energy surface for substituted silylenes and silicon nitrides is lower in energy than the triplet potential energy surface in our previous studies.[56, 57, 186, 187, 217, 218] For all results reported, the electronic wavefunctions for all silyl amines, silylenes, ammonia, transition states, and adducts were optimized in the singlet state. Geometries and harmonic frequencies of the lowest-energy conformers were determined at the B3LYP/6-31G(d) level. The harmonic frequencies and zero-point energy (ZPE) were scaled by factors of 0.96 and 0.98, respectively, to account for anharmonicity in the normal vibrational modes as suggested by Scott and Radom.[98] The potential energy surface interpolation method, the Synchronous Transit-guided Quasi-Newton method (QST3), was used for finding transition states. Each transition state was confirmed that it has one imaginary frequency and follows the intrinsic reaction coordinate to the desired reactants and product.

A good approximation is important to increase the accuracy of the calculation. The potential energy surface scan depicting the barriers to internal rotation for several selected reacting species were conducted. In the silylene addition and elimination reactions, all bonds can be canceled out because these bonds exist in all steps of the reaction. However, in cyclization and ring-opening reactions, the bonds are not canceled out, the internal rotation barrier calculation was necessary. When the distance between divalent Si and N is shorter, the rotation barrier of the bond which has :Si is higher. Therefore,

the energy for rotating bonds between Si: and any atom, Si, N, or H, is too high to rotate freely, the harmonic oscillator approximation considering anharmonicity was a reasonable choice. Using conventional statistical thermodynamics, partition functions based on the harmonic oscillator and rigid rotor approximations were used to calculate thermodynamic and kinetic properties. Rate coefficients were calculated by conventional transition state theory[102] according to the **equation(5.1)** at 1 atm assuming an ideal gas state,

$$k^{TST}(\text{T}) = n_d \tilde{k} = n_d \Lambda \exp\left(\frac{\Delta S^{\neq}}{R}\right) exp\left(\frac{-\Delta H^{\neq}}{RT}\right) \qquad eq(5.1)$$

Where Λ, defined in **equation(5.2)**,

$$\Lambda = \kappa(\text{T}) \frac{k_B T (V_m^0)^{-\Delta n}}{h} \qquad eq(5.2)$$

$\tilde{k}$ is the single event rate coefficient: $\kappa(\text{T})$ is the Wigner tunneling correction(ref) at temperature T; k_B is Boltzmann's constant; h is Planck's constant; $\Delta H^{\neq}$ is the enthalpy of activation; Δn is the change in the number of moles going from the reactant to the transition state (i.e., zero in both directions for isomerization); and n_d is the reaction path degeneracy, or number of single events. $\Delta H^{\neq}$ and $\Delta S^{\neq}$ are calculated using standard formulae. [102]

The single event parameters of the Arrhenius relationship, $\tilde{A}$ and E_a, were obtained by fitting ln k versus T^{-1} over the temperature range 298-1500 K. This calculation was performed using the CalcK script previously employed by our group for both reaction families, siliylene addition & elimination and cyclization & decyclization reactions. [56, 57, 186, 187, 218] The rate coefficient is important for constructing a mechanistic model. One of method for predicting E_a is the Evans-Polanyi correlation[156] in **equation(5.3)**,

$$E_a = E_0 + \alpha \Delta H_{Rxn} \qquad eq(5.3)$$

where E_0 and α are parameters that are determined from linear regression against predicted values and are constant for a hydrogen shift between Si and N in silicon nitrides. E_0 is the intrinsic barrier of the reaction and ΔH_{Rxn} is the standard enthalpy of reaction. ΔH_{Rxn} is calculated using the the CalcK script. Generalized models for predicting the activation energies for both silylene addition & elimination and cyclization & ring-opening reactions were obtained by the least-squares method, the intrinsic barrier, E_0, for the both forward and reverse reactions were constrained to be equal to maintain enthalpic consistency.

K-fold cross-validation was conducted for regression models for predicting the activation barrier of silylene addition and elimination reaction of silicon nitrides. The k value for the silyene addition & elimination reaction is 11 and one for cyclization & decyclization reactions is 7. All the dataset was shuffled randomly and was split into 11 or 7 for each groups. A group out of k groups was considered a validation set and the remaining k-1 groups as a training set. The regression was conducted k times, and the k regression models were statistically analyzed. And ANOVA anlaysis was conducted to compared the generalized model and the average model of k cross validation.

5.3 Results and Discussion

5.3.1 Silylene Addition & Elimination Reaction

A total of 40 silylene addition and elimination reactions and silyl amines were mapped using G3//B3LYP. Two different silylene addition reactions can occur under silane-ammonia co-pyrolysis conditions.[219] One is substituted silylene reaction with ammonia (P1 reactions), and the other is silylene addition to silicon nitrides (P2 reactions), as depicted in **Figure 5.1** and **Figure 5.2**, respectively. For substituted silylene reaction with ammonia, there are 11 reactions with various substituted silylenes from acyclic species SiH_2 to cyclic species 6-membered ring. For silicon nitrides, reactions with silylene, 9 acyclic silicon nitrides and 22 cyclic silicon nitrides were investigated.

All 11 of P1 reactions were exothermic reactions and showed a single barrier between reactants and products. In the P2 reactions, however, because silylene can approach either Si or N of silicon nitrides, P2 reactions were subdivided into two subcategories; i) silylene addition to N of silicon nitrides and ii) silylene addition to Si of silicon nitride. For P2 group, 7 acyclic silicon nitrides and 22 cyclic silicon nitrides were studied. The reactions in the group (P2-i) silylene addition to N are exothermic reactions and showed a single barrier as like the reactions of P1. The reactions of group (P2-ii) silylene addition to Si in silicon nitride are exothermic, but presented two distinct barriers linked by a hydrogen bridged intermediate. Unfortunately, these passages for silicon nitrides have not been corroborated by experiments unlike the same reactions of silicon hydrides by Becerra et al. However, passage through an adduct by way of two steps in series agrees with our previous study, H migration reactions between Si and Si, and H_2 addition and elimination reactions to Si atom.

Various conformations of reactant silicon nitrides were prepared, such as silicon nitrides of $D_{rel}=1$, D_{rel} is defined by a relative distance between reaction center (Si) to N within the molecule, $D_{rel}=2$ or higher of silicon nitrides reactants, and silicon nitride which has an N-Si-N configuration.

Interestingly, different conformation of reactant was not a significant factor for silylene addition reaction unlike the hydrogen transfer reaction. All reactions showed two different passages depending on the reacting atoms. The differences between group (P2-i) and group (P2-ii) can be found on the Gibbs free energy surface. A notable difference between group (P2-i) and group (P2-ii) is the activation energy. The average activation barrier of group (P2-i) was 4.88 kcal.mol^{-1}, which was similar regardless of the size or type of reactants. The average activation energy of group (P2-ii) is -13.71 kcal.mol^{-1}, which is negative value. This is consistent with that the SiH_2 insertion reactions to H_2, SiH_4, Si_2H_6, and Si_3H_8 have small negative activation energies, which indicates these are barrierless processes. [56, 114] These barrierless reactions slow down with increasing temperature. And the mechanism of barrierless reactions depends on the capture of the molecules in a potential well. SiH_2 has negative activation energy for insertion not only to silicon hydride but also to carbon hydride.[56, 220] Other analogue species of SiH_2 in the group 14, CH_2 and GeH_2, also require negative energy for addition reaction.[221, 222] These analogues are enormously reactive and high-energy species.

5.3.2 Rate-determining Step

Even though our calculations finds a stable adduct for reactions in the group (P2-ii), it is more convenient to combine the two-step conversion of a substituted silicon nitrides and silylene to a product of an aminosilane and its reverse reaction into one overall step.

Prior to consolidation of the two-step conversion, the rate-determining step was first validated by monitoring the reaction dynamics of Reaction p2r01b. Three microkinetic models were created assuming: 1) a full model, 2) that the first step is rate-determining, and 3) that the second step is rate-

determining. Model 1) explicitly includes the kinetic parameters for both reaction steps without assuming a rate-determining step. The rate coefficient for the barrierless step to form the adduct from the reactants was calculated using one-dimensional variational transition-state theory. Model 2) calculates the overall rate coefficient as $k = k_1 K_2$ where k_1 is the rate coefficient for the first step, K_2 is the equilibrium coefficient for the second step. The overall rate coefficient for model 3) was calculated as $k = K_1 k_2$, where K_1 is the equilibrium coefficient for the first step and k_2 is the rate coefficient for the second step. Over the temperature range of 298.15–1500 K, model 3) is superior in predicting the reaction dynamics of the full model for Reaction p2r01b. Thus, for reaction b, c, d of P2 in **Figure 5.1** and **5.2**, the transition states were located using the QST3 potential energy surface interpolation method for only the rate-determining step, the second step of silylene addition direction.

Figure 5.3 shows the transition-state geometries of several key silylene addition reactions. The structural difference were observed in the atom of the reactive center. The addition of various substituents to either side of the reactive center does not make a significant structural difference in transition states. It was observed that the TS shape of the group (P2-i) and group (P2-ii) was slightly different. The angle :Si-H-X was 80.0 degrees in the group (P2-i) and 95.0 degrees in the group (P2-ii). Also, when Si and :Si were reactive centers, the reactive center structures of TS of acyclic species and TS of cyclic species were different. Endocyclic substituted silylenes reduce the central bond angle even lower due to additional ring strain across the divalent center (**Figure 5.3 h and i**). When acyclic substituents are added to the silylene, they change the reactive center by increasing the Si-:Si bond length central to the reactive center (**Figures 5.3 d, e, and f**). The structure of the reactive center changes the most when the attacking silylene has an endocyclic divalent center or the donating silicon center is part of a ring. However, no difference was found in N-:Si reactive centers by different substituents.

SiH_2 insertion to silicon nitrides is also a barrierless reaction, which has smaller negative

activation energies (more negative). This can be interpreted that the greater the absolute value of the activation energy of SiH_2 insertion to silicon nitrides, the greater the driving force for addition reaction. There is no experimental data for direct comparison, however, we can figure out by comparing the calculated activation energies of silylene addition reactions to disilane and silyl amine, -10.2[56] and -13.59 kcal.mol^{-1} respectively, listed in **Table 5.3**. The silyl amino reaction (p2r01b) has slightly more negative activation energy value. These are nevertheless fast reactions, SiH_2 addition to a Si-H bond in silicon nitrides has been found to have a much higher *A* factor than the reaction to a Si-H bond in disilane does, the silylene addition reaction to silicon nitrides will be superior in silane and ammonia pyrolysis.

Group (P2-i), p2a reactions, a showed similar kinetic behaviors to the P1 reactions, the rate constants of both reactions were more affected by the temperature than reactions in the group (P2-ii), except the fact that the activation barrier of the P1 reaction was twice higher than that of the P2a reactions. Compared to the P1 reactions, the linearity between *lnk* and T^{-1} decreased slightly in P2a at high temperature condition (600-1500 K). The nonlinearity characteristic is stronger in the 6-membered ring species, reactions p2r06a, p2r08a, p2r09a, p2r10a and p2r12a. No more severe curvature than the 6-membered ring type was found in the acyclic species and the 4- and 5-membered species. The activation barrier of the acyclic species was higher than that of the cyclic species, indicating that the rate constant was more affected by temperature. In addition, it can be seen that at a temperature higher than 600 K, SiH_2 insertion occurs more in acyclic species or small ring species, and at a temperature below 600 K, it occurs more in larger species.

For the elimination reaction, classic Arrhenius behavior is observed for reactions for both P1 and P2. The activation energies increase with the increasing strength of the breaking X-Si bond (X= Si or N) and X-H bond and decrease with the strength of the forming X- H bond.[56] From the differences in bond dissociation energy of Si-Si and N-Si, which are 327 and 439 kcal.mol^{-1}, and Si-H and N-H

198.46 and 314 kcal.mol^{-1}, activation barriers of group (P2-i) are expected to be higher than activation energies of group (P2-ii). The activation energies of the group (P2-i) are twice as higher as one of the group (P2-ii), it resulted in **Table 5.1** and **5.2.**

The temperature dependence of the rate coefficient for the unimolecular decomposition reaction of amino silanes to form either silylene and silyl amines, or ammonia and substituted silylenes is linear over all temperatures.

Instantaneous selectivity is the ratio of the two rates in parallel reactions, providing information on which reaction prevails in the system. However, there is no concentration of reactants and it can vary depending on the reaction system, we assumed that each comparable reactions have the same concentration and reaction order. The ratio of two rate coefficients means sensitivity of the rate selectivity parameter to temperature. In the reaction between silicon nitrides and silyene, the sensitivity of the rate selectivity parameter to temperature is in the range from 10^{12} to 10^2 at from 298.15 K to 1500 K, respectively. The silylene insertion to a Si-H bond in silicon nitrides always dominate the insertion to a N-H bond in the whole range of temperature.
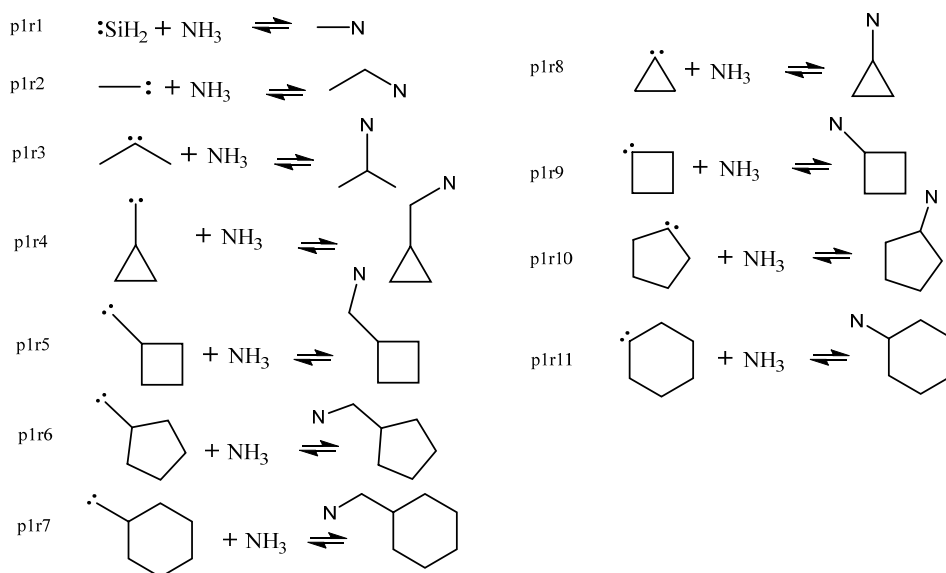
Figure 5.1. Various substituted silylenes reaction with ammonia. Unlabeled atoms in each molecules are Si atom, not C atom.

171
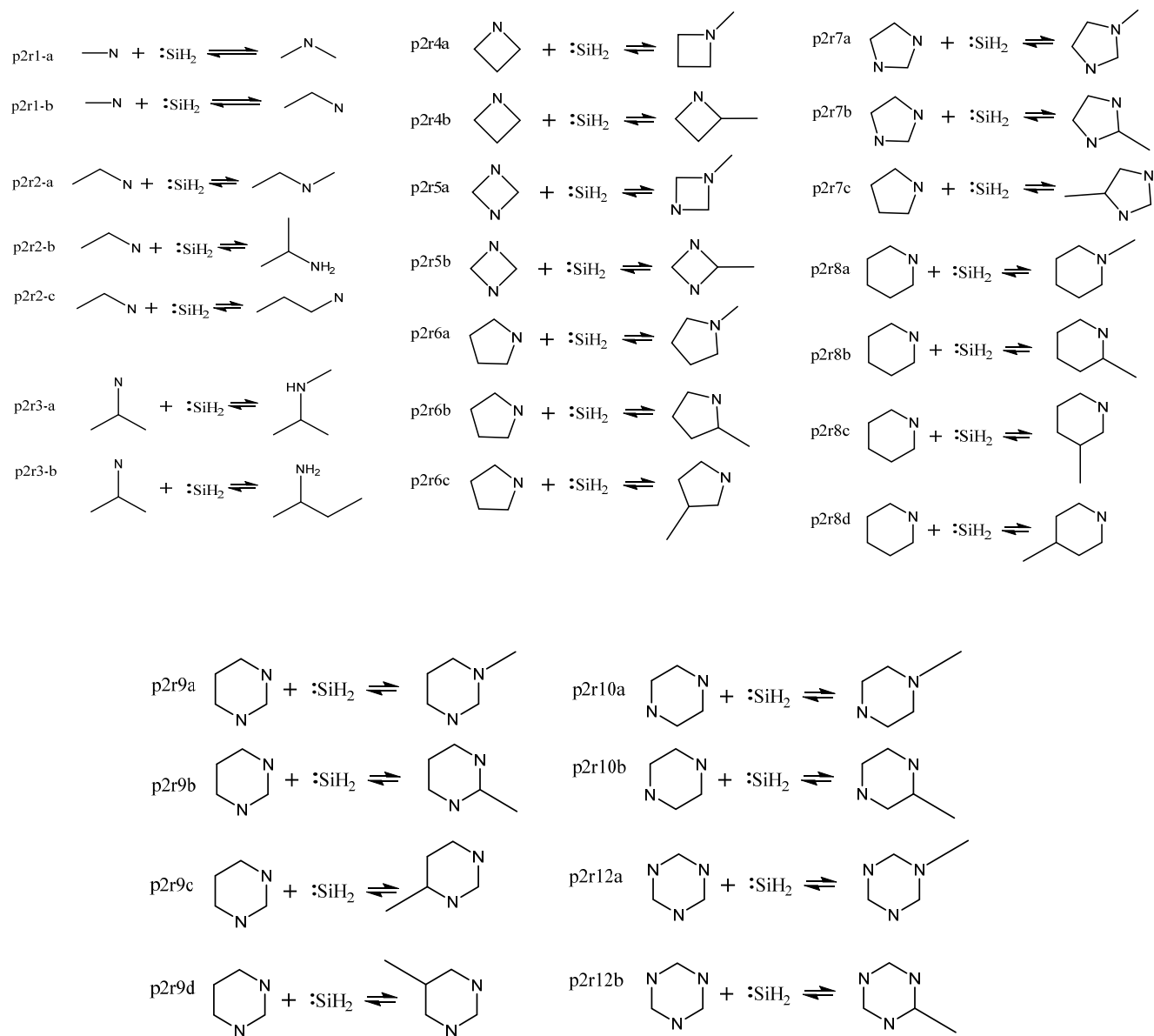
Figure 5.2 Various silicon nitride reaction with silylene. Unlabeled atoms in each molecules are Si atom, not C atom.
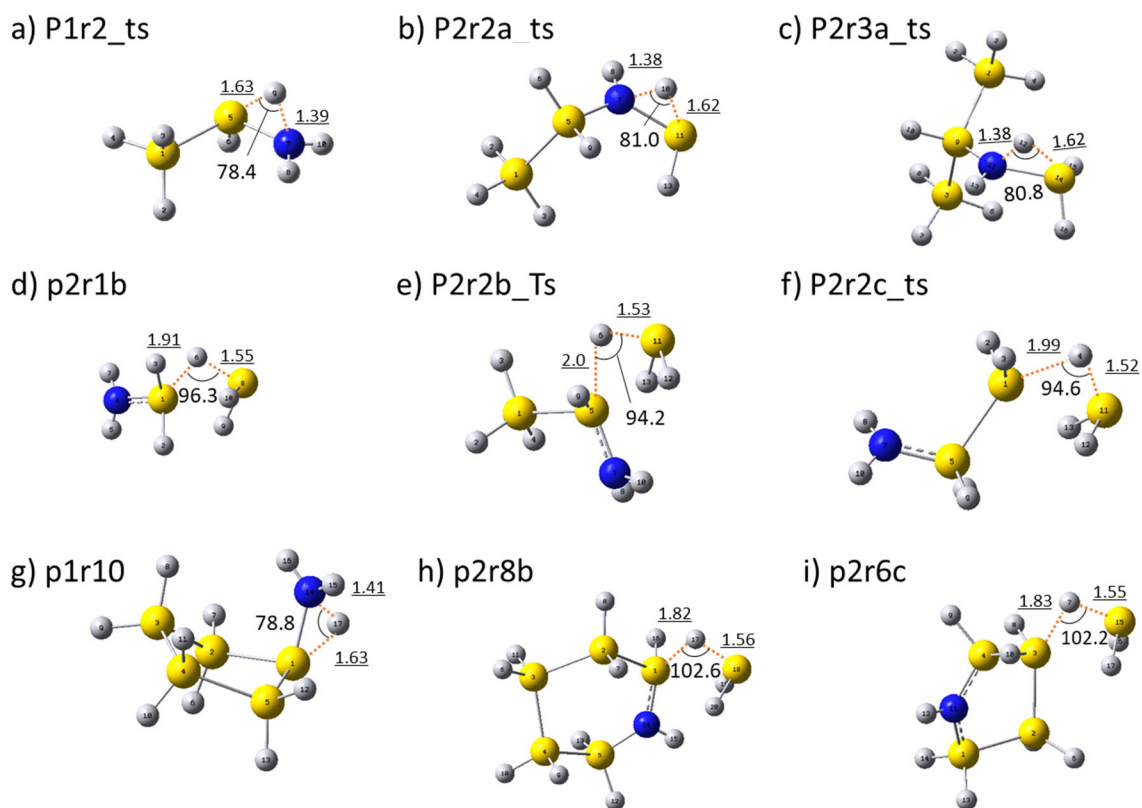
Figure 5.3 B3LYP/6-31G(d) optimized geometries of the lowest-energy conformer of the rate-determining transition state for key reactions in silylene addition and elimination.

Table 5.1 Arrhenius parameters of substituted silylenes reaction with ammonia at 298.15 K and 1 atm, A has units of $cm^3 \cdot mol^{-1} \cdot s^{-1}$ and s^{-1} for addition and elimination reaction, respectively

reaction	E_0 kcal·mol^{-1}	logA	E_a kcal·mol^{-1}	E_{o_r} kcal·mol^{-1}	Log A_r	E_{a_r} kcal·mol^{-1}	ΔH_{Rxn} kcal·mol^{-1}	ΔG kcal·mol^{-1}
p1r01	11.08	11.48	11.11	73.21	18.22	73.1	-63.65	-52.98
p1r02	9.43	10.86	9.94	70.21	18.57	70.22	-62.11	-49.96
p1r03	8.19	11.82	9.19	66.67	18.62	66.63	-59.49	-48.37
p1r04	26.04	12.42	27.32	68.02	18.32	67.84	-42.59	-32.69
p1r05	16.44	12.19	17.56	68.68	18.53	68.61	-53.05	-42.60
p1r06	9.87	10.02	10.48	68.14	18.14	67.99	-59.43	-46.63
p1r07	10.72	10.97	11.53	69.05	18.68	69.03	-59.43	-47.18
p1r08	10.72	10.97	11.53	69.05	18.68	69.03	-59.43	-47.18
p1r09	10.48	11.17	11.42	67.07	18.38	66.92	-57.6	-45.89
p1r10	9.19	11.79	10.29	64.71	18.45	64.69	-56.46	-45.54
p1r11	8.97	11.15	10.01	65.17	18.37	65.06	-57.16	-45.43

Table 5.2 Arrhenius parameters of substituted silicon nitrides reaction with silylene at 298.15 K and 1 atm, A has units of $cm^3 \cdot mol^{-1} \cdot s^{-1}$ and s^{-1} for addition and elimination reaction, respectively

reaction	E_0 kcal·mol^{-1}	logA	E_a kcal·mol^{-1}	E_{o_r} kcal·mol^{-1}	Log A_r	E_{a_r} kcal·mol^{-1}	ΔH_{Rxn} kcal·mol^{-1}	ΔG kcal·mol^{-1}
p2r01a	4.48	10.39	4.66	70.44	17.43	70.09	-66.99	-55.98
p2r01b*	-14.85	10.97	-13.59	36.18	17.76	36.51	-51.91	-41.02
p2r02a	6.08	11.07	6.83	72.42	18.07	72.51	-67.26	-56.29
p2r02b	-16.3	11.05	-14.51	36.82	18.06	37.44	-53.76	-42.56
p2r02c	-13.52	11.48	-11.65	40.38	18.42	41.2	-54.62	-43.55
p2r03a	5.68	11.13	6.52	72.29	18.52	72.5	-67.57	-56.07
p2r03b	-13.05	10.95	-11.71	41.44	17.63	41.71	-55.19	-44.48
p2r04a	4.76	11.38	5.9	72.91	18.1	73.11	-68.88	-58.22
p2r04b	-15.92	11.25	-14.18	37.69	17.9	38.16	-54.17	-43.45
p2r05a	5.17	11.61	6.24	75.34	17.91	75.46	-70.84	-60.79
p2r05b	-17.39	11.01	-15.85	34.29	17.59	34.51	-52.23	-41.57
p2r06a	2.86	11.16	3.78	70.57	18.59	70.74	-68.59	-57.00
p2r06b*	-16.2	10.75	-14.67	37.43	17.14	37.67	-54.18	-43.80
p2r06c*	-13.89	11.46	-12.02	42.54	18.16	43.27	-57.02	-46.32
p2r07a	4.06	10.84	4.88	72.3	17.23	72.38	-69.09	-58.94
p2r07b	-17.42	11.27	-15.7	34.07	18.05	34.53	-52.11	-41.17
p2r07c	-15.69	11.12	-13.94	37.8	17.79	38.27	-54.04	-43.30
p2r08a	3.34	10.5	4.09	72.02	17.71	72.06	-69.56	-58.29
p2r08b	-14.36	10.92	-12.68	39.53	17.65	39.86	-54.37	-43.54
p2r08c	-15.55	11.54	-13.48	40.9	18.38	41.72	-56.97	-46.04
p2r08d	-13.34	11.25	-11.42	43.19	18.17	43.88	-57.06	-46.05
p2r09a	2.42	10.49	3.23	70.84	18.1	71.08	-69.42	-57.64
p2r09b	-16.63	10.07	-15.48	35.32	16.95	35.27	-52.60	-41.56
p2r09c	-16.64	10.36	-15.27	37.34	17.46	37.49	-54.58	-43.25
p2r09d	-15.82	11.17	-14.06	40.64	18.03	41.2	-57.01	-46.07
p2r10a	2.23	9.99	2.93	70.57	18.02	70.61	-69.31	-56.89
p2r10b	-15.05	9.85	-13.78	38.58	17.18	38.62	-54.23	-42.60
p2r12a	3.73	10.75	4.62	72.44	18.23	72.62	-69.59	-57.96
p2r12b	-14.43	10.83	-12.96	37.55	17.85	37.69	-52.54	-41.27

Table 5.3 Comparison Arrhenius parameters between silicon hydrides and silicon nitrides at 298.15 K and 1 atm, A has units of $cm^3 \cdot mol^{-1} \cdot s^{-1}$ and s^{-1} for addition and elimination reaction, respectively

reaction	E_0 kcal·mol^{-1}	logA	Ea kcal·mol-1	Eo_r kcal·mol-1	Log A_r	Ea_r kcal·mol-1	ΔHRxn kcal·mol-1	Ref.
:SiH$_2$ + Si$_2$H$_6$	-12.7	-12.3	-10.2	41.1	13.7	43.0	-54.7	56
:SiH$_2$ + SiH$_3$NH$_2$	-14.85	10.97	-13.59	36.18	17.76	36.51	-51.91	p2r01b
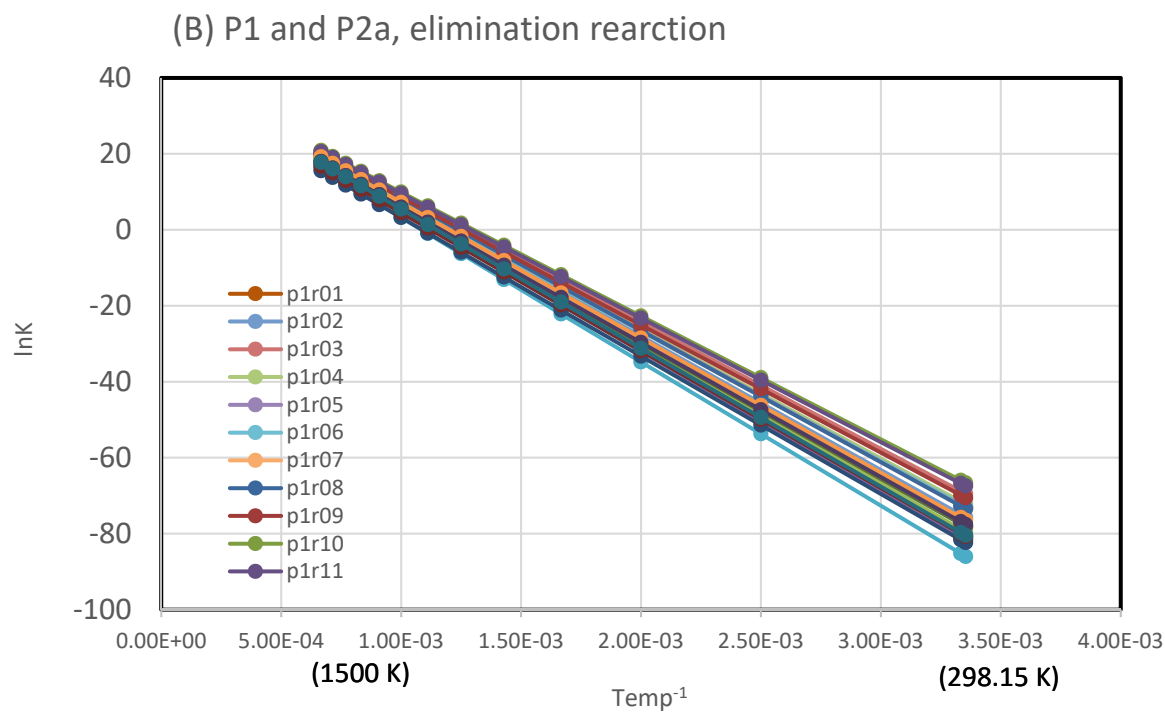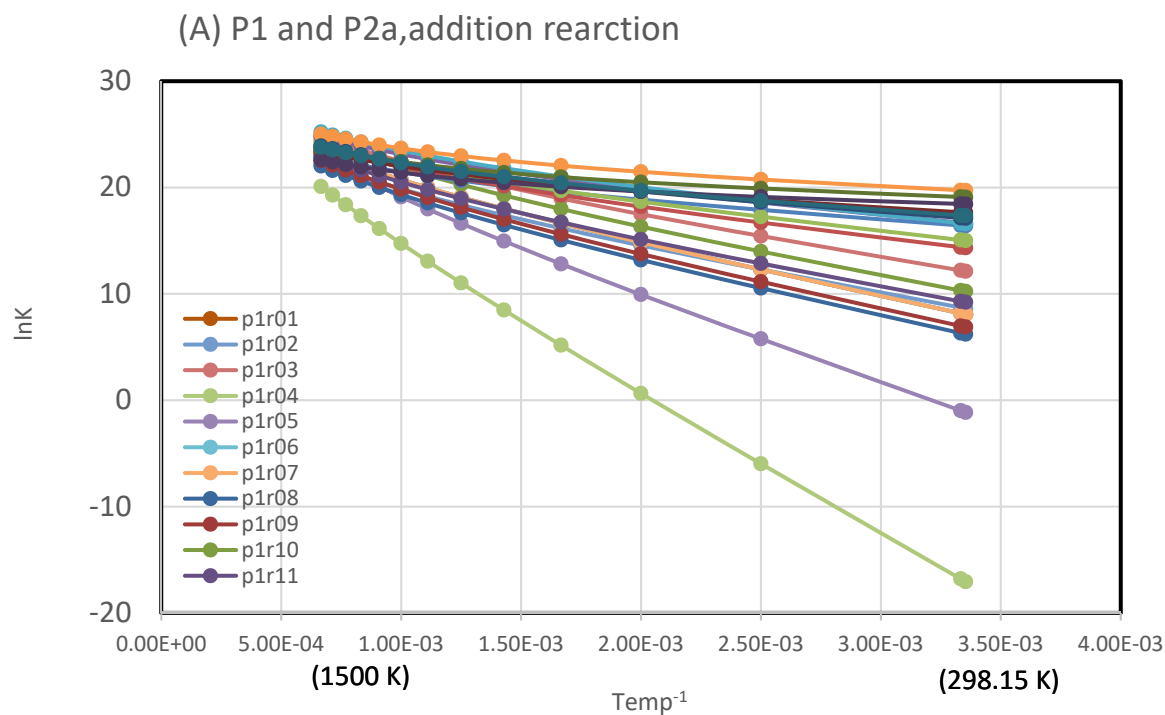
Figure 5.4 The Arrhenius plots of (A) P1 and P2a addition reactions, (B) P1 and P2a elimination reactions, (c) P2 b,c,d addition reactions, and (D) P2b,c,d elimination reactions.

(C) P2b,c,d, addition reactions
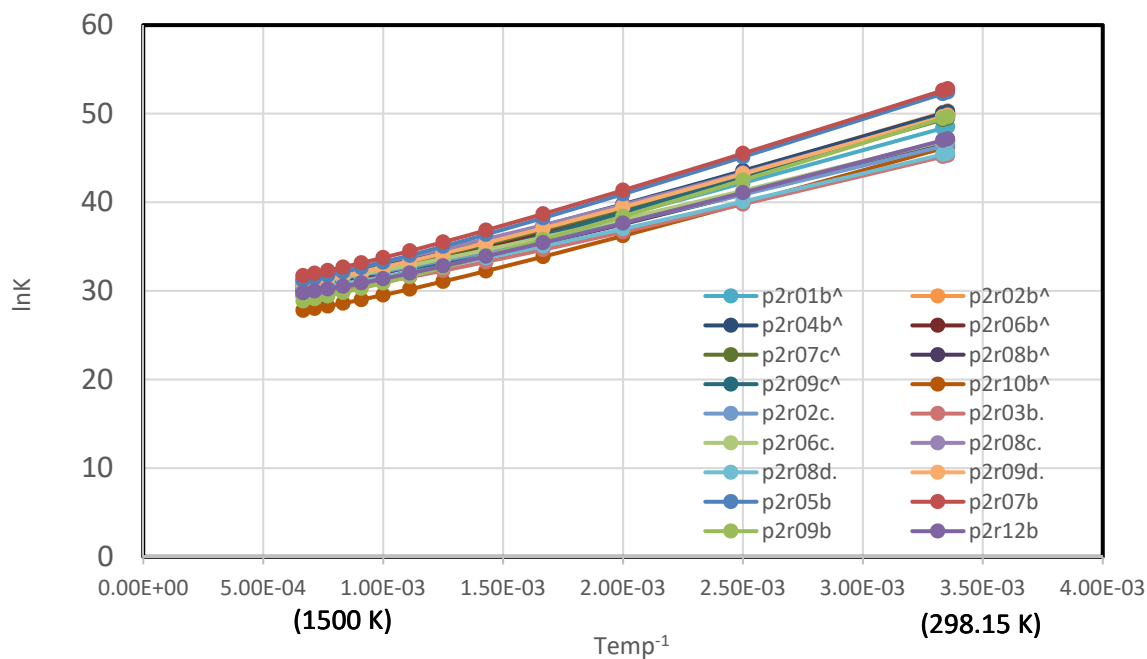
(D) P2b,c,d, elimination rearctions
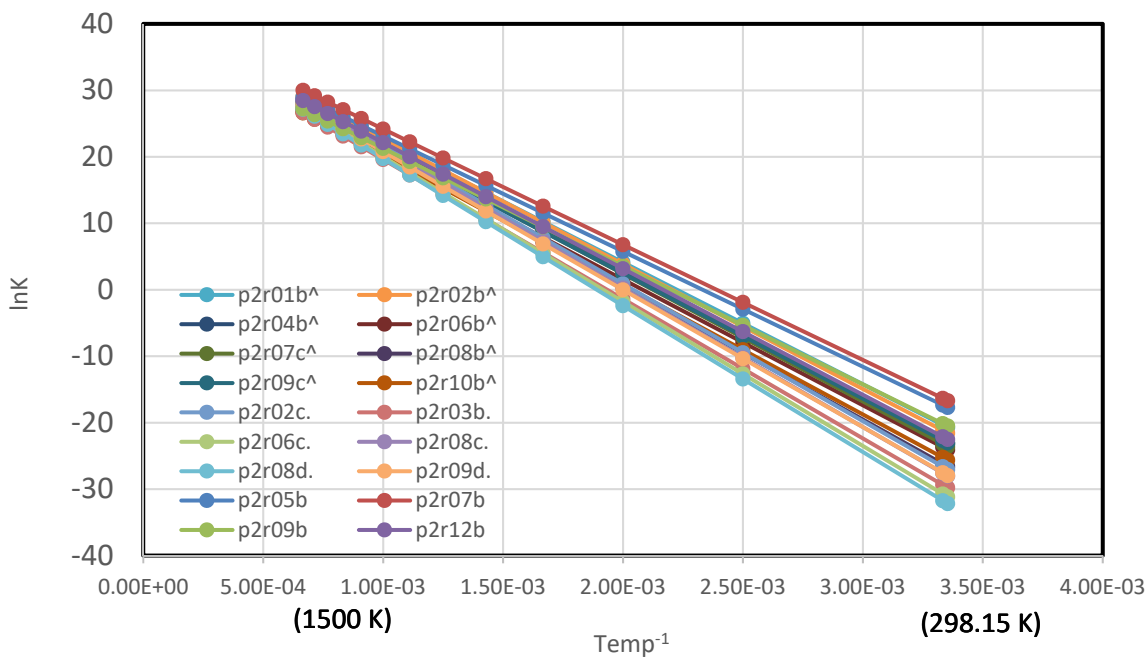
Figure 5.4 Continued.

5.3.3 Cyclization and Ring-opening Reaction

A total of 23 cyclization and ring-opening reactions of substituted silenes with nitrogen doping were mapped using G3//B3LYP, as depicted in **Figure 5.5**. Initially, a total of 31 reactions were sorted out according to the number of atoms in the reactants; 5 reactions for 4-membered acyclic species, 15 reactions for 5-membered acyclic species, and 11 reactions for 6-membered acyclic species. An acyclic molecule composed of three atoms cannot form a ring due to the nature of N with sp^2 hybridized orbital. Acyclic species consisting of 4, 5 or 6 atoms can form rings with n, n-1 or n-2 atoms (n = 4, 5, and 6). All rings that can be formed by 4-, 5-, and 6-membered acyclic species containing one N atom were included.

5.3.4 The Presence of a Cyclic Intermediate and Rate-determining Step

All cyclization reactions are 2-step reactions, except for 4-1, 5-01, 5-07, and 6-1, where N atom is the reaction center. Mapping of the cyclization/ring-opening potential energy surface showed two distinct barriers linked by a common cyclic intermediate, which is a stable hydrogen-bridged species for three-, four-, five- and six-membered ring formation reactions, respectively, as depicted in **Figure 5. 5.** Unfortunately, there is no experimental evidence for the intramolecular formation of a hydrogen-bridged intermediate for ring formation reactions of silicon nitrides. However, we have observed similar trends in our previous hydrogen migration reactions.[186]

To consolidate two-step of cyclization and ring-opening reactions into overall one transformation, we monitored reactions; 4-3, 5-2, and 6-3. In the same way for SiH_2 addition reactions, three microkinetic models were created as (1) a full model, (2) that the first step is rate-determining, and (3) that the second step is rate-determining. The model 3), the overall rate coefficient as $k = K_1 k_2$, where K_1 is the equilibrium coefficient for the first step, and k_2 is the rate coefficient for the second

step, is superior in predicting reaction dynamics of the selected reactions in the whole range of temperature. Hence, all cyclization and ring opening except for 4-1, 5-01, 5-07, and 6-1 were assumed to be controlled by the second step as the rate-determining step under pyrolysis conditions. All the transition states were located using the QST3 potential energy surface interpolation method for the rate-determining step. **Figure 5.7** shows the rate-determining transition state geometries for several key reactions of cyclization.

The cyclization between divalent Si and N does not change the reactive center greatly with the size of silicon nitride chains **(Figure 5.7a and e)**. However, in the reactive center between divalent Si and Si, the steric hindrance of the rings plays a role in cyclization and ring opening reactions **(Figure 5.7b, c, d, and e)**. The structure of the reactive center changes the most as the ring formed or dissociated becomes smaller. The larger ring size cyclization has the looser transition states, as depicted in **Figure 5.7.**

5.3.5 Internal Rotation Consideration

Due to high the rotation barrier, cyclic isomerization was not easy in certain molecules. For instance, in 4-membered acyclic reactants, there are three rotatable bonds; silicon-silicon, silicon-nitrogen, silicon-divalent silicon, nitrogen-divalent silicon. In order for the reactant to form a 4-memberd ring, the dihedral N1- Si4-Si7 -:Si10 (Si-Si sigma) bond of reactant 4-1 and the dihedral Si8-N6 -Si5-:Si1 of Reactant 4-2 should rotate to either around 0 or 180 degree point. To find how much energy is required for rotating each bonds, potential energy surface (PES) calculations for reaction 4-1, 4-2 and 4-3 were performed and summarized in **Table 5.4**. The rotational barrier was 16.29 and 1.13 kcal.mol^{-1}, for 4-1 and 4-2 reactant, respectively. The Rotational barrier of 4-1 is much higher than the 4-2, because the N-:Si atom groups in 4-1 create the significantly larger eclipsed interaction

than the Si-:Si groups in 4-2. Forming a ring means that the steric repulsion must be overcome, and it is predictable that reaction 4-1 with a large rotational barrier requires higher activation energy, which are 36.98 and -7.14 kcal.mol^{-1} in **Table 5.6**, respectively.
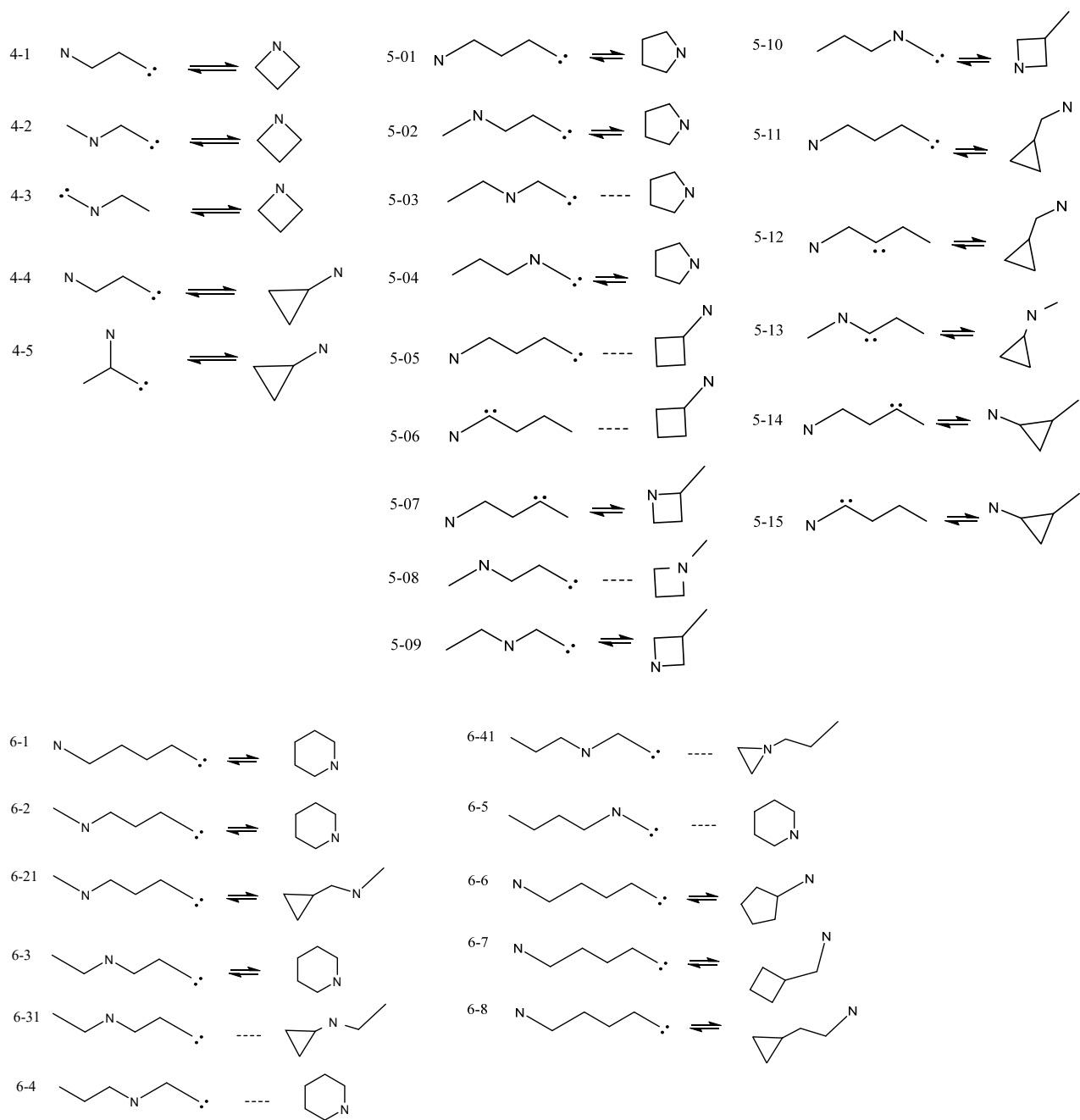
Figure 5.5 Cyclization and decyclization reactions. Unlabeled atoms in each molecules are Si atom, not C atom.

Figure 5.6 The number labels for reactant 4-1 and 4-2.

Table 5.4 Rotational barrier of silicon-nitrogen bonds. Other parts of molecule were frozen for PES calculation.

Reaction		Rotation barrier (kcal.mol^{-1})		
4-1	N-Si-Si-:Si	1.32	16.29	1.57
4-2	Si-N-Si-:Si	0.30	1.13	6.42
4-3	Si-Si-N-:Si	1.19	0.47	21.34

Table 5.5 Key Vibrational modes of reactant 4-1

Mode #	Freq	Vibrational types	
1	27.94	si7-si4 rotating	coupled with si10-si7-si4 bending mode
2	59.24	Si7-Si10 rotating	coupled with si7-si4-n1 bending mode
3	109.17	Si7-Si10 rotating	coupled with si4-n1 rotating
4	157.24	Si7-Si10 rotating	coupled with si7-si10 rotating
5	217.9	si4-n1 rotating	coupled with si10-si7 rotating
6	367.88	si7-si4 rotating	coupled with H3 stretching

181

In addition to the high rotational barriers, the fact that cyclization would occur in an appropriate angles and distances make it difficult to form the largest ring of reactants. This is because as the length of the chain increases, the number of bonds that require rotation increases. Especially in silicon nitrides, as more complexity is added along the position of the nitrogen atom in the main chain. It was confirmed that cyclization of the same mechanism did not occur in the examples of 5-03, 5-05, 5-06, 5-08, 6-31, 6-4, 6-41 , and 6-5 reaction, also included in **Figure 5.5**.

In the cyclization reactions, normal vibrational modes are treated as free rotations that are more appropriate. Because each rotatable corresponding bond between reactants, transition states, and products do not cancel out during the cyclization. However, due to the high rotational barriers in silicon nitrides, free rotation was rarely possible. Thus, we made an approximation that normal vibrational modes are one-dimensional hindered rotor then calculated rate coefficients for reactant 4-1, 4-2, 4-3, and 4-4. There was no difference in the rate coefficients between one-dimensional hindered rotor and harmonic oscillator except negligible difference in the reaction 4-2. This is because, it is difficult to treat only the rotational vibration separately from the coupled several vibrational modes consisted the same frequency. For easy understanding, the significant frequencies and their vibrational modes composition are represented in **Table 5.5**.

5.3.6 Kinetic of Cyclization and Ring-opening Reaction of Silicon Nitrides

A summary of Arrhenius parameters and the standard enthalpies of reaction for the conversion of the substituted amino silylene to a cyclic species is given in **Table 5.5**. The formation of a cyclic species from a substituted amino silylene is always exothermic. The formation of a cyclic silicon nitrides from a substituted amino silylene was more exothermic for the formation of larger rings as the heats of reactions ranged from -1.66 to -19.07 kcal mol^{-1} for three- membered ring formation reactions

and -21.94 to -38.07 kcal.mol^{-1} for four-membered ring formation reactions and -33.92 to -55.07 kcal mol^{-1} for five- and six-membered ring formation reactions. A plot of the temperature dependence of free energy values for the conversion of the substituted silylene to the cyclic silicon nitrides for several key reactions is provided in Figure 8. Free energy for the conversion of the substituted silylene to the cyclic species increase with increasing temperature, or the equilibrium shifts to favor substituted silylenes for all ring sizes except 3-membered ring. However, it can be said that there was little effect of temperature on Gibbs free energy of cyclization of silicon nitrides.

A cyclization reaction can be considered as a combination of a silylene addition reaction and a hydrogen migration reaction within a molecule. But, the difference is that the formation of a stable intermediate, the first step of cyclization, is associated with the torsional and scissoring normal vibrational models along the chain of silicon-silicon and silicon-nitrogen bonds. Since an amino silylene, which has a :Si-N bond within, also has an extra pi bond between :Si and N, either rotation or torsion are restricted. Because of these limitations, cyclization reactions are less desirable in amino siylenes with a :Si-N bond than in other amino silylenes.

Instantaneous selectivity is the ratio of the two reaction rates in parallel reactions, providing information on which reaction prevails in the system. Aforementioned, there is no concentration of reactants and it can vary depending on reaction system, we assumed that each comparable reaction have the same concentration and reaction order. The sensitivity of decyclization reactions can be observed by comparing reverse reactions that has the same reactant (reverse direction) such as 4-1, 4-2, and 4-3. All decyclization reactions are endothermic processes, their rate coefficients are much smaller than that of the reverse reactions (cyclization). Decyclization of ring-type silicon nitrides starts with breaking a Si-Si or Si-N bond, breaking a Si-Si bond is always easier than breaking a Si-N bond. A Si-Si bond located the furthest from the N is the weakest bond among Si-Si bonds, due to the least hyperconjugation effect. In the comparison of rate coefficients of reverse reactions of 4-1, 4-2, and 4-

3, the rate coefficient of 4-1 decyclization, which should break the Si-N bond and requires the highest activation energy, is the smallest value from 5.62E $^{-38}$ to 3.08E^3 at from 198.15 K to 1500 K and the temperature dependence is also the strongest.

Among Si-Si bonds, the rate coefficient of 4-2 reaction, that is not adjacent to the N atom, is from 3.56E-10 to 7.48E8 at the temperature range from 298.15 K to 1500 K, is much larger than that of 4-3 reaction, which is from 5.53E-22 to 1.58E6 at the temperature range from 298.15 K to 1500 K. The decyclization will proceed smoothly with the order of 4-2, 4-3, and 4-1 in all temperature ranges, and the other ring species showed the same trend.
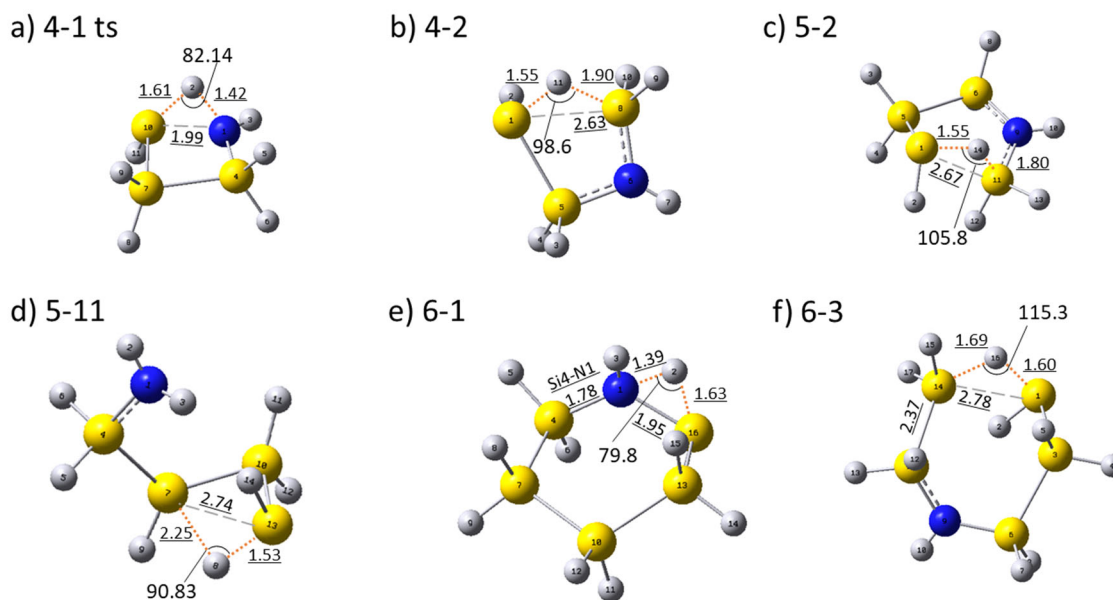
Figure 5.7 B3LYP/6-31G(d) optimized geometries of the lowest-energy conformer of the rate-determining transition state for several key reactions in cyclization and ring-opening reactions.
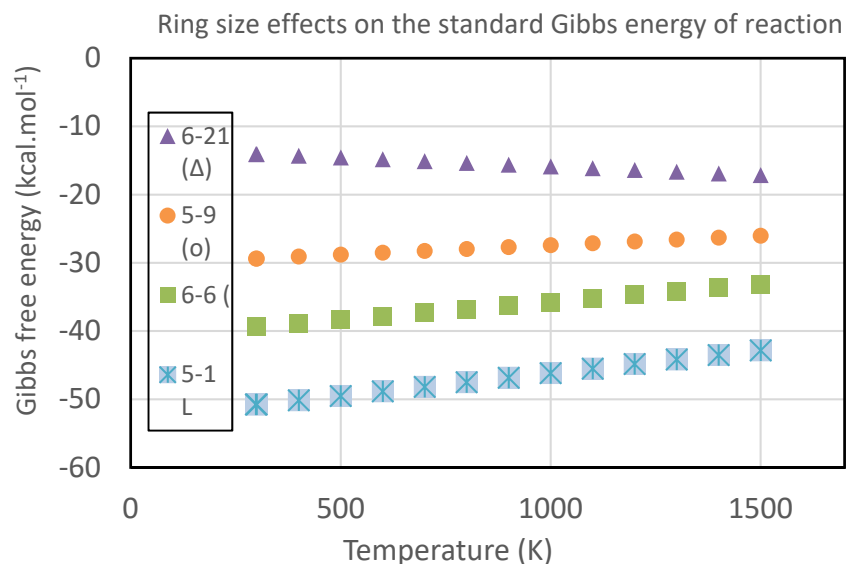
Figure 5.8. Ring size effects on the standard Gibbs free energy of reaction for several key cyclization reactions.

Table 5.6. Arrhenius parameters of cyclization and ring-opening reaction of silicon nitrides at 298.15 K and 1atm, A has units of s^{-1} for both direction of reaction

reaction	E_0 kcal·mol^{-1}	logA	E_a kcal·mol^{-1}	E_{o_r} kcal·mol^{-1}	Log A_r	E_{a_r} kcal·mol^{-1}	ΔH_{Rxn} kcal·mol^{-1}	ΔG kcal·mol^{-1}
4-1 L	20.34	10.29	18.8	69.14	13.54	69.35	-50.13	-46.06
4-2	-6.24	10.2	-7.14	30.66	13.4	31.19	-38.07	-33.95
4-3	25.1	11.44	24.67	46.4	12.98	46.74	-21.94	-19.96
4-4	-0.57	11.54	-0.54	16.12	12.79	16.45	-17.02	-15.29
4-5	-2.09	11.93	-2.08	15.02	13.08	15.46	-17.53	-15.96
5-1	32.29	13.36	32.45	68.98	13.06	69.12	-36.78	-37.09
5-2	-11.63	9.45	-12.58	36.1	12.55	36.5	-48.84	-44.82
5-4	11.47	10.51	10.78	44.62	12.48	44.86	-33.92	-31.37
5-7	18.94	10.61	17.79	65.48	13.53	65.63	-47.63	-43.83
5-9	-0.09	12.62	0.24	29.95	13.23	30.45	-30.23	-29.38
5-10	22.34	11.04	21.99	46.42	12.94	46.85	-24.7	-22.25
5-11	2.03	12.81	2.55	14.92	12.38	15.12	-12.7	-13.17
5-12	-4.94	10.75	-5.31	1.17	12.82	1.6	-6.81	-4.09
5-13	19.75	12.19	20.25	21.75	12.54	22.18	-2.1	-1.47
5-14	-5.34	11.43	-5.19	13.16	12.86	13.51	-18.8	-16.76
5-15	20.23	12.84	21.23	21.88	13.67	22.7	-1.66	-0.35
6-1	14.3	10.56	13.14	68.6	13	68.42	-55.07	-51.94
6-2*	-2.17	10.52	-2.4	38.68	12.42	39.05	-41.4	-38.85
6-21	3.22	13.43	3.91	16.86	12.87	17.21	-13.43	-14.08
6-3	-12.2	8.82	-13.29	39.41	12.6	39.8	-52.79	-47.91
6-6	-7.91	11.69	-7.67	32.74	12.82	33.23	-40.92	-39.37
6-7	0.11	12.35	0.42	33.28	13.18	33.77	-33.34	-32.21
6-8	3.48	13.33	4.19	17.04	13.06	17.45	-13.38	-13.64

5.3.7 Kinetic Parameter Prediction Model Generalization

Regression Analysis for SiH₂ Addition and Elimination Reactions

To develop a model for predicting activation energy, the activation energies of all reactions were plotted against the corresponding enthalpy of the reactions in **Figure 5.9**. The range of activation energies is apparently distinct according to the type of silylene addition reactions. Both silylene addition and elimination reactions of amino silylenes; group (P2-i) and group(P2-ii) have a strong linear correlation with the enthalpy of the reaction. silylene addition and elimination reaction of silicon nitride were captured well by two regression models with different ZPE corrected barriers. The Evans−Polanyi parameters, E_o, and α, were calculated from linear regression with the least-squares method to maintain thermodynamic consistency. The generalized SiH₂ addition and elimination reaction model predicted the activation energy with a 99% R square value. The parameters were obtained using linear regression analysis for all reactions in **Table 5.4.**
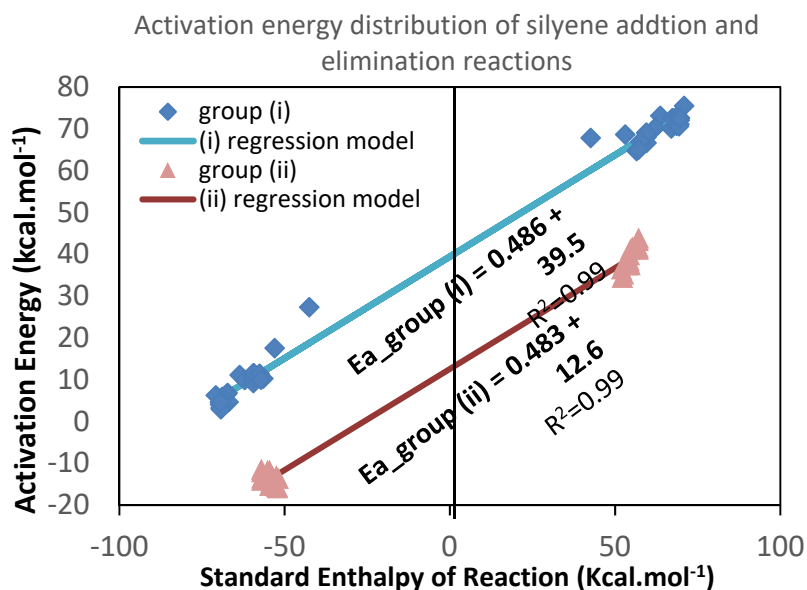
Figure 5.9. Activation energy distribution and regression models for silylene addition and elimination reactions. Blue diamond represents the reactions between divalent Si and N, and orange triangle represents the reactions between divalent Si and Si.

186

Regression Analysis for cyclization and ring-opening reactions

The activation energies of all cyclization reactions were plotted against the corresponding enthalpy of the reactions in **Figure 5.10**. Although the activation energies are widespread, we were able to find regression models for each ring formation on the size of the rings, summarized in **Table 5.8**. Cyclization and decyclizaiton reaction of silicon nitride were well-captured by four regression models. The activation barrier of each group categorized by the ring size has a strong linear correlation with the enthalpy of the reaction. The Evans−Polanyi parameters, E_o, and α, were calculated from linear regression with the least-squares method to maintain thermodynamic consistency. The generalized cyclization and ring-opening reaction model predicted the activation energy with a 99% R square value.

Validation of Regression parameters

k-Fold Cross-Validation of silylene addition & elimination reaction

The numerous case of the atomic arrangement of silicon nitrides made it difficult to construct a validation set and remain complex in reactions of silicon nitrides. Hence k-fold cross-validation is conducted to evaluate our regression models for group (P2-i) and group (P2-ii). The k value are 11 and 9 for group (P2-i) and group (P2-ii), respectively. The results of both k-fold cross validation analysis are summarized with the mean of the model, minimum, maximum and standard deviation in **Table 5.6**.

To check the variance between the regressed model and the averaged model from k-fold cross-validation, we also conducted ANOVA tests. In the result of the ANOVA test, the F test statistics is less than the F critical value, which are 1.36E -06 and the 18.51, respectively. In addition, the both p-value of ANOVA test were 0.999, which indicated there is no sufficient evidence to distinguish the regressed model and averaged model.

Table 5.7. k-Fold cross-validation analysis result of generalized model for predicting activation energy for the silylene addition and elimination reaction in silicon nitrides.

A) Group i (k=11)

	E_0	α
Min	38.811	0.484
Average	39.398	0.486
Max	39.832	0.489
variance	0.088	0.000
standard deviation	0.297	0.002
standard error	0.090	0.001

	E_0	α
regression	39.46	0.49
k-fold (average)	39.40	0.49

Anova: Single Factor

SUMMARY

Groups	Count	Sum	Average	Variance
regression	2	39.948	19.974	759.568
k-fold (average)	2	39.884	19.942	757.055

ANOVA

Source of Variation	SS	df	MS	F	P-value	F crit
Between Groups	0.001	1	0.001035	0.000001	0.999174	18.512821
Within Groups	1516.6	2	758.311895			
Total	1516.6	3				

B) Group ii (k=9)

	E_0	α
Min	12.18	0.48
Average	12.52	0.48
Max	12.75	0.49
variance	0.04	0.00
standard deviation	0.21	0.00
standard error	0.06	0.00

	E_0	α
regression	12.56	0.48
k-fold (average)	12.52	0.48

Anova: Single Factor

SUMMARY

Groups	Count	Sum	Average	Variance
Row 1	2	13.040	6.520	72.886
Row 2	2	13.002	6.501	72.418

ANOVA

Source of Variation	SS	df	MS	F	P-value	F crit
Between Groups	0.00037	1	0.00037	0.00001	0.99841	18.51282
Within Groups	145.304	2	72.65195			
Total	145.304	3				

k-Fold Cross-Validation of cyclization and ring-opening reaction

The numerous case of the atomic arrangement of silicon nitrides made it difficult to construct a validation set and remain complex. Even cyclization reactions are subcategorized into four group by the size of ring, the number of each training set for validation was not sufficient. However, k-fold cross-validations were conducted to evaluate each regression models. The k value for each group of cyclization reactions are 4, 5, 5, and 4 for 3 membered-ring, 4membered-ring, 5 & larger rings and substituted silyl amine (N and :Si are located at the end of the chain). The results of each k-fold cross validation analysis are summarized with the mean of the model, minimum, maximum and standard deviation in **Table 5.8.**

To check the variance between the regressed model and the averaged model from k-fold cross-validation, we also conducted ANOVA tests. In the result of the ANOVA test, all F test statistics

is less than the corresponding F critical value, and all the p-value of ANOVA tests was higher than 0.97, which indicated there is no sufficient evidence to distinguish the two models.
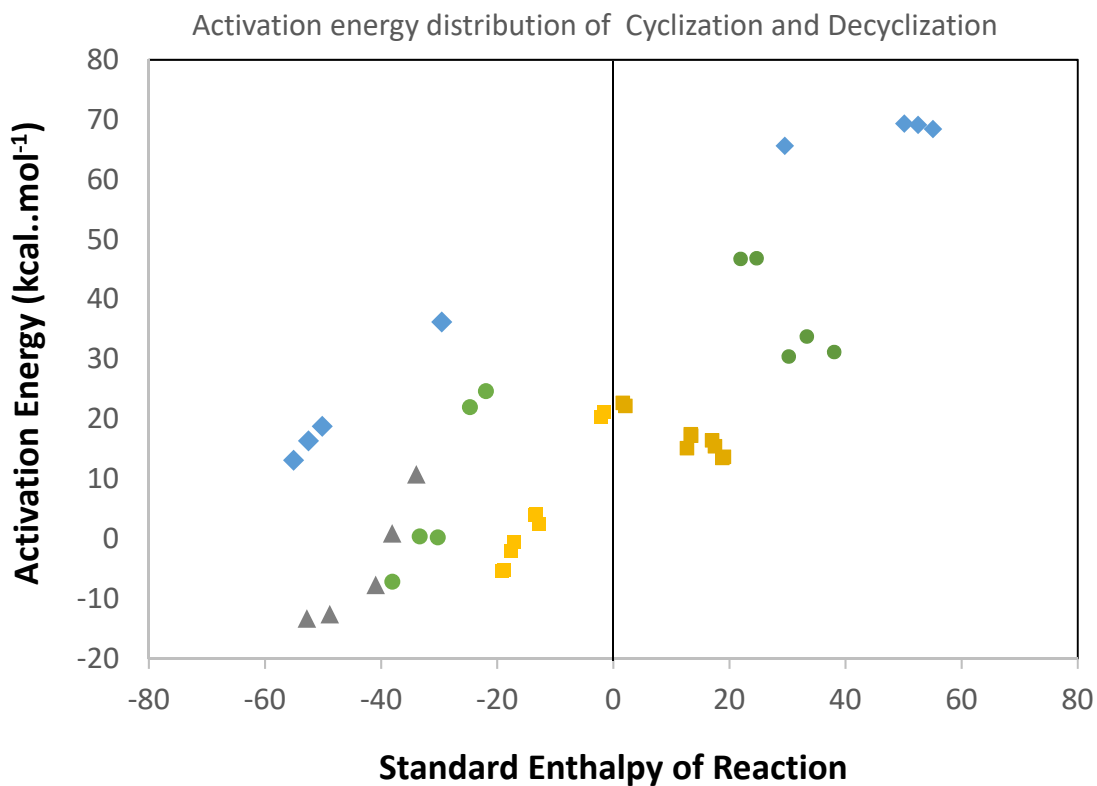
Figure 5.10. Activation energy distribution for cyclization and ring-opening reactions of silicon nitrides. Blue diamond represents the largest ring formation from the reactants, yellow square represents 3-membered ring formations, green circle represents 4-membered ring formations, and gray triangle represents 5-memberd or larger ring formations.

Table 5.8. Generalized model for predicting activation energy for the cyclization and ring-opening reactions in silicon nitrides

	α (cyclization)	α '(ring-opening)	E_0	R^2
3-member ring	1.49	-0.49	23.36	0.99
4-member ring	2.12	-1.12	70.90	0.96
5 or larger ring	1.21	-0.21	47.48	0.98
N---------Si:	0.87	0.13	62.12	1.00

Table 5.9. k-Fold cross-validation analysis result of generalized model for predicting activation energy for the cyclization and ring-opening reactions in silicon nitrides.

k=4

3-membered ring	α	E0
Min	1.47	23.21
Average	1.49	23.36
Max	1.50	23.62
variance	0.00	0.02
standard deviation	0.01	0.15
standard error	0.00	0.07

	α	E0
regression	1.49	23.36
k-fold (average)	1.49	23.36

Anova: Single Factor

SUMMARY

Groups	Count	Sum	Average	Variance
Row 1	2	24.854	12.427	239.210
Row 2	2	24.846	12.423	239.175

ANOVA

Source of Variation	SS	df	MS	F	P-value	F crit
Between Groups	1.64696E-05	1	0.000	0.0000001	0.9998145	18.513
Within Groups	478.3846637	2	239.192			
Total	478.3846802	3				

k=5

4-membered ring	α	E0
Min	1.96	65.21
Average	2.14	71.78
Max	2.47	80.04
variance	0.03	23.07
standard deviation	0.17	4.80
standard error	0.08	2.15

	α	E0
regression	2.12	70.90
k-fold (average)	2.14	71.78

Anova: Single Factor

SUMMARY

Groups	Count	Sum	Average	Variance
Row 1	2	73.021	36.511	2365.695
Row 2	2	73.922	36.961	2425.264

ANOVA

Source of Variation	SS	df	MS	F	P-value	F crit
Between Groups	0.2029	1	0.203	0.00008	0.993	18.513
Within Groups	4791	2	2395.480			
Total	4791.2	3				

k=5

5 or larger ring	α	E0
Min	0.73	24.81
Average	1.20	46.90
Max	1.54	60.64
variance	0.07	145.40
standard deviation	0.26	12.06
standard error	0.12	5.39

	α	E0
regression	1.21	47.48
k-fold (average)	1.20	46.90

Anova: Single Factor

SUMMARY

Groups	Count	Sum	Average	Variance
Row 1	2	48.686	24.343	1070.598
Row 2	2	48.100	24.050	1044.312

ANOVA

Source of Variation	SS	df	MS	F	P-value	F crit
Between Groups	0.085904956	1	0.086	0.00008	0.994	18.513
Within Groups	2114.91012	2	1057.455			
Total	2114.996025	3				

k=4

N--------Si:	α	E0
Min	0.85	61.21
Average	0.94	65.81
Max	1.17	77.66
variance	0.02	47.01
standard deviation	0.13	6.86
standard error	0.07	3.43

	α	E0
regression	0.87	62.12
k-fold (average)	0.94	65.81

Anova: Single Factor

SUMMARY

Groups	Count	Sum	Average	Variance
Row 1	2	62.994	31.497	1875.603
Row 2	2	66.752	33.376	2103.838

ANOVA

Source of Variation	SS	df	MS	F	P-value	F crit
Between Groups	3.5296	1	3.530	0.002	0.970	18.513
Within Groups	3979.4	2	1989.721			
Total	3983	3				

5.4 Conclusions

The Rate coefficients and Arrhenius parameters for the silylene addition & elimination reaction and cyclization and decyclization reactions in silicon nitride species have been calculated for 40 silylene addition & elimination, 23 cyclization and ring-opening reactions using G3//B3LYP, statistical thermodynamics, and conventional transition state theory.

The overall silylene addition and elimination reactions were categorized in two sub-group; (i) reaction between divalent Si and N and (ii) reaction between divalent Si and Si. The silylene addition reactions in the group (2-i) are one-step reaction but, the reactions in the group (2-ii) were two-step reactions through a stable intermediate to a saturated silicon nitride product. It was observed that the TS shape of the group (P2-i) and group (P2-ii) was slightly different.

For the silylene addition reaction, the different conformation of the reactant was not a significant factor, unlike the hydrogen transfer reaction. Adding various substituents to either side of the reactive center does not make a significant structural difference in transition states. SiH_2 insertion to silicon nitrides is also a barrierless reaction and a fast reaction, SiH_2 addition to a Si-H bond in silicon nitrides has been found to have a much higher A factor than the reaction to a Si-H bond in disilane does, the silylene addition reaction to silicon nitrides will be superior in silane and ammonia pyrolysis. For the elimination reaction, classic Arrhenius behavior is observed for reactions for both P1 and P2, the activation energies of the group (P2-i) are twice as higher as one of the group (P2-ii). From the comparisons of instantaneous selectivity, the silylene insertion to a Si-H bond in silicon nitrides always dominates the insertion to a N-H bond in the whole range of temperature.

All cyclization and ring opening except for 4-1, 5-01, 5-07, and 6-1(reaction center is between N and Si:) were two-step reactions though a stable intermediate to a saturated silicon nitride product and were controlled by the second step as the rate-determining step under pyrolysis conditions. The cyclization between divalent Si and N does not change the reactive center greatly with the size of

silicon nitride chains while the steric hindrance of the rings, in the reactive center between divalent Si and Si, plays a role in cyclization and ring opening reactions. The high rotational barriers, and the fact that most of the vibrational frequencies are coupled with several different vibrational modes, make atoms challenging to rotate. Thus, the internal rotation effect was negligible in silicon nitrides. All decyclization reactions are endothermic processes, their rate coefficients are much smaller than the reverse reactions (cyclization). Decyclization of ring-type silicon nitrides starts with breaking a Si-Si or Si-N bond, breaking a Si-Si bond is always easier than breaking a Si-N bond.

In order to predict activation energy, the generalized models for Silylene addition-elimination and cyclization-decyclization reactions were proposed with the Evans−Polanyi parameters, E_o, and α, calculated from linear regression with the least-squares method. Both generalized models predicted the activation energy with a 99% R square value.

Chapter 6

Silyl Radical Reaction in Plasma Condition

6.1 Introduction

Silicon nanoparticle formation under plasma conditions is governed by reactions between cations, anions, and neutral molecules. Under low-pressure non-thermal plasma conditions, three dominant phenomena include particle nucleation, particle surface growth, and coagulation. The study herein will focus on particle nucleation and growth involving the formation of small clusters, which is dominated by reactions between anions and neutral molecules or radicals. Particle surface growth predominantly involves reactions of neutral molecules or radicals at the surfaces of negatively charged nanoparticles. Beyond the scope of this study, coagulation is then dominated by collisions between very small neutral nanoparticles and charged nanoparticles.[223]

Anionic species are very important because these species play a key role in nanoparticle formation in the plasma.[224-228] Reactions involving anions can increase the average residence time of the clusters and thus enable growth to a critical size.[226] Fridman et al. presented that small particle generation begins mainly with SiH_3^- negative-ion formation through theoretical modeling.[227] This negatively charged cluster growth is due to ion-neutral molecular reactions. When the particle size reaches a critical value (about 2nm at room temperature), the chain reaction of cluster growth becomes much slower and is finally stopped by the ion-ion recombination process.[227] The efficient negative-ion formation could be due to enhanced electron attachment to one or more radicals, vibrationally excited states relative to the ground state, or electronically excited states produced in the discharge.[228]

Numerous radio-frequency driven non-equilibrium plasma cases have been popularly applied for the chemical deposition processes involving silicon, and modeling of those experimental processes has been suggested.[229] Bouhekkaa et al. conducted a Monte-Carlo simulation of the growth of hydrogenated amorphous silicon (a-Si:H) thin films deposited by plasma enhanced chemical vapor deposition (PECVD).[230] The goal of this model was to predict the bulk and the surface properties of films (i.e., hydrogen content, dangling bonds, surface roughness) with varying thicknesses and deposited at different substrate temperatures. The team determined a correlation between the average thickness and the radical incident flux of SiH_3. Barwe et al. showed that the mode of operation of the plasma depends on the means by which the electric field is applied, the gas flow, and the varying gas mixture or feed ratio.[231] With regard to silicon doping, Bartlome et al. observed different catalytic effects from trimethyl boron (TMB) and disilane under silane plasma conditions by clarifying the silane consumption efficiency and depletion fraction.[232] The use of a low TMB flow rate contributed to a higher deposition rate, but the use of a small Si_2H_6 flow rate contributes to a lower deposition rate.

Experiments[224, 225, 233-236] and modeling[237-239] of ground states of ionic and neutral species under plasma conditions have been studied, but studies on excited states with regard to reaction pathways are lacking. One study presented evidence that electron attachment to high-lying electronically excited states (i.e., high-Rydberg states) of silane have much larger electron attachment cross sections than radicals or vibrationally excited states.[228] Thus, the high-Rydberg states could be mainly responsible for the presence of large negative-ion densities in silane discharges.[228]

Computational studies offer an alternative (not necessarily an easier) approach to understanding and harnessing such complex reaction networks.[240] Computer simulated investigations are especially demanding in this case and special attention is needed on the methods to be employed and the reaction network to be considered. The goal of this work is to report electronic structure data (ground and several excited electronic states) for the mono-silicon species $SiH_x^{0,+,-}$ (x = 0 − 4) at high-

level computational methods. This work is our first effort to provide useful information with the inclusion of excited states analysis for the elucidation the initial steps of silicon nanoparticles formation under plasma conditions, where previous efforts were largely focused on non-plasma conditions and electronic ground states.[55, 57]

6.2 Computational Methodology

Multi-reference calculations

Density Functional Theory (DFT) calculations (CAM-B3LYP functional)[241] were initially applied to obtain the optimal geometry for the ground state of the reported species. Multi-reference wavefunctions were then applied to solve the electronic Schrödinger equation. The complete active space self-consistent field (CASSCF) reference wavefunction was constructed by allotting all valence electrons in molecular orbitals composed of the 3s, 3p, 4s, 4p, and 3d atomic orbitals of silicon and the 1s of each hydrogen. This extended space was necessary for the study of higher energy excited states. The internally contracted multi-reference configuration interaction (MRCI) technique[242] was subsequently employed to improve the accuracy of our wavefunction, where any one or two valence electrons are promoted in the virtual orbital space. Additionally, the Davidson correction was added to the MRCI energy (MRCI+Q) to obtain part of the remaining electron correlation. In cases of single reference wavefunctions (large coefficient of the primary electron configuration in the MRCI expansion), we performed the more accurate coupled cluster singles, doubles, and perturbative triples [CCSD(T)] method. [243, 244] A restricted Hartree-Fock reference wavefunction was used for these calculations. For the diatomic species, we obtained harmonic frequencies using numerical Hessian elements calculated with steps of 0.01 bohr. Gaussian 16[90] was used for the DFT calculations and MOLPRO2015[245] was used for all other calculations. The IboView software was used to visualize the molecular orbitals.[246]

Kinetic study of substituted silylene radicals with silane

Quantum chemical calculations were performed with Gaussian 16. Geometry optimizations are carried out with the B3LYP functional and 6-31G(d) basis set. All electronic energies for silyl radicals, silanes, molecular hydrogen, silylenes, and transition states, and adducts were calculated with the G3//B3LYP method. Frequency analysis were conducted to characterize the stationary points as either equilibrium structures or transition structures with one imaginary frequency. The harmonic frequencies and zero-point energy (ZPE) were scaled by factors of 0.96 and 0.98, respectively, to account for anharmonicity in the normal vibrational modes as suggested by Scott and Radom. The potential energy surface interpolation method, the Synchronous Transit-guided Quasi-Newton method (QST3), was used for finding transition states. Each transition state was confirmed that it has one imaginary frequency and follows the intrinsic reaction coordinate to the desired reactants and product.

Using conventional statistical thermodynamics, partition functions based on the harmonic oscillator and rigid rotor approximations were used to calculate thermodynamic and kinetic properties. Rate coefficients were calculated by conventional transition state theory[102] according to the ***equation*** (**6.1**) at 1 atm assuming an ideal gas state,

$$k^{TST}(\text{T}) = n_d \tilde{k} = n_d \Lambda \exp\left(\frac{\Delta S^{\neq}}{R}\right) exp\left(\frac{-\Delta H^{\neq}}{RT}\right) \qquad \boldsymbol{eq(6.1)}$$

Where Λ, defined in ***equation*** (**6.2**),

$$\Lambda = \kappa(\text{T}) \frac{k_B T (V_m^0)^{-\Delta n}}{h} \qquad \boldsymbol{eq(6.2)}$$

$\tilde{k}$ is the single event rate coefficient: $\kappa(\text{T})$ is the Wigner tunneling correction[155] at temperature T; k_B is Boltzmann's constant; h is Planck's constant; $\Delta H^{\neq}$ is the enthalpy of activation; Δn is the change in the number of moles going from the reactant to the transition state (i.e., zero in both directions for isomerization); and n_d is the reaction path degeneracy, or number of single events. $\Delta H^{\neq}$ and $\Delta S^{\neq}$ are calculated using standard formulae.[102]

The single event parameters of the Arrhenius relationship, Ã and E_a, were obtained by fitting ln k versus T^{-1} over the temperature range 298-1500 K. This calculation was performed using the CalcK script previously employed by our group for both silicon hydride and silicon nitride chemistry [55-57, 186, 217, 218]. The rate coefficient is important for constructing a mechanistic model.

6.3 Results and Discussions

6.3.1 Multi-reference Calculations

We investigated the ground and excited states of mono-silicon hydrides ($SiH_{1-4}^{0,\pm}$) using multi-reference calculations.[247] Our study elucidates their electronic structure and provides accurate energetics. Our calculation results will be valuable for the study of reactions between mono-silicon hydrides towards the synthesis of silicon nanoparticles under low temperature plasma conditions. From the technical standpoint, we found that the inclusion of the 4s, 4p, 3d orbitals of silicon besides its valence 3s, 3p orbitals is essential for correct and smooth convergence of the calculations. In addition, we demonstrated that diffuse basis functions are important and that aug-cc-pVTZ is a good compromise between accuracy and computational cost.

From the electronic structure point of view, the density of low-lying electronic states (number of electronic states per energy unit) generally drops as we add hydrogen atoms to the system. For example, there are 16 states for SiH_2 within 7 eV, five states for SiH_3 and just one state for SiH_4. The lowest excitations for cationic and neutral species pertain to excitations within localized silicon orbitals, then excitations from the bonding SiH orbitals to localized silicon orbitals follow, and finally electronic promotions to Rydberg silicon orbitals (4s, 4p) occur. The population of the latter orbitals happen at around 4 eV for Si, 4.5 eV for SiH, 6 eV for SiH_2, 5.5 eV for SiH_3, and 9.0 eV for SiH_4. The

latter is unstable and dissociates to $SiH_3 + H$. The same energy threshold for SiH_2^+ and SiH_3^+ is slightly higher (7 and 9 eV) than their neutral species, and SiH_4^+ dissociates spontaneously to $SiH_2^+ + H_2$. The anionic species bear only a few stable states with respect to ionization. SiH^- has three states, SiH_2^- and SiH_3^- have one, while SiH_4^- dissociates to $SiH_2^- + H_2$.

6.3.2 Kinetic Study of Substituted Silylene Radicals with Silane

The reactions that can increase the average residence time of the clusters[248] and enable their growth to a critical size are silylene anion–neutral silane reactions and silyl anion–neutral silane reactions.

Hollenstein et al. concluded that the anionic pathway is the main pathway for generating nanoparticles in silane plasmas.[249] Howling et al. also experimentally observed the existence of anionic species with various sizes ranging from monosilicon anions to nanometer clusters and inferred that anions are the initial precursors of particles for plasma conditions. Bhandarkar et al studied the two classes of anion–neutral particle growth reactions.[250] Both anion-neutral reactions result in higher-order homologs of silylene anion or silyl anion clusters by eliminating molecular hydrogen.
Truhlar et al. elucidated the detailed mechanisms of the first step of anionic-neutral polymerization under the plasma conditions at the molecular level and calculated reaction rates.[251]

It is important to understand the entire reaction system in order to control the desired species to a targeted size. Because the rate coefficient is important for constructing a mechanistic model. For growing nanoparticles, the anionic neutral reaction is dominant, but polymerization also occurs by the neutral-neutral molecule reaction, which is poorly understood compared to the anionic-neutral reaction. In particular, the Langevin rate coefficient is mostly used for the rate coefficient of neutral reactions

and the quantum calculation result has not been reported yet to our best knowledge. In addition, ring formation, another route of particle clustering, mostly occurs through neutral reactions, elucidating the neutral reaction mechanism is inevitable.

The objective of this chapter is to understand the mechanisms of neutral radical-neutral molecule reaction at the molecular level and to investigate differences by comparing them with the anionic radical-neutral molecule reaction mechanism.

Both the thermodynamic and kinetic feasibilities should be taken into account in order to propose a reasonable reaction pathway. Since there is little experimental information to guide the selection of a pathway, we postulated all possible pathway from the reactions of two silicon radicals (neutral and anionic) and monosilane. Therefore, to find chemically rational mechanisms, we counted primarily on the exploration of thermodynamic and kinetic requirements for generating possible intermediates. The reactions we studied are given in **Figure 6.1**. [252]

Neutral	H_3SiSiH_2 +	SiH_4	$\longleftrightarrow$	$H_3SiSiHSiH_3$ + H_2

| Anionic | $H_3SiSiH_2^{\ominus}$ + | SiH_4 | $\longleftrightarrow$ | $H_3SiSiHSiH_3^{\ominus}$ + H_2 |
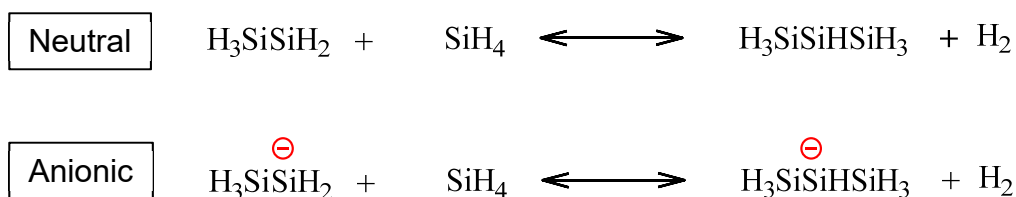
Figure 6.1 Neutral and Anionic disilyl radicals reactions with silane.

The neutral radical and silane reaction is a three-step of reaction that has two different paths for the first and third steps. The first step starts with migration of a H atom from silane to disilyl radical and results in a silyl radical and disilane. The first step is the free radical reaction that involves a

hydrogen abstraction from silane and addition to radical Si atom of disilan-1-yl radical. All neutral radical reaction of this study occurs by the propagation of electron. In particular, depending on the phase of propagation, there are two different routes to produce disilane and silyl radical. In the second step, the silyl radical offers the free electron to a Si in disilane. The Si conveys the free electron to one of H bonded to the radical Si and results in trisilane and hydrogen radical. At the last step, the hydrogen radical can abstract any H atom from trisilane resulting in molecular hydrogen and trisilyl radical. Further 1,2 hydrogen migration with in trisilyl radical could occur to find a isomer with lower energy. Neutral radical reaction mechanisms are depicted in the **Figure 6.2**

For disilyl anion and silane reaction, there are three pathways to form trisilyl anion radicals. The reaction begins with the abstraction of a H atom from disilan-1yl anion to H atom from silane to form trisilyl anion and molecular hydrogen. Here, according to which H atom from disilan-1-yl, the type of trisilyl anion can be determined. When a H atom from silane approached to a H atom bonded with negative formal charged Si, trisilan-2-yl anion will be formed, while a H atom from silane approached to a H atom bonded with neutral Si will form trisilan-1-yl anion and molecular hydrogen. These two reactions are an one-step reaction which passes through a 4-centered transition structure. We labeled these reactions as m and t, respectively in **Figure 6.3**. The other route is an two-step reaction which starts with the abstraction of Hydrogen atom from SiH_4 by the negatively charged Si atom from disilan-1-yl anion to form a trisilyl radical, Si_3H_9 which has no negative formal charge. Then the second step is the formation of molecular hydrogen and trisilyl anion from the trisilyl radical, Si_3H_9. The negatively charged (formal charge) trisilyl anions which are formed by aforementioned reactions could react with another silane molecule and thus produce higher order silyl anions. In order to get an isomer of trisilyl anion with lower energy, 1,2 hydrogen migration from trisilan-1-yl anion to trisilan-2-yl anion could proceed. These reaction mechanisms are depicted in the **Figure 6.3**.
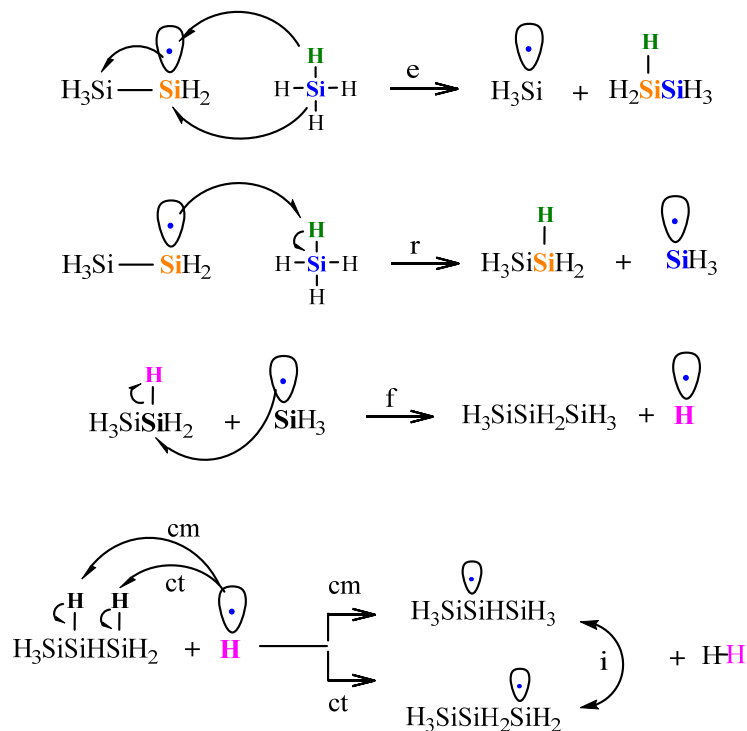
Figure 6.2 Detailed neutral reaction pathways for three-Si particle synthesis.
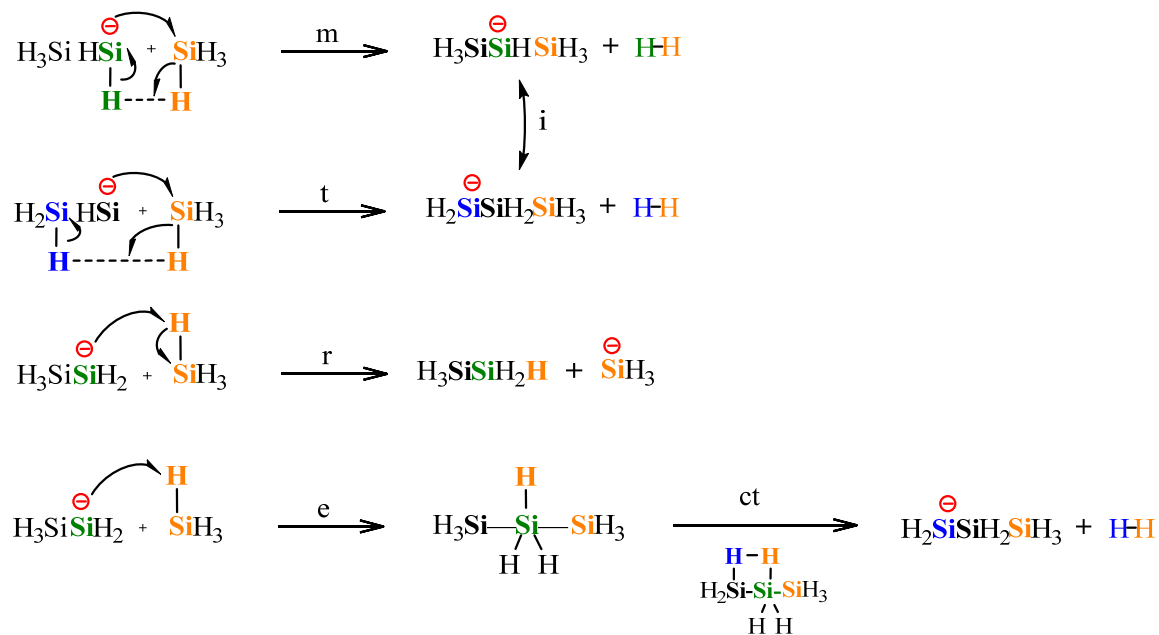
Figure 6.3 Detailed anionic reaction pathways for three-Si particle synthesis.

Both free and anion radical reactions with silane are summarized in **Figures 6.2** and **6.3,** and the potential energy profiles for the mechanical pathways of the two reaction systems are shown in **Figures 6.4** and **6.5.**

In free radical reactions, between two pathways forming silyl radical and disilane from the disilyl radical and silane of the first step, the pathway that the electron of disilyl radical propagates to one of the hydrogens of silane by abstracting the hydrogen (reaction e) is the major pathway. Then The silyl radical offers an electron to a Si atom of disilane by forming a Si—Si sigma bond which results in trisilane with hydrogen radical. Hydrogen abstraction from the secondary Si of trisilane by the hydrogen radical in the third reaction step needs slightly lower activation energy than the abstraction from the primary Si of trisilane and results in the more stable form of trisilyl radical.
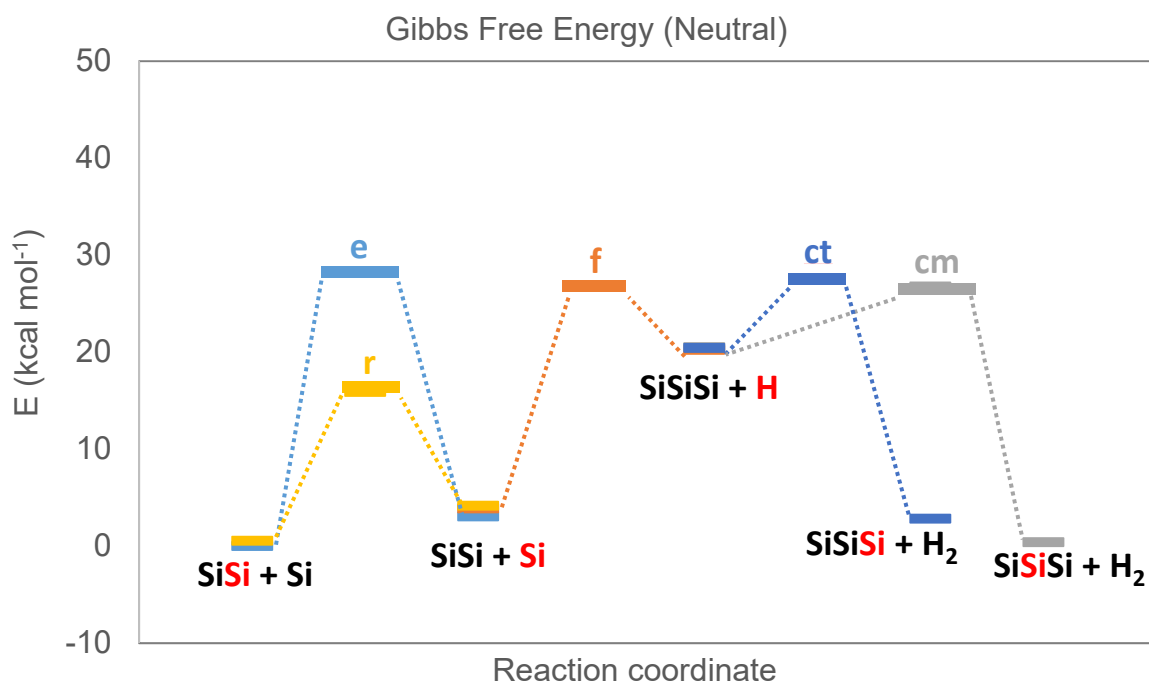
Figure 6.4 Detailed nuetral radical reaction mechanism profile for three-Si particle synthesis.
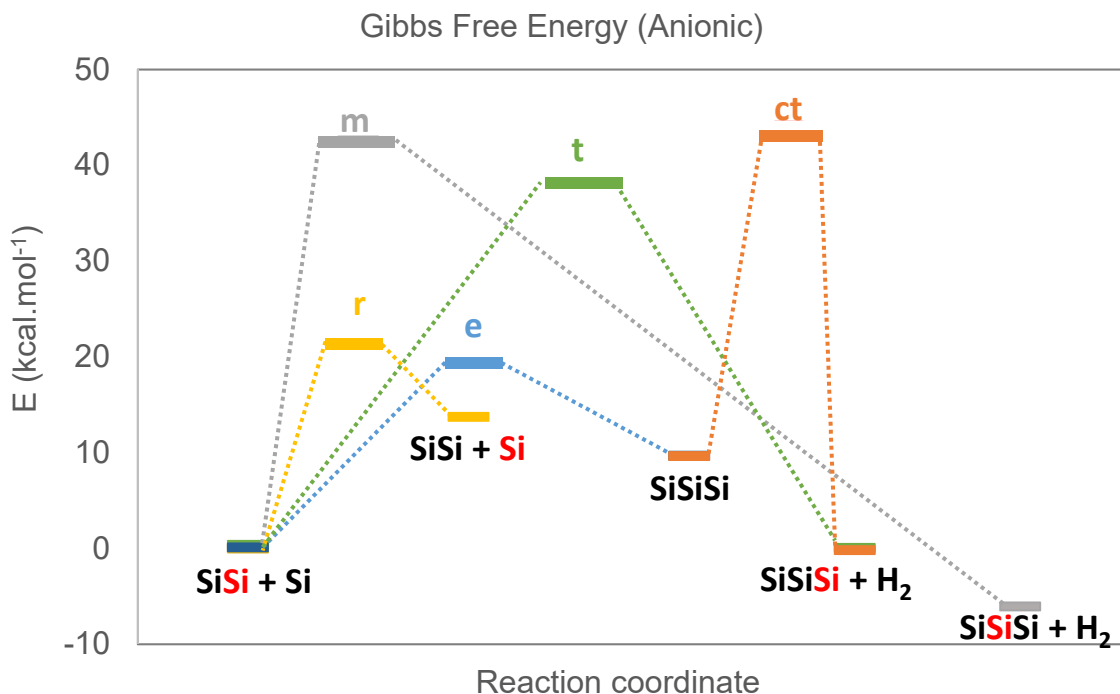
Figure 6.5 Detailed anionic reaction mechanism profile for three-Si particle synthesis.

For anionic radical reaction, one-step reactions that have a 4atom centered transition state (reaction m and t) require high activation energies for forming trisilyl anionic radical and a hydrogen molecule. Two-step reaction through the stable intermediate, $SiH_3SiH_3SiH_3$ which secondary Si atom has 5 sigma bonds. The first step of two-step reaction needs much smaller activation energy than one-step reactions (reaction m and it) and by 1,2 hydrogen elimination reaction, trisilyl anion radical and molecular hydrogen are formed.

Kinetic parameters for both free and anionic radical reactions are also listed in **Table 6.1**. In general, activation energies of anionic radical reactions are higher than those of free radical reactions. The steps of forming silyl radical and trisilane are endothermic processes in both reactions while converting to trisilyl radicals by H abstraction is all exothermic processes in both reaction systems.

Table 6.1 Kinetic parameters for radical reactions

	E_0 kcal·mol^{-1}	logA	E_a kcal·mol^{-1}	E_{o_r} kcal·mol^{-1}	Log A_r	E_{a_r} kcal·mol^{-1}	ΔH_{Rxn} kcal·mol^{-1}
n-e	19.31	12.28	21.59	16.54	12.54	18.71	2.8
n-r	9.27	14.8	12.25	6.5	15.07	9.38	2.8
n-f	15.37	13.39	18.33	2.04	13.1	1.37	14.72
n-cm	2.44	13.55	1.9	21.27	13.41	22.17	-18.58
n-ct	3.11	13.46	2.47	19.97	13.51	20.71	-16.64
n-i	34.55	12.7	34.83	32.57	12.88	32.79	1.95
a-e	10.4	11.2	11.98	7.3	16.15	6.1	3.47
a-r	15.99	15.16	19.35	2.58	15.29	5.81	13.47
a-t	29.62	11.78	31.25	34.27	11.69	33.49	-2.97
a-m	34.2	11.94	35.8	45.32	12.07	44.7	-9.52
a-ct	31.67	11.92	30.64	39.4	11.97	38.76	-6.43
a-I	27.33	12.69	27.57	33.82	12.91	34.23	-6.56

Rate constants for each reaction steps of both reactions in the temperature range from 298.15 K to 1500 K are tabulated in **Table 6.2**. In both radical systems, reaction equilibriums of only forming 3-atoms silyl radical are located closer to the products of the steps. In other reaction steps in both systems, reaction equilibrium is closer to reactants. The reaction r and f in neutral radical reactions can be compared with the reaction e of anionic reaction. The rate constants of free radical reaction r and f are higher (or similar at some temperature conditions) than one of anionic reaction e. And the rate constants of all one-step synthesis pathways (reaction a-t and a-m) in anionic system are the lowest due to the highest activation barriers.

Table 6.2 Rate constants of each reaction steps at various temperature. (Units for isomerization reaction: s^{-1} and all other reaction cm^{3}molecule^{-1}s^{-1}.

T (K)	n-e		n-r		n-f		n-cm		n-ct		n-i	
	k	k_r	k	k_r	k	k_r	k	k_r	k	k_r	k	k_r
298.15	4.45E-04	1.04E-01	1.08E+06	2.54E+08	1.47E+00	1.25E+12	1.48E+12	1.95E-03	4.60E+11	2.83E-02	1.60E-13	7.52E-12
300	5.46E-04	1.24E-01	1.20E+06	2.74E+08	1.74E+00	1.27E+12	1.51E+12	2.42E-03	4.71E+11	3.47E-02	2.30E-13	1.05E-11
400	2.33E+00	1.62E+02	9.40E+07	6.55E+09	1.80E+03	2.27E+12	3.24E+12	1.72E+01	1.27E+12	1.36E+02	4.41E-07	8.84E-06
500	4.15E+02	1.41E+04	1.57E+09	5.34E+10	1.40E+05	3.20E+12	5.14E+12	3.83E+03	2.33E+12	2.09E+04	2.70E-03	3.27E-02
600	1.48E+04	3.11E+05	1.18E+10	2.47E+11	2.91E+06	4.03E+12	7.05E+12	1.51E+05	3.50E+12	6.43E+05	9.29E-01	7.99E+00
700	2.08E+05	3.09E+06	5.46E+10	8.10E+11	2.79E+07	4.75E+12	8.87E+12	2.19E+06	4.72E+12	7.84E+06	6.12E+01	4.11E+02
800	1.61E+06	1.84E+07	1.85E+11	2.11E+12	1.62E+08	5.36E+12	1.06E+13	1.71E+07	5.94E+12	5.35E+07	1.43E+03	7.98E+03
900	8.33E+06	7.75E+07	5.05E+11	4.70E+12	6.73E+08	5.90E+12	1.22E+13	8.77E+07	7.12E+12	2.47E+08	1.68E+04	8.07E+04
1000	3.23E+07	2.54E+08	1.18E+12	9.28E+12	2.19E+09	6.36E+12	1.36E+13	3.35E+08	8.26E+12	8.68E+08	1.21E+05	5.16E+05
1100	1.01E+08	6.95E+08	2.43E+12	1.67E+13	5.92E+09	6.77E+12	1.50E+13	1.03E+09	9.34E+12	2.49E+09	6.08E+05	2.36E+06
1200	2.68E+08	1.65E+09	4.56E+12	2.81E+13	1.39E+10	7.13E+12	1.63E+13	2.68E+09	1.04E+13	6.11E+09	2.35E+06	8.42E+06
1300	6.25E+08	3.50E+09	7.95E+12	4.45E+13	2.94E+10	7.45E+12	1.74E+13	6.12E+09	1.13E+13	1.33E+10	7.39E+06	2.47E+07
1400	1.32E+09	6.79E+09	1.31E+13	6.73E+13	5.68E+10	7.74E+12	1.85E+13	1.27E+10	1.23E+13	2.64E+10	1.98E+07	6.23E+07
1500	2.56E+09	1.23E+10	2.04E+13	9.78E+13	1.02E+11	7.99E+12	1.95E+13	2.41E+10	1.31E+13	4.85E+10	4.64E+07	1.39E+08

T (K)	a-e		a-r		a-t		a-m		a-ct		a-i	
	k	k_r	k	k_r	k	k_r	k	k_r	k	k_r	k	k_r
298.15	3.94E+02	4.82E+11	1.54E+01	1.73E+11	1.22E-11	1.76E-13	8.06E-15	2.62E-21	3.18E-11	4.63E-17	3.13E-08	7.01E-13
300	4.39E+02	5.14E+11	1.84E+01	1.79E+11	1.65E-11	2.48E-13	1.15E-14	4.13E-21	4.36E-11	6.88E-17	4.16E-08	9.99E-13
400	3.59E+04	6.68E+12	2.86E+04	9.76E+11	3.94E-06	2.28E-07	1.85E-08	4.06E-13	1.47E-05	5.64E-10	4.17E-03	1.59E-06
500	5.81E+05	3.06E+13	2.87E+06	3.27E+12	7.83E-03	8.91E-04	1.15E-04	2.63E-08	3.09E-02	8.24E-06	4.24E+00	8.53E-03
600	4.13E+06	8.41E+13	7.09E+07	8.33E+12	1.40E+00	2.31E-01	4.42E-02	4.47E-05	5.19E+00	5.18E-03	4.32E+02	2.65E+00
700	1.82E+07	1.74E+14	7.69E+08	1.78E+13	6.25E+01	1.28E+01	3.40E+00	9.54E-03	2.06E+02	5.43E-01	1.18E+04	1.62E+02
800	5.86E+07	3.00E+14	4.92E+09	3.36E+13	1.16E+03	2.72E+02	9.50E+01	5.56E-01	3.30E+03	1.86E+01	1.42E+05	3.54E+03
900	1.53E+08	4.61E+14	2.19E+10	5.80E+13	1.19E+04	3.02E+03	1.34E+03	1.36E+01	2.89E+04	3.00E+02	9.82E+05	3.93E+04
1000	3.41E+08	6.52E+14	7.56E+10	9.34E+13	7.95E+04	2.14E+04	1.16E+04	1.82E+02	1.65E+05	2.87E+03	4.63E+06	2.70E+05
1100	6.80E+08	8.67E+14	2.15E+11	1.43E+14	3.91E+05	1.09E+05	7.03E+04	1.55E+03	6.93E+05	1.86E+04	1.65E+07	1.31E+06
1200	1.24E+09	1.10E+15	5.28E+11	2.08E+14	1.51E+06	4.32E+05	3.25E+05	9.51E+03	2.30E+06	9.08E+04	4.75E+07	4.88E+06
1300	2.10E+09	1.35E+15	1.15E+12	2.93E+14	4.88E+06	1.41E+06	1.21E+06	4.49E+04	6.37E+06	3.53E+05	1.16E+08	1.49E+07
1400	3.37E+09	1.61E+15	2.30E+12	4.00E+14	1.36E+07	3.95E+06	3.83E+06	1.72E+05	1.53E+07	1.15E+06	2.51E+08	3.88E+07
1500	5.14E+09	1.87E+15	4.24E+12	5.33E+14	3.35E+07	9.79E+06	1.06E+07	5.62E+05	3.27E+07	3.24E+06	4.90E+08	8.90E+07

6.4 Summary

In order to investigate the particle nucleation and growth involving the formation of small clusters under the plasma, multi-reference wavefunctions were applied to solve the electronic Schrödinger equation for mono-silicon hydrides (SiH$_{1-4}^{0,\pm}$). The inclusion of the 4s, 4p, 3d orbitals of silicon besides its valence 3s, 3p orbitals is essential for correct and smooth convergence of the calculations. The density of low-lying electronic states (number of electronic states per energy unit)

generally drops as we add hydrogen atoms to the system. The lowest excitations for cationic and neutral species pertain to excitations within localized silicon orbitals, then excitations from the bonding SiH orbitals to localized silicon orbitals follow, and finally electronic promotions to Rydberg silicon orbitals (4s, 4p) occur.

Based on knowledge of mono-silicon hydrides ($SiH_{1-4}^{0,\pm}$), detailed mechanism of radical-neutral molecule reaction at the molecular level were studied to investigate differences between the anionic radical-neutral molecule and neutral radical-neutral reaction mechanisms for nucleation and growth of silicon hydrides. Various pathways of growth of silicon hydride from two-Si to tri-Si were investigated in both free radical and anionic radical systems, and the rate constants for each step were calculated using TST in the temperature range from 298.15 K to 1500 K. Three reaction steps are found for forming trisilyl free radical in the neutral radical and neutral molecule reaction while anionic trisilyl radical were synthesized by one step or two-steps of reactions. The high rate constant indicates that the two-step reaction is a more dominant pathway than the one-step reaction with a high activation barrier. Furthermore, it was observed that the neutral system contributes more to the growth of nanoparticles than the anionic system by comparing the rate constant of each reaction step.

Chapter 7

Conclusion and Recommendations for Future Research

7.1 Summary of Conclusions

Considerable progress in developing the understanding of the reaction kinetics and thermochemistry underlying silicon nitride nanoparticle formation were made in this Ph.D. research. The general conclusions for Chapters 2 through 6 have been summarized below.

Chapter 2. Thermodynamic Properties of SiGe and SiN Nano Clusters

The relative stabilities, thermo-dynamic properties and electronic properties of hydrogenated Si, Ge, N, SiGe and SiN nanoclusters were investigated using quantum chemical calculations and conventional statistical thermodynamics.

The geometry parameters of all the molecules increased nominally as Ge atoms were substituted for Si atoms; however, the geometric change was small when compared to the changes observed in the electronic properties. As Si atoms were exchanged for Ge atoms in a given cluster geometry, the calculated thermochemical properties increased proportionally with the number of Ge atoms in the cluster. The calculated HOMO-LUMO energy gaps are proportionally decreased, as the cluster size increases in total heavy atom count, Si or Ge atoms. Using a machine learning approach to predict the reactivity of Si, Ge, and SiGe alloy clusters and acyclic species in the gas phase.

A statistically significant predictive model at the 99.9% confidence interval was regressed to allow for nanomaterials design efforts independent of the need to perform computationally expensive quantum chemical calculations during the initial screening efforts of nanomaterials design.

The G3//B3LYP composite method was validated against the B3LYP functional and various basis sets for silicon nitrides. The geometry parameters (bond lengths, bond angles, cluster diameter) of all the species decreased on average and the calculated thermochemical properties (H_f, S, and C_p) reduced proportionally as the nitrogen content of the cluster increased. The cluster geometry of the planar type is more probable than the 3-dimensional structure due to introduced geometric strain. The calculated HOMO LUMO energy gaps are proportionally increased with increase in nitrogen content in both cyclic planar and clusters. To assess the stability of the hydrogenated silicon and silicon-nitride nanoclusters, natural bonding orbital (NBO) analysis was performed to measure the degree of hyperconjugation for selected species. Species with a large number of Si-N bonds showed generally lower reactivity and higher stability than those that did not, and the contribution of Si-N bonding to the lower reactivity and higher stability was well correlated with the degree of hyperconjugation from NBO analysis.

Chapter 3. 1, 2-Hydrogen Migration

Rate coefficients and Arrhenius parameters for the hydrogen migration (or shift) reaction in silicon nitride species have been calculated for 52 reactions using G3//B3LYP, statistical thermodynamics, and conventional transition state theory. The overall reaction of substituted cyclic and acyclic silylenes to their respective silene and imine species by 1,2-hydrogen shift reaction was analyzed by three different types of H shift reaction using overall reaction thermodynamics: (1)

endothermic H shift between N and Si:, (2) endothermic H shift between Si and Si: and (3) exothermic H shift between Si and Si:. The single event pre-exponential factors, $\tilde{A}$, and activation energies, E_a, for the three different classes of hydrogen shift reactions of silicon nitrides were computed. Type of hydrogen shift reaction gives the most significant influence on the kinetic parameters. The reactant geometry should be considered first to understand which H shift reaction is most competitive among three different types of hydrogen migration. For the reactant, where D_{rel} is 1, it was discovered that the endothermic hydrogen shift between Si-Si was the most competitive pathway between the two types of endothermic hydrogen migration. However, SiN is thermodynamically more favorable to maintain divalent Si: than to form a double bond through hydrogen migration. This indicates that nanoparticles can be grown from the residual divalent Si by reacting with other radical species under silane and ammonia co-pyrolysis. On the other hand, for the reactant with D_{rel} of 2 or higher, exothermic hydrogen transfer between Si and Si: occurs favorably. Since the species with double bonds are more stable thermodynamically, this result indicates that nanoparticle growth will be more difficult under these conditions.

Chapter 4. H₂ Addition and Elimination Reaction

The Rate coefficients and Arrhenius parameters for the hydrogen addition and elimination reaction in silicon nitride species have been calculated for 21 reactions. The overall reaction of substituted cyclic and acyclic amino silylenes to their respective amino silanes by 1,1-hydrogen addition and elimination was analyzed by three different types patterns depending on the geometry of reactants. Only reactions of the group (C), Amionsilylene has two nitrogen and D_{rel} is 1, were found to as two-step reactions that pass through a stable intermediate to produce saturated silicon nitrides. Although the reaction pathways are different, all hydrogen addition and removal reactions are similar

in the structure of the reaction centers of the rates determining transition state. The reactant conformation give no influence on kinetic parameters. The mechanism of hydrogen addition and elimination reaction was intuitively explained through NBO analysis, and the stability of amino siylene species was explained by the resonance and hyperconjugation effects.

Chapter 5. Silylene Addition-elimination and Cyclization-decyclization Reaction

The Rate coefficients and Arrhenius parameters for the silylene addition-elimination reaction and cyclization-decyclization reactions in silicon nitride species have been calculated for 40 silylene addition & elimination, 23 cyclization and ring-opening reactions using G3//B3LYP, statistical thermodynamics, and conventional transition state theory.

The overall silylene addition and elimination reactions were categorized in two sub-group; (i) reaction between divalent Si and N and (ii) reaction between divalent Si and Si. The silylene addition reactions in the group (i) are one-step reaction but, the reactions in the group (ii) were two-step reactions through a stable intermediate to a saturated silicon nitride product.

For the silylene addition reaction, the different conformation of the reactant was not a significant factor, unlike the hydrogen transfer reaction. Adding various substituents to either side of the reactive center does not make a significant structural difference in transition states. SiH_2 insertion to silicon nitrides is also a barrierless reaction and a fast reaction, SiH_2 addition to a Si-H bond in silicon nitrides has been found to have a much higher A factor than the reaction to a Si-H bond in disilane does, the silylene addition reaction to silicon nitrides will be superior in silane and ammonia pyrolysis.

All cyclization and ring opening except for 4-1, 5-01, 5-07, and 6-1(reaction center is between

N and Si:) were two-step reactions though a stable intermediate to a saturated silicon nitride product and were controlled by the second step as the rate-determining step under pyrolysis conditions. The cyclization between divalent Si and N does not change the reactive center greatly with the size of silicon nitride chains while the steric hindrance of the rings, in the reactive center between divalent Si and Si, plays a role in cyclization and ring opening reactions. Due to the high rotational barriers and multi-coupled vibrational modes, the internal rotation effect was negligible in silicon nitrides. All decyclization reactions are endothermic processes, their rate coefficients are much smaller than the reverse reactions (cyclization). Decyclization of ring-type silicon nitrides starts with breaking a Si-Si or Si-N bond, breaking a Si-Si bond is always easier than breaking a Si-N bond.

Comprehensive Conclusions for Silane and Ammonia Co-pyrolysis

Comparing each primary reaction of the amino silylene form with various conformations with the concept of instantaneous selectivity of the elementary reactions that have been individually investigated in Chapters 2-6 can bring a comprehensive picture of the reaction system.

Overall, the rate constants of amino silylene with $D_{rel} = 2$ are the highest, and those of the species with $D_{rel}=1$ are the smallest among various conformation isomers. For the 4-atom acyclic species shown in Figure 7.1, for instance, the order of rate constants are reaction $5 > 4 > 6$ in the H_2 addition and elimination reaction and $C3 > C4$ in the 1,2-H-shift reaction. In addition, in the silylene addition and elimination reaction, both the reaction p2r2-c forming acyclic amino silanes and the reaction p2r2-b forming isopropyl silyl amine showed similar rate constant values, which are the highest. In the cyclization reaction system, the species with $D_{rel} = 2$ had the highest rate constant.
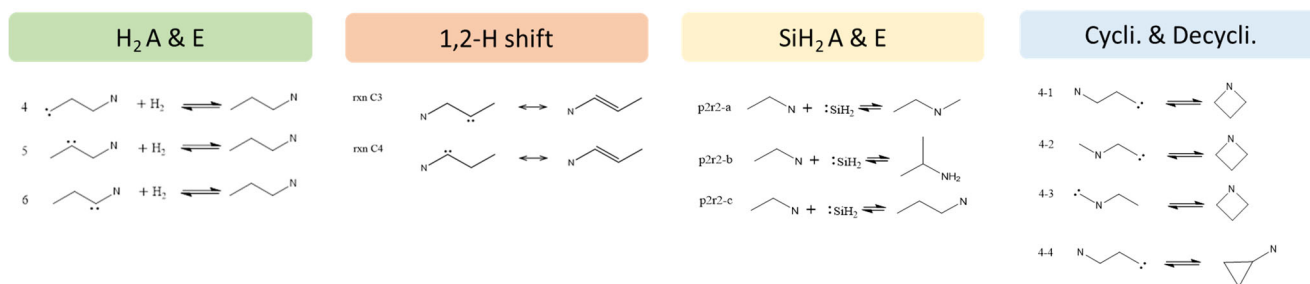
Figure 7.1 Examples of 4-atom acyclic species' four elementary reactions under co-pyrolysis silane and ammonia.

It was investigated that reactions of molecules with $D_{rel}=2$ have the highest reaction constants, and those with $D_{rel}=1$ have the lowest reaction constants due to the hyper-conjugation effect of divalent Si and lone pair of N by NBO (natural bond orbital) analysis. The lower reactivity and relative stability of species is attributed to the hyper-conjugation effect.
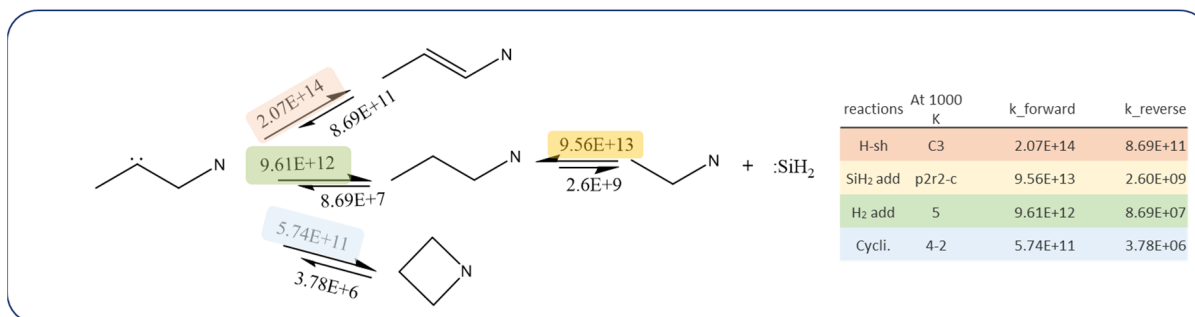
Figure 7.2 Simple Reaction schematic of 4-atom amino silylenes.

A simple schematic of four elementary reactions of the 4-atom amino silylene with $D_{rel}=2$ is shown in **Figure 7.2**. The most dominant reaction is the H shift reaction, followed by the silylene addition reaction, the H_2 addition reaction, and the cyclization, which were the least dominant.
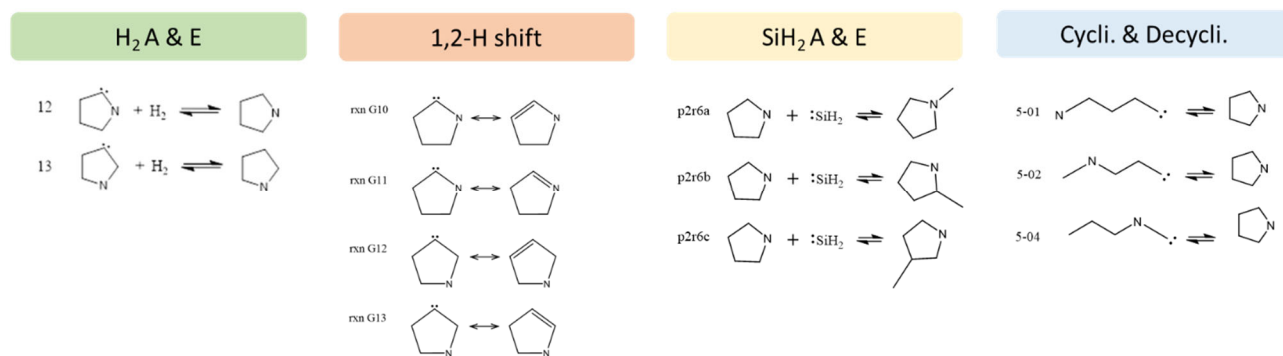
Figure 7.3 Examples of 5-atom cyclic species' four elementary reactions under co-pyrolysis silane and ammonia.

It was also observed the same trend in 5atom cyclic amino silylene species from the comparison between four elementary reactions. The cyclic species with $D_{rel}=2$ has the highest rate constant than its isomers from all four elementary reactions. The cyclic species with $D_{rel}=1$ has the lowest rate constant value, which is depicted in **Figure 7.3**. The order of probable reactions for cyclic species is H-shift, SiH$_2$ addition, H$_2$ addition, and cyclization reaction.

The order of rate constants are the reaction 13 > 12 in the H$_2$ addition and elimination reaction and the reaction G13 > G12 > G10 > G11 in the 1,2-H-shift reaction, the reaction 6c > 6b > 6a in the silylene addition and elimination reaction. In cyclization reaction, the rate constants of species with $D_{rel}=2$ or higher are higher than other species.

reaction	1000 K	kf	kr
H sh	~	1.73E+14	4.67E+12
SiH2 add	~	1.11E+14	4.98E+08
H2 ane	·	5.81E+12	2.25E+08
cycl	~	1.58E+12	3.77E+04
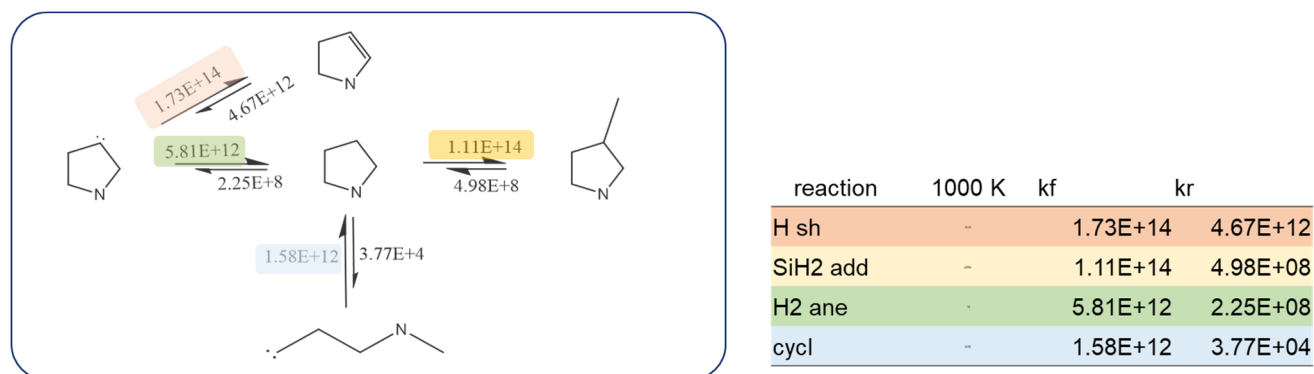
Figure 7.4 Simple Reaction schematic of 5-atom amino silylenes.

Elementary reactions of amino silylene consisting of 4 atoms, and the simplest reference reactions are schematically illustrated in **Figure 7.5**. For 4-atom silicon nitrides, the H-shift reaction was most prevalent, whereas it was the least probable reaction for reference reaction. It was observed that SiH_2 addition to Si atom is one of the major reactions for both sizes of silicon nitrides, which leads to SiN nanocluster growth.
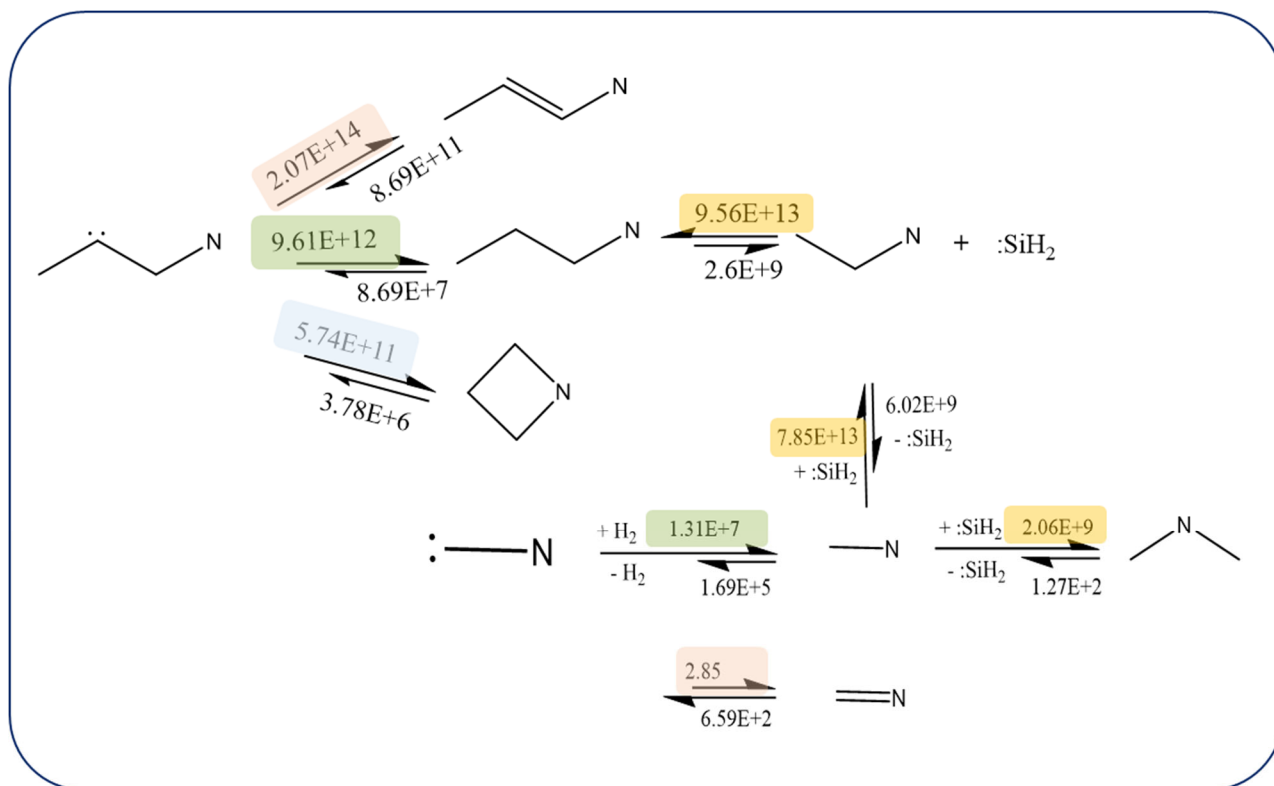
Figure 7.5 Simple reaction schematic of small silicon nitrides.

Specification Rate Constants for Four Elementary Reactions under Sillane and Ammonia Co-pyrolysis

Activation energy prediction models under silane and ammonia co-pyrolysis conditions are summarized and categorized from the investigations of four different elementary classes in Figure 7.6. Although unfortunately, the available experimental data for silane and ammonia co-pyrolysis kinetics are limited, this schematic diagram can be used for predicting rate constants for silicon nitrides elementary reactions. In order to calculate the activation barrier of an elementary reaction, the conformation characteristic of reacting species should be considered. For activation energy calculation of cyclization and decyclization, the model can be chosen depending on the size of cyclic molecules or D_{rel} value of the acyclic species. For hydrogen molecule addition and elimination reaction, two prediction models can be used whether the interest of reaction is forward or reverse with the enthalpy of reaction, the number of N atom of a reactant, and the D_{rel} of the reactant. In hydrogen shift reactions, the reaction center was the first factor to be considered, then activation energy can be predicted with the enthalpy of reaction, the number of N atoms of a reactant, the D_{rel} of the reactant, and the direction of H migrating. For silylene addition reactions, the atom in the reaction center is the most significant factor. Once the activation energy is computed, the rate constants of silicon nitrides synthesis reaction can be calculated using the predicted activation energy and the suggested pre-exponential factor in Figure 7.6. Another advantage of this study's listed generalized models for specific elementary reactions is their broad applicability for various silicon nitrides species beyond this study. Using these models, a database of calculated rate constants of silicon nitrides will bring a fundamental understanding of silane and ammonia co-pyrolysis to the near future, eventually leading to novel material design and optimization of reaction systems, improve the efficiency of reaction systems, and development of analytical tools.

H₂ A & E

1,2-H shift

SiH₂ A & E

Cycli. & Decycli.

Check the conformation of reacting species (reactants and products) and define characteristic parameters

N : the number of N atom in the molecule

d : direction of hydrogen migration (where H is transferring towards N atom, $d = 1$, where H is transferring away from N atom, or where there is no N atom in the species, $d = 0$).

D_{rel} : Distance between N atom to nearest divalent Si atom (=reaction center)

$$E_a = E_0 + \alpha\Delta H_{Rxn} + \beta N + \gamma d + \delta D_{rel}$$

Select a proper model for calculating E_a

If a species is NH₂-(SiH₂)ₙ-H-Si:

$(Cycl.)\ E_a = 23.36 + 1.49\Delta H_{Rxn}$
Log A =11.38
$(Decycl.)\ E_a = 23.36 - 0.49\Delta H_{Rxn}$
Log A =13.28

Check the size of the cyclic species (the number of atoms)

If 3-membered ring,
$(Cycl.)\ E_a = 23.36 + 1.49\Delta H_{Rxn}$
Log A =12.25
$(Decycl.)\ E_a = 23.36 - 0.49\Delta H_{Rxn}$
Log A =12.81

If H₂ addition,

$E_a = 60.96 + 1.55\Delta H_{Rxn} + 11.57N + 1.95D_{rel}$
Log A = 12.44

If H₂ elimination,

$E_a = 60.96 - 0.55\Delta H_{Rxn} + 11.57N + 1.95D_{rel}$
Log A =18.54

H-shift   N ↔ Si:

$E_a = 52.72 + 0.43\Delta H_{Rxn}$
Log A = 13.30

N ↔ Si: (Group i)

$E_a = 39.5 + 0.486\Delta H_{Rxn}$
Log A =11.10

If 4-membered ring,
$(Cycl.)\ E_a = 70.9 + 2.12\Delta H_{Rxn}$
Log A =11.53
$(Decycl.)\ E_a = 70.9 - 1.12\Delta H_{Rxn}$
Log A =13.15

H-shift Si ↔ Si:

If D_{rel} =1 and d=1
$E_a = 54.73 + 0.48\Delta H_{Rxn} - 9.8N - 19.7d$
Log A = 12.54

If D_{rel} >1
$E_a = 2.99 + 0.49\Delta H_{Rxn} + 2.04D_{rel}$
Log A = 13.04

Si ↔ Si: (Group ii)

$E_a = 12.6 + 0.483\Delta H_{Rxn}$
Log A = 10.96

If 5-membered or larger then #5 ring,
$(Cycl.)\ E_a = 47.48 + 1.21\Delta H_{Rxn}$
Log A =10.55
$(Decycl.)\ E_a = 47.48 - 0.21\ \Delta H_{Rxn}$
Log A =12.57

Figure 7.6 Activation energy prediction models for four elementary reactions under silane and ammonia co-pyrolysis.

Chapter 6. Silicon nanoparticle growth in plasma condition

In order to investigate the particle nucleation and growth involving the formation of small clusters under the plasma, multi-reference wavefunctions were applied to solve the electronic Schrödinger equation for mono-silicon hydrides ($SiH_{1-4}^{0,\pm}$). The inclusion of the 4s, 4p, 3d orbitals of silicon besides its valence 3s, 3p orbitals is essential for correct and smooth convergence of the calculations. The density of low-lying electronic states (number of electronic states per energy unit) generally drops as we add hydrogen atoms to the system. The lowest excitations for cationic and neutral species pertain to excitations within localized silicon orbitals, then excitations from the bonding SiH orbitals to localized silicon orbitals follow, and finally electronic promotions to Rydberg silicon orbitals (4s, 4p) occur.

Based on knowledge of mono-silicon hydrides ($SiH_{1-4}^{0,\pm}$), detailed mechanism of radical-neutral molecule reaction at the molecular level were studied to investigate differences between the anionic radical-neutral molecule and neutral radical-neutral reaction mechanisms for nucleation and growth of silicon hydrides. Various pathways of growth of silicon hydride from two-Si to tri-Si were investigated in both free radical and anionic radical systems, and the rate constants for each step were calculated using TST in the temperature range from 298.15 K to 1500 K. Three reaction steps are found for forming trisilyl free radical in the neutral radical and neutral molecule reaction while anionic trisilyl radical were synthesized by one step or two-steps of reactions. The high rate constant indicates that the two-step reaction is a more dominant pathway than the one-step reaction with a high activation barrier. Furthermore, it was observed that the neutral system contributes more to the growth of nanoparticles than the anionic system by comparing the rate constant of each reaction step.

7.2 Recommendations for Future Research

The accomplishments in this Ph.D. thesis research suggest likely directions for future research.

Extension of Rate Coefficient database for large silicon nitride clusters and multifunctional silicon nitrides under silane and ammonia co-pyrolysis.

- Transition state theory has been used to successfully predict the kinetic parameters for the major monofunctional silicon nitride reaction families, and extension of this approach to multifunctional silicon nitrides is the next step.

- In this study, elementary reactions for the synthesis of small-sized silicon nitride in the initial stage of pyrolysis were studied, and most acyclic species are silyl amine species with one N atom.

- However, the type of the widely used silicon nitride is either crystalline Si_3N_4 or amorphous Si_3N_4, which ratio of Si to N in silicon nitrides is mostly 1 : 1.33 or 1 : 1. Extending the range of silicon nitrides with more than two nitrogen atoms for rate coefficient calculation will bring the kinetic modeling of silicon nitride particle growth into the near future.

- The reactants were limited to mono-ring type cyclic species from 4-membered to 6-membered size, but an extension to 7 or larger-membered ring or polycyclic ring species is suggested to compute rate coefficients for synthesizing clusters like Si_3N_4.

Exploration to another elementary reaction classes under co-pyrolysis of chlorinated silane and ammonia and Extension of Rate Coefficient database for silicon nitride formation under plasma, laser enhanced condition.

- The development of rate coefficient databases for the major reaction families for silicon nitrides decomposition in low-pressure plasma enhanced chemical vapor deposition (PECVD) or laser-assisted chemical vapor decomposition processes (that include silyl amine radicals and anionic species) is a fertile area. This development would also reveal more details at the molecular level with extensive quantum chemical calculations regarding the effect of radical and anionic species on the reactive center for these reaction classes.

Automated Network generation

- The major monofunctional reaction families during silicon nitride pyrolysis (Chapters 3 through 5), the modification of existing automated network generation scripts to accommodate this new approach is the next step. The incorporation of a different set of group additivity parameters that account for anharmonicity in more detail and multiple pre-exponential factors for each reaction family into automated network generation models is expected to reveal modified dominant pathways and critical particles sizes (or particle sizes where growth is irreversible).

Microkinetic modeling of silicon nitride using the predicted rate coefficients

- A deterministic microkinetic modeling of silicon nitride nanoparticle formation would be available with the Monte Carlo simulation technic and comprehensive rate coefficients in the pyrolytic conditions.

- This method uses many of the same tools as automated reaction mechanism generation. In this approach, progress of a single cluster is followed as it undergoes reaction events that are selected according to rates derived from probabilities. Using the same algorithms for identifying reactions and estimating their rate parameters as in the deterministic modeling (i.e., automated network generation), all possible reactions of the cluster are enumerated, and their rates are calculated.

Optimize the reaction conditions for targeting silicon nitrides synthesis

- It is acknowledged that the pyrolysis of SiH_4 and NH_3 is more energetically favorable compared to the pyrolysis of SiH_4 alone, due to the formation of N–Si ion clusters in the gas mixture. In this study, we only focused on neutral species in the ground state, knowledge of ionic reactions are prerequisite for modeling and optimizing the synthesis process for the desired material.

References

1.   Ulvestad, A.; Andersen, H. F.; Jensen, I. J. T.; Mongstad, T. T.; Maehlen, J. P.; Prytz, O.; Kirkengen, M., Substoichiometric Silicon Nitride - an Anode Material for Li-Ion Batteries Promising High Stability and High Capacity. *Sci Rep* **2018,** *8*, 8634.

2.   Holst, A.   https://www.statista.com/statistics/266973/global-semiconductor-sales-since-1988/

3.   Kaloyeros, A. E.; Jové, F. A.; Goff, J.; Arkles, B., Review—Silicon Nitride and Silicon Nitride-Rich Thin Film Technologies: Trends in Deposition Techniques and Related Applications. *ECS Journal of Solid State Science and Technology* **2017,** *6*, P691-P714.

4.   Fessenden, R.; Fessenden, J. S., The Chemistry of Silicon-Nitrogen Compounds. *Chemical Reviews* **2002,** *61*, 361-388.

5.   Adamczyk, A.; E, V. Use of Silyl Bridged Alkyl Compounds for Dense Organosilicate Glass (Osg) Films U.S. Patent Application No. 15/789,790. 2018.

6.   Eom, T.; Gwon, T.; Yoo, S.; Choi, B. J.; Kim, M.-S.; Ivanov, S.; Adamczyk, A.; Buchanan, I.; Xiao, M.; Hwang, C. S., Chemical Interaction and Ligand Exchange between a [(Ch3)3si]3sb Precursor and Atomic Layer Deposited Sb2te3 Films. *Journal of Materials Chemistry C* **2015,** *3*, 1365-1370.

7.   H. E. O'Neal, M. A. R., J. G. Martin, and M. T. Navio, Kinetics of Silylene Insertion into N-H Bonds and the Mechanism and Kinetics of the Pyrolysis of Dimethylsilylamine. *J. Phys. Chem. A* **1998,** *102*, , 8493.

8.   Jensen, K. F. R. a. K. F., Low Pressure Cvd of Silicon Nitride. *J. Electrochem. Soc.* **1987,** *134*, 1777-1785.

9.   Jones, A. C. H., Michael L., *Chemical Vapour Deposition - Precursors, Processes and Applications* Thomas Graham House, Science Park, Milton Road, Cambridge CB4 0WF, UK: 2009.

10.   Kaloyeros, A. E.; Pan, Y.; Goff, J.; Arkles, B., Review—Silicon Nitride and Silicon Nitride-Rich Thin Film Technologies: State-of-the-Art Processing Technologies, Properties, and Applications. *ECS Journal of Solid State Science and Technology* **2020,** *9*.

11.   Hood Chatham, M. M. a. H. T., Low-Temperature Deposition of Silicon Dioxide and Silicon Nitride for Dual Spacer Application. In *IEEE*, 2007.

12.   Jones, A. C.; Hitchman, M. L., Chapter 1. Overview of Chemical Vapour Deposition. In *Chemical Vapour Deposition*, 2008; pp 1-36.

13.   Hegedus, N.; Balazsi, K.; Balazsi, C., Silicon Nitride and Hydrogenated Silicon Nitride Thin Films: A Review of Fabrication Methods and Applications. *Materials (Basel)* **2021,** *14*.

14.   C. H. Lee, S. M., R. G. Southwick, J. Li, X. Miao, R. Bao, T. Ando, R. Galatage, S. Siddiqui, C. Labelle, A. Knorr, J. H. Stathis, D. Guo, V. Narayanan, B. Haran, H. Jagannathan, A Comparative Study of Strain and Ge Content in Si1-Xgex Channel Using Planar Fets,

Finfets and Strained Relaxed Buffer Layer Finfets. In *2017 IEEE International Electron Devices Meeting (IEDM)*, IEEE: San Francisco, CA, USA 2017.

15.   Pi, X. D.; Kortshagen, U., Nonthermal Plasma Synthesized Freestanding Silicon-Germanium Alloy Nanocrystals. *Nanotechnology* **2009,** *20*, 295602.

16.   Ang, K.-W.; Lin, J.; Tung, C.-H.; Balasubramanian, N.; Samudra, G. S.; Yeo, Y.-C., Strained N-Mosfet with Embedded Source/Drain Stressors and Strain-Transfer Structure (Sts) for Enhanced Transistor Performance. *IEEE transactions on electron devices* **2008,** *55*, 850-857.

17.   Krimmel, E. F.; Hezel, R.; Nohl, U.; Bohrer, R., Silicon Nitride in Integrated Circuit (Ic) Technology. In *Si Silicon*, Springer: 1991; pp 221-232.

18.   Di Valentin, C.; Palma, G.; Pacchioni, G., Ab Initio Study of Transition Levels for Intrinsic Defects in Silicon Nitride. *The Journal of Physical Chemistry C* **2011,** *115*, 561-569.

19.   Kim, J. E.; Lee, K. D.; Kang, Y.; Lee, H.-S.; Kim, D., Comparison of Passivation Property on Hydrogenated Silicon Nitrides Whose Antireflection Properties Are Identical. *Korean Journal of Materials Research* **2016,** *26*, 47-53.

20.   de Guzman, R. C.; Yang, J.; Cheng, M. M.-C.; Salley, S. O.; Ng, K. S., High Capacity Silicon Nitride-Based Composite Anodes for Lithium Ion Batteries. *Journal of Materials Chemistry A* **2014,** *2*, 14577-14584.

21.   Weeks, S. L.; Leick, N.; Agarwal, S., Silicon Nitride Encapsulated Silicon Nanocrystals for Lithium Ion Batteries. *Plasma Processes and Polymers* **2016,** *13*, 116-123.

22.   Mouchet, C.; Latu-Romain, L.; Cayron, C.; Rouviere, E.; Celle, C.; Simonato, J.-P., Growth of One-Dimensional Si/Sige Heterostructures by Thermal Cvd. *Nanotechnology* **2008,** *19*, 335603.

23.   Rostislav_A__Andrievskii_Russ., Silicon Nitride: Synthesis and Properties. *Chem._Rev._* **1995,** *64*, 291-308.

24.   Avvakumov, E., Mekhanokhimicheskii Sintez V Neorganicheskoi Khimii. Nauka Novosibirsk: 1991.

25.   Suryanarayana, C.; Froes, F. In *Light Metals Synthesis by Mechanical Alloying*, Materials Science Forum, Trans Tech Publ: 1992; pp 445-452.

26.   Andrievskii, R., Production and Properties of Nanocrystalline High-Melting Compounds. *Usp. Khim* **1994,** *63*, 431-448.

27.   BRASIL, O. R. N.; II, P., Recommend Stories.

28.   Chen, M.; Zheng, A.; Lu, H.; Zhou, M., Reactions of Atomic Silicon and Germanium with Ammonia: A Matrix-Isolation Ftir and Theoretical Study. *The Journal of Physical Chemistry A* **2002,** *106*, 3077-3083.

29.   Kilian, S. O.; Wiggers, H., Gas-Phase Synthesis of Silicon-Rich Silicon Nitride Nanoparticles for High Performance Lithium–Ion Batteries. *Particle & Particle Systems Characterization* **2021,** *38*, 2100007.

30.   Mukas' yan, A.; Martynenko, V.; Merzhanov, A.; Borovinskaya, I.; Blinov, M. Y., Mechanism and Principles of Silicon Combustion in Nitrogen. *Combustion, Explosion and Shock Waves* **1986,** *22*, 534-540.

31.   Mukas' yan, A.; Stepanov, B.; Gal'chenko, Y. A.; Borovinskaya, I., Mechanism of

Structure Formation of Silicon Nitride with Combustion of Silicon in Nitrogen. *Combustion, Explosion and Shock Waves* **1990,** *26*, 39-45.

32.　　Mukasyan, A.; Borovinskaya, I., Structure Formation in Shs Nitrides. *Int. J. SHS* **1992,** *1*, 55-63.

33.　　Skibska, M.; Szulc, A.; Mukasyan, A.; Shugaev, V.; Shiryaev, A., Microstructural Peculiarities of Silicon Nitride Formation under High Nitrogen Pressures. Part Ii: The Effect of Nitrogen Pressure on Shs Si3n4 Morphology and Phase Composition. *Inr. J. SHS* **1993,** *2*.

34.　　Merzhanov, A., Theory and Practice of Shs: Worldwide State of the Art and the Newest Results. *Int. J. SHS* **1993,** *2*, 113-158.

35.　　Cano, I. G.; Rodríguez, M. A., Synthesis of B-Silicon Nitride by Shs: Fiber Growth. *Scripta Materialia* **2004,** *50*, 383-386.

36.　　Jiang, Y.; Wu, L.; Wang, P.; Huang, Z., Pretreatment and Sintering of Si3n4 Powder Synthesized by the High-Temperature Self-Propagation Method. *Materials Research Bulletin* **2009,** *44*, 21-24.

37.　　L. N. Chukhlomina, Y. F. I., Yu. M. Maksimov, Z. S. Akhunova, and E. N. Krivosheeva, Preparation of Submicron Silicon Nitride Powders Via Self-Propagating High-Temperature Synthesis. *Inorganic Materials* **2005,** *41*, 1294–1299.

38.　　Forslund, M. E. a. B., Carbothermal Preparation of Silicon Nitride: Influence of Starting Material and Synthesis Parameters. *J Am Ceram Soc* **1992,** *75*, 532-539.

39.　　Gu, Q.; Zhang, J.; Li, H.; Liu, G.; Sun, H.; Fan, B., Synthesis of A-Si3n4 Powder by High Energy Ball Milling Assisting Molten Salt Nitridation Method at Low Temperature. *Ceramics International* **2019,** *45*, 18445-18451.

40.　　Lange, H.; Wötting, G.; Winter, G., Silicon Nitride—from Powder Synthesis to Ceramic Materials. *Angewandte Chemie International Edition in English* **1991,** *30*, 1579-1597.

41.　　Hyung Jik Lee, K. E., and Toyonobu Yoshida, Preparation of Ultrafine Silicon Nitride, and Silicon Nitride and Silicon Carbide Mixed Powders in a Hybrid Plasma. *J Am Cerom Soc* **1990,** *73*.

42.　　F. ALLAIRE, S. D., Synthesis and Characterization of Silicon Nitride Powders Produced in a D.C. Thermal Plasma Reactor. *JOURNAL OF MATERIALS SCIENCE* **1991**, 6736-6740.

43.　　Robert A. Bauer, J. G. M. B., *,* F. Einar Kruis,+ Brian Scarlett,+ and Joop Schoonman*,*, Laser Synthesis of Low-Agglomerated Submicrometer Silicon Nitride Powders from Chlorinated Silanes. *J Am Cerom SOC.* **1991,** *74*, 2759-2768.

44.　　Danforth, S. C., Synthesis and Processing of Ultrafine Powders for Si3n4 Ceramics *nanoSTRUCTUREDMATERIALS VOL* **1992,** *1*, 197-202.

45.　　W. Chang, G. S., S.C. Danforth, and B.H. Kear, Chemical Vapor Processing and Applications for Nanostructured Ceramic Powders and Whiskers. *NanoSTRUCTUREDMATERIALS VOL* **1994,** *4*, 507-520.

46.　　Cooke, T. F., Inorganic Fibers—a Literature Review. *Journal of the American Ceramic Society* **1991,** *74*, 2959-2978.

47.　　Daru, J.; Stirling, A., Divided Saddle Theory: A New Idea for Rate Constant

Calculation. *J Chem Theory Comput* **2014,** *10,* 1121-1127.

48.   Harame, D.; Koester, S.; Freeman, G.; Cottrel, P.; Rim, K.; Dehlinger, G.; Ahlgren, D.; Dunn, J.; Greenberg, D.; Joseph, A., The Revolution in Sige: Impact on Device Electronics. *Applied Surface Science* **2004,** *224,* 9-17.

49.   Pham, D. P.; Kim, S.; Park, J.; Tuan Le, A. H.; Cho, J.; Jung, J.; Iftiquar, S.; Yi, J., Reduction in Photocurrent Loss and Improvement in Performance of Single Junction Solar Cell Due to Multistep Grading of Hydrogenated Amorphous Silicon Germanium Active Layer. *Silicon* **2018,** *10,* 759-767.

50.   Yang, Q.; Chen, Z.; Yang, X.; Zhou, D.; Qian, X.; Zhang, J.; Zhang, D., Facile Synthesis of Si3n4 Nanowires with Enhanced Photocatalytic Application. *Materials Letters* **2018,** *212,* 41-44.

51.   Leitz, C.; Currie, M.; Lee, M.; Cheng, Z.-Y.; Antoniadis, D.; Fitzgerald, E., Hole Mobility Enhancements and Alloy Scattering-Limited Mobility in Tensile Strained Si/Sige Surface Channel Metal–Oxide–Semiconductor Field-Effect Transistors. *Journal of Applied physics* **2002,** *92,* 3745-3751.

52.   Yoffe, A. D., Semiconductor Quantum Dots and Related Systems: Electronic, Optical, Luminescence and Related Properties of Low Dimensional Systems. *Advances in physics* **2001,** *50,* 1-208.

53.   Petit, L.; Eenink, H. G. J.; Russ, M.; Lawrie, W. I. L.; Hendrickx, N. W.; Philips, S. G. J.; Clarke, J. S.; Vandersypen, L. M. K.; Veldhorst, M., Universal Quantum Logic in Hot Silicon Qubits. *Nature* **2020,** *580,* 355-359.

54.   Adamczyk, A.; Liu, W.; Lee, Y. Etching Solution for Selectively Removing Silicon over Silicon-Germanium Alloy from a Silicon-Germanium/Silicon Stack During Manufacture of a Semiconductor Device. Us Patent App. 16/109,172. 2019.

55.   Adamczyk, A. J.; Broadbelt, L. J., The Role of Multifunctional Kinetics During Early-Stage Silicon Hydride Pyrolysis: Reactivity of Si2h2 Isomers with Sih4 and Si2h6. *J Phys Chem A* **2011,** *115,* 2409-2422.

56.   Adamczyk, A. J.; Reyniers, M. F.; Marin, G. B.; Broadbelt, L. J., Kinetics of Substituted Silylene Addition and Elimination in Silicon Nanocluster Growth Captured by Group Additivity. *Chemphyschem* **2010,** *11,* 1978-1994.

57.   Adamczyk, A. J.; Reyniers, M. F.; Marin, G. B.; Broadbelt, L. J., Kinetic Correlations for H2 Addition and Elimination Reaction Mechanisms During Silicon Hydride Pyrolysis. *Phys Chem Chem Phys* **2010,** *12,* 12676-12696.

58.   Adamczyk, A.; Liu, W.; Lee, Y. Etching Solution for Selectively Removing Silicon-Germanium Alloy from a Silicon-Germanium/Silicon Stack During Manufacture of a Semiconductor Device. Us Patent App. 16/108,499. 2019.

59.   Adamczyk, A.; Ge, J.; Lee, Y.; Liu, W.; Kuo, C.-H. Etching Solution for Simultaneously Removing Silicon and Silicon-Germanium Alloy from a Silicon-Germanium/Silicon Stack During Manufacture of a Semiconductor Device Us Patent App. 16/142,291. 2019.

60.   Moss, S. J.; Ledwith, A., *The Chemistry of the Semiconductor Industry*. 1987.

61.   Petkov, V.; Hessel, C. M.; Ovtchinnikoff, J.; Guillaussier, A.; Korgel, B. A.; Liu, X.;

Giordano, C., Structure–Properties Correlation in Si Nanoparticles by Total Scattering and Computer Simulations. *Chemistry of Materials* **2013,** *25*, 2365-2371.

62.   Yoo, S.; Shao, N.; Zeng, X. C., Reexamine Structures and Relative Stability of Medium-Sized Silicon Clusters: Low-Lying Endohedral Fullerene-Like Clusters Si30–Si38. *Physics Letters A* **2009,** *373*, 3757-3760.

63.   Galashev, A. Y., Molecular Dynamics Study of Hydrogenated Silicon Clusters at High Temperatures. *Molecular Physics* **2009,** *107*, 2555-2568.

64.   Singh, R., Effect of Hydrogen on Ground State Properties of Silicon Clusters (Sinhm; N= 11–15, M= 0–4): A Density Functional Based Tight Binding Study. *Journal of Physics: Condensed Matter* **2008,** *20*, 045226.

65.   Crosby, L. D.; Kurtz, H. A., Application of Electronic Structure and Transition State Theory: Reaction of Hydrogen with Silicon Radicals. *International Journal of Quantum Chemistry* **2006,** *106*, 3149-3159.

66.   Zhao, M.; Gimarc, B. M., Strain Energies of Silicon Rings and Clusters. *Inorganic Chemistry* **1996,** *35*, 5378-5386.

67.   Raghavachari, K., Theoretical Study of Small Silicon Clusters: Equilibrium Geometries and Electronic Structures of Si N (N= 2–7, 10). *The Journal of chemical physics* **1986,** *84*, 5672-5686.

68.   Bandyopadhyay, D., Study of Pure and Doped Hydrogenated Germanium Cages: A Density Functional Investigation. *Nanotechnology* **2009,** *20*, 275202.

69.   Mahtout, S.; Tariket, Y., Electronic and Magnetic Properties of Crgen (15⩽ N⩽ 29) Clusters: A Dft Study. *Chemical Physics* **2016,** *472*, 270-277.

70.   Simmie, J. M., A Database of Formation Enthalpies of Nitrogen Species by Compound Methods (Cbs-Qb3, Cbs-Apno, G3, G4). *J Phys Chem A* **2015,** *119*, 10511-10526.

71.   Baboul, A. G.; Curtiss, L. A.; Redfern, P. C.; Raghavachari, K., Gaussian-3 Theory Using Density Functional Geometries and Zero-Point Energies. *The Journal of Chemical Physics* **1999,** *110*, 7650-7657.

72.   Kwok, S. H.; Yu, P. Y.; Tung, C. H.; Zhang, Y. H.; Li, M. F.; Peng, C. S.; Zhou, J. M., Confinement and Electron-Phonon Interactions of the E-1 Exciton in Self-Organized Ge Quantum Dots. *Physical Review B* **1999,** *59*, 4980-4984.

73.   Weissker, H. C.; Furthmuller, J.; Bechstedt, F., Excitation Energies and Radiative Lifetimes of Ge1-Xsix Nanocrystals: Alloying Versus Confinement Effects. *Physical Review Letters* **2003,** *90*.

74.   Balasubramanian, S.; Ceder, G.; Kolenbrander, K. D., Three-Dimensional Epitaxy: Thermodynamic Stability Range of Coherent Germanium Nanocrystallites in Silicon. *Journal of Applied Physics* **1996,** *79*, 4132-4136.

75.   Ren, S. F.; Cheng, W.; Yu, P. Y., Microscopic Investigation of Phonon Modes in Sige Alloy Nanocrystals. *Physical Review B* **2004,** *69*.

76.   Ramos, L. E.; Furthmuller, J.; Bechstedt, F., Quantum Confinement in Si- and Ge-Capped Nanocrystallites. *Physical Review B* **2005,** *72*.

77.   Viswanathan, R.; Schmude, R. W.; Gingerich, K. A., Molar Atomization Enthalpies and Molar Enthalpies of Formation of Gesi, Gesi2, Ge2si, and Ge2si2 by Knudsen-Effusion Mass-Spectrometry. *Journal of Chemical Thermodynamics* **1995,** *27*, 763-770.

78.   Drowart, J.; Demaria, G.; Boerboom, A. J. H.; Inghram, M. G., Mass Spectrometric Study of Inter-Group-Ivb Molecules. *Journal of Chemical Physics* **1959,** *30*, 308-313.

79.   Li, S.; Vanzee, R. J.; Weltner, W., Infrared-Spectra of the Gesi and Snsi Molecules in Argon Matrices. *Chemical Physics Letters* **1994,** *229*, 531-536.

80.   Andzelm, J.; Russo, N.; Salahub, D. R., Ground and Excited-States of Group Iva Diatomics from Local-Spin-Density Calculations - Model Potentials for Si, Ge, and Sn. *Journal of Chemical Physics* **1987,** *87*, 6562-6572.

81.   Sari, L.; Yamaguchi, Y.; Schaefer, H. F., (3)Sigma(-) and (3)Pi States of Gec and Gesi: The Problematic Dissociation Energy of Gec. *Journal of Chemical Physics* **2003,** *119*, 8266-8275.

82.   Palummo, M.; Onida, G.; Del Sole, R., Optical Properties of Germanium Nanocrystals. *Physica Status Solidi a-Applied Research* **1999,** *175*, 23-31.

83.   Jo, C.; Lee, K., Ionization Potentials and Cohesive Energies of Silicon Clusters from the Semi-Empirical Total Energy Tight Binding Method. *Physics Letters A* **1999,** *263*, 376-381.

84.   Li, S. D.; Zhao, Z. G.; Zhao, X. F.; Wu, H. S.; Jin, Z. H., Structural and Electronic Properties of Semiconductor Binary Microclusters a(M)B(N) (a,B = Si,Ge,C): A B3lyp-Dft Study. *Physical Review B* **2001,** *64*.

85.   Zhu, X. L.; Zeng, X. C., Structures and Stabilities of Small Silicon Clusters: Ab Initio Molecular-Orbital Calculations of Si-7-Si-11. *Journal of Chemical Physics* **2003,** *118*, 3558-3570.

86.   Broadbelt, L. J.; Stark, S. M.; Klein, M. T., Computer Generated Reaction Modelling: Decomposition and Encoding Algorithms for Determining Species Uniqueness. *Computers & Chemical Engineering* **1996,** *20*, 113-129.

87.   Wong, H.-W.; Li, X.; Swihart, M. T.; Broadbelt, L. J., Detailed Kinetic Modeling of Silicon Nanoparticle Formation Chemistry Via Automated Mechanism Generation. *The Journal of Physical Chemistry A* **2004,** *108*, 10122-10132.

88.   Slakman, B. L.; Simka, H.; Reddy, H.; West, R. H., Extending Reaction Mechanism Generator to Silicon Hydride Chemistry. *Industrial & Engineering Chemistry Research* **2016,** *55*, 12507-12515.

89.   Adamczyk, A. J.; Broadbelt, L. J., Thermochemical Property Estimation of Hydrogenated Silicon Clusters. *Journal of Physical Chemistry A* **2011,** *115*, 8969-8982.

90.   Frisch, M. J.; Trucks, G. W.; Schlegel, H. B.; Scuseria, G. E.; Robb, M. A.; Cheeseman, J. R.; Scalmani, G.; Barone, V.; Petersson, G. A.; Nakatsuji, H. et al. *Gaussian 16 Rev. C.01*, Wallingford, CT, 2016.

91.   Andzelm, J.; Russo, N.; Salahub, D. R., Ground and Excited-States of Group Iva Diatomics from Local-Spin-Density Calculations - Model Potentials for Si, Ge, and Sn. *J. Chem. Phys.* **1987,** *87*, 6562.

92.   Curtiss, L. A.; Redfern, P. C.; Rassolov, V.; Kedziora, G.; Pople, J. A., Extension of Gaussian-3 Theory to Molecules Containing Third-Row Atoms K, Ca, Ga–Kr. *J. Chem. Phys.* **2001,** *114*, 9287.

93.   Montgomery, J. A.; Frisch, M. J.; Ochterski, J. W.; Petersson, G. A., A Complete Basis Set Model Chemistry. Vi. Use of Density Functional Geometries and Frequencies. *The Journal of Chemical Physics* **1999,** *110*, 2822-2827.

94.   Kalcher, J.; Sax, A. F., Singlet Triplet Splittings and Electron-Affinities of Some Substituted Silylenes. *J. Mol. Struct.: THEOCHEM* **1992,** *253*, 287.

95.   Kassaee, M. Z.; Buazar, F.; Soleimani-Amiri, S., Triplet Germylenes with Separable Minima at Ab Initio and Dft Levels. *J. Mol. Struct.: THEOCHEM* **2008,** *866*, 52.

96.   Apeloig, Y.; Pauncz, R.; Karni, M.; West, R.; Steiner, W.; Chapman, D., Why Is Methylene a Ground State Triplet While Silylene Is a Ground State Singlet? *Organometallics* **2003,** *22*, 3250.

97.   Brulin, Q.; Ning, N.; Vach, H., Hydrogen-Induced Crystallization of Amorphous Silicon Clusters in a Plasma Reactor. *J. Non-Cryst. Solids* **2006,** *352*, 1055.

98.   Radom, A. P. S. a. L., Harmonic Vibrational Frequencies: An Evaluation of Hartree-Fock, Møller-Plesset, Quadratic Configuration Interaction, Density Functional Theory, and Semiempirical Scale Factors. *J. Phys. Chem.* **1996,** *100*, 16502-16513.

99.   Alecu, I. M.; Zheng, J.; Zhao, Y.; Truhlar, D. G., Computational Thermochemistry: Scale Factor Databases and Scale Factors for Vibrational Frequencies Obtained from Electronic Model Chemistries. *J. Chem. Theory Comput.* **2010,** *6*, 2872.

100.   Katzer, G.; Sax, A. F., Beyond the Harmonic Approximation: Impact of Anharmonic Molecular Vibrations on the Thermochemistry of Silicon Hydrides. *J. Phys. Chem. A* **2002,** *106*, 7204.

101.   Vansteenkiste, P.; Van Speybroeck, V.; Verniest, G.; De Kimpe, N.; Waroquier, M., Applicability of the Hindered Rotor Scheme to the Puckering Mode in Four-Membered Rings. *J. Phys. Chem. A* **2006,** *110*, 3838.

102.   McQuarrie, D. A. S., J. D. , *Molecular Thermodynamics;*. University Science Book: Sausalito, CA, 1999.

103.   Pfaendtner, J.; Yu, X.; Broadbelt, L. J., The 1-D Hindered Rotor Approximation. *Theoretical Chemistry Accounts* **2007,** *118*, 881-898.

104.   Petersson, G. A.; Malick, D. K.; Wilson, W. G.; Ochterski, J. W.; Montgomery, J. A.; Frisch, M. J., Calibration and Comparison of the Gaussian-2, Complete Basis Set, and Density Functional Methods for Computational Thermochemistry. *J. Chem. Phys.* **1998,** *109*, 10570.

105.   Wong, H. W.; Li, X.; Swihart, M. T.; Broadbelt, L. J., Detailed Kinetic Modeling of Silicon Nanoparticle Formation Chemistry Via Automated Mechanism Generation. *J. Phys. Chem. A* **2004,** *108*, 10122.

106.   Geerlings, P.; De Proft, F.; Langenaeker, W., Conceptual Density Functional Theory. *Chem. Rev.* **2003,** *103*, 1793.

107.   Pearson, R. G., Absolute Electronegativity and Hardness - Application to Inorganic-Chemistry. *Inorg. Chem.* **1988,** *27*, 734.

108.   Parr, R. G.; Pearson, R. G., Absolute Hardness - Companion Parameter to Absolute Electronegativity. *J. Am. Chem. Soc.* **1983,** *105*, 7512.

109.   Parr, R. G.; Donnelly, R. A.; Levy, M.; Palke, W. E., Electronegativity - Density

Functional Viewpoint. *J. Chem. Phys.* **1978,** *68*, 3801.

110.	Stein, T.; Autschbach, J.; Govind, N.; Kronik, L.; Baer, R., Curvature and Frontier Orbital Energies in Density Functional Theory. *J. Phys. Chem. Lett.* **2012,** *3*, 3740.

111.	Salzner, U.; Baer, R., Koopmans' Springs to Life. *J. Chem. Phys.* **2009,** *131*, 231101.

112.	Wielgus, P.; Roszak, S.; Majumdar, D.; Saloni, J.; Leszczynski, J., Theoretical Studies on the Bonding and Thermodynamic Properties of Gensim(M+N) Clusters: The Precursors of Germanium/Silicon Nanomaterials. *J. Chem. Phys.* **2008,** *128*, 144305.

113.	Chase, M. W., Nist-Janaf Thermochemical Tables for Oxygen Fluorides. *Journal of physical and chemical reference data* **1996,** *25*, 551-603.

114.	Swihart, M. T.; Girshick, S. L., Thermochemistry and Kinetics of Silicon Hydride Cluster Formation During Thermal Decomposition of Silane. *The Journal of Physical Chemistry B* **1999,** *103*, 64-76.

115.	Gordeychuk, M. V.; Katin, K. P.; Grishakov, K. S.; Maslov, M. M., Silicon Buckyballs Versus Prismanes: Influence of Spatial Confinement on the Structural Properties and Optical Spectra of the Si18h12 and Si19h12 Clusters. *Int. J. Quantum Chem.* **2018,** *118*, e25609.

116.	Coats, A. M.; McKean, D. C.; Steele, D., Infrared Intensities of Nu3 and Nu4 in Sih4, Geh4 and Snh4. *J. Mol. Struct.* **1994,** *320*, 269.

117.	Lattanzi, F.; Di Lauro, C.; Horneman, V. M., The N6, N8 3v4+N12 Infrared System of Si2h6 under High Resolution: Rotational and Torsional Analysis. *Mol. Phys.* **2003,** *101*, 2895.

118.	Bocanegra-Bernal, M. H.; Matovic, B., Mechanical Properties of Silicon Nitride-Based Ceramics and Its Use in Structural Applications at High Temperatures. *Materials Science and Engineering: A* **2010,** *527*, 1314-1338.

119.	Julian-Jankowiak, A.; Valle, R.; Parlier, M., Potential of Innovative Ceramics for Turbine Applications. *Materials at High Temperatures* **2016,** *33*, 578-585.

120.	Bocanegra-Bernal, M. H.; Matovic, B., Dense and near-Net-Shape Fabrication of Si3n4 Ceramics. *Materials Science and Engineering: A* **2009,** *500,* 130-149.

121.	Di Valentin, C.; Palma, G.; Pacchioni, G., Ab Initio Study of Transition Levels for Intrinsic Defects in Silicon Nitride. *The Journal of Physical Chemistry C* **2010,** *115*, 561-569.

122.	Peter Eigen, H. K.-R., Wolfgang Kurtz, Peter Me rlet , Hans Schafer, Friedrich SchrOder, *Gmelin Handbook of Inorganic Chemistry_System Si-N. Binary and Ternary Silicon Nitrides*. 1989.

123.	A.Zerr, Rapid Researchnote_a New High-Pressure D-Phaseof Si3n4. *phys. stat. sol. (b)* **2001,** *227*, R4–R6

124.	Zerr, A., Synthesis of Cubic Silicon Nitride. *Nature* **1999,** *400*, 340-342.

125.	Kroke, E., Novel Group 14 Nitrides. *Coordination Chemistry Reviews* **2004,** *248*, 493-532.

126.	Jaglarz, J.; Jurzecka-Szymacha, M.; Kluska, S., Film Materials Based on a-Sinx:H with High Refractive Index Obtained by Plasma Enhanced Chemical Vapour Deposition Technology. *Thin Solid Films* **2019,** *669*, 564-570.

127.	Torchynska, T. V.; Casas Espinola, J. L.; Vergara Hernandez, E.; Khomenkova, L.; Delachat, F.; Slaoui, A., Effect of the Stoichiometry of Si-Rich Silicon Nitride Thin Films on Their Photoluminescence and Structural Properties. *Thin Solid Films* **2015,** *581*, 65-69.

128.   Massines, F.; Silva, J.; Lelièvre, J.-F.; Bazinette, R.; Vallade, J.; Lecouvreur, P.; Pouliquen, S., Hydrogenated Silicon Nitride Sinx:H Deposited by Dielectric Barrier Discharge for Photovoltaics. *Plasma Processes and Polymers* **2016,** *13*, 170-183.

129.   Edwin Kroke, Y.-L. L., Christoph Konetschny, Emmanuel Lecomte, Claudia Fasel, Ralf Riedel, Silazane Derived Ceramics and Related Materials. *Materials Science and Engineering* **2000,** *26*, 97-199.

130.   F. Giorgis, C. F. P., E. Tresso, Structural Properties of a-Sil_Xn-H Films Grown by Plasma Enhanced Chemical Vapour Deposition by Sir 4 + Nh 3 + H 2 Gas Mixtures. *Thin Solid Films* **1997,** *307*, 298-305.

131.   Karouta, F.; Vora, K.; Tian, J.; Jagadish, C., Structural, Compositional and Optical Properties of Pecvd Silicon Nitride Layers. *Journal of Physics D: Applied Physics* **2012,** *45*.

132.   Chae, S.; Park, S.; Ahn, K.; Nam, G.; Lee, T.; Sung, J.; Kim, N.; Cho, J., Gas Phase Synthesis of Amorphous Silicon Nitride Nanoparticles for High-Energy Libs. *Energy & Environmental Science* **2020,** *13*, 1212-1221.

133.   Shi, B. D. E. a. Y., Formation-of-Aminosilanes-in-the-Hot-Wire-Chemical-Vapor. *ARKIVOC: Online Journal of Organic Chemistry* **2009**, 75-89.

134.   Yacoubi, K.; Azzaro, C.; Couderc, J. P., Low Pressure Cvd of Silicon Nitride from a Silane-Ammonia Mixture : Analysis of Preliminary Experimental and Simulation Results. *Le Journal de Physique IV* **1995,** *05*, C5-291-C295-298.

135.   O. Parise!, M. H., Y. Ellinger, Interstellar Silicon-Nitrogen Chemistry. I. The Microwave and the Infrared Signatures of the Hsin, Hnsi, Hsinh 2, Hnsih 2 and Hsinh. *Chemical Physics* **1996,** *212*, 331-351.

136.   Shao-Wen Hu, Y. W., Xiang-Yun Wang, Ti-Wei Chu, and Xin-Qi Liu, Gas-Phase Reactions between Silane and Ammonia a Theoretical Study. *J. Phys. Chem. A* **2003,** *107*, 9189-9196.

137.   Kovacevic, G.; Pivac, B., Reactions in Silicon-Nitrogen Plasma. *Phys Chem Chem Phys* **2017,** *19*, 3826-3836.

138.   Slakman, B. L.; Simka, H.; Reddy, H.; West, R. H., Extending Reaction Mechanism Generator to Silicon Hydride Chemistry. *Ind. Eng. Chem. Res.* **2016,** *55*, 12507.

139.   Broadbelt, L. J.; Stark, S. M.; Klein, M. T., Computer Generated Reaction Modelling: Decomposition and Encoding Algorithms for Determining Species Uniqueness. *Comput. Chem. Eng.* **1996,** *20*, 113.

140.   Curtiss, L. A.; Raghavachari, K.; Redfern, P. C.; Rassolov, V.; Pople, J. A., Gaussian-3 (G3) Theory for Molecules Containing First and Second-Row Atoms. *The Journal of Chemical Physics* **1998,** *109*, 7764-7776.

141.   Andrew J. Adamczyk, M.-F. R., ‡ Guy B. Marin,‡,§ and Linda J. Broadbelt*,, Exploring 1,2-Hydrogen Shift in Silicon Nanoparticles: Reaction Kinetics from Quantum Chemical Calculations and Derivation of Transition State Group Additivity Database. *J. Phys. Chem. A* **2009**, 10933–10946.

142.   Adamczyk, A. J.; Reyniers, M.-F.; Marin, G. B.; Broadbelt, L. J., Hydrogenated Amorphous Silicon Nanostructures: Novel Structure–Reactivity Relationships for

Cyclization and Ring Opening in the Gas Phase. *Theoretical Chemistry Accounts* **2010,** *128*, 91-113.

143.   Robert C. Parr, W. Y., Density-Functional Theory of the Electronic Structure of Molecules. *Annu. Rev. Phys. Chem.* **1995,** *46*, 701–728.

144.   Geerlings, P., Conceptual Density Functional Theory. *Chem. Rev.* **2003,** *103*, 1793-1873.

145.   Parr, R. G.; Pearson, R. G., Absolute Hardness: Companion Parameter to Absolute Electronegativity. *Journal of the American Chemical Society* **2002,** *105*, 7512-7516.

146.   Weinhold, F., Natural Bond Orbital Analysis: A Critical Overview of Relationships to Alternative Bonding Perspectives. *J Comput Chem* **2012,** *33*, 2363-2379.

147.   Mo, Y.; Zhang, Y.; Gao, J., A Simple Electrostatic Model for Trisilylamine: Theoretical Examinations of the N→Σ* Negative Hyperconjugation, Pπ→Dπbonding, and Stereoelectronic Interaction. *Journal of the American Chemical Society* **1999,** *121*, 5737-5742.

148.   B. BEAGLEY, A. R. C., New Electron-Diffraction Study of the Molecular Dimensions and Planarity of Trisilylamine. *Trans. Faraday Soc., 1970,66,* **1970,** *66*, 2740-2744.

149.   Hedberg, K., The Molecular Structure of Trisilylamine (Sih3)3n1,2. *Journal of the American Chemical Society* **1955,** *77*, 6491-6492.

150.   Choi, Y.; Adamczyk, A. J., Tuning Hydrogenated Silicon, Germanium, and Sige Nanocluster Properties Using Theoretical Calculations and a Machine Learning Approach. *J Phys Chem A* **2018,** *122*, 9851-9868.

151.   Yashima, M.; Ando, Y.; Tabira, Y., Crystal Structure and Electron Density of A-Silicon Nitride: Experimental and Theoretical Evidence for the Covalent Bonding and Charge Transfer. *The Journal of Physical Chemistry B* **2007,** *111*, 3609-3613.

152.   Shimanouchi, T., *Tables of Molecular Vibrational Frequencies*. National Bureau of Standards Washington, DC: 1972; Vol. 1.

153.   Beach, D. B., Infrared and Mass Spectroscopic Study of the Reaction of Silyl Iodide and Ammonia. Infrared Spectrum of Silylamine. *Inorganic Chemistry* **1992,** *31*, 4174-4177.

154.   Dean, J.; Lange, N., Section 4 Properties of Atoms, Radicals, and Bonds. *Lange's Handbook of Chemistry, 15th ed.; McGraw-Hill, Inc.: New York, NY, USA* **1999**.

155.   Hirschfelder, J. O.; Wigner, E., Some Quantum-Mechanical Considerations in the Theory of Reactions Involving an Activation Energy. *The Journal of Chemical Physics* **1939,** *7*, 616-628.

156.   Walsh, R. B. a. R., Mechanism of Formation of Trl- and Tetrasllane in the Reaction of Atomic Hydrogen with Monosilane and the Thermochemistry of the Si2h4 Isomers. *J. Phys. Chem.* **1987,** *91*, 5765-5770.

157.   Li-Feng Cui, Y. Y., Ching-Mei Hsu, and Yi Cui, Carbon-Silicon Core-Shell Nanowires as High Capacity Electrode for Lithium Ion Batteries. *Nano Lett* **2009,** *9*, 3370-3374.

158.   Son, Y.; Sim, S.; Ma, H.; Choi, M.; Son, Y.; Park, N.; Cho, J.; Park, M., Exploring Critical Factors Affecting Strain Distribution in 1d Silicon-Based Nanostructures for Lithium-Ion Battery Anodes. *Adv Mater* **2018,** *30*, e1705430.

159.   Ahmad, M.; Zhao, J.; Pan, C.; Zhu, J., Ordered Arrays of High-Quality Single-

Crystalline A-Si3n4 Nanowires: Synthesis, Properties and Applications. *Journal of Crystal Growth* **2009,** *311*, 4486-4490.

160.   Mi-Hee Park, M. G. K., Jaebum Joo, Kitae Kim, Jeyoung Kim, Soonho Ahn, Yi Cui and Jaephil Cho, Silicon Nanotube Battery Anodes. *Nano Lett* **2009,** *9*, 3844-3847.

161.   Nguyen, B. M.; Swartzentruber, B.; Ro, Y. G.; Dayeh, S. A., Facet-Selective Nucleation and Conformal Epitaxy of Ge Shells on Si Nanowires. *Nano Lett* **2015,** *15*, 7258-7264.

162.   Xiao, W.; Zhou, J.; Yu, L.; Wang, D.; Lou, X. W., Electrolytic Formation of Crystalline Silicon/Germanium Alloy Nanotubes and Hollow Particles with Enhanced Lithium-Storage Properties. *Angew Chem Int Ed Engl* **2016,** *55*, 7427-7431.

163.   Park, H.; Yoon, N.; Kang, D.; Young, C.; Lee, J. K., Electrochemical Characteristics and Energy Densities of Lithium-Ion Batteries Using Mesoporous Silicon and Graphite as Anodes. *Electrochimica Acta* **2020,** *357*.

164.   Yoon, N.; Young, C.; Kang, D.; Park, H.; Lee, J. K., High-Conversion Reduction Synthesis of Porous Silicon for Advanced Lithium Battery Anodes. *Electrochimica Acta* **2021,** *391*.

165.   Guler, I., Optical and Structural Characterization of Silicon Nitride Thin Films Deposited by Pecvd. *Materials Science and Engineering: B* **2019,** *246*, 21-26.

166.   Jiang, W.; Xu, D.; Xiong, B.; Wang, Y., Effects of Rapid Thermal Annealing on Lpcvd Silicon Nitride. *Ceramics International* **2016,** *42*, 1217-1224.

167.   Kuboi, N.; Tatsumi, T.; Minari, H.; Fukasawa, M.; Zaizen, Y.; Komachi, J.; Kawamura, T., Influence of Hydrogen in Silicon Nitride Films on the Surface Reactions During Hydrofluorocarbon Plasma Etching. *Journal of Vacuum Science & Technology A: Vacuum, Surfaces, and Films* **2017,** *35*.

168.   Gernot Katzer, M. C. E., Alexander F. Sax, and Josef Kalcher, Computational Thermochemistry of Medium-Sized Silicon Hydrides. . *J. Phys. Chem. A* **1997,** *101*, 3942-3958.

169.   Rosa Becerra, R. W., Some Mechanistic Problems in the Kinetic Modeling of Monosilane Pyrolysis. *J. Phys. Chem.* **1992,** *96*, 10856-10862.

170.   O'Neal, M. A. R. a. E., Mechanism of the Thermally Induced Gas-Phase Decomposition of Silane: A Revisitation. *J phys Chem* **1992,** *96*, 10848-10855.

171.   Giunta, C. J.; McCurdy, R. J.; Chapple-Sokol, J. D.; Gordon, R. G., Gas-Phase Kinetics in the Atmospheric Pressure Chemical Vapor Deposition of Silicon from Silane and Disilane. *Journal of Applied Physics* **1990,** *67*, 1062-1075.

172.   PARENT, F. S. a. J.-C., Homogeneous Gas-Phase Nucleation in Silane Pyrolysis. *J. Aerosol Sci.* **1994,** *25*, 15-21.

173.   Keiji Matsumoto, S. J. K., Kenichi Tonokura, and Mitsuo Koshi, Channel Specific Rate Constants Relevant to the Thermal Decomposition of Disilane. *J. Phys. Chem. A* **2005,** *109*, 4911-4920.

174.   A. P. Dickinson, E. O. N., and . A. Ring, Decomposition Kinetics and Thermochemistry of Butyl- and Pentylsilylenes. *Organometallics* **1991,** *10*, 3513-3520.

175.   Ekerdt, J. E. J. a. J. G., Gas-Phase Reaction Study of Disilane Pyrolysis: Applications to Low Pressure Chemical Vapor Deposition. *J._Electrochem._Soc.* **1994,** *141*, 2135.

176.   W. L. M. Weerts, M. H. J. M. d. C. a. G. B. M., The Kinetics of the Low-Pressure Chemical Vapor Deposition of Polycrystalline Silicon from Silane. *Journal of The Electrochemical Society* **1998,** *145,* 1318-1330.

177.   Nguyen, H. T.; Hang, T. D.; Nguyen, M. T., Theoretical Study of Silicon Monoxide Reactions with Ammonia and Methane. *J Phys Chem A* **2017,** *121,* 1032-1040.

178.   R. T. Conlin, D. L., and Paul Marshall*, A Theoretical Investigation of Donor-Acceptor Bonding between Amines and Silylenes. *Organometallics* **1994,** *13,* 838-842.

179.   Badaruddin, M. R.; Muhamad, M. R.; Rahman, S. A., Multi-Phase Structured Silicon Carbon Nitride Thin Films Prepared by Hot-Wire Chemical Vapour Deposition. *Thin Solid Films* **2011,** *519,* 5082-5085.

180.   Ma, Z.; Zhou, J.; Chen, Z.; Xie, E., Luminescence Properties of Terbium-Doped Sicn Thin Films by Rf Magnetron Reactive Sputtering. *Diamond and Related Materials* **2011,** *20,* 475-479.

181.   Bulou, S.; Brizoual, L. L.; Miska, P.; Poucques, L. d.; Hugon, R.; Belmahi, M., A-Sicxnythin Films Deposited by a Microwave Plasma Assisted Cvd Process Using a Ch4/N2/Ar/Hmdsn Mixture: Methane Rate Effect. *IOP Conference Series: Materials Science and Engineering* **2010,** *12.*

182.   Belmahi, M.; Bulou, S.; Thouvenin, A.; de Poucques, L.; Hugon, R.; Le Brizoual, L.; Miska, P.; Genève, D.; Vasseur, J.-L.; Bougdira, J., Microwave Plasma Process for Sicn:H Thin Films Synthesis with Composition Varying from Sic:H to Sin:H in H2

/N2

/Ar/Hexamethyldisilazane Gas Mixture. *Plasma Processes and Polymers* **2014,** *11,* 551-558.

183.   Becke, A. D., Density-Functional Thermochemistry. Iii. The Role of Exact Exchange. *The Journal of Chemical Physics* **1993,** *98,* 5648-5652.

184.   Glendening, E. D.; Landis, C. R.; Weinhold, F., Nbo 7.0: New Vistas in Localized and Delocalized Chemical Bonding Theory. *J Comput Chem* **2019,** *40,* 2234-2241.

185.   Weinhold, F.; Landis, C. R.; Glendening, E. D., What Is Nbo Analysis and How Is It Useful? *International Reviews in Physical Chemistry* **2016,** *35,* 399-440.

186.   Choi, Y.; Adamczyk, A. J., Competitive Hydrogen Migration in Silicon Nitride Nanoclusters: Reaction Kinetics Generalized from Supervised Machine Learning. *J Phys Chem A* **2022,** *126,* 2677-2689.

187.   Choi, Y.; Preston, T. J.; Adamczyk, A. J., Data-Driven Investigation of Monosilane and Ammonia Co-Pyrolysis to Silicon-Nitride-Based Ceramic Nanomaterials. *Chemphyschem* **2020,** *21,* 2627-2642.

188.   Mokrane, Z.; Zouchoune, B.; Zaiter, A., Coordination's Preference and Electronic Structure of N-Heterocyclic Carbene–Monometallic Complexes: Dft Evaluation of Σ-Bonding and Π-Backbonding Interactions. *Theoretical Chemistry Accounts* **2020,** *139.*

189.   Wu, W.; Li, X.; Meng, L.; Zheng, S.; Zeng, Y., Understanding the Properties of Inorganic Benzenes Based on Pi-Electron Densities. *J Phys Chem A* **2015,** *119,* 2091-2097.

190.   Stasyuk, O. A.; Szatylowicz, H.; Krygowski, T. M.; Fonseca Guerra, C., How Amino

and Nitro Substituents Direct Electrophilic Aromatic Substitution in Benzene: An Explanation with Kohn-Sham Molecular Orbital Theory and Voronoi Deformation Density Analysis. *Phys Chem Chem Phys* **2016,** *18*, 11624-11633.

191.   Yeseul Choi, A. J. A., Stabilizing Silicon Nitride Nanoparticles in Hydrogen Atmosphere: Electronic Characteristics and Reaction Kinetics. 2022.

192.   Role of Frontier Orbitals in Chemical Reaction. *Chemical Reactions. Science* **1982,** *218*, 474-754.

193.   Prabhaharan, M.; Prabakaran, A. R.; Gunasekaran, S.; Srinivasan, S., Dft Studies on Vibrational Spectra, Homo-Lumo, Nbo and Thermodynamic Function Analysis of Cyanuric Fluoride. *Spectrochim Acta A Mol Biomol Spectrosc* **2015,** *136 Pt B*, 494-503.

194.   R. William S. Aird, C. E. C.-M., David J. Cook, George Marston, Paul S. Monks and Richard P. Wayne, Kinetics of the Reactions of the Nitrate Radical with a Series of Halogenobutenes. *J. CHEM. SOC. FARADAY TRANS* **1992,** *88*, 1093-1099.

195.   Frontier Molecular Orbital Correlations for Predicting Rate Constants between Alkenes and the Tropospheric Oxidants No3, Oh and O3. *Phys. Chem. Chem. Phys.* **1999,** *1*, 2231-2238.

196.   Nori-Shargh, D.; Roohi, F.; Deyhimi, F.; Naeem-Abyaneh, R., Dft Study and Nbo Analysis of the Metallotropic Shifts in Cyclopentadienyl(Trimethyl)Silane, -Germane and -Stannane. *Journal of Molecular Structure: THEOCHEM* **2006,** *763*, 21-28.

197.   Glendening, E. D.; Landis, C. R.; Weinhold, F., Natural Bond Orbital Methods. *WIREs Computational Molecular Science* **2011,** *2*, 1-42.

198.   Natural Bond Orbital (Nbo) Analysis and Binding Affinity Towards Protein Kinase 2: Dft and Docking Studies of Coumarin Derivatives. *Chemical Science Transactions* **2014**.

199.   Gangadharan, R. P.; Sampath Krishnan, S., Natural Bond Orbital (Nbo) Population Analysis of 1-Azanapthalene-8-Ol. *Acta Physica Polonica A* **2014,** *125*, 18-22.

200.   Mary, Y. S.; El-Brollosy, N. R.; El-Emam, A. A.; Al-Deeb, O. A.; Jojo, P. J.; Panicker, C. Y.; Van Alsenoy, C., Vibrational Spectra, Nbo Analysis, Homo-Lumo and First Hyperpolarizability of 2-{[(2-Methylprop-2-En-1-Yl)Oxy]Methyl}-6-Phenyl-2,3,4,5-Tetrahydro-1,2,4-Triazin E-3,5-Dione, a Potential Chemotherapeutic Agent Based on Density Functional Theory Calculations. *Spectrochim Acta A Mol Biomol Spectrosc* **2014,** *133*, 449-456.

201.   Sinha, L.; Karabacak, M.; Narayan, V.; Cinar, M.; Prasad, O., Molecular Structure, Electronic Properties, Nlo, Nbo Analysis and Spectroscopic Characterization of Gabapentin with Experimental (Ft-Ir and Ft-Raman) Techniques and Quantum Chemical Calculations. *Spectrochim Acta A Mol Biomol Spectrosc* **2013,** *109*, 298-307.

202.   Ishitani, A.; Koseki, S., A Model for Sinx Cvd Film Growth Mechanism by Using Sih4 and Nh3 Source Gases. *Japanese journal of applied physics* **1990,** *29*, L2322.

203.   Tachibana, A.; Yamaguchi, K.; Kawauchi, S.; Kurosaki, Y.; Yamabe, T., Silyl Radical Mechanisms for Silicon-Nitrogen Bond Formation. *Journal of the American Chemical Society* **1992,** *114*, 7504-7507.

204.   Umemoto, H.; Morimoto, T.; Yamawaki, M.; Masuda, Y.; Masuda, A.; Matsumura, H., Deposition Chemistry in the Cat-Cvd Processes of the Sih4/Nh3 System. *Thin Solid Films* **2003,**

430, 24-27.

205.   Kushner, M. J., Simulation of the Gas-Phase Processes in Remote-Plasma-Activated Chemical-Vapor Deposition of Silicon Dielectrics Using Rare Gas–Silane-Ammonia Mixtures. *Journal of Applied Physics* **1992,** *71*, 4173-4189.

206.   Viera, G.; Andújar, J.; Sharma, S.; Bertran, E., Nanopowder of Silicon Nitride Produced in Radio Frequency Modulated Glow Discharges from Sih4 and Nh3. *Surface and Coatings Technology* **1998,** *100*, 55-58.

207.   Neumayer, D. *Pecvd Silicon Nitride Films*; IBM Research Report: Yorktown Heights, NY 10598 USA, 2013.

208.   Lanford, W. A.; Rand, M. J., The Hydrogen Content of Plasma-Deposited Silicon Nitride. *Journal of Applied Physics* **1978,** *49*.

209.   Karouta, F.; Vora, K.; Tian, J.; Jagadish, C., Structural, Compositional and Optical Properties of Pecvd Silicon Nitride Layers. *Journal of Physics D: Applied Physics* **2012,** *45*, 445301.

210.   Eustergerling, B. D.; Shi, Y., Formation of Aminosilanes in the Hot-Wire Chemical Vapor Deposition Process Using Sih 4-Nh 3 Gas Mixtures. *ARKIVOC: Online Journal of Organic Chemistry* **2009**.

211.   Adamczyk, A. J.; Cooper, A. C.; Kim, M.-S.; Ivanov, S. V., Leveraging Atomistic Modeling During Precursor Design for Cobalt Film Deposition. In *Computer Aided Chemical Engineering*, Eden, M. R.; Ierapetritou, M. G.; Towler, G. P., Eds. Elsevier: 2018; Vol. 44, pp 157-162.

212.   Petersen, E. L.; Crofton, M. W., Measurements of High-Temperature Silane Pyrolysis Using Sih4 Ir Emission and Sih2 Laser Absorption. *The Journal of Physical Chemistry A* **2003,** *107*, 10988-10995.

213.   Tonokura, K.; Murasaki, T.; Koshi, M., Formation Mechanism of Hydrogenated Silicon Clusters During Thermal Decomposition of Disilane. *The Journal of Physical Chemistry B* **2002,** *106*, 555-563.

214.   Blum, Y.; Laine, R., Catalytic Methods for the Synthesis of Oligosilazanes. *Organometallics* **1986,** *5*, 2081-2086.

215.   Parisel, O.; Hanus, M.; Ellinger, Y., Interstellar Silicon-Nitrogen Chemistry. I. The Microwave and the Infrared Signatures of the Hsin, Hnsi, Hsinh2, Hnsih2 and Hsinh+ Species. *Chemical physics* **1996,** *212*, 331-351.

216.   Hu, S.-W.; Wang, Y.; Wang, X.-Y.; Chu, T.-W.; Liu, X.-Q., Gas-Phase Reactions between Silane and Ammonia: A Theoretical Study. *The Journal of Physical Chemistry A* **2003,** *107*, 9189-9196.

217.   Adamczyk, A. J.; Reyniers, M. F.; Marin, G. B.; Broadbelt, L. J., Exploring 1,2-Hydrogen Shift in Silicon Nanoparticles: Reaction Kinetics from Quantum Chemical Calculations and Derivation of Transition State Group Additivity Database. *J. Phys. Chem. A* **2009,** *113*, 10933.

218.   Adamczyk, A. J.; Broadbelt, L. J., Thermochemical Property Estimation of Hydrogenated Silicon Clusters. *J. Phys. Chem. A* **2011,** *115*, 8969.

219. Yeseul Choi, A. J. A., Reaction Kinetics of Size Control of Silicon Nitride Nanoparticles: Silylene Addition-Elimination and Cyclization-Decyclization Reaction. 2022.

220. Becerra, R.; Cannady, J.; Walsh, R., The Gas-Phase Reaction of Silylene with Acetaldehyde Part 1. Direct Rate Studies, Isotope Effects, Rrkm Modelling and Ab Initio Studies of the Potential Energy Surface. *Physical Chemistry Chemical Physics* **2001,** *3*, 2343-2351.

221. Katritzky, A.; Ramsden, C.; Scriven, E.; Taylor, R., Three-Membered Heterocycles, Together with All Fused Systems Containing a Three-Membered Heterocyclic Ring. In *Comprehensive Heterocyclic Chemistry Iii*, Elsevier Ltd Emory University, Atlanta, GA, USA: 2008; Vol. 1, pp 1-104.

222. Becerra, R.; Walsh, R., Time-Resolved Gas-Phase Kinetic Study of the Reaction of Germylene with Propene over the Temperature Range 293–415 K: The Thermal Stabilities of Germiranes. *Journal of Organometallic Chemistry* **2001,** *636*, 49-55.

223. Girshick, S. L., Particle Nucleation and Growth in Dusty Plasmas: On the Importance of Charged-Neutral Interactions. *Journal of Vacuum Science & Technology A* **2020,** *38*.

224. A. A. Howling, C. C., J.-L. Dorier, L. Sansonnens, and Ch. Hollenstein, From Molecules to Particles in Silane Plasmas. *Pure & Appl. Chem.* **1996,** *68*, 1017-1022.

225. AA Howling, L. S., J.-L. Dorier and Ch. Hollenstein, Negative Hydrogenated Silicon Ion Clusters as Particle Precursors in Rf Silane Plasma Depostion Experiments. *J. Phys. D: Appl Phys* **1993**.

226. Chen, Z.; Wang, C.; Lopez, J.; Lu, Z.; Cui, Y.; Bao, Z., High-Areal-Capacity Silicon Electrodes with Low-Cost Silicon Particles Based on Spatial Control of Self-Healing Binder. *Advanced Energy Materials* **2015,** *5*, 1401826.

227. Fridman, A.; Boufendi, L.; Hbid, T.; Potapkin, B.; Bouchoule, A., Dusty Plasma Formation: Physics and Critical Phenomena. Theoretical Approach. *Journal of Applied Physics* **1996,** *79*, 1303-1314.

228. Pinnaduwage, L. A.; Datskos, P. G., Electron Attachment to Excited States of Silane: Implications for Plasma Processing Discharges. *Journal of applied physics* **1997,** *81*, 7715-7727.

229. Kushner, M. J., A Model for the Discharge Kinetics and Plasma Chemistry During Plasma Enhanced Chemical Vapor Deposition of Amorphous Silicon. *Journal of Applied Physics* **1988,** *63*, 2532-2551.

230. Bouhekka, A.; Kebab, A.; Sib, J. D.; Bouizem, Y.; Benbekhti, M.; Chahed, L., Monte-Carlo Simulation of Hydrogenated Amorphous Silicon Growth. *Journal of the Association of Arab Universities for Basic and Applied Sciences* **2018,** *12*, 11-16.

231. Barwe, B.; Riedel, F.; Cibulka, O. E.; Pelant, I.; Benedikt, J., Silicon Nanoparticle Formation Depending on the Discharge Conditions of an Atmospheric Radio-Frequency Driven Microplasma with Argon/Silane/Hydrogen Gases. *Journal of Physics D: Applied Physics* **2015,** *48*.

232. Bartlome, R.; De Wolf, S.; Demaurex, B.; Ballif, C.; Amanatides, E.; Mataras, D., Practical Silicon Deposition Rules Derived from Silane Monitoring During Plasma-Enhanced Chemical Vapor Deposition. *Journal of Applied Physics* **2015,** *117*.

233. Boufendi, A. B. a. L., Particulate Formation and Dusty Plasma Behaviour in Argon-

Silane Rf Discharge. *Plasma_Sources_Sci._Technol.* **1993,** *2*, 204-213.

234.   Gallagher, A.; Howling, A. A.; Hollenstein, C., Anion Reactions in Silane Plasma. *Journal of Applied Physics* **2002,** *91*, 5571-5580.

235.   Horvath, P.; Rozsa, K.; Gallagher, A., Production of Higher Silanes in Radio Frequency Sih4 and H2-Sih4 Plasmas. *Journal of Applied Physics* **2004,** *96*, 7660-7664.

236.   Kramer, N. J.; Anthony, R. J.; Mamunuru, M.; Aydil, E. S.; Kortshagen, U. R., Plasma-Induced Crystallization of Silicon Nanoparticles. *Journal of Physics D: Applied Physics* **2014,** *47*.

237.   U V Bhandarkar, M. T. S., S L Girshick and U R Kortshagen, Modelling of Silicon Hydride Clustering in a Low-Pressure Silane Plasma. *J. Phys. D: Appl. Phys.* **2000,** *33*, 2731–2746.

238.   Le Picard, R.; Markosyan, A. H.; Porter, D. H.; Girshick, S. L.; Kushner, M. J., Synthesis of Silicon Nanoparticles in Nonthermal Capacitively-Coupled Flowing Plasmas: Processes and Transport. *Plasma Chemistry and Plasma Processing* **2016,** *36*, 941-972.

239.   Nguyen, T.-N.; Lin, M. C., Ab Initio Chemical Kinetics for Sihxreactions with Si2hy(X= 1,2,3,4;Y= 6,5,4,3;X+Y= 7) under a-Si:H Cvd Condition. *International Journal of Chemical Kinetics* **2017,** *49*, 197-208.

240.   Jacoby, M., How Computers Are Helping Chemists Discover Materials That Don't yet Exist. *Chem. Eng. News* **2015,** *93*, 8-11.

241.   Yanai, T.; Tew, D. P.; Handy, N. C., A New Hybrid Exchange–Correlation Functional Using the Coulomb-Attenuating Method (Cam-B3lyp). *Chemical physics letters* **2004,** *393*, 51-57.

242.   Shamasundar, K.; Knizia, G.; Werner, H.-J., A New Internally Contracted Multi-Reference Configuration Interaction Method. *The Journal of chemical physics* **2011,** *135*, 054101.

243.   Deegan, M. J. O.; Knowles, P. J., Perturbative Corrections to Account for Triple Excitations in Closed and Open Shell Coupled Cluster Theories. *Chemical Physics Letters* **1994,** *227*, 321-326.

244.   Hampel, C.; Peterson, K. A.; Werner, H.-J., A Comparison of the Efficiency and Accuracy of the Quadratic Configuration Interaction (Qcisd), Coupled Cluster (Ccsd), and Brueckner Coupled Cluster (Bccd) Methods. *Chemical Physics Letters* **1992,** *190*, 1-12.

245.   H.-J. Werner, P. J. K., G. Knizia, F. R. Manby, M. Schütz, P. Celani, W. Györffy, D. Kats, T. Korona, R. Lindh, A. Mitrushenkov, G. Rauhut, K. R. Shamasundar, T. B. Adler, R. D. Amos, A. Bernhardsson, A. Berning, D. L. Cooper, M. J. O. Deegan, A. J. Dobbyn, F. Eckert, E. Goll, C. Hampel, A. Hesselmann, G. Hetzer, T. Hrenar, G. Jansen, C. Köppl, Y. Liu, A. W. Lloyd, R. A. Mata, A. J. May, S. J. McNicholas, W. Meyer, M. E. Mura, A. Nicklaß, D. P. O'Neill, P. Palmieri, D. Peng, K. Pflüger, R. Pitzer, M. Reiher, T. Shiozaki, H. Stoll, A. J. Stone, R. Tarroni, T. Thorsteinsson, M. Wang *Molpro 2015.1*.

246.   Warren, W. L.; Kanicki, J.; Robertson, J.; Lenahan, P. M., Energy Level of the Nitrogen Dangling Bond in Amorphous Silicon Nitride. *Applied Physics Letters* **1991,** *59*, 1699-1701.

247.   Claveau, E. E.; Choi, Y.; Adamczyk, A. J.; Miliordos, E., Electronic Structure of the Ground and Excited States of Neutral and Charged Silicon Hydrides, Sihx(0/+/-), X = 1-4. *Phys Chem Chem Phys* **2022,** *24*, 11782-11790.

248.	Choi, S. J.; Kushner, M. J., The Role of Negative Ions in the Formation of Particles in Low-Pressure Plasmas. *Journal of Applied Physics* **1993,** *74*, 853-861.

249.	Hollenstein, C., The Physics and Chemistry of Dusty Plasmas. *Plasma Physics and Controlled Fusion* **2000,** *42*, R93-R104.

250.	Bhandarkar, U.; Kortshagen, U.; Girshick, S. L., Numerical Study of the Effect of Gas Temperature on the Time for Onset of Particle Nucleation in Argon–Silane Low-Pressure Plasmas. *Journal of Physics D: Applied Physics* **2003,** *36*, 1399-1408.

251.	Bao, J. L.; Seal, P.; Truhlar, D. G., Nanodusty Plasma Chemistry: A Mechanistic and Variational Transition State Theory Study of the Initial Steps of Silyl Anion–Silane and Silylene Anion–Silane Polymerization Reactions. *Physical Chemistry Chemical Physics* **2015,** *17*, 15928-15935.

252.	Yeseul Choi, E. E. C., Evangelos Miliordos, Andrew J. Adamczyk, Micro Kinetic Study of Initial Steps of Silicon Nanocluster Synthesis by Free Radical-Silane and Anionic Radical-Silane. 2022.

Appendix

Appendix A.1. Calculated standard entropies and constant pressure heat capacities at elevated temperatures using the G3//B3LYP method for all hydrogenated Si, Ge, and SiGe clusters and acyclic species in this study.

Entropy (J/mol-K)

Temp (K) / Symmetry group / σ_{ext}	Acyclic structure							Trigonal Planar				Trigonal Pyramidal				
	Si_1H_4	Si_2H_6	Si_3H_8	$SiGeH_6$	Ge_1H_4	Ge_2H_6	Ge_3H_8	T-0	T-1	T-2	T-3	TP-0	TP-1	TP-2	TP-3	TP-4
Symmetry group	T_d	D_{3d}	C_{2v}	C_{3v}	T_d	D_{3d}	C_{2v}	D_{3h}	C_{2v}	C_{2v}	D_{3h}	T_d	C_{3v}	C_{2v}	C_{3v}	T_d
σ_{ext}	12	6	2	3	12	6	2	6	2	2	6	12	3	2	3	12
298.15	204.5	273.4	346.9	294.2	217.5	304.0	418.9	304.5	333.3	352.8	363.1	331.9	350.2	361.9	366.9	363.8
300	204.8	273.9	347.7	294.7	217.7	304.5	419.8	305.2	334.0	353.5	363.9	332.6	351.0	362.6	367.7	364.6
400	218.4	299.3	385.1	321.1	232.0	331.8	460.2	338.5	368.6	389.2	400.6	369.8	388.4	400.2	405.5	402.7
500	230.7	322.3	418.8	344.8	245.0	356.2	495.9	367.9	398.7	420.0	432.0	400.8	419.5	431.5	436.9	434.3
600	242.2	343.3	449.3	366.4	257.0	378.3	528.1	394.1	425.4	447.2	459.7	427.4	446.1	458.3	463.9	461.4
800	262.9	380.7	503.3	404.5	278.6	417.2	584.3	439.4	471.5	493.9	507.1	471.6	490.6	502.9	508.8	506.6
900	272.3	397.5	527.4	421.6	288.4	434.6	609.3	459.4	491.8	514.4	527.8	490.5	509.6	522.1	528.0	526.0
1000	281.2	413.2	549.8	437.5	297.6	450.8	632.4	478.0	510.5	533.4	547.0	507.8	527.0	539.6	545.7	543.7
1100	289.6	427.9	570.9	452.5	306.2	465.9	654.1	495.3	528.0	551.0	564.8	523.9	543.1	555.8	561.9	560.1
1200	297.5	441.8	590.7	466.5	314.4	480.1	674.3	511.5	544.4	567.5	581.4	538.8	558.1	570.8	577.0	575.2
1300	305.0	454.9	609.4	479.8	322.0	493.5	693.4	526.8	559.7	583.0	597.0	552.7	572.1	584.8	591.1	589.4
1400	312.2	467.3	627.0	492.3	329.3	506.1	711.4	541.2	574.2	597.6	611.7	565.8	585.2	598.0	604.3	602.6
1500	318.9	479.0	643.7	504.1	336.2	518.1	728.4	554.8	587.9	611.4	625.6	578.1	597.5	610.4	616.7	615.1

Constant Pressure Heat Capacity (J/mol-K)

Temp (K)	Si_1H_4	Si_2H_6	Si_3H_8	$SiGeH_6$	Ge_1H_4	Ge_2H_6	Ge_3H_8	T-0	T-1	T-2	T-3	TP-0	TP-1	TP-2	TP-3	TP-4
298.15	42.7	79.4	117.0	82.9	44.9	86.1	128.2	105.3	110.2	114.6	118.6	121.9	122.6	123.3	124.2	125.4
300	42.8	79.7	117.5	83.2	45.0	86.4	128.7	105.7	110.6	115.0	119.0	122.2	122.9	123.6	124.5	125.6
400	51.3	95.7	140.2	98.9	54.0	101.8	149.9	123.6	127.3	130.6	133.7	133.5	134.1	134.7	135.4	136.3
500	58.9	108.5	157.9	111.4	61.8	114.3	166.7	136.5	139.5	142.2	144.9	140.7	141.3	142.0	142.7	143.6
600	65.6	119.1	172.4	122.0	68.7	124.7	180.7	146.7	149.4	151.8	154.3	146.3	147.0	147.8	148.6	149.6
800	76.5	135.9	195.0	138.4	79.5	141.0	202.3	162.7	164.8	166.9	169.0	155.2	156.1	156.9	157.8	158.8
900	80.8	142.4	203.8	144.8	83.7	147.1	210.4	168.9	170.8	172.8	174.7	158.9	159.7	160.5	161.4	162.3
1000	84.5	147.9	211.1	150.1	87.1	152.2	217.2	174.1	175.9	177.6	179.4	162.0	162.7	163.5	164.4	165.2
1100	87.6	152.5	217.3	154.5	90.0	156.5	222.8	178.5	180.1	181.7	183.3	164.6	165.4	166.1	166.9	167.7
1200	90.2	156.4	222.4	158.2	92.4	160.0	227.4	182.2	183.7	185.1	186.5	166.9	167.6	168.2	168.9	169.7
1300	92.3	159.6	226.8	161.3	94.3	162.9	231.3	185.4	186.7	187.9	189.2	168.8	169.4	170.0	170.7	171.4
1400	94.2	162.4	230.5	163.9	96.0	165.3	234.5	188.0	189.2	190.3	191.5	170.4	171.0	171.6	172.2	172.8
1500	95.8	164.7	233.6	166.1	97.4	167.4	237.2	190.3	191.3	192.3	193.4	171.8	172.3	172.9	173.4	174.0

Appendix A.1 (continued)

Temp. (K)		ST-0	ST-1a	ST-1b	ST-1c	ST-2a	ST-2b	ST-2c	ST-2d	ST-3a	ST-3b	ST-3c	ST-4
							Entropy (J/mol-K)						
		Substituted trigonal planar											
	Symmetry group	Cs	Cs	Cs	C1	Cs	C1	C1	Cs	C1	Cs	Cs	Cs
	σ_{ext}	1	1	1	1	1	1	1	1	1	1	1	1
298.15		381.3	402.4	394.3	402.4	417.5	425.1	412.8	423.8	437.2	451.2	431.6	464.0
300		382.2	403.3	395.3	403.3	418.5	426.1	413.8	424.8	438.2	452.2	432.6	465.1
400		427.2	449.4	441.3	449.6	465.4	473.4	460.9	472.2	486.3	500.7	480.8	514.2
500		466.9	489.9	481.6	490.1	506.5	514.6	502.0	513.4	528.0	542.6	522.5	556.6
600		502.5	526.0	517.6	526.2	543.0	551.3	538.4	550.0	565.0	579.8	559.5	594.1
800		564.2	588.6	579.8	588.6	606.0	614.6	601.3	613.1	628.7	643.8	623.0	658.5
900		591.5	616.1	607.2	616.1	633.7	642.4	629.0	640.9	656.7	671.8	650.9	686.7
1000		616.8	641.7	632.6	641.6	659.4	668.1	654.6	666.6	682.6	697.8	676.8	712.8
1100		640.4	665.5	656.4	665.4	683.3	692.1	678.5	690.5	706.6	721.9	700.8	737.0
1200		662.5	687.8	678.6	687.6	705.7	714.6	700.8	712.9	729.2	744.5	723.3	759.7
1300		683.3	708.7	699.4	708.6	726.7	735.6	721.8	733.9	750.3	765.7	744.4	780.9
1400		702.9	728.5	719.1	728.3	746.5	755.5	741.6	753.8	770.2	785.6	764.3	800.9
1500		721.5	747.1	737.7	746.9	765.3	774.2	760.3	772.5	789.0	804.5	783.0	819.8
						Constant Pressure Heat Capacity (J/mol-K)								
298.15		141.9	145.7	146.1	146.9	149.5	150.7	150.5	151.5	153.9	155.2	154.8	158.1
300		142.5	146.2	146.6	147.4	150.0	151.2	151.1	152.0	154.4	155.7	155.3	158.6
400		167.0	170.3	170.0	170.7	173.1	174.0	173.3	174.1	176.4	177.5	176.6	179.6
500		184.8	188.0	187.1	187.9	190.1	191.0	190.0	190.8	192.9	193.9	192.7	195.6
600		199.1	202.1	201.0	201.8	203.9	204.8	203.6	204.4	206.4	207.3	206.1	208.9
800		221.2	223.8	222.6	223.4	225.2	226.0	224.7	225.5	227.4	228.2	226.9	229.5
900		229.7	232.2	231.0	231.7	233.4	234.2	232.9	233.6	235.3	236.1	234.9	237.3
1000		236.9	239.1	238.0	238.7	240.3	240.9	239.8	240.4	242.0	242.7	241.5	243.8
1100		242.9	245.0	243.9	244.5	246.0	246.6	245.5	246.1	247.5	248.2	247.1	249.1
1200		248.0	249.8	248.9	249.4	250.7	251.3	250.3	250.8	252.1	252.7	251.7	253.6
1300		252.2	253.9	253.0	253.5	254.7	255.2	254.3	254.8	256.0	256.5	255.6	257.3
1400		255.8	257.3	256.5	257.0	258.1	258.5	257.7	258.2	259.2	259.7	258.9	260.4
1500		258.9	260.3	259.5	259.9	260.9	261.3	260.6	261.0	261.9	262.4	261.6	263.0

Entropy (J/mol-K)												
	Trigonal Bipyramidal											
Temp. (K)	Symmetry group σ_{ext}	TBP-0 D_{3h} 6	TBP-1a C_{3v} 3	TBP-1b C_{2v} 2	TBP-2a D_{3h} 6	TBP-2b C_s 1	TBP-2c C_{2v} 2	TBP-3a C_{2v} 2	TBP-3b D_{3h} 6	TBP-3c C_s 1	TBP-4a C_{3v} 3	TBP-4b C_{2v} 2	TBP-5 D_{3h} 6
298.15		358.8	376.3	386.2	381.1	403.1	405.4	406.5	417.2	421.9	433.1	424.1	433.9
300		359.8	377.3	387.2	382.2	404.1	406.5	407.6	418.4	423.0	434.2	425.2	435.0
400		410.0	428.2	438.9	433.5	456.3	459.5	460.1	472.7	476.5	489.0	478.8	489.9
500		454.6	473.2	484.3	478.8	502.1	505.8	506.1	519.9	523.0	536.3	525.5	537.3
600		494.4	513.3	524.7	519.0	542.7	546.8	546.8	561.4	564.2	578.1	566.8	579.1
800		563.2	582.4	594.2	588.5	612.6	617.1	616.9	632.5	634.8	649.5	637.6	650.6
900		593.4	612.7	624.7	618.9	643.2	647.8	647.6	663.5	665.7	680.6	668.5	681.8
1000		621.3	640.8	652.9	647.1	671.5	676.2	676.0	692.2	694.2	709.3	697.1	710.6
1100		647.4	666.9	679.1	673.3	697.8	702.6	702.4	718.7	720.7	736.0	723.7	737.3
1200		671.8	691.4	703.6	697.8	722.3	727.3	727.0	743.5	745.4	760.8	748.5	762.3
1300		694.6	714.3	726.6	720.8	745.4	750.4	750.1	766.8	768.6	784.1	771.7	785.6
1400		716.2	735.9	748.3	742.4	767.1	772.2	771.9	788.6	790.4	806.0	793.5	807.5
1500		736.6	756.3	768.7	762.9	787.6	792.7	792.4	809.3	811.0	826.7	814.1	828.2
Constant Pressure Heat Capacity (J/mol-K)												
298.15		157.4	160.1	162.8	162.2	165.2	168.3	166.6	173.7	170.3	175.4	171.2	175.8
300		158.1	160.8	163.5	162.8	165.8	168.9	167.2	174.3	170.9	176.0	171.8	176.4
400		187.2	189.0	191.3	190.4	192.9	195.4	193.7	199.5	196.7	200.6	197.2	200.7
500		207.1	208.6	210.5	209.7	211.8	213.8	212.6	217.2	215.0	218.2	215.5	218.5
600		222.4	223.8	225.4	224.8	226.6	228.3	227.4	231.2	229.4	232.2	230.0	232.7
800		245.4	246.6	247.8	247.5	248.9	250.2	249.7	252.5	251.2	253.5	251.9	254.1
900		254.2	255.2	256.3	256.1	257.3	258.4	258.1	260.6	259.4	261.5	260.1	262.1
1000		261.5	262.5	263.4	263.3	264.3	265.3	265.0	267.2	266.2	268.1	266.9	268.7
1100		267.6	268.5	269.3	269.2	270.2	271.0	270.8	272.8	271.8	273.5	272.5	274.1
1200		272.8	273.5	274.3	274.2	275.0	275.8	275.6	277.3	276.5	278.0	277.1	278.6
1300		277.1	277.8	278.4	278.4	279.1	279.8	279.7	281.2	280.4	281.8	281.0	282.3
1400		280.7	281.3	281.9	281.9	282.5	283.1	283.0	284.4	283.7	285.0	284.2	285.4
1500		283.8	284.3	284.9	284.8	285.4	286.0	285.9	287.1	286.5	287.6	287.0	288.0

		Entropy (J/mol-K)												
		Prismane Pri-0	Pri-1	Pri-2a	Pri-2b	Pri-2c	Pri-3a	Pri-3b	Pri-3c	Pri-4a	Pri-4b	Pri-4c	Pri-5	Pri-6
Temp (K)	Symmetry group σ_{ext}	D_{3h} 6	C_s 1	C_s 1	C_{2v} 2	$C2$ 4	C_{3v} 3	$C1$ 2	C_s 1	C_s 1	C_{2v} 2	$C2$ 4	C_s 1	D_{3h} 6
	298.15	378.7	405.5	416.5	409.7	411.8	417.9	427.0	428.7	437.9	430.9	432.8	448.3	443.9
	300	379.8	406.6	417.6	410.8	412.9	419.0	428.1	429.8	439.1	432.1	434.0	449.5	445.0
	400	433.3	460.8	472.3	465.3	467.7	474.2	483.2	485.1	494.7	487.4	489.6	505.4	501.3
	500	479.3	507.2	519.0	511.9	514.4	521.2	530.1	532.1	541.9	534.6	536.8	552.9	549.0
	600	519.4	547.6	559.7	552.5	555.1	562.1	571.0	573.0	583.0	575.6	577.9	594.2	590.5
	800	587.1	615.7	628.1	620.9	623.5	630.9	639.8	641.9	652.1	644.6	647.0	663.6	660.3
	900	616.3	645.0	657.6	650.4	653.1	660.5	669.4	671.5	681.9	674.4	676.8	693.5	690.3
	1000	643.1	672.0	684.7	677.4	680.1	687.7	696.6	698.7	709.2	701.7	704.1	720.9	717.9
	1100	668.0	696.9	709.7	702.5	705.2	712.8	721.7	723.8	734.4	726.9	729.3	746.2	743.3
	1200	691.1	720.1	733.0	725.7	728.4	736.2	745.0	747.2	757.8	750.3	752.8	769.7	766.8
	1300	712.7	741.8	754.7	747.4	750.2	758.0	766.8	769.0	779.7	772.1	774.6	791.7	788.8
	1400	732.9	762.1	775.1	767.8	770.6	778.4	787.3	789.4	800.2	792.6	795.1	812.2	809.4
	1500	752.0	781.3	794.3	787.0	789.8	797.7	806.5	808.7	819.5	811.9	814.4	831.5	828.8
		Constant Pressure Heat Capacity (J/mol-K)												
	298.15	171.2	173.8	176.0	175.3	176.3	177.9	177.6	178.2	179.6	178.8	179.6	181.0	182.6
	300	171.8	174.4	176.5	175.9	176.8	178.5	178.1	178.8	180.1	179.3	180.1	181.5	183.1
	400	195.6	197.5	199.1	198.6	199.3	200.5	200.2	200.7	201.6	201.1	201.7	202.7	203.8
	500	210.8	212.4	213.7	213.4	213.9	215.0	214.8	215.1	216.1	215.7	216.1	217.1	218.2
	600	222.0	223.5	224.8	224.5	224.9	226.0	225.9	226.1	227.2	226.8	227.2	228.2	229.3
	800	238.6	239.9	241.1	240.9	241.1	242.2	242.2	242.3	243.3	243.1	243.4	244.4	245.5
	900	244.9	246.1	247.2	247.0	247.2	248.2	248.2	248.3	249.3	249.1	249.3	250.3	251.3
	1000	250.1	251.2	252.2	252.1	252.2	253.2	253.1	253.2	254.2	254.0	254.2	255.1	256.1
	1100	254.4	255.4	256.3	256.3	256.4	257.3	257.2	257.3	258.2	258.0	258.2	259.0	259.9
	1200	258.1	259.0	259.8	259.7	259.8	260.6	260.6	260.7	261.4	261.3	261.5	262.2	263.0
	1300	261.1	261.9	262.7	262.6	262.7	263.4	263.4	263.5	264.2	264.1	264.2	264.9	265.6
	1400	263.7	264.4	265.1	265.1	265.1	265.8	265.8	265.8	266.5	266.4	266.5	267.1	267.7
	1500	265.9	266.5	267.2	267.1	267.2	267.8	267.8	267.8	268.4	268.3	268.4	269.0	269.5

Appendix. A.2 Calculated standard entropies and constant pressure heat capacities at elevated temperatures using the G3//B3LYP method for all hydrogenated Si and SiN clusters and acyclic species in this study.

	Entropy (J/mol.K)															
Symmetry group	D3d	Cs	C2v	C1	Cs	C2	C2h	C1	C1	C1	C2h	C2	C1	C1	Cs	C1
σext	6	1	2	1	1	2	2	1	1	1	2	2	1	1	1	1
Temp. (K)	A2N0	A2N1	A3N0	A3N1a	A3N1b	A3N2	A4N0	A4N1a	A4N1b	A4N2a	A4N2b	A5N0	A5N1a	A5N1b	A5N1c	A5N2a
298.15	273.42	262.46	346.74	323.31	327.97	288.00	412.12	387.54	388.50	356.15	350.99	476.41	452.98	454.01	448.79	416.58
300	273.92	262.87	347.49	323.95	328.56	288.55	413.11	388.43	389.34	356.90	351.79	477.64	454.12	455.10	449.88	417.58
400	299.33	283.28	384.89	356.58	359.11	316.52	462.51	433.07	432.22	394.90	391.57	539.05	510.77	509.98	505.06	467.91
500	322.34	301.88	418.56	385.98	387.34	341.74	506.82	473.14	471.33	429.69	427.34	594.01	561.48	559.74	555.02	513.58
600	343.37	318.94	449.13	412.69	413.46	364.62	546.94	509.40	507.13	461.58	459.71	643.67	607.28	605.09	600.51	555.16
700	362.75	334.67	477.16	437.16	437.67	385.54	583.62	542.52	540.10	490.95	489.26	689.00	649.06	646.70	642.23	593.28
800	380.73	349.28	503.06	459.75	460.20	404.82	617.45	573.04	570.63	518.13	516.46	730.75	687.50	685.16	680.75	628.46
900	397.49	362.92	527.14	480.74	481.25	422.72	648.84	601.34	599.04	543.42	541.68	769.45	723.12	720.88	716.52	661.12
1000	413.19	375.70	549.62	500.35	500.97	439.44	678.10	627.74	625.59	567.06	565.19	805.50	756.29	754.21	749.89	691.59
1100	427.93	387.74	570.69	518.74	519.50	455.14	705.50	652.46	650.48	589.26	587.24	839.22	787.34	785.43	781.14	720.14
1200	441.80	399.10	590.49	536.06	536.97	469.95	731.22	675.70	673.90	610.16	607.99	870.87	816.51	814.77	810.51	747.00
1300	454.90	409.87	609.16	552.41	553.47	483.96	755.46	697.62	695.99	629.92	627.59	900.68	844.01	842.43	838.20	772.35
1400	467.29	420.08	626.81	567.90	569.10	497.27	778.37	718.36	716.90	648.64	646.17	928.84	870.00	868.59	864.37	796.34
1500	479.05	429.81	643.54	582.60	583.94	509.94	800.07	738.04	736.72	666.43	663.83	955.51	894.65	893.38	889.17	819.11

	Heat Capacity (J/mol.K)															
Temp. (K)	A2N0	A2N1	A3N0	A3N1a	A3N1b	A3N2	A4N0	A4N1a	A4N1b	A4N2a	A4N2b	A5N0	A5N1a	A5N1b	A5N1c	A5N2a
298.15	79.40	63.77	117.00	102.07	94.20	87.53	154.68	139.81	133.02	117.69	124.52	192.35	177.50	170.71	171.74	156.54
300	79.74	64.04	117.50	102.50	94.65	87.90	155.33	140.40	133.63	118.24	125.04	193.15	178.24	171.46	172.50	157.24
400	95.71	77.22	140.23	122.46	116.30	105.08	184.76	167.05	161.90	143.86	149.08	229.29	211.59	206.43	207.41	189.47
500	108.47	87.97	157.90	138.02	133.93	118.43	207.31	187.48	184.23	164.11	167.48	256.72	236.90	233.65	234.47	214.42
600	119.10	96.81	172.40	150.64	148.31	129.03	225.67	203.95	202.31	180.30	182.11	278.94	257.22	255.58	256.26	234.30
700	128.16	104.26	184.64	161.19	160.24	137.79	241.10	217.67	217.30	193.58	194.17	297.55	274.14	273.75	274.31	250.64
800	135.88	110.62	195.01	170.15	170.22	145.24	254.14	229.29	229.84	204.69	204.38	313.25	288.41	288.95	289.42	264.31
900	142.40	116.10	203.77	177.80	178.59	151.73	265.11	239.17	240.36	214.11	213.17	326.45	300.51	301.69	302.09	275.88
1000	147.90	120.84	211.12	184.36	185.63	157.45	274.32	247.58	249.19	222.16	220.80	337.52	310.79	312.39	312.73	285.72
1100	152.51	124.96	217.28	190.00	191.57	162.52	282.04	254.76	256.63	229.08	227.45	346.79	319.52	321.37	321.67	294.14
1200	156.38	128.54	222.45	194.84	196.59	167.02	288.50	260.90	262.90	235.04	233.27	354.55	326.95	328.94	329.20	301.35
1300	159.64	131.65	226.80	199.02	200.84	171.01	293.94	266.16	268.21	240.19	238.36	361.08	333.30	335.34	335.56	307.56
1400	162.40	134.36	230.47	202.63	204.46	174.55	298.53	270.68	272.72	244.65	242.82	366.58	338.74	340.77	340.97	312.91
1500	164.74	136.74	233.58	205.75	207.56	177.69	302.42	274.59	276.57	248.53	246.74	371.25	343.42	345.40	345.58	317.54

Appendix. A.2. Continued

	Entropy (J/mol.K)															
Symmetry group	C1	C2	C2	Cs	C2h	C1	C1	C1	C1	C1	C1	C1	C1	C2	C1	C1
σext	1	2	2	1	2	1	1	1	1	1	1	1	1	2	1	1
Temp. (K)	A5N2b	A5N2c	A5N2d	A5N3	A6N0	A6N1a	A6N1b	A6N1c	A6N2a	A6N2b	A6N2c	A6N2d	A6N2e	A6N2f	A6N3a	A6N3b
298.15	421.04	415.42	413.38	384.40	541.11	517.75	519.49	513.14	481.55	487.13	487.41	488.63	483.57	479.67	453.08	449.12
300	422.04	416.46	414.33	385.31	542.58	519.13	520.82	514.48	482.80	488.38	488.65	489.92	484.77	480.86	454.18	450.27
400	472.08	468.27	462.35	430.81	615.98	587.78	587.69	581.65	545.14	550.79	550.71	553.79	545.17	541.15	509.89	507.75
500	517.56	514.69	506.71	472.17	681.60	649.15	648.09	642.26	601.45	607.15	606.85	610.90	600.42	596.33	560.93	559.76
600	559.03	556.61	547.61	509.85	740.79	704.50	702.97	697.29	652.58	658.32	657.86	662.38	651.02	646.90	607.70	607.00
700	597.08	594.81	585.41	544.37	794.78	754.93	753.24	747.65	699.35	705.14	704.56	709.24	697.59	693.45	650.70	650.20
800	632.22	629.93	620.49	576.20	844.45	801.29	799.61	794.10	742.45	748.28	747.62	752.29	740.67	736.53	690.46	689.98
900	664.86	662.45	653.17	605.74	890.45	844.21	842.64	837.18	782.42	788.28	787.57	792.13	780.72	776.58	727.41	726.86
1000	695.32	692.75	683.73	633.30	933.28	884.17	882.75	877.33	819.67	825.56	824.81	829.22	818.12	813.98	761.91	761.23
1100	723.86	721.12	712.41	659.16	973.33	921.55	920.30	914.91	854.55	860.47	859.68	863.92	853.16	849.03	794.26	793.44
1200	750.72	747.80	739.41	683.50	1010.91	956.64	955.56	950.20	887.33	893.28	892.46	896.52	886.11	881.98	824.71	823.73
1300	776.07	772.97	764.91	706.51	1046.29	989.71	988.80	983.45	918.25	924.22	923.37	927.27	917.20	913.07	853.46	852.33
1400	800.06	796.81	789.04	728.32	1079.70	1020.96	1020.21	1014.88	947.49	953.48	952.62	956.36	946.60	942.48	880.69	879.42
1500	822.83	819.43	811.94	749.06	1111.34	1050.58	1049.97	1044.65	975.23	981.24	980.36	983.96	974.48	970.37	906.54	905.14
	Heat Capacity (J/mol.K)															
Temp. (K)	A5N2b	A5N2c	A5N2d	A5N3	A6N0	A6N1a	A6N1b	A6N1c	A6N2a	A6N2b	A6N2c	A6N2d	A6N2e	A6N2f	A6N3a	A6N3b
298.15	155.52	162.32	147.79	141.36	230.03	215.21	208.34	209.39	194.23	194.50	193.32	200.25	186.80	186.47	172.18	178.92
300	156.21	162.99	148.50	142.00	230.98	216.10	209.24	210.29	195.07	195.35	194.16	201.08	187.67	187.33	172.99	179.70
400	188.53	193.65	182.61	171.53	273.81	256.13	250.92	251.92	234.00	234.22	233.11	238.36	228.33	227.95	210.85	216.02
500	213.71	216.90	209.78	194.36	306.12	286.32	283.03	283.87	263.84	264.07	263.13	266.45	260.18	259.91	240.47	243.83
600	233.80	235.37	231.54	212.32	332.20	310.50	308.83	309.51	287.57	287.83	287.06	288.74	285.61	285.46	263.90	265.73
700	250.29	250.61	249.34	226.93	354.00	330.59	330.18	330.75	307.08	307.37	306.73	307.14	306.44	306.39	282.96	283.58
800	264.08	263.49	264.11	239.17	372.36	347.53	348.05	348.52	323.42	323.71	323.18	322.66	323.76	323.76	298.79	298.52
900	275.74	274.50	276.46	249.63	387.79	361.86	363.02	363.42	337.21	337.51	337.06	335.89	338.25	338.28	312.14	311.23
1000	285.64	283.99	286.84	258.69	400.72	373.99	375.58	375.92	348.91	349.21	348.83	347.23	350.42	350.47	323.49	322.15
1100	294.10	292.20	295.59	266.58	411.53	384.27	386.11	386.41	358.88	359.16	358.83	356.98	360.67	360.72	333.20	331.59
1200	301.34	299.32	303.01	273.48	420.60	393.00	394.98	395.23	367.39	367.66	367.38	365.39	369.34	369.40	341.54	339.78
1300	307.56	305.50	309.32	279.53	428.21	400.44	402.47	402.69	374.68	374.94	374.69	372.65	376.70	376.75	348.72	346.90
1400	312.93	310.88	314.71	284.84	434.63	406.80	408.82	409.01	380.96	381.19	380.98	378.95	382.98	383.02	354.94	353.11
1500	317.57	315.58	319.33	289.50	440.08	412.26	414.23	414.40	386.37	386.59	386.40	384.42	388.35	388.39	360.34	358.54

	Entropy (J/mol.K)															
Symmetry group	D3h	C2v	Td	C3v	D3h	C3v	Cs	D3h	Cs	Cs	Cs	C1	C1	D2d	C2v	C2h
σext	6	2	12	3	6	3	1	6	1	1	1	2	2	4	2	2
Temp. (K)	TN0	TN1	TPyN0	TPyN1	TBPyN0	TBPyN1a	TBPyN1b	TBPyN2	STN0	STN1a	STN1b	STN1c_ch	STN2_ch	SN0	SN1	SN2
298.15	304.46	281.95	332.08	316.37	358.80	333.47	353.57	303.44	381.21	355.46	355.25	347.18	317.62	348.33	324.56	299.07
300	305.13	282.47	332.85	316.99	359.80	334.32	354.46	304.16	382.11	356.29	355.98	347.94	318.29	349.21	325.29	299.68
400	338.44	308.75	370.07	347.47	410.06	377.55	399.30	341.71	427.10	397.06	393.06	386.58	352.42	393.26	362.52	331.16
500	367.80	332.76	401.04	373.50	454.66	416.88	439.52	376.58	466.86	432.92	426.95	421.39	383.13	432.59	396.55	360.55
600	394.00	354.63	427.59	396.15	494.47	452.52	475.60	408.52	502.42	464.85	457.91	452.88	410.85	467.92	427.56	387.64
700	417.69	374.64	450.91	416.22	530.42	484.99	508.27	437.79	534.64	493.66	486.37	481.58	436.04	500.03	455.95	412.60
800	439.36	393.06	471.79	434.28	563.23	514.79	538.10	464.74	564.15	519.96	512.66	507.95	459.13	529.48	482.12	435.66
900	459.36	410.12	490.73	450.70	593.43	542.30	565.56	489.68	591.39	544.19	537.08	532.34	480.44	556.69	506.37	457.06
1000	477.92	426.00	508.08	465.77	621.40	567.84	591.00	512.86	616.68	566.67	559.84	555.02	500.26	581.98	528.94	477.01
1100	495.24	440.85	524.11	479.68	647.45	591.66	614.69	534.49	640.29	587.65	581.14	576.20	518.78	605.58	550.06	495.68
1200	511.46	454.79	539.01	492.62	671.81	613.96	636.86	554.76	662.40	607.32	601.14	596.07	536.16	627.70	569.87	513.23
1300	526.72	467.93	552.93	504.70	694.69	634.92	657.68	573.81	683.20	625.83	619.98	614.78	552.55	648.50	588.54	529.78
1400	541.11	480.33	566.00	516.03	716.24	654.67	677.31	591.78	702.83	643.31	637.76	632.44	568.05	668.13	606.17	545.43
1500	554.72	492.09	578.31	526.69	736.62	673.35	695.88	608.77	721.40	659.87	654.61	649.17	582.75	686.70	622.87	560.27
	Heat Capacity (J/mol.K)															
Temp. (K)	TN0	TN1	TPyN0	TPyN1	TBPyN0	TBPyN1a	TBPyN1b	TBPyN2	STN0	STN1a	STN1b	STN1c_ch	STN2_ch	SN0	SN1	SN2
298.15	25.16	19.40	29.15	23.52	37.62	31.81	33.32	27.21	33.92	30.87	27.40	28.79	25.46	32.94	27.41	22.87
300	25.26	19.49	29.22	23.59	37.79	31.97	33.47	27.37	34.05	30.98	27.53	28.92	25.57	33.08	27.55	22.99
400	29.54	23.83	31.92	26.56	44.74	39.07	40.19	34.38	39.91	36.08	33.55	34.68	30.62	39.33	33.72	28.88
500	32.61	27.03	33.63	28.53	49.50	44.06	44.81	39.34	44.18	39.76	38.14	38.96	34.35	43.82	38.26	33.30
600	35.06	29.50	34.96	30.01	53.17	47.86	48.29	43.07	47.59	42.65	41.80	42.31	37.21	47.37	41.78	36.66
700	37.12	31.50	36.11	31.20	56.16	50.91	51.07	46.00	50.44	45.05	44.80	45.04	39.50	50.31	44.64	39.32
800	38.87	33.15	37.10	32.17	58.66	53.40	53.36	48.38	52.86	47.09	47.28	47.31	41.41	52.79	47.00	41.49
900	40.36	34.53	37.97	32.98	60.75	55.45	55.27	50.32	54.90	48.83	49.35	49.22	43.04	54.86	48.97	43.28
1000	41.61	35.69	38.72	33.65	62.50	57.15	56.87	51.91	56.61	50.34	51.06	50.82	44.43	56.60	50.62	44.78
1100	42.67	36.67	39.35	34.20	63.97	58.55	58.22	53.23	58.05	51.63	52.48	52.16	45.65	58.05	52.00	46.06
1200	43.55	37.50	39.89	34.66	65.19	59.72	59.36	54.32	59.26	52.75	53.66	53.30	46.71	59.27	53.17	47.15
1300	44.30	38.22	40.35	35.05	66.22	60.70	60.32	55.23	60.28	53.72	54.65	54.27	47.63	60.30	54.16	48.09
1400	44.94	38.82	40.74	35.37	67.09	61.53	61.15	56.00	61.14	54.55	55.48	55.10	48.44	61.16	55.01	48.89
1500	45.48	39.35	41.07	35.65	67.82	62.22	61.85	56.65	61.88	55.28	56.19	55.81	49.15	61.89	55.73	49.59

Appendix. A.2. Continued

Entropy (J/mol.K)										
Symmetry group	C1	C2	C2v	D3d	Cs	C1	C2h	Cs	D3h	Cs	C2
σext	1	2	2	6	1	1	2	1	6	1	2
Temp. (K)	PN0	PN1	PN2	HN0	HN1	HN2a	HN2b	HN3	PriN0	PriN1	PriN2
298.15	426.97	385.89	352.76	444.00	433.80	408.57	402.95	375.50	378.71	364.80	335.19
300	428.08	386.86	353.60	445.35	435.02	409.66	404.02	376.45	379.81	365.74	336.00
400	483.71	436.01	396.58	512.62	496.21	464.72	458.55	424.94	433.33	412.39	376.79
500	533.46	480.61	436.20	572.81	551.47	515.05	508.55	470.07	479.31	453.26	413.14
600	578.20	521.09	472.54	626.97	601.50	560.96	554.26	511.68	519.41	489.32	445.48
700	618.88	558.08	505.93	676.22	647.16	603.02	596.22	550.03	555.02	521.54	474.50
800	656.19	592.13	536.77	721.42	689.14	641.78	634.92	585.49	587.09	550.66	500.79
900	690.67	623.66	565.39	763.18	727.99	677.70	670.80	618.43	616.30	577.24	524.80
1000	722.71	653.00	592.06	801.98	764.12	711.14	704.24	649.15	643.14	601.69	546.90
1100	752.62	680.43	617.02	838.20	797.88	742.43	735.52	677.92	667.97	624.31	567.35
1200	780.65	706.16	640.47	872.15	829.55	771.79	764.89	704.96	691.07	645.37	586.39
1300	807.01	730.39	662.57	904.08	859.35	799.46	792.56	730.47	712.66	665.06	604.18
1400	831.88	753.27	683.46	934.20	887.49	825.60	818.71	754.60	732.94	683.55	620.89
1500	855.42	774.94	703.27	962.70	914.13	850.37	843.49	777.48	752.05	700.97	636.63
Heat Capacity (J/mol.K)											
Temp. (K)	PN0	PN1	PN2	HN0	HN1	HN2a	HN2b	HN3	PriN0	PriN1	PriN2
298.15	41.54	36.38	31.52	50.21	45.44	40.58	40.10	35.32	40.91	35.17	30.38
300	41.72	36.55	31.68	50.43	45.65	40.77	40.30	35.51	41.05	35.31	30.52
400	49.68	44.27	39.08	60.07	54.94	49.79	49.40	44.33	46.76	41.25	36.46
500	55.43	49.97	44.69	67.05	61.80	56.55	56.25	51.05	50.37	45.10	40.34
600	59.95	54.43	49.04	72.55	67.18	61.80	61.60	56.23	53.06	47.91	43.10
700	63.69	58.06	52.53	77.10	71.57	66.03	65.90	60.35	55.23	50.10	45.20
800	66.83	61.07	55.40	80.89	75.22	69.52	69.44	63.71	57.02	51.86	46.86
900	69.45	63.59	57.78	84.07	78.26	72.43	72.38	66.49	58.52	53.30	48.19
1000	71.65	65.69	59.77	86.72	80.81	74.86	74.85	68.83	59.77	54.48	49.28
1100	73.48	67.45	61.45	88.94	82.94	76.91	76.91	70.81	60.81	55.46	50.16
1200	75.02	68.94	62.88	90.79	84.74	78.65	78.66	72.50	61.68	56.27	50.89
1300	76.31	70.20	64.09	92.34	86.25	80.13	80.14	73.94	62.41	56.94	51.50
400	77.40	71.26	65.13	93.65	87.54	81.39	81.41	75.18	63.03	57.50	52.00
1500	78.32	72.17	66.03	94.76	88.63	82.47	82.49	76.26	63.55	57.98	52.43

Appendix A.3.

Figure A3. Calculated contour surfaces of frontier molecular orbitals (HOMO, LUMO) for all Hydrogenated Si and SiN clusters using the G3//B3LYP level of theory. The HOMO and LUMO orbital distributions for all clusters are presented using an isovalue of 0.02.
The nomenclature to identify cluster geometries is the same as in Figure 2.1.1.

Figure A3. (continued)

HOM	LUM	HOM	LUM	HOM	LUM

A5N1

A5N2a

A5N2b

A5N2c

A5N2d

A5N3

A6N0

A6N1a

A6N1b

A6N1

A6N2a

A6N2b

A6N2c

A6N2d

A6N2e

A6N2f

A6N3

A6N3b

Figure A3. (continued)

HOMO	LUMO	HOMO	LUMO	HOMO	LUMO

TN0   TN1

SN0   SN1   SN2

STN0   STN1a   STN1b

STN1c_ch   STN2_ch

PN0   PN1   PN2

Figure A3. (continued)

HOMO	LUMO	HOMO	LUMO	HOMO	LUMO

HN0 HN1 HN
2a

HN2b HN3

TPyN0 TPyN1 TBPyN0

TBPyN1a TBPyN1b TBPyN2

PriN0 PriN1 PriN2
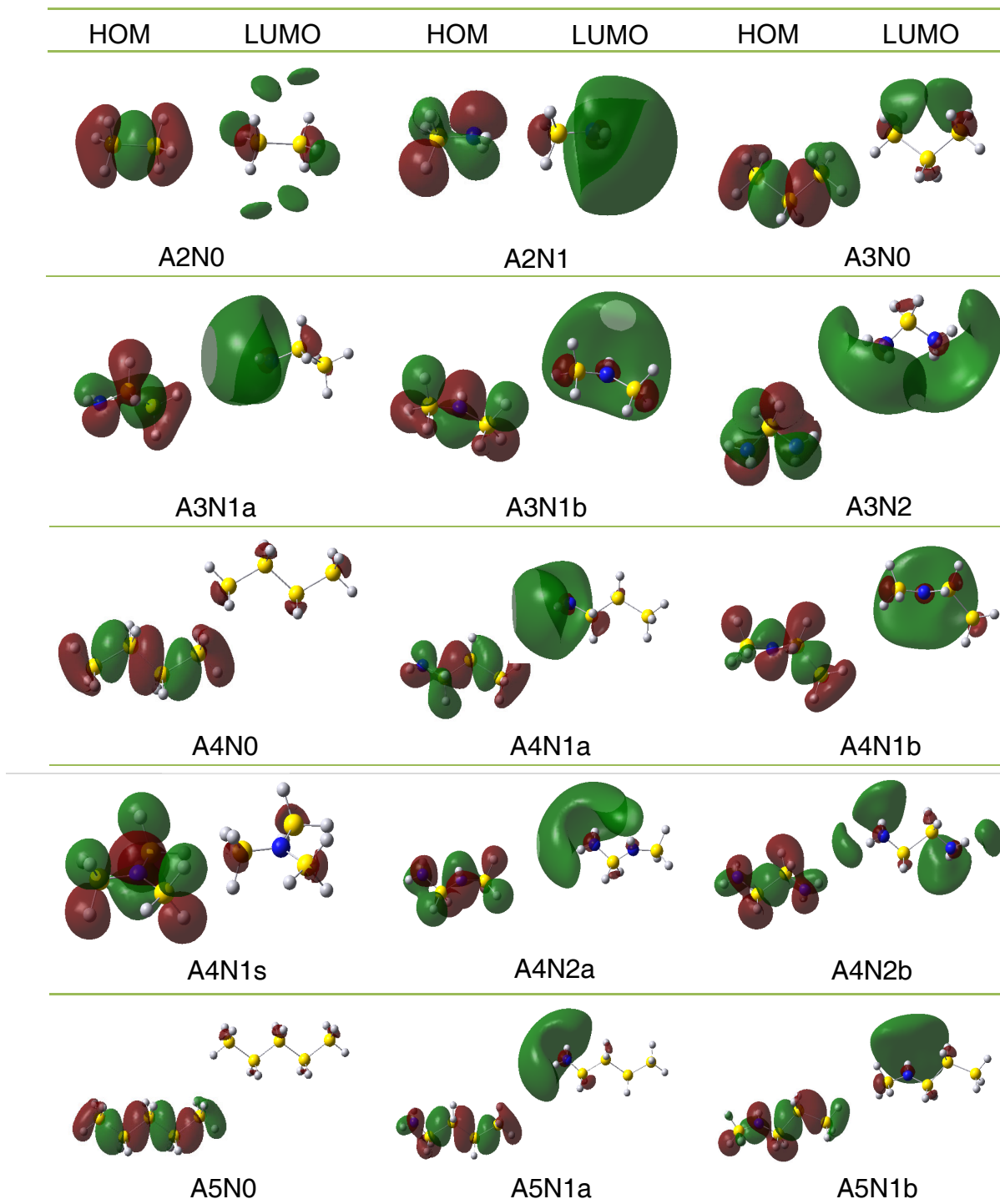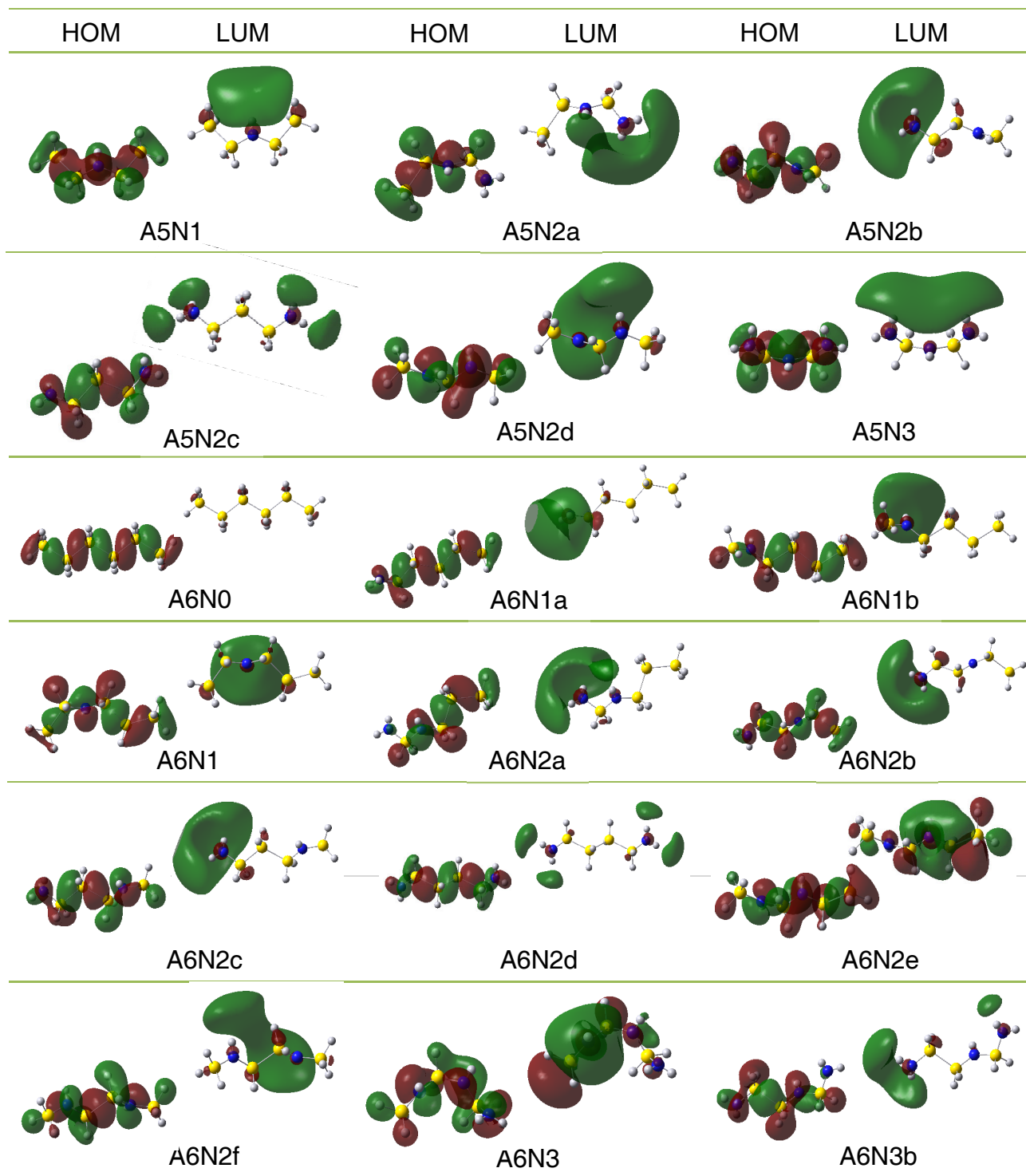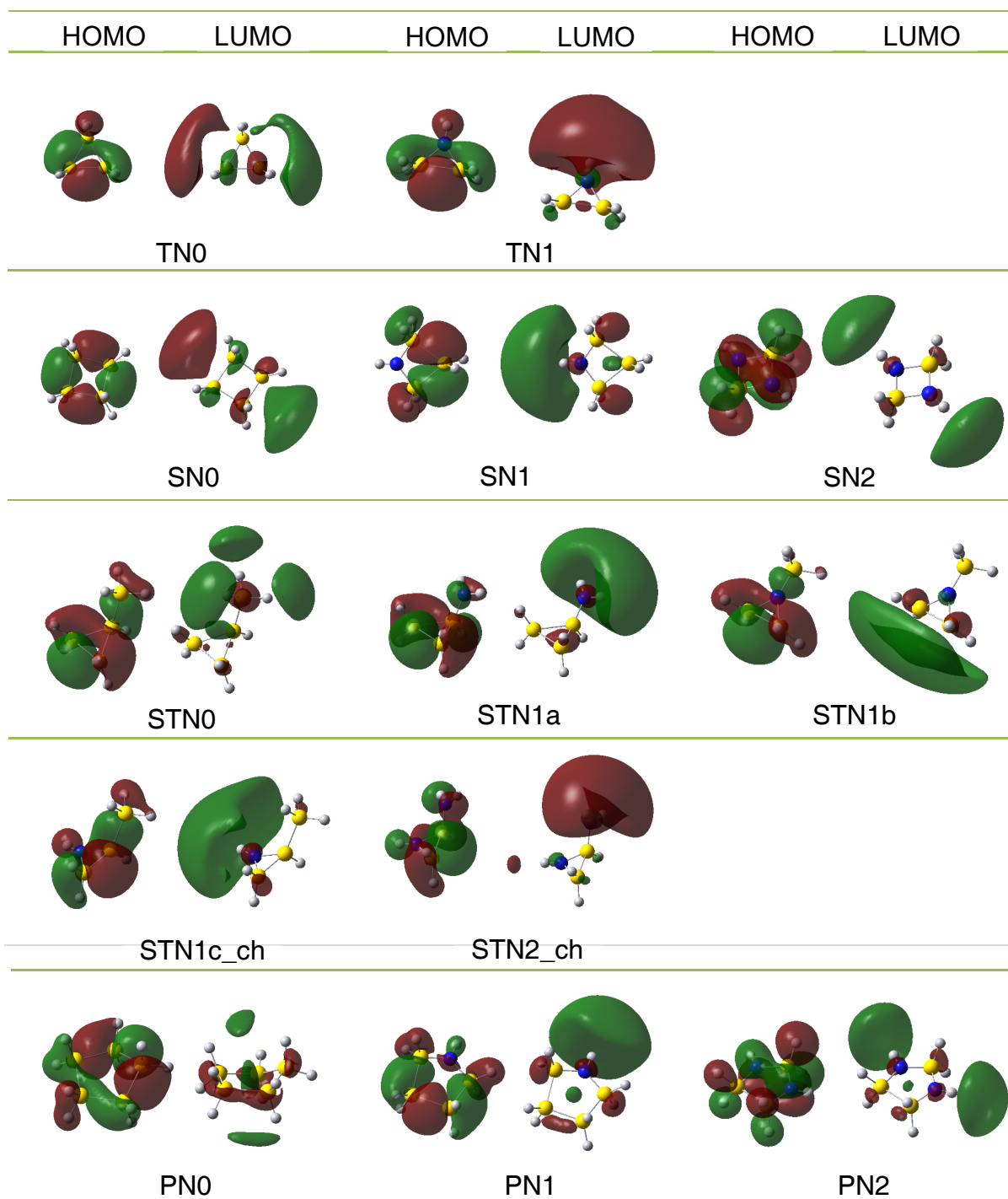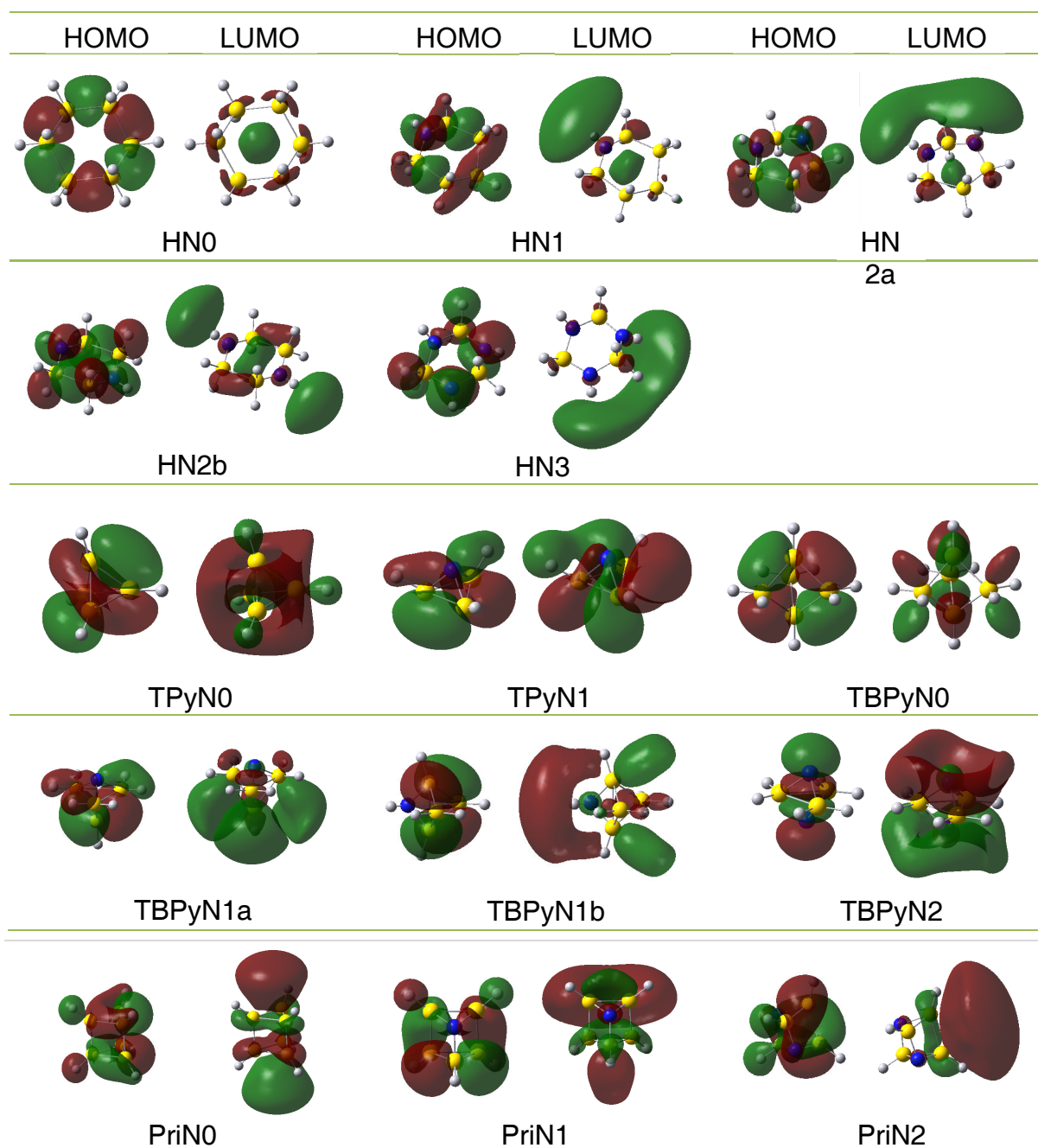
Appendix A.4

Table A4.
a) Second order perturbation theory analysis of Fock matrix in NBO basis for A4N0

A4N0

A4N0

Donor (i)				type	Acceptor (j)					type	E(2) kcal/mol	E(j)-E(i) a.u.	F(i,j) a.u.
Si	1			CR(2)	Si	1	-	Si	4	σ*	0.67	5.72	0.055
					H	2	-			RY*(1)	0.66	6.48	0.058
					H	3	-			RY*(1)	0.66	6.48	0.058
Si	4			CR(2)	Si	1	-	Si	4	σ*	0.62	5.78	0.053
					H	5	-			RY*(1)	0.64	6.53	0.058
					H	6	-			RY*(1)	0.62	6.53	0.057
					H	7	-			RY*(1)	0.64	6.53	0.058
Si	8			CR(2)	Si	8	-	Si	11	σ*	0.67	5.72	0.055
					H	9	-			RY*(1)	0.66	6.48	0.058
					H	10	-			RY*(1)	0.66	6.48	0.058
Si	11			CR(2)	Si	8	-	Si	11	σ*	0.62	5.78	0.053
					H	12	-			RY*(1)	0.62	6.53	0.057
					H	13	-			RY*(1)	0.64	6.53	0.058
					H	14	-			RY*(1)	0.64	6.53	0.058
Si1	-	H	2	σ	Si	1	-	H	3	σ*	1.36	0.67	0.027
					Si	1	-	Si	4	σ*	1.37	0.56	0.025
					Si	1	-	Si	8	σ*	1.27	0.56	0.024
					Si	4	-	H	7	σ*	1.05	0.66	0.024
					Si	8	-	H	9	σ*	1.20	0.67	0.025
Si1	-	H	3	σ	Si	1	-	H	2	σ*	1.36	0.67	0.027
					Si	1	-	Si	4	σ*	1.37	0.56	0.025
					Si	1	-	Si	8	σ*	1.27	0.56	0.024
					Si	4	-	H	5	σ*	1.05	0.66	0.024
					Si	8	-	H	10	σ*	1.20	0.67	0.025
Si1	-	Si	4	σ	Si	1	-	H	2	σ*	1.02	0.68	0.024
					Si	1	-	H	3	σ*	1.02	0.68	0.024
					Si	1	-	Si	8	σ*	0.79	0.57	0.019
					Si	4	-	H	5	σ*	1.17	0.68	0.025
					Si	4	-	H	6	σ*	1.28	0.68	0.026
					Si	4	-	H	7	σ*	1.17	0.68	0.025
					Si	8	-	Si	11	σ*	1.26	0.57	0.024
					Si	8				RY	0.54	0.89	0.02
Si1	-	Si	8	σ	Si	1	-	H	2	σ*	0.91	0.68	0.022
					Si	1	-	H	3	σ*	0.91	0.68	0.022

250

					Si	1	-	Si	4	σ*	1.12	0.58	0.023

Donor					Acceptor					Type	val1	val2	val3
					Si	1	-	Si	4	σ*	1.12	0.58	0.023
					Si	4	-	H	6	σ*	0.98	0.68	0.023
					Si	8	-	H	9	σ*	0.91	0.68	0.022
					Si	8	-	H	10	σ*	0.91	0.68	0.022
					Si	8	-	Si	11	σ*	1.12	0.58	0.023
					Si	11	-	H	12	σ*	0.98	0.68	0.023
Si4	-	H	5	σ	Si	1	-	H	3	σ*	1.23	0.67	0.026
					Si	1	-	Si	4	σ*	1.55	0.56	0.026
					Si	4	-	H	6	σ*	1.55	0.66	0.029
					Si	4	-	H	7	σ*	1.58	0.66	0.029
Si4	-	H	6	σ	Si	1	-	Si	4	σ*	1.34	0.56	0.024
					Si	1	-	Si	8	σ*	1.26	0.56	0.024
					Si	4	-	H	5	σ*	1.58	0.67	0.029
					Si	4	-	H	7	σ*	1.58	0.67	0.029
Si4	-	H	7	σ	Si	1	-	H	2	σ*	1.23	0.67	0.026
					Si	1	-	Si	4	σ*	1.55	0.56	0.026
					Si	4	-	H	5	σ*	1.58	0.66	0.029
					Si	4	-	H	6	σ*	1.55	0.66	0.029
Si8	-	H	9	σ	Si	1	-	H	2	σ*	1.20	0.67	0.025
					Si	1	-	Si	8	σ*	1.27	0.56	0.024
					Si	8	-	H	10	σ*	1.36	0.67	0.027
					Si	1	-	Si	11	σ*	1.37	0.56	0.025
					Si	11	-	H	14	σ*	1.05	0.66	0.024
Si8	-	H	10	σ	Si	1	-	H	3	σ*	1.20	0.67	0.025
					Si	1	-	Si	8	σ*	1.27	0.56	0.024
					Si	8	-	H	9	σ*	1.36	0.67	0.027
					Si	1	-	Si	11	σ*	1.37	0.56	0.025
					Si	11	-	H	13	σ*	1.05	0.66	0.024
Si8	-	Si	11	σ	Si	1	-	Si	4	σ*	1.26	0.57	0.024
					Si	1	-	Si	8	σ*	0.79	0.57	0.019
					Si	8	-	H	9	σ*	1.02	0.68	0.024
					Si	8	-	H	10	σ*	1.02	0.68	0.024
					Si	11	-	H	12	σ*	1.28	0.68	0.026
					Si	11	-	H	13	σ*	1.17	0.68	0.025
					Si	11	-	H	14	σ*	1.17	0.68	0.025
					Si	1				RY	0.54	0.89	0.02
Si11	-	H	12	σ	Si	1	-	Si	8	σ*	1.26	0.56	0.024
					Si	8	-	Si	11	σ*	1.34	0.56	0.024
					Si	11	-	H	13	σ*	1.58	0.67	0.029
					Si	11	-	H	14	σ*	1.58	0.67	0.029
Si11	-	H	13	σ	Si	8	-	H	10	σ*	1.23	0.67	0.026
					Si	8	-	Si	11	σ*	1.55	0.56	0.026
					Si	11	-	H	12	σ*	1.55	0.66	0.029
					Si	11	-	H	14	σ*	1.58	0.66	0.029
Si11	-	H	14	σ	Si	8	-	H	9	σ*	1.23	0.67	0.026
					Si	8	-	Si	11	σ*	1.55	0.56	0.026
					Si	11	-	H	12	σ*	1.55	0.66	0.029
					Si	11	-	H	13	σ*	1.58	0.66	0.029

Table A4.
b) Second order perturbation theory analysis of Fock matrix in NBO basis for A4N1a
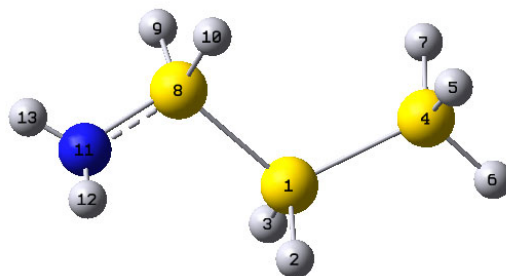
A4N1a

Donor (i)				type	Acceptor (j)					type	E(2)	E(j)-E(i)	F(i,j)
											kcal/mol	a.u.	a.u.
Si	1			CR(2)	Si	1	-	Si	4	σ*	0.54	5.7	0.05
					Si	1	-	Si	8	σ*	0.62	5.71	0.053
					H	2				RY*(1)	0.65	6.46	0.058
					H	3				RY*(1)	0.67	6.46	0.059
Si	4			CR(2)	Si	1	-	Si	4	σ*	0.63	5.78	0.054
					Si	1				RY*(1)	0.64	5.95	0.055
					H	5				RY*(1)	0.64	6.53	0.058
					H	6				RY*(1)	0.63	6.54	0.057
					H	7				RY*(1)	0.63	6.53	0.057
Si	8			CR(2)	Si	8	-	N	11	σ*	1.37	5.99	0.081
					N	11	-	H	12	σ*	0.99	6.24	0.07
					N	11	-	H	13	σ*	0.96	6.24	0.069
					H	9				RY*(1)	0.58	6.66	0.055
					H	10				RY*(1)	0.53	6.67	0.053
N	11			LP(1)	Si	1	-	Si	8	σ*	1.73	0.43	0.024
					Si	8	-	H	9	σ*	1.88	0.54	0.028
					Si	8	-	H	10	σ*	10.03	0.53	0.065
					Si	8				RY*(1)	3.56	0.87	0.05
					Si	8				RY*(8)	0.66	0.74	0.02
Si	1	-	H	2	σ	Si	1	-	H	3	σ*	1.33	0.67	0.027
						Si	1	-	Si	4	σ*	1.27	0.56	0.024
						Si	1	-	Si	8	σ*	1.41	0.57	0.025
						Si	4	-	H	7	σ*	1.11	0.66	0.024
						Si	8	-	H	9	σ*	0.89	0.69	0.022
Si	1	-	H	3	σ	Si	1	-	H	2	σ*	1.29	0.66	0.026
						Si	1	-	Si	4	σ*	1.41	0.56	0.025
						Si	1	-	Si	8	σ*	1.28	0.57	0.024
						Si	4	-	H	5	σ*	1.09	0.66	0.024
						Si	8	-	H	10	σ*	0.86	0.68	0.022
Si	1	-	Si	4	σ	Si	1	-	H	2	σ*	0.94	0.68	0.023
						Si	1	-	H	3	σ*	1.02	0.68	0.023
						Si	1	-	Si	8	σ*	1.28	0.59	0.024
						Si	4	-	H	5	σ*	1.16	0.67	0.025

					Si	4	-	H	6	σ*	1.28	0.67	0.026

Donor					Acceptor					Type	E(2)	E(j)-E(i)	F(i,j)
					Si	4	-	H	6	σ*	1.28	0.67	0.026
					Si	4	-	H	7	σ*	1.15	0.67	0.025
					Si	8	-	N	11	σ*	1.17	0.66	0.025
Si	1	-	Si	8	σ	Si	1	-	H	2	σ*	0.97	0.67	0.023
					Si	1	-	H	3	σ*	1.01	0.68	0.023
					Si	1	-	Si	4	σ*	1.05	0.57	0.022
					Si	4	-	H	6	σ*	1.1	0.67	0.024
					Si	8	-	H	9	σ*	1.14	0.69	0.025
					Si	8	-	H	10	σ*	1.84	0.69	0.032
					Si	8	-	N	11	σ*	1.12	0.66	0.024
					N	11	-	H	13	σ*	1.65	0.91	0.035
					Si	4				RY*(1)	0.53	0.86	0.019
					N	11				RY*(1)	0.52	1.37	0.024
Si	4	-	H	5	σ	Si	1	-	Si	3	σ*	1.17	0.67	0.025
					Si	1	-	Si	4	σ*	1.55	0.56	0.026
					Si	4	-	H	6	σ*	1.54	0.66	0.029
					Si	4	-	H	7	σ*	1.56	0.66	0.029
Si	4	-	H	6	σ	Si	1	-	Si	4	σ*	1.29	0.56	0.024
					Si	1	-	Si	8	σ*	1.13	0.58	0.023
					Si	4	-	H	5	σ*	1.57	0.66	0.029
					Si	4	-	H	7	σ*	1.56	0.66	0.029
Si	4	-	H	7	σ	Si	1	-	H	2	σ*	1.16	0.66	0.025
					Si	1	-	Si	4	σ*	1.58	0.56	0.027
					Si	4	-	H	5	σ*	1.57	0.66	0.029
					Si	4	-	H	6	σ*	1.52	0.66	0.028
Si	8	-	H	9	σ	Si	1	-	H	2	σ*	1.19	0.66	0.025
					Si	1	-	Si	8	σ*	1.45	0.57	0.026
					Si	8	-	H	10	σ*	2.31	0.68	0.035
					Si	8	-	N	11	σ*	1.37	0.64	0.027
					N	11	-	H	12	σ*	1.81	0.9	0.036
Si	8	-	H	10	σ	Si	1	-	H	3	σ*	1.31	0.66	0.026
					Si	1	-	Si	8	σ*	2.12	0.57	0.031
					Si	8	-	H	9	σ*	2.12	0.68	0.034
					Si	8	-	N	11	σ*	2.19	0.64	0.033
Si	8	-	N	11	σ	Si	1	-	Si	4	σ*	0.57	0.78	0.019
					Si	1	-	Si	8	σ*	1.2	0.79	0.028
					Si	8	-	H	9	σ*	1.92	0.91	0.037
					Si	8	-	H	10	σ*	1.67	0.9	0.035
					N	11	-	H	12	σ*	0.69	1.13	0.025
					N	11	-	H	13	σ*	0.73	1.12	0.026
N	11	-	H	12	σ	Si	8	-	H	9	σ*	0.68	0.9	0.022
N	11	-	H	13	σ	Si	1	-	Si	8	σ*	0.94	0.78	0.024
					Si	8	-	H	9	σ*	0.62	0.89	0.021
					Si	11	-	H	12	σ*	1.55	0.66	0.029
					Si	11	-	H	14	σ*	1.58	0.66	0.029
	Si11	-	H	14	σ	Si	8	-	H	9	σ*	1.23	0.67	0.026
					Si	8	-	Si	11	σ*	1.55	0.56	0.026
					Si	11	-	H	12	σ*	1.55	0.66	0.029
					Si	11	-	H	13	σ*	1.58	0.66	0.029

253

Table A4.
c) Second order perturbation theory analysis of Fock matrix in NBO basis for A4N1s

A4N1s
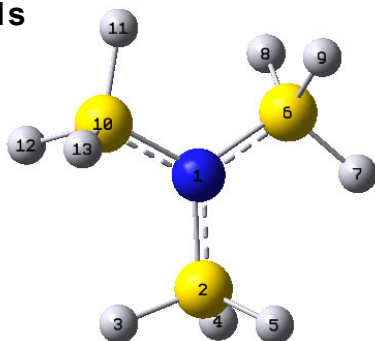
A4N1s

Donor (i)				type	Acceptor (j)					type	E(2)	E(j)-E(i)	F(i,j)
											kcal/mol	a.u.	a.u.
Si	2			CR(2)	N	1	-	Si	2	σ*	1.11	5.99	0.073
					N	1	-	Si	6	σ*	2.35	5.99	0.106
					N	1	-	Si	10	σ*	2.29	5.99	0.105
					Si	2	-	H	4	σ*	0.52	6.05	0.05
					Si	2	-	H	5	σ*	0.52	6.05	0.05
					H	3				RY*(1)	0.51	6.69	0.052
					H	4				RY*(1)	0.57	6.68	0.055
					H	5				RY*(1)	0.57	6.68	0.055
Si	6			CR(2)	N	1	-	Si	2	σ*	2.29	5.99	0.105
					N	1	-	Si	6	σ*	1.1	5.99	0.073
					N	1	-	Si	10	σ*	2.35	5.99	0.106
					Si	6	-	H	8	σ*	0.52	6.05	0.05
					Si	6	-	H	9	σ*	0.52	6.05	0.05
					H	7				RY*(1)	0.51	6.69	0.052
					H	8				RY*(1)	0.57	6.68	0.055
					H	9				RY*(1)	0.57	6.68	0.055
Si	10			CR(2)	N	1	-	Si	2	σ*	2.35	5.99	0.106
					N	1	-	Si	6	σ*	2.29	5.99	0.105
					N	1	-	Si	10	σ*	1.1	5.99	0.073
					Si	10	-	H	12	σ*	0.52	6.05	0.05
					Si	10	-	H	13	σ*	0.52	6.05	0.05
					H	11				RY*(1)	0.51	6.69	0.052
					H	12				RY*(1)	0.57	6.68	0.055
					H	13				RY*(1)	0.57	6.68	0.055
N	1			LP(1)	Si	2	-	H	4	σ*	5.8	0.51	0.049
					Si	2	-	H	5	σ*	5.8	0.51	0.049
					Si	6	-	H	8	σ*	5.8	0.51	0.049
					Si	6	-	H	9	σ*	5.8	0.51	0.049
					Si	10	-	H	12	σ*	5.81	0.51	0.049
					Si	10	-	H	13	σ*	5.81	0.51	0.049
					Si	2				RY*(1)	2.51	0.94	0.043
					Si	2				RY*(4)	1.34	0.56	0.024
					Si	6				RY*(1)	2.53	0.94	0.044
					Si	6				RY*(4)	1.33	0.56	0.024
					Si	10				RY*(1)	2.5	0.94	0.043
					Si	10				RY*(4)	1.33	0.56	0.024
N	1	-	Si	2	σ	N	1	-	Si	2	σ*	0.51	0.84	0.018
					N	1	-	Si	6	σ*	1.91	0.84	0.036
					N	1	-	Si	10	σ*	1.87	0.84	0.035
					Si	2	-	H	3	σ*	2.38	0.89	0.041
					Si	2	-	H	4	σ*	2.08	0.9	0.039
					Si	2	-	H	5	σ*	2.08	0.9	0.039
					Si	6	-	H	7	σ*	1.3	0.89	0.03
					Si	10	-	H	11	σ*	0.74	0.89	0.023
N	1	-	Si	6	σ	N	1	-	Si	2	σ*	1.88	0.84	0.035

						N	1	-	Si	6	σ*	0.51	0.84	0.018
						N	1	-	Si	10	σ*	1.91	0.84	0.036
						Si	2	-	H	3	σ*	0.74	0.89	0.023
						Si	6	-	H	7	σ*	2.38	0.89	0.041
						Si	6	-	H	8	σ*	2.09	0.9	0.039
						Si	6	-	H	9	σ*	2.09	0.9	0.039
						Si	10	-	H	11	σ*	1.3	0.89	0.03
N	1	-	Si	10	σ	N	1	-	Si	2	σ*	1.9	0.84	0.036
						N	1	-	Si	6	σ*	1.87	0.84	0.035
						N	1	-	Si	10	σ*	0.51	0.84	0.019
						Si	2	-	H	3	σ*	1.3	0.89	0.03
						Si	6	-	H	7	σ*	0.74	0.89	0.023
						Si	10	-	H	11	σ*	2.38	0.89	0.041
						Si	10	-	H	12	σ*	2.08	0.9	0.039
						Si	10	-	H	13	σ*	2.08	0.9	0.039
Si	2	-	H	3	σ	N	1	-	Si	2	σ*	1.66	0.62	0.029
						N	1	-	Si	6	σ*	1.71	0.62	0.029
						N	1	-	Si	10	σ*	0.83	0.62	0.02
						Si	2	-	H	4	σ*	2.2	0.68	0.035
						Si	2	-	H	5	σ*	2.2	0.68	0.035
						Si	10	-	H	11	σ*	0.87	0.68	0.022
Si	2	-	H	4	σ	N	1	-	Si	2	σ*	1.63	0.62	0.028
						N	1	-	Si	6	σ*	0.72	0.62	0.019
						N	1	-	Si	10	σ*	1.05	0.62	0.023
						Si	2	-	H	3	σ*	2.04	0.68	0.033
						Si	2	-	H	5	σ*	2.65	0.68	0.038
Si	2	-	H	5	σ	N	1	-	Si	2	σ*	1.63	0.62	0.028
						N	1	-	Si	6	σ*	0.72	0.62	0.019
						N	1	-	Si	10	σ*	1.05	0.62	0.023
						Si	2	-	H	3	σ*	2.04	0.68	0.033
						Si	2	-	H	4	σ*	2.65	0.68	0.038
Si	6	-	H	7	σ	N	1	-	Si	2	σ*	0.83	0.62	0.02
						N	1	-	Si	6	σ*	1.66	0.62	0.029
						N	1	-	Si	10	σ*	1.71	0.62	0.029
						Si	2	-	H	3	σ*	0.87	0.68	0.022
						Si	6	-	H	8	σ*	2.2	0.68	0.035
						Si	6	-	H	9	σ*	2.2	0.68	0.035
Si	6	-	H	8	σ	N	1	-	Si	2	σ*	1.05	0.62	0.023
						N	1	-	Si	6	σ*	1.63	0.62	0.028
						N	1	-	Si	10	σ*	0.72	0.62	0.019
						Si	6	-	H	7	σ*	2.04	0.68	0.033
						Si	6	-	H	9	σ*	2.65	0.68	0.038
Si	6	-	H	9	σ	N	1	-	Si	2	σ*	1.05	0.62	0.023
						N	1	-	Si	6	σ*	1.63	0.62	0.028
						N	1	-	Si	10	σ*	0.72	0.62	0.019
						Si	6	-	H	7	σ*	2.04	0.68	0.033
						Si	6	-	H	8	σ*	2.65	0.68	0.038
Si	10	-	H	11	σ	N	1	-	Si	2	σ*	1.71	0.62	0.029
						N	1	-	Si	6	σ*	0.83	0.62	0.02
						N	1	-	Si	10	σ*	1.66	0.62	0.029
						Si	6	-	H	7	σ*	0.87	0.68	0.022
						Si	10	-	H	12	σ*	2.19	0.68	0.035
						Si	10	-	H	13	σ*	2.19	0.68	0.035
Si	10	-	H	12	σ	N	1	-	Si	2	σ*	0.72	0.62	0.019
						N	1	-	Si	6	σ*	1.05	0.62	0.023
						N	1	-	Si	10	σ*	1.63	0.62	0.028
						Si	10	-	H	11	σ*	2.04	0.68	0.033
						Si	10	-	H	13	σ*	2.65	0.68	0.038
Si	10	-	H	13	σ	N	1	-	Si	2	σ*	0.72	0.62	0.019
						N	1	-	Si	6	σ*	1.05	0.62	0.023
						N	1	-	Si	10	σ*	1.63	0.62	0.028
						Si	10	-	H	11	σ*	2.04	0.68	0.033
						Si	10	-	H	12	σ*	2.65	0.68	0.038

255

Table A4.
d) Second order perturbation theory analysis of Fock matrix in NBO basis for A4N2a

A4N2a

A4N2a

Donor (i)				type	Acceptor (j)					type	E(2) kcal/mol	E(j)-E(i) a.u.	F(i,j) a.u.
Si	1			CR(2)	Si	1	-	N	8	σ*	0.85	6.15	0.065
					Si	1	-	N	10	σ*	1.09	6.16	0.073
					Si	4	-	N	8	σ*	2.65	6.12	0.114
					N	8	-	H	9	σ*	0.74	6.37	0.061
					N	10	-	H	11	σ*	1.17	6.38	0.077
					N	10	-	H	12	σ*	1.03	6.38	0.072
Si	4			CR(2)	Si	1	-	N	8	σ*	2.41	6.08	0.108
					Si	4	-	N	8	σ*	1.23	6.05	0.077
					N	8	-	H	9	σ*	0.78	6.3	0.063
					H	5				RY*(1)	0.54	6.72	0.054
					H	6				RY*(1)	0.57	6.71	0.055
					H	7				RY*(1)	0.54	6.71	0.054
N	8			LP(1)	Si	1	-	H	3	σ*	7.05	0.53	0.055
					Si	1	-	N	10	σ*	5.91	0.51	0.049
					Si	4	-	H	5	σ*	8.34	0.51	0.058
					Si	4	-	H	6	σ*	1.2	0.51	0.022
					Si	4	-	H	7	σ*	3.52	0.5	0.038
					Si	1				RY*(2)	2.56	1.01	0.045
					Si	4				RY*(1)	2.86	0.9	0.045
					Si	4				RY*(4)	1.19	0.67	0.025
N	10			LP(1)	Si	1	-	H	2	σ*	8.48	0.54	0.061
					Si	1	-	H	3	σ*	0.65	0.54	0.017
					Si	1	-	N	8	σ*	6.84	0.52	0.053
					Si	1				RY*(1)	2.27	0.94	0.041
					Si	1				RY*(2)	0.86	1.03	0.027
					Si	1				RY*(8)	0.58	0.95	0.021
Si	1	- H	2	σ	Si	1	-	H	3	σ*	2.64	0.7	0.038
					Si	1	-	N	8	σ*	2.02	0.67	0.033
					Si	1	-	N	10	σ*	2.22	0.68	0.035
					Si	4	-	N	8	σ*	0.75	0.64	0.019
					N	8	-	H	9	σ*	1.66	0.89	0.034
Si	1	- H	3	σ	Si	1	-	H	2	σ*	2.74	0.69	0.039
					Si	1	-	N	8	σ*	1.66	0.67	0.03
					Si	1	-	N	10	σ*	1.87	0.68	0.032
					Si	4	-	N	8	σ*	0.97	0.64	0.022
					N	10	-	H	11	σ*	2.27	0.9	0.04
Si	1	- N	8	σ	Si	1	-	H	2	σ*	3.1	0.93	0.048
					Si	1	-	H	3	σ*	1.53	0.93	0.034
					Si	1	-	N	10	σ*	1.38	0.91	0.032

						Si	4	-	H	6	σ*	0.75	0.9	0.023
						Si	4	-	N	8	σ*	1.37	0.87	0.031
						N	8	-	H	9	σ*	1.12	1.12	0.032
						N	10	-	H	12	σ*	0.56	1.13	0.022
Si	1	-	N	10	σ	Si	1	-	H	2	σ*	1.62	0.93	0.035
						Si	1	-	H	3	σ*	2.97	0.93	0.047
						Si	1	-	N	8	σ*	1.61	0.9	0.034
						Si	4	-	N	8	σ*	0.75	0.87	0.023
						N	10	-	H	11	σ*	0.76	1.14	0.026
						N	10	-	H	12	σ*	0.74	1.13	0.026
Si	4	-	H	5	σ	Si	1	-	N	8	σ*	0.74	0.68	0.02
						Si	4	-	H	6	σ*	2.24	0.68	0.035
						Si	4	-	H	7	σ*	2.51	0.68	0.037
						Si	4	-	N	8	σ*	1.78	0.64	0.03
Si	4	-	H	6	σ	Si	4	-	H	5	σ*	2.34	0.68	0.036
						Si	4	-	H	7	σ*	1.98	0.68	0.033
						Si	4	-	N	8	σ*	1.63	0.65	0.029
						N	8	-	H	9	σ*	1.36	0.9	0.031
Si	4	-	H	7	σ	Si	1	-	N	8	σ*	1.5	0.68	0.028
						Si	4	-	H	5	σ*	2.66	0.68	0.038
						Si	4	-	H	6	σ*	1.92	0.68	0.032
						Si	4	-	N	8	σ*	1.46	0.65	0.027
Si	4	-	N	8	σ	Si	1	-	H	2	σ*	0.78	0.93	0.024
						Si	1	-	N	8	σ*	1.06	0.9	0.028
						Si	1	-	N	10	σ*	0.53	0.91	0.02
						Si	4	-	H	5	σ*	1.92	0.9	0.037
						Si	4	-	H	6	σ*	2.1	0.9	0.039
						Si	4	-	H	7	σ*	2.02	0.9	0.038
						N	8	-	H	9	σ*	1.12	1.12	0.032
N	8	-	H	9	σ	Si	1	-	N	8	σ*	0.51	0.88	0.019
						Si	4	-	H	6	σ*	0.68	0.88	0.022
						Si	4	-	H	7	σ*	0.52	0.88	0.019
N	10	-	H	12	σ	Si	1	-	H	3	σ*	0.74	0.91	0.023
						Si	1	-	N	8	σ*	0.73	0.89	0.023

Table A4.
e) Second order perturbation theory analysis of Fock matrix in NBO basis for HN0

HN0
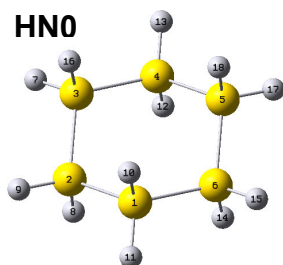
Donor (i)					type	Acceptor (j)					type	E(2) kcal/mol	E(j)-E(i) a.u.	F(i,j) a.u.
Si	1				CR(2)	H	10				RY*(1)	0.66	6.51	0.058
						H	11				RY*(1)	0.64	6.52	0.058
Si	2				CR(2)	H	8				RY*(1)	0.66	6.51	0.058
						H	9				RY*(1)	0.64	6.52	0.058
Si	3				CR(2)	H	7				RY*(1)	0.64	6.52	0.058
						H	16				RY*(1)	0.66	6.51	0.058
Si	4				CR(2)	H	12				RY*(1)	0.66	6.51	0.058
						H	13				RY*(1)	0.64	6.52	0.058
Si	5				CR(2)	H	17				RY*(1)	0.64	6.52	0.058
						H	18				RY*(1)	0.66	6.51	0.058
Si	6				CR(2)	H	14				RY*(1)	0.66	6.51	0.058
						H	15				RY*(1)	0.64	6.52	0.058
Si	1	-	Si	2	σ	Si	1	-	Si	6	σ*	0.94	0.57	0.021
						Si	1	-	H	10	σ*	0.93	0.68	0.022
						Si	1	-	H	11	σ*	1.01	0.68	0.023
						Si	2	-	Si	3	σ*	0.95	0.57	0.021
						Si	2	-	H	8	σ*	0.93	0.68	0.022
						Si	2	-	H	9	σ*	1.01	0.68	0.023
						Si	3	-	H	7	σ*	1.23	0.68	0.026
						Si	6	-	H	15	σ*	1.22	0.68	0.026
						Si	6	-			RY*(1)	0.50	1.02	0.02
Si	1	-	Si	6	σ	Si	1	-	Si	2	σ*	0.94	0.57	0.021
						Si	1	-	H	10	σ*	0.93	0.68	0.022
						Si	1	-	H	11	σ*	1.02	0.68	0.023
						Si	2	-	H	9	σ*	1.23	0.68	0.026
						Si	5	-	Si	6	σ*	0.95	0.57	0.021
						Si	5	-	H	17	σ*	1.23	0.68	0.026
						Si	6	-	H	14	σ*	0.93	0.68	0.022
						Si	6	-	H	15	σ*	1.02	0.68	0.023
						Si	2	-			RY*(1)	0.50	1.02	0.02
Si	1	-	H	10	σ	Si	1	-	Si	2	σ*	1.27	0.56	0.024
						Si	1	-	Si	6	σ*	1.27	0.56	0.024
						Si	1	-	H	11	σ*	1.34	0.67	0.027
						Si	2	-	H	8	σ*	1.18	0.67	0.025
						Si	6	-	H	14	σ*	1.18	0.67	0.025
Si	1	-	H	11	σ	Si	1	-	Si	2	σ*	1.07	0.56	0.022
						Si	1	-	Si	6	σ*	1.08	0.56	0.022
						Si	1	-	H	10	σ*	1.37	0.67	0.027
						Si	2	-	Si	3	σ*	1.16	0.56	0.023
						Si	5	-	Si	6	σ*	1.16	0.56	0.023
Si	2	-	Si	3	σ	Si	1	-	Si	2	σ*	0.95	0.57	0.021
						Si	1	-	H	11	σ*	1.22	0.68	0.026
						Si	2	-	H	8	σ*	0.93	0.68	0.022
						Si	2	-	H	9	σ*	1.00	0.68	0.023
						Si	3	-	Si	4	σ*	0.95	0.57	0.021
						Si	3	-	H	7	σ*	1.00	0.68	0.023

258

						Si	3	-	H	16	σ*	0.93	0.68	0.022
						Si	4	-	H	13	σ*	1.21	0.68	0.026
Si	2	-	H	8	σ	Si	1	-	Si	2	σ*	1.27	0.56	0.024
						Si	1	-	H	10	σ*	1.19	0.67	0.025
						Si	2	-	Si	3	σ*	1.27	0.56	0.024
						Si	2	-	H	9	σ*	1.34	0.67	0.027
						Si	3	-	H	16	σ*	1.19	0.67	0.025
Si	2	-	H	9	σ	Si	1	-	Si	2	σ*	1.07	0.56	0.022
						Si	1	-	Si	6	σ*	1.16	0.56	0.023
						Si	2	-	Si	3	σ*	1.07	0.56	0.022
						Si	2	-	H	8	σ*	1.37	0.67	0.027
						Si	3	-	Si	4	σ*	1.16	0.56	0.023
Si	3	-	Si	4	σ	Si	2	-	Si	3	σ*	0.95	0.57	0.021
						Si	2	-	H	9	σ*	1.23	0.68	0.026
						Si	3	-	H	7	σ*	1.02	0.68	0.023
						Si	3	-	H	16	σ*	0.93	0.68	0.022
						Si	4	-	Si	5	σ*	0.94	0.57	0.021
						Si	4	-	H	12	σ*	0.93	0.68	0.022
						Si	4	-	H	13	σ*	1.02	0.68	0.023
						Si	5	-	H	17	σ*	1.23	0.68	0.026
						Si	5	-			RY*(1)	0.50	1.02	0.02
Si	3	-	H	7	σ	Si	1	-	Si	2	σ*	1.16	0.56	0.023
						Si	2	-	Si	3	σ*	1.07	0.56	0.022
						Si	3	-	Si	4	σ*	1.08	0.56	0.022
						Si	3	-	H	16	σ*	1.37	0.67	0.027
						Si	4	-	Si	5	σ*	1.16	0.56	0.023
Si	3	-	H	16	σ	Si	2	-	Si	3	σ*	1.27	0.56	0.024
						Si	2	-	H	8	σ*	1.19	0.67	0.025
						Si	3	-	Si	4	σ*	1.27	0.56	0.024
						Si	3	-	H	7	σ*	1.34	0.67	0.027
						Si	4	-	H	12	σ*	1.19	0.67	0.025
Si	4	-	Si	5	σ	Si	3	-	Si	4	σ*	0.94	0.57	0.021
						Si	3	-	H	7	σ*	1.22	0.68	0.026
						Si	4	-	H	12	σ*	0.93	0.68	0.022
						Si	4	-	H	13	σ*	1.01	0.68	0.023
						Si	5	-	Si	6	σ*	0.95	0.57	0.021
						Si	5	-	H	17	σ*	1.01	0.68	0.023
						Si	5	-	H	18	σ*	0.93	0.68	0.022
						Si	6	-	H	15	σ*	1.23	0.68	0.026
						Si	3	-			RY*(1)	0.50	1.02	0.02
Si	4	-	H	12	σ	Si	3	-	Si	4	σ*	1.27	0.56	0.024
						Si	3	-	H	16	σ*	1.18	0.67	0.025
						Si	4	-	Si	5	σ*	1.27	0.56	0.024
						Si	4	-	H	13	σ*	1.34	0.67	0.027
						Si	5	-	H	18	σ*	1.18	0.67	0.025
Si	4	-	H	13	σ	Si	2	-	Si	3	σ*	1.16	0.56	0.023
						Si	3	-	Si	4	σ*	1.07	0.56	0.022
						Si	4	-	Si	5	σ*	1.07	0.56	0.022
						Si	4	-	H	12	σ*	1.37	0.67	0.027
						Si	5	-	Si	6	σ*	1.16	0.56	0.023
Si	5	-	Si	6	σ	Si	1	-	Si	6	σ*	0.95	0.57	0.021
						Si	1	-	H	11	σ*	1.21	0.68	0.026
						Si	4	-	Si	5	σ*	0.95	0.57	0.021
						Si	4	-	H	13	σ*	1.22	0.68	0.026
						Si	5	-	H	17	σ*	1.00	0.68	0.023
						Si	5	-	H	18	σ*	0.93	0.68	0.022
						Si	6	-	H	14	σ*	0.93	0.68	0.022
						Si	6	-	H	15	σ*	1.01	0.68	0.023
Si	5	-	H	17	σ	Si	1	-	Si	6	σ*	1.16	0.56	0.023
						Si	3	-	Si	4	σ*	1.16	0.56	0.023
						Si	4	-	Si	5	σ*	1.07	0.56	0.022
						Si	5	-	Si	6	σ*	1.07	0.56	0.022
						Si	5	-	H	18	σ*	1.37	0.67	0.027
Si	5	-	H	18	σ	Si	4	-	Si	5	σ*	1.27	0.56	0.024
						Si	4	-	H	12	σ*	1.19	0.67	0.025
						Si	5	-	Si	6	σ*	1.27	0.56	0.024

Donor (i)				type	Acceptor (j)				type	E(2)	E(j)-E(i)	F(i,j)
					Si	5	-	H	17	σ*	1.34	0.67	0.027
					Si	6	-	H	14	σ*	1.19	0.67	0.025
Si	6	-	H 14	σ	Si	1	-	Si	6	σ*	1.27	0.56	0.024
					Si	1	-	H	10	σ*	1.19	0.67	0.025
					Si	5	-	Si	6	σ*	1.27	0.56	0.024
					Si	5	-	H	18	σ*	1.19	0.67	0.025
					Si	6	-	H	15	σ*	1.34	0.67	0.027
Si	6	-	H 15	σ	Si	1	-	Si	2	σ*	1.16	0.56	0.023
					Si	1	-	Si	6	σ*	1.08	0.56	0.022
					Si	4	-	Si	5	σ*	1.16	0.56	0.023
					Si	5	-	Si	6	σ*	1.07	0.56	0.022
					Si	6	-	H	14	σ*	1.37	0.67	0.027

Table A4.
f) Second order perturbation theory analysis of Fock matrix in NBO basis for HN1

HN1
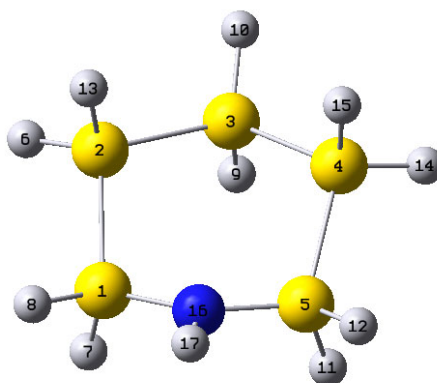
HN1

Donor (i)		type	Acceptor (j)					type	E(2)	E(j)-E(i)	F(i,j)
									kcal/mol	a.u.	a.u.
Si	1	CR(2)	Si	1	-	N	16	σ*	1.2	5.96	0.075
			Si	5	-	N	16	σ*	2.79	5.96	0.115
			N	16	-	H	17	σ*	0.62	6.21	0.055
			H	7				RY*(1)	0.57	6.65	0.055
			H	8				RY*(1)	0.55	6.65	0.054
Si	2	CR(2)	Si	1	-	Si	2	σ*	0.56	5.73	0.051
			H	6				RY*(1)	0.65	6.5	0.058
			H	13				RY*(1)	0.67	6.5	0.059
Si	3	CR(2)	H	9				RY*(1)	0.66	6.5	0.058
			H	10				RY*(1)	0.65	6.5	0.058
Si	4	CR(2)	Si	4	-	Si	5	σ*	0.56	5.73	0.051
			H	14				RY*(1)	0.65	6.5	0.058
			H	15				RY*(1)	0.67	6.5	0.059
Si	5	CR(2)	Si	1	-	N	16	σ*	2.79	5.96	0.115
			Si	5	-	N	16	σ*	1.2	5.96	0.075
			N	16	-	H	17	σ*	0.62	6.21	0.055
			H	11				RY*(1)	0.57	6.65	0.055
			H	12				RY*(1)	0.55	6.65	0.054
N	16	LP(1)	Si	1	-	Si	2	σ*	3.66	0.4	0.034
			Si	1	-	H	7	σ*	8.38	0.51	0.059

Donor	Type	Acceptor	Type			
		Si 4 - Si 5	σ*	3.67	0.4	0.034
		Si 5 - H 11	σ*	8.38	0.51	0.059
		Si 1	RY*(1)	3.01	0.9	0.046
		Si 1	RY*(6)	0.96	0.73	0.024
		Si 5	RY*(1)	3.01	0.9	0.046
		Si 5	RY*(6)	0.96	0.73	0.024
Si 1 - Si 2	σ	Si 1 - H 7	σ*	1.82	0.69	0.032
		Si 1 - H 8	σ*	1.37	0.69	0.027
		Si 1 - N 16	σ*	1.21	0.64	0.025
		Si 2 - Si 3	σ*	0.87	0.57	0.020
		Si 2 - H 6	σ*	0.96	0.68	0.023
		Si 2 - H 13	σ*	1.04	0.68	0.024
		Si 3 - H 10	σ*	1.59	0.68	0.029
		Si 5 - N 16	σ*	0.76	0.64	0.020
		N 16 - H 17	σ*	0.89	0.9	0.025
Si 1 - H 7	σ	Si 1 - Si 2	σ*	2.23	0.56	0.032
		Si 1 - H 8	σ*	1.91	0.68	0.032
		Si 1 - N 16	σ*	1.74	0.63	0.030
		Si 2 - H 13	σ*	1.24	0.66	0.026
		Si 5 - N 16	σ*	0.74	0.63	0.019
Si 1 - H 8	σ	Si 1 - Si 2	σ*	1.37	0.57	0.025
		Si 1 - H 7	σ*	2.13	0.68	0.034
		Si 1 - N 16	σ*	1.45	0.64	0.027
		Si 2 - Si 3	σ*	1.08	0.56	0.022
		Si 5 - N 16	σ*	2.09	0.64	0.033
Si 1 - N 16	σ	Si 1 - Si 2	σ*	1.37	0.79	0.029
		Si 1 - H 7	σ*	1.8	0.91	0.036
		Si 1 - H 8	σ*	1.87	0.91	0.037
		Si 2 - H 6	σ*	0.52	0.89	0.019
		Si 5 - N 16	σ*	1.44	0.86	0.031
		N 16 - H 17	σ*	1.05	1.12	0.031
Si 2 - Si 3	σ	Si 1 - Si 2	σ*	1.08	0.58	0.022
		Si 1 - H 8	σ*	0.96	0.69	0.023
		Si 2 - H 6	σ*	0.98	0.68	0.023
		Si 2 - H 13	σ*	0.88	0.68	0.022
		Si 3 - Si 4	σ*	0.91	0.57	0.020
		Si 3 - H 9	σ*	0.92	0.68	0.022
		Si 3 - H 10	σ*	0.98	0.68	0.023
		Si 4 - H 14	σ*	1.46	0.68	0.028
		Si 4	RY*(1)	0.55	0.99	0.021
Si 2 - H 6	σ	Si 1 - Si 2	σ*	1.51	0.57	0.026
		Si 1 - N 16	σ*	1.28	0.64	0.026
		Si 2 - Si 3	σ*	1.04	0.56	0.022
		Si 2 - H 13	σ*	1.38	0.67	0.027
		Si 3 - Si 4	σ*	0.97	0.56	0.021
Si 2 - H 13	σ	Si 1 - Si 2	σ*	1.26	0.57	0.024
		Si 1 - H 7	σ*	0.88	0.68	0.022
		Si 2 - Si 3	σ*	1.19	0.56	0.023
		Si 2 - H 6	σ*	1.42	0.67	0.028
		Si 3 - H 9	σ*	1.18	0.66	0.025
Si 3 - Si 4	σ	Si 2 - Si 3	σ*	0.91	0.57	0.020
		Si 2 - H 6	σ*	1.46	0.68	0.028
		Si 3 - H 9	σ*	0.92	0.68	0.022
		Si 3 - H 10	σ*	0.98	0.68	0.023
		Si 4 - Si 5	σ*	1.08	0.58	0.022
		Si 4 - H 14	σ*	0.98	0.68	0.023
		Si 4 - H 15	σ*	0.88	0.68	0.022

						Si	5	-	H	12	σ*	0.96	0.69	0.023
						Si	2				RY*(1)	0.55	0.99	0.021
Si	3	-	H	9	σ	Si	2	-	Si	3	σ*	1.22	0.56	0.023
						Si	2	-	H	13	σ*	1.16	0.67	0.025
						Si	3	-	Si	4	σ*	1.22	0.56	0.023
						Si	3	-	H	10	σ*	1.47	0.67	0.028
						Si	4	-	H	15	σ*	1.16	0.67	0.025
Si	3	-	H	10	σ	Si	1	-	Si	2	σ*	0.93	0.57	0.021
						Si	2	-	Si	3	σ*	1.11	0.56	0.022
						Si	3	-	Si	4	σ*	1.11	0.56	0.022
						Si	3	-	H	9	σ*	1.41	0.67	0.027
						Si	4	-	Si	5	σ*	0.93	0.57	0.021
Si	4	-	Si	5	σ	Si	1	-	N	16	σ*	0.76	0.64	0.020
						Si	3	-	Si	4	σ*	0.87	0.57	0.020
						Si	3	-	H	10	σ*	1.59	0.68	0.029
						Si	4	-	H	14	σ*	0.96	0.68	0.023
						Si	4	-	H	15	σ*	1.04	0.68	0.024
						Si	5	-	H	11	σ*	1.82	0.69	0.032
						Si	5	-	H	12	σ*	1.37	0.69	0.027
						Si	5	-	N	16	σ*	1.21	0.64	0.025
						N	16	-	H	17	σ*	0.89	0.9	0.025
Si	4	-	H	14	σ	Si	2	-	Si	3	σ*	0.97	0.56	0.021
						Si	3	-	Si	4	σ*	1.04	0.56	0.022
						Si	4	-	Si	5	σ*	1.51	0.57	0.026
						Si	4	-	H	15	σ*	1.38	0.67	0.027
						Si	5	-	N	16	σ*	1.28	0.64	0.026
Si	4	-	H	15	σ	Si	3	-	Si	4	σ*	1.19	0.56	0.023
						Si	3	-	H	9	σ*	1.18	0.66	0.025
						Si	4	-	Si	5	σ*	1.26	0.57	0.024
						Si	4	-	H	14	σ*	1.43	0.67	0.028
						Si	5	-	H	11	σ*	0.88	0.68	0.022
Si	5	-	H	11	σ	Si	1	-	N	16	σ*	0.74	0.63	0.019
						Si	4	-	Si	5	σ*	2.23	0.56	0.032
						Si	4	-	H	15	σ*	1.24	0.66	0.026
						Si	5	-	H	12	σ*	1.91	0.68	0.032
						Si	5	-	N	16	σ*	1.74	0.63	0.030
Si	5	-	H	12	σ	Si	1	-	N	16	σ*	2.09	0.64	0.033
						Si	3	-	Si	4	σ*	1.08	0.56	0.022
						Si	4	-	Si	5	σ*	1.37	0.57	0.025
						Si	5	-	H	11	σ*	2.13	0.68	0.034
						Si	5	-	N	16	σ*	1.45	0.64	0.027
Si	5	-	N	16	σ	Si	1	-	N	16	σ*	1.44	0.86	0.031
						Si	4	-	Si	5	σ*	1.37	0.79	0.029
						Si	4	-	H	14	σ*	0.52	0.89	0.019
						Si	5	-	H	11	σ*	1.8	0.91	0.036
						Si	5	-	H	12	σ*	1.87	0.91	0.037
						N	16	-	H	17	σ*	1.05	1.12	0.031
N	16	-	H	17	σ	Si	1	-	Si	2	σ*	0.74	0.77	0.021
						Si	1	-	H	8	σ*	0.99	0.89	0.026
						Si	1	-	N	16	σ*	0.54	0.84	0.019
						Si	4	-	Si	5	σ*	0.73	0.77	0.021
						Si	5	-	H	12	σ*	0.99	0.89	0.026
						Si	5	-	N	16	σ*	0.54	0.84	0.019

Table A4.

g) Second order perturbation theory analysis of Fock matrix in NBO basis for HN3

HN3

HN3

Donor (i)		type	Acceptor (j)					type	E(2) kcal/mol	E(j)-E(i) a.u.	F(i,j) a.u.
Si	1	CR(2)	Si	1	-	N	10	σ*	0.9	6.12	0.066
			Si	1	-	N	12	σ*	0.92	6.12	0.067
			Si	2	-	N	12	σ*	2.5	6.12	0.110
			Si	3	-	N	10	σ*	2.52	6.12	0.111
			N	10	-	H	11	σ*	0.7	6.35	0.059
			N	12	-	H	13	σ*	0.91	6.36	0.068
			H	4	-			RY*(1)	0.5	6.77	0.052
			H	5	-			RY*(1)	0.51	6.77	0.052
Si	2	CR(2)	Si	1	-	N	12	σ*	2.49	6.12	0.110
			Si	2	-	N	12	σ*	1.08	6.11	0.072
			Si	2	-	N	14	σ*	1.08	6.11	0.072
			Si	3	-	N	14	σ*	2.49	6.12	0.110
			N	12	-	H	13	σ*	0.84	6.35	0.065
			N	14	-	H	15	σ*	0.84	6.35	0.065
			H	6	-			RY*(1)	0.55	6.77	0.054
Si	3	CR(2)	Si	1	-	N	10	σ*	2.52	6.12	0.111
			Si	2	-	N	14	σ*	2.5	6.12	0.110
			Si	3	-	N	10	σ*	0.9	6.12	0.066
			Si	3	-	N	14	σ*	0.93	6.12	0.067
			N	10	-	H	11	σ*	0.7	6.35	0.059
			N	14	-	H	15	σ*	0.91	6.36	0.068
			H	8	-			RY*(1)	0.5	6.77	0.052
			H	9	-			RY*(1)	0.51	6.77	0.052
N	10	LP(1)	Si	1	-	H	4	σ*	0.87	0.53	0.019
			Si	1	-	H	5	σ*	7.61	0.53	0.057
			Si	1	-	N	12	σ*	5.31	0.5	0.046
			Si	2	-	H	7	σ*	0.7	0.53	0.017
			Si	3	-	H	8	σ*	0.87	0.53	0.019
			Si	3	-	H	9	σ*	7.61	0.53	0.057
			Si	3	-	N	14	σ*	5.31	0.5	0.046
			Si	1	-			RY*(1)	0.91	0.97	0.026
			Si	1	-			RY*(2)	1.97	1.02	0.040
			Si	1	-			RY*(7)	0.78	0.77	0.022
			Si	3	-			RY*(1)	0.91	0.97	0.027
			Si	3	-			RY*(2)	1.97	1.02	0.040
			Si	3	-			RY*(7)	0.78	0.77	0.022
N	12	LP(1)	Si	1	-	H	4	σ*	7.83	0.53	0.057
			Si	1	-	H	5	σ*	3.16	0.53	0.036
			Si	1	-	N	10	σ*	1.75	0.49	0.026
			Si	2	-	H	6	σ*	5.46	0.54	0.048
			Si	2	-	N	14	σ*	8.27	0.49	0.057
			Si	1	-			RY*(1)	1.59	0.97	0.035
			Si	1	-			RY*(2)	1.74	1.02	0.038
			Si	2	-			RY*(1)	1.71	0.97	0.036
			Si	2	-			RY*(2)	0.63	1.01	0.023
			Si	2	-			RY*(7)	0.8	0.67	0.021
N	14	LP(1)	Si	2	-	H	6	σ*	5.45	0.54	0.048
			Si	2	-	N	12	σ*	8.29	0.49	0.057

263

Donor		Acceptor		E(2)		
		Si 3 - H 8	σ*	7.83	0.53	0.057
		Si 3 - H 9	σ*	3.15	0.53	0.036
		Si 3 - N 10	σ*	1.76	0.49	0.026
		Si 2 -	RY*(1)	1.71	0.97	0.036
		Si 2 -	RY*(2)	0.63	1.01	0.023
		Si 2 -	RY*(7)	0.8	0.67	0.021
		Si 3 -	RY*(1)	1.58	0.97	0.035
		Si 3 -	RY*(2)	1.74	1.02	0.038
Si 1 - H 4	σ	Si 1 - H 5	σ*	3.32	0.7	0.043
		Si 1 - N 10	σ*	1.74	0.66	0.030
		Si 1 - N 12	σ*	1.6	0.67	0.029
		Si 2 - N 12	σ*	0.86	0.66	0.021
		Si 3 - N 10	σ*	2	0.66	0.032
Si 1 - H 5	σ	Si 1 - H 4	σ*	3.19	0.7	0.042
		Si 1 - N 10	σ*	1.77	0.66	0.031
		Si 1 - N 12	σ*	2.11	0.67	0.034
		Si 2 - N 12	σ*	1.53	0.66	0.028
		Si 3 - N 10	σ*	0.63	0.66	0.018
Si 1 - N 10	σ	Si 1 - H 4	σ*	2.61	0.93	0.044
		Si 1 - H 5	σ*	1.61	0.92	0.034
		Si 1 - N 12	σ*	2.08	0.89	0.038
		Si 2 - N 12	σ*	0.56	0.89	0.020
		Si 3 - N 10	σ*	1.26	0.89	0.030
		Si 3 - N 14	σ*	0.58	0.89	0.020
		N 10 - H 11	σ*	1.11	1.12	0.031
		N 12 - H 13	σ*	0.73	1.13	0.026
Si 1 - N 12	σ	Si 1 - H 4	σ*	1.57	0.92	0.034
		Si 1 - H 5	σ*	2.78	0.92	0.045
		Si 1 - N 10	σ*	1.99	0.88	0.037
		Si 2 - H 7	σ*	0.66	0.92	0.022
		Si 2 - N 12	σ*	1.27	0.88	0.030
		N 12 - H 13	σ*	1.12	1.12	0.032
Si 2 - H 6	σ	Si 1 - N 12	σ*	0.78	0.67	0.020
		Si 2 - H 7	σ*	2.47	0.7	0.037
		Si 2 - N 12	σ*	2.17	0.66	0.034
		Si 2 - N 14	σ*	2.17	0.66	0.034
		Si 3 - N 14	σ*	0.78	0.66	0.020
		N 12 - H 13	σ*	0.71	0.9	0.022
		N 14 - H 15	σ*	0.71	0.9	0.023
Si 2 - H 7	σ	Si 1 - N 12	σ*	1.76	0.67	0.031
		Si 2 - H 6	σ*	2.62	0.71	0.039
		Si 2 - N 12	σ*	2.01	0.67	0.033
		Si 2 - N 14	σ*	2.01	0.67	0.033
		Si 3 - N 14	σ*	1.76	0.67	0.031
Si 2 - N 12	σ	Si 1 - N 10	σ*	1.5	0.88	0.032
		Si 1 - N 12	σ*	1.51	0.89	0.033
		Si 2 - H 6	σ*	2.62	0.93	0.044
		Si 2 - H 7	σ*	2.03	0.92	0.039
		Si 2 - N 12	σ*	0.54	0.88	0.019
		Si 2 - N 14	σ*	1.84	0.88	0.036
		N 12 - H 13	σ*	1.01	1.12	0.030
Si 2 - N 14	σ	Si 2 - H 6	σ*	2.62	0.93	0.044
		Si 2 - H 7	σ*	2.03	0.92	0.039
		Si 2 - N 12	σ*	1.84	0.88	0.036
		Si 2 - N 14	σ*	0.54	0.88	0.019
		Si 3 - N 10	σ*	1.5	0.88	0.032
		Si 3 - N 14	σ*	1.51	0.89	0.033
		N 14 - H 15	σ*	1.01	1.12	0.030
Si 3 - H 8	σ	Si 1 - N 10	σ*	2	0.66	0.032
		Si 2 - N 14	σ*	0.86	0.66	0.021
		Si 3 - H 9	σ*	3.31	0.7	0.043
		Si 3 - N 10	σ*	1.74	0.66	0.030
		Si 3 - N 14	σ*	1.6	0.67	0.029
Si 3 - H 9	σ	Si 1 - N 10	σ*	0.63	0.66	0.018
		Si 2 - N 14	σ*	1.53	0.66	0.028
		Si 3 - H 8	σ*	3.19	0.7	0.042
		Si 3 - N 10	σ*	1.77	0.66	0.031
		Si 3 - N 14	σ*	2.11	0.67	0.034
Si 3 - N 10	σ	Si 1 - N 10	σ*	1.26	0.89	0.030
		Si 1 - N 12	σ*	0.58	0.89	0.020

											σ*	0.56	0.89	0.020
						Si	2	-	N	14	σ*	0.56	0.89	0.020
						Si	3	-	H	8	σ*	2.61	0.93	0.044
						Si	3	-	H	9	σ*	1.61	0.92	0.034
						Si	3	-	N	14	σ*	2.08	0.89	0.038
						N	10	-	H	11	σ*	1.11	1.12	0.031
						N	14	-	H	15	σ*	0.73	1.13	0.026
Si	3	-	N	14	σ	Si	2	-	H	7	σ*	0.66	0.92	0.022
						Si	2	-	N	14	σ*	1.27	0.88	0.030
						Si	3	-	H	8	σ*	1.57	0.92	0.034
						Si	3	-	H	9	σ*	2.78	0.92	0.045
						Si	3	-	N	10	σ*	1.99	0.88	0.037
						N	14	-	H	15	σ*	1.12	1.12	0.032
N	10	-	H	11	σ	Si	1	-	H	4	σ*	0.77	0.91	0.024
						Si	3	-	H	8	σ*	0.77	0.91	0.024
N	12	-	H	13	σ	Si	1	-	N	10	σ*	0.59	0.88	0.020
						Si	2	-	H	7	σ*	0.65	0.91	0.022
N	14	-	H	15	σ	Si	2	-	H	7	σ*	0.65	0.91	0.022
						Si	3	-	N	10	σ*	0.59	0.88	0.020